



University of HUDDERSFIELD

University of Huddersfield Repository

Zeng, Shengyue

Bonnet Polishing of Cobalt Chrome Alloys for Artificial Implants

Original Citation

Zeng, Shengyue (2014) Bonnet Polishing of Cobalt Chrome Alloys for Artificial Implants. Doctoral thesis, University of Huddersfield.

This version is available at <http://eprints.hud.ac.uk/id/eprint/19751/>

The University Repository is a digital collection of the research output of the University, available on Open Access. Copyright and Moral Rights for the items on this site are retained by the individual author and/or other copyright owners. Users may access full items free of charge; copies of full text items generally can be reproduced, displayed or performed and given to third parties in any format or medium for personal research or study, educational or not-for-profit purposes without prior permission or charge, provided:

- The authors, title and full bibliographic details is credited in any copy;
- A hyperlink and/or URL is included for the original metadata page; and
- The content is not changed in any way.

For more information, including our policy and submission procedure, please contact the Repository Team at: E.mailbox@hud.ac.uk.

<http://eprints.hud.ac.uk/>

**BONNET POLISHING OF COBALT CHROME ALLOYS FOR
ARTIFICIAL IMPLANTS**

SHENGYUE ZENG

Supervisor: Prof. Liam Blunt

A thesis submitted to the University of Huddersfield in partial fulfilment of the
requirements for the degree of Doctor of Philosophy

The University of Huddersfield

January 2014

COPYRIGHT STATEMENT

i. The author of this thesis (including any appendices and/or schedules to this thesis) owns any copyright in it (the “Copyright”) and s/he has given The University of Huddersfield the right to use such Copyright for any administrative, promotional, educational and/or teaching purposes.

ii. Copies of this thesis, either in full or in extracts, may be made only in accordance with the regulations of the University Library. Details of these regulations may be obtained from the Librarian. This page must form part of any such copies made.

iii. The ownership of any patents, designs, trademarks and any and all other intellectual property rights except for the Copyright (the “Intellectual Property Rights”) and any reproductions of copyright works, for example graphs and tables (“Reproductions”), which may be described in this thesis, may not be owned by the author and may be owned by third parties. Such Intellectual Property Rights and Reproductions cannot and must not be made available for use without the prior written permission of the owner(s) of then relevant Intellectual Property Rights and/or Reproductions.

ABSTRACT

Cobalt chrome (CoCr) alloys are the most extensively used biomaterials for manufacturing artificial implants which need nanometre scale surface finish and micrometre scale form tolerance to allow long term survival in vivo. Traditional finishing of these devices is usually carried out by manual or simple robot polishing which are time-consuming and labour-intensive. The aim of this thesis is to investigate and develop a deterministic polishing process for improving the surface finish and form tolerance of the bearing surfaces of artificial implants.

In order to improve the surface finish for CoCr alloys, a Taguchi method with the consideration of interaction effects was applied to optimise the process parameters. By using the optimised process parameters, the surface roughness of workpieces can be improved up to 8nm Sa, which is far better than 50nm Ra, the recommended value of ISO 7206-2:2011 for metallic bearing surface of artificial implants.

The evolution of all 15 parameters of surface topography during polishing process has been investigated. In addition, the effects of the combination of polishing cloths/pads and abrasives on surface topography have been investigated as well, indicating that both polishing cloths/pads and abrasives can affect the improvement of surface topography.

A deterministic polishing process is dependent on the material removal which is controlled by process parameters. The way of which material removal and polishing forces were affected by the process parameters has been investigated. Based on the experimental data, a modified Preston equation model was created to predict the material removal rate for bonnet polishing of CoCr alloys.

Form tolerance plays a very significant role in the bearing surfaces of artificial implants. By using the method of form correction, a new design of multi-radius femoral head which is unable to be fabricated by traditional polishing process was successfully manufactured. In addition, form correction was also applied to a roughly ground freeform knee femoral component. The success of the form correction experiments indicated that bonnet polishing is a robust technology when applied to the surfaces of artificial implants.

ACKNOWLEDGEMENT

It would be impossible to finish this research work without the assistance and encouragement of many people who are always willing to give me help. While it may not be a complete list, I am very happy to give my acknowledgments to all of the people who have continuously supported me over the past years.

First and foremost, I would like to express my deepest gratitude to my main supervisor, Prof. Liam Blunt, who has led me into the remarkable field of precision engineering and always gives me the essential support. I am very fortunate to have such a supervisor who is always ready to applaud when I succeed and encourage when I fail. I have learnt a lot from him which I will benefit from forever. Special thanks go to my co-supervisor, Prof. Jane Xiangqian Jiang, who offered me a lot of comments and suggestions on my work.

I would like to thank University of Huddersfield, UK and China Scholarship Council (CSC) for providing me the generous financial support in the form of 100% fee waiver and living expense respectively.

I would also express my thanks to Mr Chris Dawson for continuously providing me the machining support, Mr Karl Walton for the language help, Dr Wenhan Zeng and Dr Radu Racasan for the metrology support, and Xiangqi Lan for the software support.

I also appreciate Dr Feng Gao, Dr Tukun Li, Dr Leigh Fleming, Dr Shan Lou, Dr Jian Wang, Hongyu Ren, Qunfen Qi, Hao Ding, Dr Haydn Martin, Dr Paul Bills and all the other colleagues in the Centre for Precision Technologies for their kind help on my research and life.

Finally, I would like to give special thanks to my parents, my parents-in-law, my beloved wife Xiaomin Chen and my little son William Weiyi Zeng for their support and encouragement.

TABLE OF CONTENTS

COPYRIGHT STATEMENT	2
ABSTRACT	3
ACKNOWLEDGEMENT	4
TABLE OF CONTENTS	5
LIST OF FIGURES	10
LIST OF TABLES	15
PUBLICATION LIST	17
LIST OF ABBREVIATIONS	18
GLOSSARY OF WORDS	21
1. INTRODUCTION	22
1.1 Research background	22
1.1.1 Surface finish	22
1.1.2 Surface geometry	23
1.2 Aim and objectives	24
1.2.1 Aim	24
1.2.2 Objectives	24
1.3 Summary of contributions.....	25
1.4 Structure of the thesis.....	26
2. MANUFACTURING AND METROLOGY FOR ARTIFICIAL IMPLANTS	28
2.1 Introduction.....	28
2.2 Total hip replacement	28
2.2.1 Fixation methods.....	29
2.2.2 Combinations of bearing surface	31
2.2.3 The failure of THR.....	38
2.3 Knee replacement.....	39
2.3.1 Total knee replacement	39
2.3.2 Partial knee replacement	43
2.4 Biomaterials for arthroplasty components	43

2.4.1	Metals and alloys	44
2.4.2	Polymers	55
2.4.3	Ceramics	57
2.4.4	Composites.....	58
2.5	Manufacturing process for CoCr alloy components of arthroplasty.....	59
2.5.1	Investment casting	59
2.5.2	Rough machining	59
2.5.3	Final finishing	61
2.6	Surface metrology.....	61
2.6.1	Geometrical specification standards for artificial joints	61
2.6.2	Instrumentation	62
2.7	Summary	68
3.	POLISHING TECHNOLOGIES FOR BEARING SURFACES OF ARTIFICIAL	
	IMPLANTS	70
3.1	Introduction.....	70
3.2	Polishing	70
3.2.1	Polishing tool	71
3.2.2	Polishing slurry	73
3.2.3	Abrasives.....	74
3.3	Material removal in polishing.....	76
3.3.1	Material removal mechanism.....	76
3.3.2	Material removal model.....	79
3.4	Surface roughness improvement.....	82
3.5	Form correction.....	83
3.6	Types of polishing.....	85
3.6.1	Elastic emission machining.....	85
3.6.2	Magnetorhological finishing.....	86
3.6.3	Ion beaming figuring.....	87
3.6.4	Bonnet tool polishing	88
3.7	Summary	96
4.	OPTIMIZATION OF PROCESS PARAMETERS FOR SURFACE ROUGHNESS	
	IMPROVEMENT	98

4.1	Introduction.....	98
4.2	Interaction effects.....	100
4.2.1	Experimental design.....	100
4.2.2	Experimental results.....	102
4.3	The application of Taguchi method to optimise process parameters.....	106
4.3.1	Experimental design.....	107
4.3.2	Experimental results and analysis	108
4.3.3	The main effects of S/N ratio.....	110
4.3.4	ANOVA	112
4.3.5	Confirmatory experiment.....	114
4.4	Summary	115
5.	THE EFFECTS OF POLISHING CONDITIONS ON SURFACE TOPOGRAPHY	
	117	
5.1	Introduction.....	117
5.2	The evolution of surface topography during polishing.....	120
5.2.1	Amplitude parameters	121
5.2.2	Spacing parameters	122
5.2.3	Hybrid parameters.....	123
5.2.4	Sk family parameters	124
5.2.5	Material/void volume parameters	125
5.2.6	Other parameters	126
5.3	The effects of the combination of polishing cloths/pads and polishing abrasives on surface topography.....	127
5.4	Summary.....	131
6.	MATERIAL REMOVAL INVESTIGATION.....	134
6.1	Introduction.....	134
6.2	The effects of process parameters on material removal.....	135
6.2.1	The effect of dwell time	135
6.2.2	The effect of precess angle	136
6.2.3	The effect of head speed	137
6.2.4	The effect of tool offset.....	139
6.2.5	The effect of tool air pressure	142

6.3	The effects of workpiece hardness.....	144
6.4	The effects of the hardness of polishing pads.....	145
6.5	The effects of process parameters on polishing forces	146
6.5.1	Calibration of force sensor.....	147
6.5.2	Force acquisition.....	148
6.5.3	The variation of polishing force.....	148
6.6	Material removal rate modelling.....	151
6.6.1	Contact pressure P	151
6.6.2	Relative velocity V	155
6.6.3	Verification of the model	157
6.7	Summary	158
7.	FORM CORRECTION.....	160
7.1	Introduction.....	160
7.2	The effect of the tool path on form correction.....	161
7.2.1	Tool path.....	161
7.2.2	Raster polishing	162
7.2.3	Spiral polishing	165
7.3	Polishing of multi-radius femoral head of hip prostheses	169
7.3.1	Experimental procedure	170
7.3.2	Experimental results and discussion	172
7.3.3	Verification of designing error map.....	176
7.4	Polishing of freeform knee femoral components.....	179
7.4.1	Description and creation of freeform surfaces based on NURBS	181
7.4.2	Evaluation of the freeform knee femoral components.....	182
7.4.3	Experimental results and discussion	184
7.5	Summary	186
8.	OVERALL DISCUSSION	188
8.1	Surface roughness improvement.....	188
8.2	The effects of experimental conditions on surface topography	190
8.3	Material removal investigation	192
8.4	Form correction.....	197
9.	CONCLUSIONS AND FUTURE WORK.....	199

9.1	Conclusions.....	199
9.2	Future work.....	201
	REFERENCES.....	203

LIST OF FIGURES

Figure 1.1: Stribeck curve.....	23
Figure 2.1: Representation of THR [26].....	29
Figure 2.2: Typical positioning of THR [27].....	29
Figure 2.3: Fixation methods of THR [27].....	30
Figure 2.4: Trends in use of fixation for hip replacement from 2003 to 2011(Data from NJR report [1]).....	30
Figure 2.5: Metal-on-polyethylene THR [31].....	31
Figure 2.6: Metal-on-metal THR [37].....	32
Figure 2.7: Ceramic-on-ceramic THR [31].....	34
Figure 2.8: Ceramic-on-metal THR [49].....	35
Figure 2.9: Ceramic-on-polymer THR [53].....	36
Figure 2.10: Hip resurfacing [58].....	37
Figure 2.11: Trends in use of bearing surface for hip replacement from 2003 to 2011 (Data from NJR report [1]).....	38
Figure 2.12:: TKR systems [68].....	39
Figure 2.13: Fixation methods of TKR [69].....	40
Figure 2.14: Trend in use of fixation for knee replacement from 2003 to 2011 (Data from NJR report [1]).....	40
Figure 2.15: Ceramic femoral component of knee prosthesis [75].....	42
Figure 2.16: Partial knee replacement [81].....	43
Figure 2.17: Grinding process for knee femoral components [127].....	60
Figure 2.18: Milling process for knee femoral components [129].....	60
Figure 2.19: The principle of RCHD grating transducer [134].....	63
Figure 2.20: Talysurf PGI Series 2.....	64
Figure 2.21: Talysurf CCI.....	65
Figure 2.22: The principle of Talysurf CCI [135].....	66
Figure 2.23: The principle of 4D laser interferometer [137].....	67
Figure 3.1: Polishing tool (Left: without pad, right: with pad).....	71
Figure 3.2: Polishing cloth (left) and polishing pad (right).....	71
Figure 3.3: Fixed-abrasive polishing cloths [141].....	71
Figure 3.4: Self-sharpening process [142].....	72
Figure 3.5: Paste slurry (left) and fluid slurry (right) [141].....	74

Figure 3.6: Graphitisation of diamond [142]	75
Figure 3.7: Material removal mechanism by polishing [150].....	77
Figure 3.8: The four hypotheses of material removal for mechanical-chemical glass polishing [140].....	78
Figure 3.9: Schematic of form correction	83
Figure 3.10: Schematic of EEM process [182].....	86
Figure 3.11: MR fluid delivery system [186]	87
Figure 3.12: Schematic of IBF [189]	88
Figure 3.13: Precession tool concept [192].....	89
Figure 3.14: Influence function obtained with non-precession process (left) and precession process (right)	89
Figure 3.15: Surface texture obtained with non-precession process (left) and precession process (right) [192].....	90
Figure 3.16: Polishing path.....	91
Figure 3.17: Random toolpath [194].....	91
Figure 3.18: IRP series polishing machine [199-201]	93
Figure 3.19: Process parameters of bonnet tool polishing.....	95
Figure 4.1: Graphical displays of process parameter effects	106
Figure 4.2: The main effects of S/N ratio	111
Figure 4.3: Surface roughness before and after polishing under the optimal condition	114
Figure 5.1: Comparison of 2D and areal measurement	117
Figure 5.2: The evolution of amplitude parameters.....	122
Figure 5.3: The evolution of spacing parameters.....	123
Figure 5.4: The evolution of hybrid parameters	124
Figure 5.5: The evolution of Sk family parameters	125
Figure 5.6: The evolution of material/void volume parameters	126
Figure 5.7: The evolution of other parameters.....	127
Figure 6.1: Measurements of the IF and profile V.S. dwell time	135
Figure 6.2: The effect of dwell time on the MRR.....	135
Figure 6.3: Measurement of the IF and profile V.S. precess angle	136
Figure 6.4: The effect of precess angle on the MRR and MRR versus surface speed.....	137
Figure 6.5: Measurements of the IF and profile V.S. head speed.....	138
Figure 6.6: The effect of head speed on the MRR.....	139

Figure 6.7: Measurements of the IF and profile V.S. tool air pressure (1.0bar tool air pressure)	140
Figure 6.8: The deformation of bonnet (FEA simulation, Abaqus 6.90)	140
Figure 6.9: Measurements of the IF and profile V.S. tool offset (0.5bar tool air pressure)	141
Figure 6.10: Measurements of the IF and profile V.S. tool offset (1.5bar tool air pressure)	141
Figure 6.11: Measurements of the IF and profile V.S. tool offset (2.0bar tool air pressure)	141
Figure 6.12: The effect of tool offset on the MRR	142
Figure 6.13: Measurements of the IF and profile V.S. tool air pressure	143
Figure 6.14: The effect of tool air pressure on the MRR	144
Figure 6.15: The effects of workpiece hardness on the MRR	144
Figure 6.16: The effects of tool hardness on the MRR	145
Figure 6.17: Experimental setup with force sensor	146
Figure 6.18: The data collection	147
Figure 6.19: Calibration results	147
Figure 6.20: Labview interface for data acquisition	148
Figure 6.21: Force as a function of precess angle	149
Figure 6.22: Force as a function of head speed	149
Figure 6.23: Force as a function of tool offset	150
Figure 6.24: Force as a function of tool air pressure	151
Figure 6.25: Schematic of the contact between polishing tool and workpiece	152
Figure 6.26: The effect of precess angle on the IF	152
Figure 6.27: The effect of head speed on the IF	152
Figure 6.28: The effect of tool offset on the IF	153
Figure 6.29: The effect of tool air pressure on the IF	153
Figure 6.30: Schematic of velocity distribution	155
Figure 6.31: The comparison of experimental data and predicted data	158
Figure 7.1: The interface of form correction process	160
Figure 7.2: Polishing tool path	161
Figure 7.3: Influence function for tool path investigation	162
Figure 7.4: Surface roughness of 12mm thick copper before polishing	162
Figure 7.5: Form error of 12mm thick copper before polishing	163
Figure 7.6: Surface roughness of 12mm thick copper after the first diamond polishing	163
Figure 7.7: Form error of 12mm thick copper after the first diamond polishing	163
Figure 7.8: Surface roughness of 12mm copper after second diamond polishing	164

Figure 7.9: Form error of 12mm thick copper after second diamond polishing.....	164
Figure 7.10: Surface roughness of 12mm thick copper after third diamond polishing	164
Figure 7.11: Form error of 12mm thick copper after third diamond polishing	165
Figure 7.12: Surface roughness of 8mm thick copper before polishing	166
Figure 7.13: Form error of 8mm thick copper before polishing	167
Figure 7.14: Surface roughness of 8mm thick copper after first polishing	167
Figure 7.15: Form error of 8mm thick copper after first polishing	167
Figure 7.16: Surface roughness of 8mm thick copper after second polishing.....	168
Figure 7.17: Form error of 8mm thick copper after second polishing.....	168
Figure 7.18: The copper before polishing (left) and after polishing (right).....	168
Figure 7.19: Influence function for multi-radius femoral head polishing	171
Figure 7.20: Schematic of the polishing zone.....	171
Figure 7.21: Error map before polishing.....	171
Figure 7.22: Form Talysurf measurement before polishing	172
Figure 7.23: Error map after polishing	173
Figure 7.24: Form Talysurf measurement after polishing	173
Figure 7.25: The surface roughness of the unpolished area, boundary and polished area	174
Figure 7.26: CMM measurement (Displayed by CATIA).....	175
Figure 7.27: Photograph of the machined multi-radius femoral head	175
Figure 7.28: The motion of the workpiece and the polishing tool.....	175
Figure 7.29: Error map of CPT	177
Figure 7.30: The measurement of CPT letters (Mirrored).....	177
Figure 7.31: The photograph of the polished CPT letters.....	178
Figure 7.32: Surface roughness of the polished CPT letters.....	178
Figure 7.33: The average depth of polished CPT letters	178
Figure 7.34: CAD model of knee femoral component	179
Figure 7.35: The influence function for knee femoral component	180
Figure 7.36: Error map of knee femoral component before polishing	180
Figure 7.37: Surface roughness of knee femoral component before polishing	181
Figure 7.38: The created NURBS surface by Rhinoceros 4.0	182
Figure 7.39: Error map of knee femoral component after polishing	184
Figure 7.40: Surface roughness of knee femoral component after polishing measured by PGI	185

Figure 7.41: Surface roughness of knee femoral component after polishing measured by CCI	185
Figure 7.42: The photograph of knee femoral component before and after polishing	186
Figure 8.1: The precess angle variation	189
Figure 8.2: The change of contact area resulting from the precess angle.....	193
Figure 8.3: The effect of the head speed on the IF [246].....	193

LIST OF TABLES

Table 2.1: Chemical composition of CoCr alloys.....	46
Table 2.2: Mechanical properties of typical cobalt based alloys	49
Table 2.3: Chemical composition of CP titanium (wt %).....	50
Table 2.4: Mechanical properties of α - β titanium alloys	52
Table 2.5: Composition of 316L stainless steel	53
Table 2.6: Mechanical properties of 316L stainless steel for implants.....	53
Table 2.7: Comparison of some of the features of metallic biomaterials	54
Table 2.8: Mechanical properties of polymers for orthopaedic devices	56
Table 2.9: Physical and mechanical properties of alumina ceramic	57
Table 2.10: The typical specification of Talysurf PGI Series 2.....	64
Table 2.11: Typical specifications of Talysurf CCI.....	65
Table 2.12 The comparison of instruments.....	67
Table 4.1: The fixed polishing factors	100
Table 4.2: Chemical composition of samples (%wt).....	100
Table 4.3: Factor levels for 16-run experiment	100
Table 4.4: Design matrix for 16-run experiments.....	101
Table 4.5: Experimental results for interaction effects	102
Table 4.6: Response table with all interaction terms	103
Table 4.7: Process parameters with their three levels.....	107
Table 4.8: L27 Orthogonal array	108
Table 4.9: The experimental results of <i>Sa</i> parameter	110
Table 4.10: The main effects of S/N ratio.....	111
Table 4.11: ANOVA.....	113
Table 4.12: The results of confirmatory experiment	115
Table 5.1: The experimental conditions.....	120
Table 5.2: The effects of the combination of LP13 and 6 μ m diamond paste on surface topography	128
Table 5.3: The effects of the combination of LP13 and 1 μ m diamond paste on surface topography	129
Table 5.4: The effects of the combination of Microcloth and 1 μ m diamond paste on surface topography	130
Table 6.1: The polishing factors used during experiments	134

Table 6.2: The machine settings for verification experiments.....	157
Table 6.3: Preston coefficient for different materials	157
Table 7.1: Process parameters for tool path investigation	161
Table 7.2: Process parameters for polishing multi-radius head.....	170

PUBLICATION LIST

1. **S. Zeng**, L. Blunt, X. Jiang, P. Bills. Investigation of the material removal characteristic for polishing CoCr alloy. Computing and Engineering Annual Researchers' Conference, University of Huddersfield, December, 2010.
2. **S. Zeng**, L. Blunt, X. Jiang. Material removal investigation in bonnet polishing of CoCr alloy. Computing and Engineering Annual Researchers' Conference, University of Huddersfield, March, 2012.
3. **Shengyue Zeng**, Liam Blunt, Xiangqian Jiang. The application of Taguchi approach to optimise the processing conditions on bonnet polishing of CoCr. Key Engineering Materials, 2012, Vol 496, pp235-240.
4. **Shengyue Zeng**, Liam Blunt, Xiangqian Jiang. The investigation of material removal in bonnet polishing of CoCr alloy artificial joints (**Heidenhain Scholarship**). 12th International Conference of the European Society for Precision Engineering and Nanotechnology, Stockholm, June, 2012.
5. **S. Zeng**, L. Blunt, R. Racasan. An investigation of the viability of bonnet polishing as a possible method to manufacture hip prostheses with multi-radius femoral heads. The International Journal of Advanced Manufacturing Technology, in press.
6. **Shengyue Zeng**, Liam Blunt. Experimental investigation and analytical modelling of the effects of process parameters on material removal rate for bonnet polishing of cobalt chrome alloy. Precision Engineering, in press.
7. **S. Zeng**, L. Blunt. An experimental study on the correlation of polishing force and material removal for bonnet polishing of cobalt chrome alloy. The International Journal of Advanced Manufacturing Technology, under review.

LIST OF ABBREVIATIONS

AJP	Abrasive jet polishing
Al ₂ O ₃	Aluminium oxide
ANOVA	Analysis of variance
ASTM	American Society for Testing and Materials
B ₄ C	Boron carbide
BCC	Body-Centred Cubic
CAD	Computer aided design
CCD	Charge coupled devices
CCI	Coherence Correlation Interferometer
CCOS	Computer Controlled Optical Surfacing
CeO ₂	Cerium oxide
CMM	Coordinate measuring machine
CMP	Chemical mechanical polishing
CNC	Computer numerical control
CoC	Ceramic-on-ceramic
CoCr	Cobalt chrome
CoM	Ceramic-on-metal
CoP	Ceramic-on-polyethylene
CP	Commercially pure
Cr ₂ O ₃	Chromium oxide
DOE	Design of experiment
DOF	Degree of freedom
EEM	Elastic emission machining
ETO	Ethylene oxide
FCC	Face-Centre Cubic
Fe ₂ O ₃	Ferric oxide
FEA	Finite element analysis
GMS	Glycerin monostearate
HA	Hydroxyapatite
HCP	Hexagonal Closed-Packed
HDP	Hydrodynamic polishing

IBF	Ion beam figuring
IF	Influence function
IRP	Intelligent Robotic Polisher
MoM	Metal-on-metal
MoP	Metal-on-polyethylene
MRF	Magnetorheological finishing
MRR	Material removal rate
NJR	National Joint Registry
NURBS	Non-uniform Rational B-Spline
OA	Orthogonal Arrays
PEEK	Polyetheretherketone
PGI	Phase grating interferometer
PMMA	Poly-methyl-methacrylate
PSI	Phase shifting interferometry
PV	Peak-to-valley
PZT	Piezo-electric actuators
RCHD	Reflective cylindrical holographic diffraction
RMS	Root-mean-square
S5z	Ten point height of the surface
Sa	Arithmetic mean of the absolute value of the height
Sal	The fastest decay auto-correlation length
Sdq	Root-mean-square slope of the assessed topographic surface
Sdr	Developed interfacial area ratio
Sds	Density of summits of the surface
SiC	Silicon carbide
Sk	Core roughness depth
Sku	Kurtosis of topography height distribution
Smr1	Peak material component
Smr2	Peak material component
Sp	The maximum surface peak height
Spk	Reduced peak height
Sq	Root-mean-square
Ssc	Arithmetic mean summit curvature of the surface

Ssk	Skewness of topography height distribution
Std	The lay direction of the surface
Str	Texture aspect ratio of the surface
Sv	The lowest valley of the surface
Svk	Reduced valley height
Sz	Maximum height of the topographic surface
TKR	Total knee replacement
THR	Total hip replacement
UHMWPE	Ultra-high molecular weight polyethylene
UHXLPE	Ultra highly molecular weight cross-linked polyethylene
Vmc	Core material volume of the topographic surface
Vmp	Peak material volume of the topographic surface
VSI	Vertical scanning interferometry
Vvc	Core void volume of the surface
Vvv	Valley void volume of the surface
XRF	X-Ray Fluorescence
ZrO ₂	Zirconium oxide

GLOSSARY OF WORDS

Acetabulum: is a concave surface of the pelvis which meets with the head of femur at the acetabulum, forming the hip joint.

Arthroplasty: is an orthopaedic surgery procedure used to replace the damaged joint to relieve pain and restore function.

Cytotoxicity: is the quality of being toxic to cells.

Endoprosthesis: is an artificial device placed inside the body to replace a missing or damaged part of a human body.

Femoral diaphysis: is a shaft of the long femoral bone.

Isostatic: the quality or state of being subjected to equal pressure from every side is the same.

Osteolysis: refers to the dissolution of bone related to an active resorption.

Periprosthetic fractures: are the fractures around joint replacement prostheses such as plates, rods, etc.

Peritrochanteric area: is the area around joint replacement prostheses.

Polyacetal: is an engineering thermoplastic used in accuracy parts demanding high stiffness, low friction and excellent dimensional stability.

Unicondylar: is partial knee joint replacement.

Vitallium: is a trademark for a cobalt chrome alloy which consists of 60% cobalt, 20% chromium, 5% molybdenum and other substances.

1. INTRODUCTION

1.1 Research background

The replacements of human joints with prosthetic devices such as hips or knees are deemed to be an effective way to restore mobility, reduce pain and improve the quality of life of patients who are suffering from debilitating joints disorders such as osteoarthritis, rheumatoid arthritis, necrosis, or serous trauma. Although the procedures such as total hip replacement (THR) have been successfully used since 1960s, around 10% of the operations performed in UK each year are revised in order to replace prosthetic implants which have failed prematurely []. A joint which fails before the natural end of a person's life or performs less than 15 years is deemed to be premature failure. Serious wear of bearing surface resulting from the surface defect is one of the primary reasons for premature failure of the joint replacements. With the increase in life expectancy and younger patients requiring joint replacement, the demand for extended lifespan joint replacement systems has greatly increased. In order to improve the lifespan of the joint replacement system, manufacturer have continually reduced both the surface finish and form tolerance limits of the implantable devices to a point where nanometer level surface finish and micrometer scale form tolerance are demanded [2].

1.1.1 Surface finish

It is well known that surface finish plays a critical role in the premature failure of artificial joints [3, 4]. According to the accepted lubrication mechanisms, in a bearing contact there are three lubrication regimes, i.e., fluid film lubrication, mixed lubrication and boundary lubrication [5]. The lubrication regimes are represented in figure 1.1, which is commonly known as the Stribeck curve. λ in the figure indicates the ratio of a representative lubricant film thickness h to the composite or cumulative roughness of the two bearing surfaces. If $\lambda > 3$ the fluid film lubrication regime predominates, in this case the two bearing surface are separated by the lubricant and the wear is minimal; if $\lambda < 3$ boundary lubrication dominates, in this case the asperities of the bearing surface would be subject to significant physical interaction and the wear is maximal; if $\lambda = 3$ then the lubrication regime is mixed, the load between the bearing surface is partially supported by the lubricant and partially by the asperities. It is considered that most prosthetic joint surfaces are working in the mixed lubrication regime [5]. In this case a decrease in the surface roughness Sa of one or both of

the contacting surfaces will dramatically reduce the coefficient friction μ and hence the friction.

Consequently, surface roughness improvement for the bearing surfaces of artificial joints has become one of the primary concerns in the field of manufacturing. Traditional smoothing of a workpiece needs several times repeated polishing which is not only time-consuming but also can deleteriously affect the form tolerance if the local surface is over polished. The improvement of the machining efficiency of medical grade cobalt chrome (CoCr) alloys as well as the ability to improve the surface finish is one of the primary aims of this thesis.

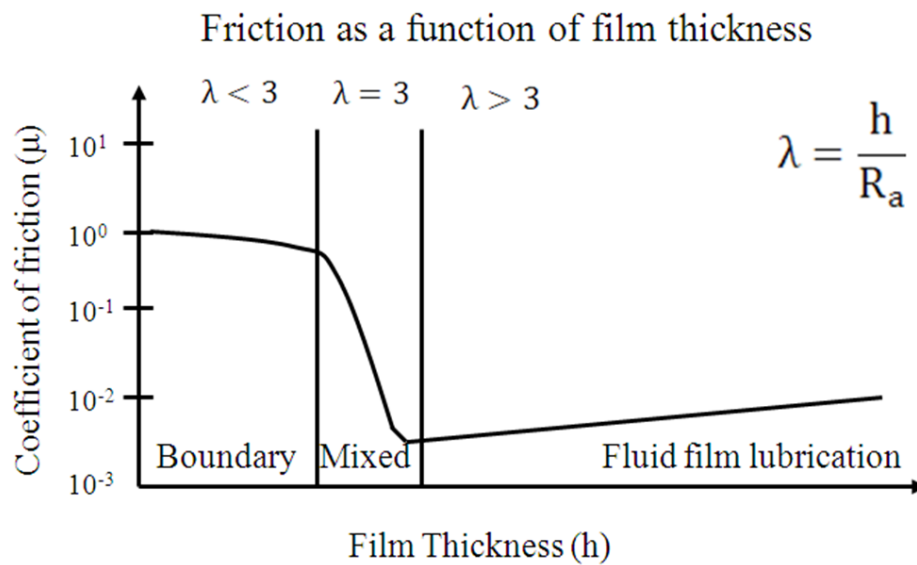


Figure 1.1: Stribeck curve

1.1.2 Surface geometry

The geometry of prostheses is another machining index that needs to be controlled to a high level during the manufacturing process. For prosthetic joints form deviation from a desired shape should be as small as possible. In the case of a hip prosthesis, the departure from sphericity of the spherical articulating surface should be not greater than 10 μm [2]. The sphericity is assessed by sphericity error which is the sum of maximal and minimal deviations from a fitted least-squares sphere [6]. Roundness error is an indicator used to evaluate the sphericity by obtaining circular traces of the implants [7]. Oonishi et al. [8] reported that metal heads with poor roundness error showed poor wear characteristics. Through evaluating the sphericity of the bearing surface in total hip arthroplasty, Ito et al. [9] concluded that the bearing surface with poor sphericity may increase ultra-high molecular weight polyethylene (UHMWPE) wear while good sphericity may prolong the functional performance of the

implants. Although conventional polishing can manufacture the spherical femoral head to a very high accuracy, it is difficult to meet the requirement of machining the next generation multi-radius femoral head [10, 11]. The situation is made more difficult where freeform knee femoral components are to be manufactured with improved geometry. For finishing these components which are mainly finished by manual polishing or semi-automated robot polishing, a new or radically improved polishing process is needed. This aspect forms a second aim of this thesis.

1.2 Aim and objectives

1.2.1 Aim

The overall aim of this research is to use the ultra-precision bonnet polishing technology to develop a deterministic finishing process for CoCr materials to improve both the surface finish and form tolerance of load-bearing surfaces for total hip replacements and total knee replacements.

1.2.2 Objectives

The specific objectives of the study are given as follows:

- ❖ To review the manufacturing process and surface metrology for load-bearing surfaces for both hip replacement and knee replacement.
- ❖ To review the ultra-precision polishing technologies for finishing the load-bearing surface of artificial joints.
- ❖ To optimise the process parameters by using the Taguchi approach for the surface roughness improvement.
- ❖ To fully study the effects of the experimental conditions on surface topography.
- ❖ To further investigate the material removal, including the effects of process parameters on material removal rate, polishing pads on material removal rate, the hardness of workpiece on material removal rate, polishing force, and finally create an empirical model of material removal rate.

- ❖ To improve the form error of hip prostheses and knee prostheses, including the effects of polishing tool path on form correction, multi-radius femoral head polishing and freeform knee component polishing.

1.3 Summary of contributions

The contributions to knowledge produced by this research consist of:

(1) The application of the Taguchi approach to optimize the process parameters for the surface roughness improvement

In this investigation, the interaction effect of process parameters was firstly investigated and then the Taguchi approach with the understanding of the interactions was used to optimize the surface roughness. Compared to previous research by using Taguchi approach, few of them have been found that ever considered the interaction effect.

(2) Understanding the evolution of surface topography during ultra-precision bonnet polishing

This was the first time an investigation of the evolution of surface topography parameters during bonnet polishing process for CoCr alloys has been carried out. In this study, the trends of all areal surface roughness parameters have been investigated.

(3) Material removal investigation

In order to obtain a deterministic polishing process, the material removal rate (MRR) of the polishing must be controlled precisely. The effects of process parameters, polishing pad and hardness of workpiece on the influence function have been investigated. In addition, the variations of polishing force with the levels of the process parameters were investigated. Based on the above investigation, an empirical model of MRR has been successfully created. In contrast to other models, this model has established the links between the MRR and process parameters. Compared with the traditional MRR model, the Preston equation [12], the created model has considered not only the contact pressure and relative velocity but also the complicated relationship of MRR with the process parameters.

(4) Form correction for multi-radius femoral head and freeform knee components

The effects of two tool paths, namely, spiral and raster, on form correction of polycrystalline copper have been investigated. Since the new design of multi radius femoral heads cannot be

finished easily by conventional polishing process, the author has developed a polishing process to manufacture such heads by further developing the form correction process. In the investigation, the author also proposed a concept of designing an “error map” as part of the polishing procedure for the bearing surfaces of hip joints. Polishing of freeform surfaces is still a challenge in the area of machining. In the final sections of this thesis, the author has developed a polishing process for finishing freeform femoral knee components. The polished freeform surface was described by a NURBS (Non-uniform Rational B-Spline) and created by the software Rhinoceros.

1.4 Structure of the thesis

Chapter 1 introduces the research background, aim and objectives, contributions to knowledge, and the basic structure of this thesis.

Chapter 2 reviews the manufacturing process and surface metrology of load-bearing surfaces for artificial joints, including hip replacements, knee replacements, and biomaterials for arthroplasty components, manufacturing process of cobalt-based artificial joint and associated surface metrology.

Chapter 3 surveys the ultra-precision polishing technologies for finishing the load-bearing surfaces of artificial joints, including polishing technologies, material removal in polishing, surface roughness improvement, form correction and types of polishing.

Chapter 4 outlines the optimization of the process parameters to improve the surface roughness including the consideration of interaction effects.

Chapter 5 focuses on the effects of experimental conditions on surface topography during bonnet polishing.

Chapter 6 further investigates material removal in bonnet polishing, including the effects of process parameters, polishing pads and hardness of workpiece on the influence function and the process parameters on the polishing force. Based on the experimental results, an MRR model resulting from the Preston equation has been created. The model has been verified experimentally and indicates that it can be used to predict the MRR for bonnet polishing.

Chapter 7 considers form correction for the load-bearing surfaces of artificial joints, including the effects of tool path on the form correction, the form correction of multi-radius femoral heads and freeform knee components.

Chapter 8 presents an overall discussion of the thesis.

Chapter 9 outlines the main conclusions of the thesis and makes suggestions for the future research.

2. MANUFACTURING AND METROLOGY FOR ARTIFICIAL IMPLANTS

2.1 Introduction

Artificial prostheses are used to replace the damaged, worn or diseased bone and cartilage around joints so that patients are able to restore mobility, reduce pain and improve their quality of life. Currently, most joints in the human body such as wrists [13], ankles [14, 15], shoulders [16], fingers [17, 18], some spinal joints [19-22], hips and knees [23, 24] can be replaced by a corresponding artificial implant. Two of the most common orthopaedic procedures are total hip replacement (THR) and total knee replacement (TKR). According to the statistic data of National Joint Registry (NJR), the hip procedures and knee procedures carried out in England and Wales in 2012 both exceed 55,000 [1], accounting for up to 98% of the total orthopaedic procedures. On the basis of the NJR, the primary reason for the THR and TKR is severe pain and immobility resulting from osteoarthritis, rheumatoid arthritis, necrosis, and serous trauma etc.

This chapter will review the related technologies of the THR and the TKR in order to develop a deeper understanding of the background knowledge of the THR and the TKR. Firstly, the deeper understanding of the need for the THR and the TKR will be developed; secondly, the biomaterials for artificial joints are reviewed, following this the manufacturing processes for artificial joints are discussed and finally the metrology technologies used to assess component quality and function are reviewed.

2.2 Total hip replacement

The modern low-friction arthroplasty, the concept of the THR which is deemed as ‘Gold standard’ procedure, was first proposed by Sir John Charnley (1911-1982) [25]. His pioneering technique is still in widespread use today although there have been many advances in terms of the surgical operation, the geometrical size and the materials used for implant components. The basic structure of the Charnley THR consists of a prosthetic ball, a femoral stem and an acetabular cup (figure 2.1) [26]. During the surgical operation for the THR, the femur head is firstly removed and a femoral stem with a prosthetic bearing head (ball) fitted on the top is then inserted into the prepared femoral canal (older joint systems use a mono-block approach where the stem and the bearing head are a single component). The

acetabular cup and liner is placed in the prepared acetabulum socket and the cup articulates with the ball to provide the bearing couple. Figure 2.2 shows the typical orientation of a THR as used in vivo [27].

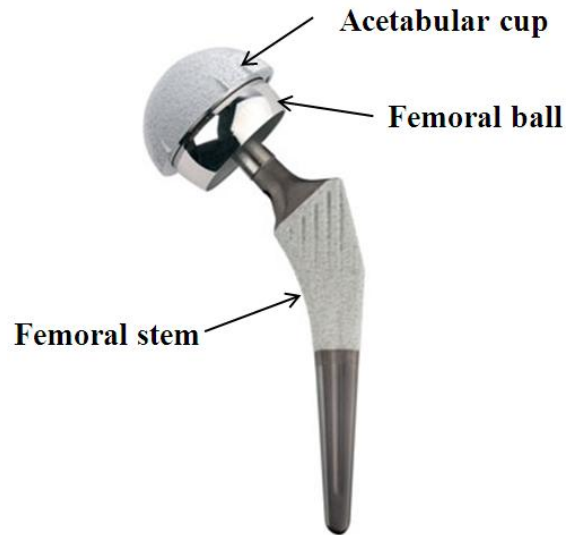


Figure 2.1: Representation of THR [26]

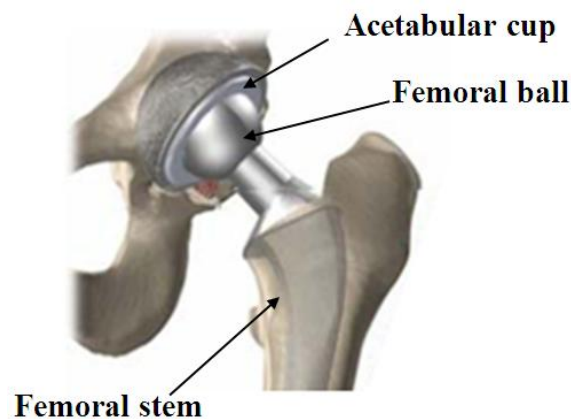


Figure 2.2: Typical positioning of THR [27]

2.2.1 Fixation methods

There are essentially two types of THR in terms of their fixation method. One is cemented, which is a more traditional method pioneered by Sir John Charnley, securing the stem by introducing a mantle made from poly-methyl-methacrylate (PMMA) between the bone and the femoral stem in the canal. The PMMA bone cement is used to fix the femoral stem as well as to transfer the physiological load from femoral stem to the femoral bone structure. The second fixation method is referred to as uncemented, which is a biological fixation

method, depending on the bone ingrowth into pores manufactured on the stem surface that is coated by hydroxyapatite (HA) or porous metal coating. The difference between cemented and uncemented THR systems is shown in figure 2.3 [27].

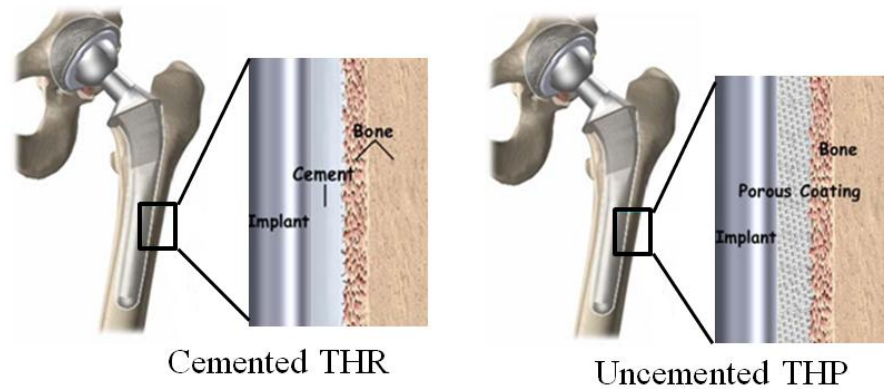


Figure 2.3: Fixation methods of THR [27]

Generally, cemented THRs are quite durable and reliable although they can cause loosening if the flimsy spicules are ruptured by the pressure resulting from the cement and/or the prosthesis and a space between the cement and the bone is left [28]. In order to prevent the loosening, cement is pressurized into the spaces between the bony spicules. Patients with cemented THRs can walk without support within 3 to 6 weeks after surgical operation and most will not undergo complications [29]. Compared to the cemented THRs, uncemented THRs demand a longer rehabilitative period because their stability relies on the new bone growth. Cementless stems are usually applied to more active younger patients and are considered less suitable for the patients with osteoporosis [30].

Trend in use of fixation 2003 to 2011

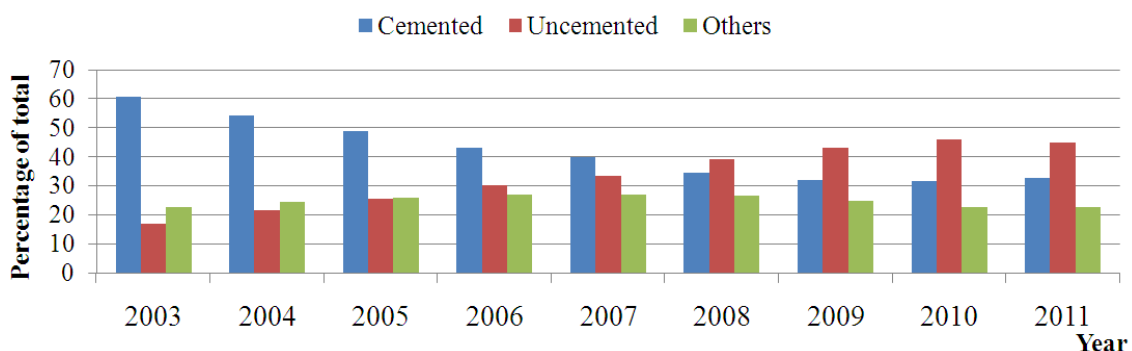


Figure 2.4: Trends in use of fixation for hip replacement from 2003 to 2011 (Data from NJR report [1])

Figure 2.4 shows the trends in use of fixation for hip replacement from 2003 to 2011 for England and Wales. As shown in the figure, the use of cemented fixation reduces from 60.5%

in 2003 to about 32% after 2009 while the uncemented fixation increases from 16.8% to 45.8% in 2010 and 44.7% in 2011. The percentages of other fixation methods, including hybrid (cementless stem, cemented socket), reverse hybrid (cemented stem, cementless socket) and resurfacing, vary between 20% and 30%.

2.2.2 Combinations of bearing surface

According to the statistics taken from the annual report of the NJR, there are essentially six types of bearing combinations used for THR, metal-on-polyethylene (MoP), metal-on-metal (MoM), ceramic-on-ceramic (CoC), ceramic-on-metal (CoM), ceramic-on-polyethylene (CoP), and resurfacing procedures [1]. In the following sections, all these six types of bearing surface combinations will be considered.

(1) Metal-on-polyethylene (MoP)

The combination of metal-on-polyethylene (MoP) bearing surface for the THR has greatly improved the life quality of patients with arthritic joint. This combination of materials was first pioneered by Sir John Charnley in 1960s [25]. MoP consists of a metallic femoral stem, a metallic femoral head, a polyethylene liner (acetabular cup) and an acetabular shell. The typical design of a MoP hip replacement is shown in figure 2.5 [31]. The most commonly employed metal for this combination of THR is a CoCr alloy and the two kinds of polyethylene are ultra highly molecular weight cross-linked polyethylene (UHXLPE) and more traditionally ultra high molecular weight polyethylene (UHMWPE).

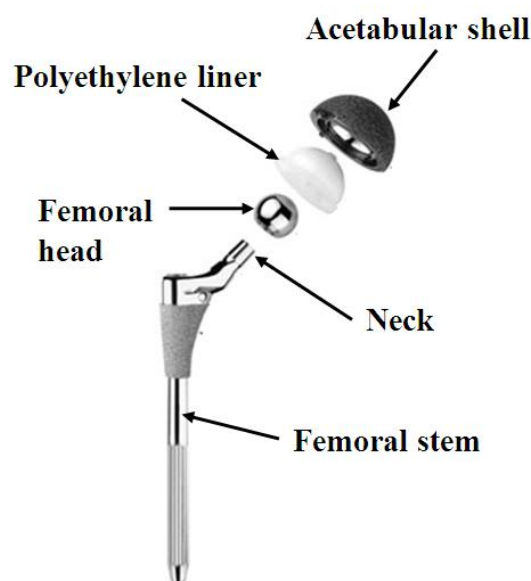


Figure 2.5: Metal-on-polyethylene THR [31]

Because of its low friction and durability, MoP has been the most commonly employed bearing surface for THR since it was first introduced and has demonstrated a very high implant survivorship for over 20 years [32], especially when combined with UHXLPE, which has showed remarkable improvement in wear properties, since it was introduced in the late 1990s. The reduced wear rates decrease the possibility of arthroplasty revision. The use of UHXLPE has facilitated the use of a wider range of head size (28mm~40mm), more elevated liners (0~10~20 degrees) and more offset selections (standard or lateralized) which can be matched to the physiology of the patient. The stability of large femoral head size with elevated liner can lower the risk of dislocation [33].

The dissolution of bone, term osteolysis, is the major complication of hip implant mainly affecting the longevity of THR. Several failures of THR, such as periprosthetic fractures which usually happens in the pelvis, peritrochanteric area, or femoral diaphysis, result from osteolysis [34]. In addition to osteolysis, polyethylene wear of MoP acetabular cups (about 0.19mm/year [35]) also reduces the range of motion as the polymer cup is penetrated by femoral head and this increases the dislocation rate and the torsional force on the interface of implant and bone which may additionally lead to mechanical loosening [36].

(2) Metal-on-metal (MoM)

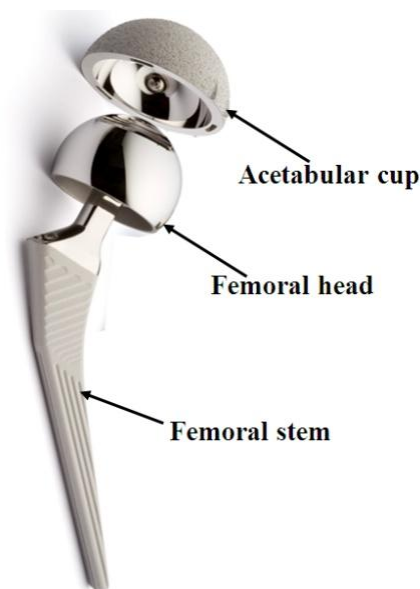


Figure 2.6: Metal-on-metal THR [37]

The use of metal-on-metal bearing surfaces for THR can be traced back to 1950s and it attracted much more interest when the McKee-Farrar hip arthroplasty was introduced in 1966

[38]. All the components of MoM are made of metallic materials. A typical design of a MoM THR can be seen in figure 2.6 [37].

It has been reported that MoM THRs are more suitable for active and younger patients due to the stability resulted from the larger femoral heads [39]. MoM components allow the largest femoral heads throughout the whole range of prostheses sizes. Larger head size is beneficial to extend the lifespan of the THR and greatly reduce the risk of dislocation and chance of device fracture. In addition, the MoM THR can provide a more normal gait pattern and increase ease of device insertion with proximal femoral deformities. Comparing to other types of THR, the revision operation of MoM is straightforward because there is no liner in the MoM THR system.

Although the MoM THR can avoid the complication of debris wear from prosthesis made of polyethylene, like other implants, it still has some adverse effects, such as infection, joint dislocation, tissue deterioration around the replaced joint, implant loosening, etc. Ultimately metal surfaces potentially corrode which can create metal debris (ions and particles) [40, 41]. This debris can invade the space around the implant and enter the bloodstream in the form of ions, leading to pain or swelling around the hip, osteolysis and other symptoms such as cytotoxicity, hypersensitivity and neoplasia [42]. This especially should be noted for younger women who are pregnant, because metallic ions can be passed to fetus through mother's placenta. How this will affect the growing fetus is still unknown so far.

(3) Ceramic-on-ceramic (CoC)

Although it is used smaller quantities, the combination of CoC THR still attracts much interest from both surgeons and patients since first being introduced in early 1970s by Pierre Boutin [43]. In these implants, the traditional metal femoral head and polyethylene liner are superseded by the use of a high strength ceramic head and liner bearing combination, usually made from yttria stabilized alumina (Al_2O_3). The CoC hip designs use a modular design having a metallic stem and metallic acetabular liner (figure 2.7 [31]).

CoC THR has the lowest wear rate of all implants, whose average linear wear rate is $0.025\mu\text{m}$ per year and is up to 4000 times less than a typical MoP system ($100\mu\text{m}/\text{year}$) [44], and ceramic bearings are highly bio-compatible and suffer no corrosion following implant surgery. Therefore, there is no inflammation, bone loss or systemic distribution of wear debris in the body. In addition, the low wear rate can minimise the risk of osteolysis.

The main limitations of the CoC THR are catastrophic fracture and failure of acetabular component fixation [45]. However, the advances of manufacturing technology have greatly improved the production of ceramics with high purity, high density and small grain size, all of which are beneficial for the reduction of fracture [46]. Consequently, fixation of the femoral component has become a focus of CoC THR research. Several different methods of uncemented fixation for CoC bearing surfaces have been developed [47]. One of the most promising fixation methods is press-fit metal-backed socket with porous coating which has demonstrated excellent mid-term survival results.

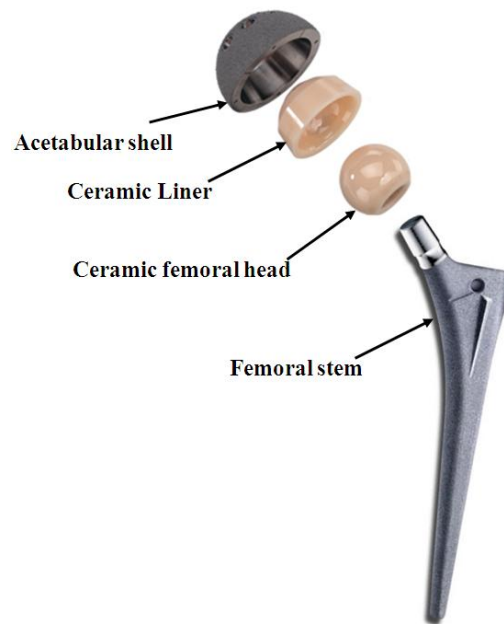


Figure 2.7: Ceramic-on-ceramic THR [31]

(4) Ceramic-on-metal (CoM)

The combination of CoM THR, which is considered to cause less damage to the surrounding tissues and bones than traditional hip prostheses, was proposed by Firkins et al. [48] in 2001 at the University of Leeds. This new and novel design of THR applies the ceramic as the material of femoral head and the metal as the acetabular cup (figure 2.8 [49]).

The CoM THR combines the advantage of MoM and CoC, and is considered more suitable for younger and more active patients [50]. This combination was found to have an approximate 10-fold reduction wear rates over MoM bearings [48], which implies that there will be less metal ions transported the body tissue of patients. This can partly reduce the risk of complications such as cytotoxicity, hypersensitivity and neoplasia caused by metal ions. It was also found that the friction of CoM is lower than MoM and similar to CoC. In

addition, CoM can avoid stripe wear which is seen with both CoC and MoM hip replacement [51].

The CoM hip implants have demonstrated excellent performance in laboratory studies and short term clinic investigations. However, little is known about the potential consequence of this kind of implants in the longer term. Several failure modes occurring in MoM and CoC are also possible with the CoM THR, although the chances may be lower.

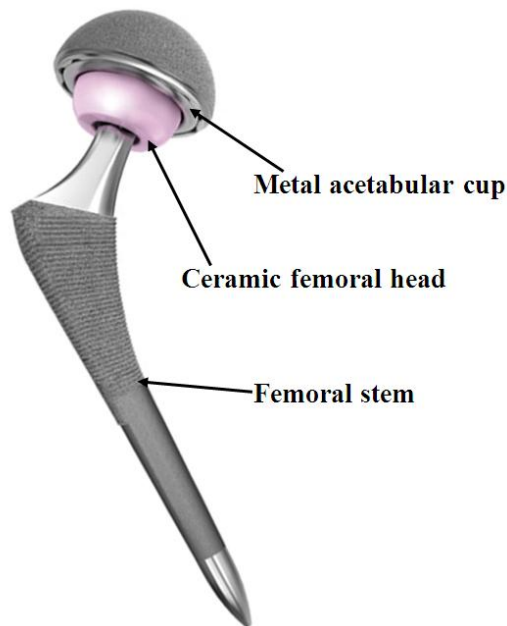


Figure 2.8: Ceramic-on-metal THR [49]

(5) Ceramic-on-polyethylene (CoP)

Based on the reality of low friction of the ceramic counterpart to ultra high molecular weight polyethylene (UHMWPE), Semlitsch et al. [52] proposed the combination of CoP hip implant in 1977. It is well-known that alumina is the most scratch-resistant prosthesis material and UHMWPE is durable and reliable. Therefore, the CoP hip replacement can combine the strong points of these two materials. The design of a representative CoP implant is schematically shown in figure 2.9 [53].

Semlitsch [52] had demonstrated the extraordinary low wear rate (about 0.022mm/year) of an alumina ceramic head on polyethylene cup combination in a wear simulator and given the reasons for this were excellent corrosion and scratching resistance, superior lubricating properties, mirror-like surface, high hardness and material inertness. These properties could potentially reduce the coefficient of friction at the contacting surface, the third-body wear,

surface scratching and biological response to the debris created by ceramic particles. In clinical practice, Oonishi et al. [54] reported a 0.1mm/year head penetration rate with ceramic heads while metal heads had a 0.25mm/year wear rate. Callaghan and Wroblewski [55, 56] even reported lower wear rate of this combination of THR, which were 0.034mm/year and 0.019mm/year respectively. These results will encourage more potential surgeons /patients to select the CoP THR. Compared to the CoC bearings, the incidence of ceramic head fracture and squeaking in CoP is rare.

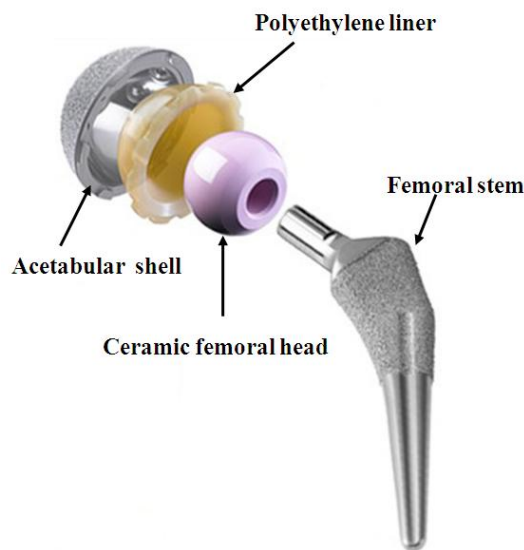


Figure 2.9: Ceramic-on-polymer THR [53]

Apart from the well-known risk of ceramic head fracture, another disadvantage of CoP THR is difficult revision operations [57]. As ceramic is a brittle material, when the femoral head fractures, the retained ceramic fragments increase the difficulty of revision surgery. This can affect the longevity of the subsequent implants.

(6) Resurfacing

Different from the traditional total hip replacement which needs to remove the head of the femur and insert a stem attached with a metal or ceramic ball into femoral shaft, hip resurfacing only reshapes the upper end of the thigh bone, installing a cap on the upper end of the femur and a metal cup in the acetabulum (Pelvis socket) (figure 2.10 [58]). The origin of hip resurfacing can be traced back to Smith Petersen [59] who used mould arthroplasty to regenerate the cartilage with the intention of removing the mould when the femoral head and acetabulum became congruent. Then Charnley [60] continued Smith-Petersen's earlier work before developing his own low friction arthroplasty. The early stage of resurfacing was

largely abandoned because of low survival rates. In the 1980s, resurfacing had a renaissance with Mckee-Farrar MoM THRs which were found to function well over 20 years after the surgery [61].

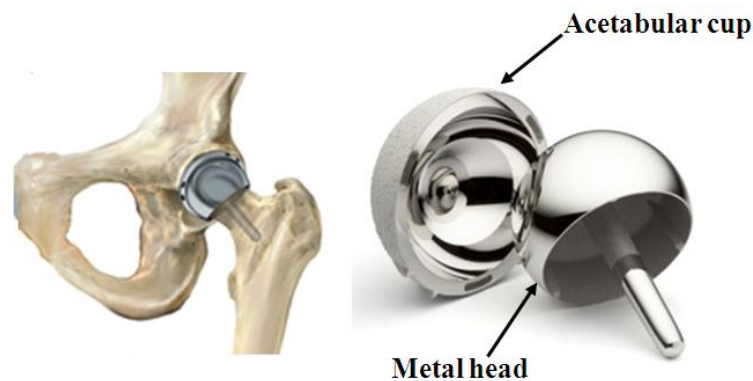


Figure 2.10: Hip resurfacing [58]

It is obvious that the first advantage of hip resurfacing is less bone resection during replacement surgery, which makes it easier to convert to a total hip replacement in the future because a surgeon will have more original bone stock available [62]. Secondly, the hip resurfacing usually employs larger size of femoral head comparable to the patient's anatomy which can minimize the risk of dislocation. Finally, the surgery of hip resurfacing causes less thigh pain and patients will recover more quickly after the operation.

Apart from the same limitations with MoM total hip replacement, hip resurfacing has its own weaknesses which include weakening or softening of the femur and narrow usage scope. The weakening or softening would result in the bone collapse or fracture under the stress of weight. The narrow usage scope means hip resurfacing is only suitable for the patients whose bones are not too damaged. In other words, if patients with serious arthritic conditions, their bones are not strong enough to sustain the replaced implants and therefore will lead to the resurfacing failure. More recently a number of joint registers in UK, Sweden and Australia have reported very high failure rates for resurfacing THRs and there are many reports of high wear, severe necrosis and extremely high blood ion levels. These have led to the withdrawal of several designs and litigation. It seems that under carefully controlled test conditions then resurfacing is highly successful however wider use of large head radius resurfacing has proved problematic for several designs namely the ASR made by Depuy which was withdrawn from use in 2011 [63].

As shown in figure 2.11, although there are several combinations of hip replacement, the MoP THR remains the main hip implants in use in England and Wales, in 2003, accounting for 70.1% of the total. This percentage decreases gradually to 54.8% in 2008 and then increases slightly from 2009 because of the rapid increase of uncemented MoP (During 2003 and 2011, cemented MoP decrease steadily from 55.4% to 27.9% while uncemented MoP gradually increase from 6.2% to 16.8%). The percentage of CoP remains relatively stable between 2003 and 2011, fluctuating between 8.3% and 12.6%. The MoM THR increases firstly from 2% in 2003 to 11.9% in 2008 then decrease sharply to 0.9% in 2011 due to well publicized problems. The bearing combination of CoC grows steadily from 4.7% to 23.2% from the beginning of the UK NJR in 2003. There is no data for CoM THR before 2007 and the percentage of CoM in total is at a low level. Before 2009, the percentage of resurfacing stays between 8.8% and 10.8%, but after that, it drops to 3.8% in 2010 and 2.5% in 2011 again due to publicized problems and withdrawal of certain designs.

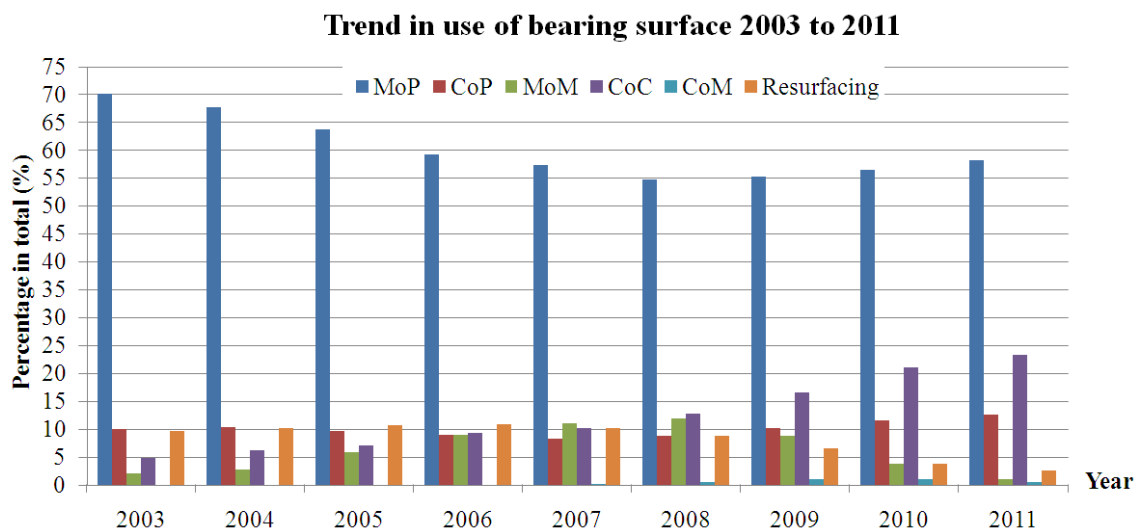


Figure 2.11: Trends in use of bearing surface for hip replacement from 2003 to 2011 (Data from NJR report [1])

2.2.3 The failure of THR

It is reported that around 10% of the hip joint replacements fail prematurely each year [1] and revision operations are needed to replace the failed implants. Compared with primary arthroplasty, revision operations are not only more expensive but also associated with a lower longevity and a higher possibility of complication and morbidity. Therefore, it is very significant to investigate the cause of implant failure. The main reason of implant failure is attributed to the aseptic loosening, which is mechanical failure of one or more components of

the replaced joint, accounting for about 75% of revision operations [64]. Aseptic loosening can occur in the absence of clinical or microbiological evidence of infection and is affected by several factors such as periprosthetic bone resorption, poor initial fixation or alignment [65, 66]. Another reason that could result in joint failure is septic loosening which is brought on by the onset of infection in the tissue surrounding the joints after the surgery.

2.3 Knee replacement

Knee replacement, involving total knee replacement (TKR) and partial knee replacement, is a surgical procedure designed for patients suffering with severe pain of knee joints from osteoporosis, rheumatoid arthritis, psoriatic arthritis or trauma and is designed to relive pain and disability [67]. The TKR is the replacement of all three components of the diseased knee joint while partial knee replacement only replaces one or two compartments of the knee joint.

2.3.1 Total knee replacement

Figure 2.12 shows a typical design of the TKR [68]. As seen in the figure, a TKR consists of a femoral component, a patellar component, a tibial insert (bearing surface) and a tibial tray. The femoral component, which has a central groove to allow the patellar component to move up and down smoothly as the knee joint flexes and extends and curves up around the end of the femur. The dome-shaped patellar component, usually made of UHWMPE, replaces the surface of the natural kneecap, running along the groove of the femoral component. The tibial tray which replaces and covers the top of the tibia is a flat metal platform. The last component, tibial insert, is used as a bearing surface, articulating with the femoral component and is inserted into the tibial tray.

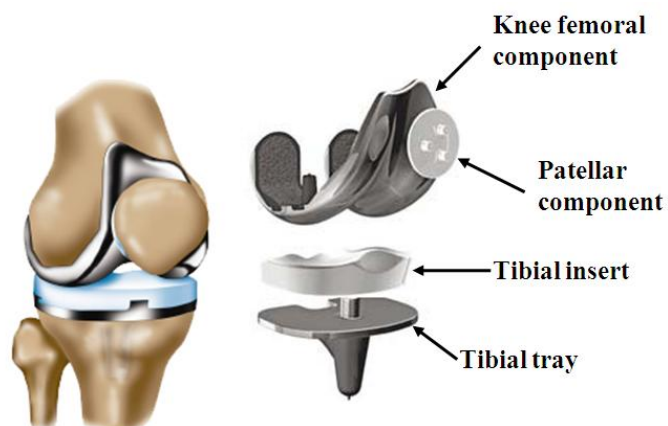


Figure 2.12:: TKR systems [68]

2.3.1.1 Fixation methods

The fixation methods for knee replacement are similar to those employed for THR and consist of cemented, uncemented and hybrid (a combination of cemented and uncemented). The cemented implants apply bone cement (PMMA) to fix the femoral component and tibial tray in place (figure 2.13 [69]). According to the statistical data of the NJR, The majority of knee replacements use cemented fixation, accounting for over 80% of the total [1]. The uncemented fixation relies on bone growth into the pores on the implant surface which is coated by hydroxyapatite (HA). Screws or pegs may also be employed to steady the prostheses until the bone ingrowth occurs. Patients who use uncemented fixation will take longer to recover as the bone grows into the implant, however the implants are considered to have better long term stability. Hybrid fixation which employs both cemented and uncemented elements is used by some small number of surgeons, accounting for 1.4% of the total [1].

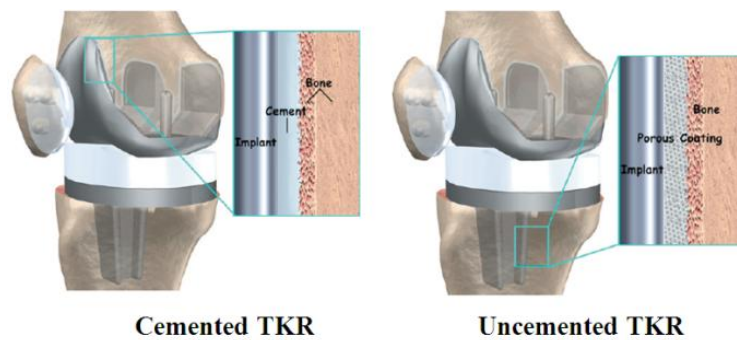


Figure 2.13: Fixation methods of TKR [69]

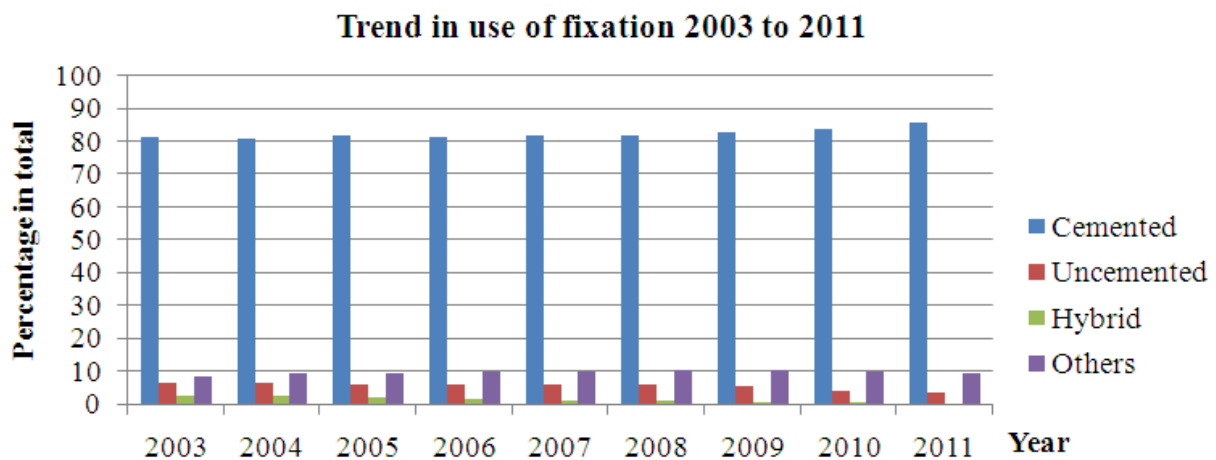


Figure 2.14: Trend in use of fixation for knee replacement from 2003 to 2011 (Data from NJR report [1])

Figure 2.14 shows the trend in use of fixation for knee replacement from 2003 to 2011. As can be seen in the figure, there was little change between 2003 and 2011 in the types of knee replacement used. “Others” in the figure refers to partial knee replacement, including unicondylar and patella-femoral.

2.3.1.2 Types of knee implant

Different from spherical hip bearing surfaces which are easy to articulate, freeform bearing surfaces of knee prostheses may need auxiliary elements to constrain the implant components. There are four types of restriction methods for knee replacement, i.e., non-constrained, semi-constrained, constrained or hinged and unicondylar [70, 71]. The non-constrained method is the most commonly used in knee replacement. The use of such an implant relies on the patient’s own ligaments and muscles to sustain the stability of artificial components. A semi-constrained implant has some stability built into it. It is used when all of the inner knee ligaments need to be removed. Constrained or hinged implants are often used when the patients’ knees are extremely unstable and the ligaments are unable to support other types of knee replacements. In this case, the femoral component and tibial insert component are linked together with a hinged mechanism. It is especially suitable for elderly patients with a revision replacement procedure and those with severely damaged knees. The unicondylar constrained implant will be discussed in section 2.3.2.

According to whether the tibial insert is fixed to tibial tray or not, the hip replacement can be categorized as a fixed bearing implant or a mobile bearing implant [72]. In the case of fixed bearing implant, the tibial insert is firmly attached to the metal tibial tray, the design provides a stable cushion for the femoral component to roll and slide over. This implant can provide a good range of gliding motion and last as long as other implants. The limitation of the fixed bearing implant is that it cannot achieve the rotational movement that would facilitate activities such as sports and climbing stairs. Mobile bearing implants are more suitable for younger, more active and overweight patients. The components used in mobile bearing implants are the same with the fixed bearing implants, the only difference being that the mobile bearing implants allow a short distance of rotation inside the metal tibial tray. However, the rotation mobility requires more support from the ligaments and soft tissues surrounding the knee. If the ligaments and soft tissues are not strong enough, this prosthesis is more likely to dislocate.

2.3.1.3 The combination of bearing surface

With the development of material science, the bearing surface combinations of hard-on-hard such as MoM, CoC, and CoM have been successfully used in total hip replacement. However, the bearing surface combination of MoP is still the most popular in the hip prosthesis industry [1]. The situation of the combination of bearing surfaces for TKR is that there are virtually few reports of other material combinations apart from the MoP. Therefore, in the annual report of NJR there is no classification of bearing surface combination for TKR.

The reason for little success in trying to develop different material combination is due to the fact that the geometry of the TKR components is not standardised compared with THR components whose geometries are normally spherical. Each TKR design has its own bearing geometry, depending on the requirement of the patients and the demanded conformity and mobility of the bearing [73]. Consequently, little attention has been paid to changing material combinations for TKR, but much to the improvement of the mobility and design of TKR [74].

Due to the potentially low wear rate and long term biocompatibility, the use of ceramics in TKR (figure 2.15 [75]) has attracted much interest of both patients and surgeons. Ceramic was first introduced to the field of knee implant by Langer in 1973 [76] and first total knee replacement was implanted by Oonishi in 1980s [77]. Most of ceramic knee implants were based on the coupling of ceramic on polyethylene [78, 79]. Although the use of ceramic knee implants is very small worldwide, this number could potentially increase with advances in ceramic properties. It is predicted that a hard on hard combination bearing will be introduced to total knee replacement system in the future [80].



Figure 2.15: Ceramic femoral component of knee prosthesis [75]

2.3.2 Partial knee replacement

The human knee is made up of medial (the inside part of the knee), lateral (the outside part of the knee) and patello-femoral (the area between the kneecap and the upper front surface of the femur) zones. Partial knee replacement, also called unicompartmental knee replacement, is the procedure that only replaces one or two parts of the damaged areas, retaining the normal/undamaged part of the natural knee (figure 2.16 [81]). In England and Wales, this procedure constitutes approximately 10% of the knee arthroplasty procedures [1]. The merits of partial knee replacement include smaller incision, less bone and cartilage removal, shorter stay at hospital, more rapid recovery, more natural motion compared to TKR, low risk of infection, etc. The potential risk of partial knee replacement may involve blood clots (deep vein thrombosis) [82] and infection [83], etc. Fortunately, both can be prevented by the medication. The causes of long term failure of partial knee replacement are similar to other implants, such as polyethylene wear, aseptic loosening, etc.



Figure 2.16: Partial knee replacement [81]

2.4 Biomaterials for arthroplasty components

Biomaterial is a material which is used to fabricate implants to replace the part of a living system. It usually remains inert to biological systems but may become mechanically integrated [84, 85]. Currently, biomaterials can be classified into four groups, i.e., metals and alloys, polymers, ceramics and composites. The general criteria for biomaterials for artificial implants are that they should meet the requirement of biocompatibility, sterilizability, manufacturability and reliability [86].

(1) Biocompatibility

The most important property of a biomaterial is biocompatibility, which means that the implanted prosthesis can stimulate a proper response of the host under specific conditions of

interactions [87]. This is not a material characteristic of the implant but a property of the implant-organism system with respect to certain conditions of contact. It does not indicate that the implant must be completely non-toxic or has no negative features but means that a response gained from implant-organism interaction can solve the stated problem. A biomaterial should play the role of medical functionality in contact with the living tissues and should be biologically compatible.

(2) Sterilizability

All prostheses must be sterilized by gamma, gas (ethylene oxide, ETO) and steam autoclaving, etc before implanting into the body of human being. Therefore, a biomaterial must be able to suffer sterilization. Different sterilization techniques should be selected for different biomaterials. For example, polyacetal is not suitable to be sterilized by gamma as it will depolymerise and give off toxic gas. These polymers can be sterilized by ETO.

(3) Manufacturability

The manufacturability of a biomaterial depends on the ability of the material to be fabricated economically using the state of the art machining process. Although many candidate materials are biocompatible, they may not be suitable for medical devices because of their manufacturability which may hinder the actual production process.

(4) Reliability [88]

Reliability is a very important and actual problem in the biomaterial science of implants. Different from the use of medicines, prostheses can only be adjusted by a surgical intervention post-operation. Therefore, the prostheses must operate without failure and maintenance for many years. This indicates that the strength and wear resistance of biomaterial should not change distinctly in the complicated biological environment with time.

2.4.1 Metals and alloys

Metals have been the primary materials used for the purpose of repairing the seriously damaged human bone due to their excellent mechanical properties such as fatigue strength, tensile strength and fracture toughness [86]. Originally, stainless steel was often used to make the femoral components of THR and TKR but now is rare as it is unable to withstand corrosion in human body in the long term. Stainless steel is more suitable for temporary implant devices such as fracture plates, screws and hip nails. The most commonly used

metals on the current market of hip and knee replacements are cobalt based and titanium based alloys. The following review will summarize the basic properties of these three metallic biomaterials.

2.4.1.1 Cobalt based alloys

At the beginning of 20th century, CoCr binary alloys which were oxidation resistant, corrosion resistant and suitable for cutting tools were patented by Elwood Haynes [89]. With the addition of Mo and W, CoCr alloys exhibited excellent strength at high temperature as well as good corrosion resistance and were patented as Stellite [90]. This alloy was originally applied in aircraft engines and then in the dentistry in the 1930s, during which time it was called Vitallium [91]. The success of these alloys in the hostile environment of the mouth attracted great interest from orthopaedic surgeons and was eventually introduced to the field of orthopaedic implants by Dr Austin Moore in 1940s [92]. In 1950 Vitallium was improved and the CoCrMo endoprosthesis, which is still used today, was developed. In 1956, Dr. McKee developed MoM CoCrMo hip implants [93]. In 1970s, high strength forged hip stems emerged in response to occasional fatigue fractures of investment cast hip stems. In 1980s, hip and knee implants with porous surfaces that can enable bone to grow into the implant were widely used. This design is still in use in current prostheses of hip and knee [94].

The cobalt based alloys can be divided into two groups: 1) cast cobalt based alloys and 2) wrought cobalt based alloys [88]. Cast cobalt based alloys originate from the Stellite group of materials. The cast alloys are famous for high stiffness and wear resistance and can be polished to excellent surface finish. Thus the majority of the femoral heads and cups of hip implants are cast form Co (66%)-Cr (27%)-Mo (7) alloys. During 1950s and 1960s, it also became very popular as stems for Moore [95], Thompson [96] and Muller prostheses [97]. The primary defect of cast cobalt based alloys is insufficient fatigue strength which will frequently result in broken stems [98]. Later the cast stems were substituted by the wrought stems. Wrought alloys which have better strength and ductility than cast alloys are processed by rolling, forging, stamping and drawing [99].

There are essentially four types of CoCr alloys suggested by the American Society for Testing and Materials (ASTM) for surgical implant applications [100]:

Cast CoCrMo alloy, F75

Wrought CoCrWNi alloy, F90

Wrought CoNiCrMo alloy, F562

Wrought CoNiCrMoWFe, F799

Table 2.1: Chemical composition of CoCr alloys

ASTM designatin	Trade-name	Alloy group	Composition, wt%												
			Co	Cr	Mo	W	C	Ni	Fe	Si	Mn	N	S	Ti	P
F75	Haynes	CoCrMo	Bal	27	5	0.2	0.35	1.0	0.75	1.0	1.0	0.25	0.01	...	0.02
	Stellite 21	Castings	Bal	30	7	max	max	max	max	max	max	max	max	...	max
F90	Haynes	CoCrWNi	Bal	19	...	14	0.05	1.0	3	0.4	1.0	...	0.03	...	0.04
	Stellite 21	Wrought	Bal	21	...	16	0.15	11	max	max	2.0	...	max	...	max
F562	MP35N	CoNiCrMo Wrought	Bal	19	9.0	...	0.025	33	1.0	0.15	0.15	0.15	0.01	1.0	0.015
			Bal	21	10.5	...	max	37	max	max	max	max	max	max	max
F563	...	CoNiCrMo	Bal	18	3.0	3.0	0.05	15	4.0	0.5	1.0	0.25	0.01	0.5	...
		WFe	Bal	22	4.0	4.0	max	25	6.0	max	max	max	max	3.5	...
F799	Haynes	CoCrMo	Bal	26	5	...	0.35	1.0	0.75	1.0	1.0	0.25
	Stellite 21	Forging	Bal	30	7	...	max	max	max	max	max	max

The chemical compositions of each alloy are shown in table 2.1 [91]. In these alloys, cobalt is the main component which forms a matrix that contains chromium and molybdenum-based phases. The chromium is added to increase the strength as well as corrosion resistance. The addition of molybdenum can refine the grain size which leads to higher resistance to corrosion, durability and reliability of the implants. Nickel is used to increase the castability and workability, but the amount is controlled to less than 1% to ensure low toxicity in the body. The interaction of iron and other minor additions with the main component of cobalt alloys forms carbides and other secondary phases which will increase the stability of the alloy matrix to abrasive wear. Carbon content in the alloy should be at a low level in order to avoid excess growth of the carbide phases, which can worsen the strength and ductility of the alloy.

(1) ASTM F75

ASTM 75 is a cast CoCrMo alloy, which has two common commercial/proprietary names, Vitallium and Haynes 21. The main feature of this alloy is corrosion resistance in chloride environments, which is attributed to its bulk composition and surface oxide (Cr_2O_3).

The casting process (lost wax) of a femoral component using F75 can be described briefly as follows [101]:

At first, a wax model near the final dimension of the implant is made.

Secondly, the wax model is coated with a special ceramic until the desired mould is formed. The rigid outer mould contains the softer inner mould, which is the exact negative of the wax model.

Thirdly, the ceramic mould with wax model is heated to remove the wax.

Fourthly, F75 is melted to 1350-1450 °C and then poured into the ceramic mould.

Finally, when the metal is solidified into the desired shape, the ceramic mould is cracked open and the cast femoral component is created.

This casting process may produce at least three microstructural features which can strongly affect the implant properties, often negatively.

The first is a 'cored' microstructure. Typically, cast F75 consists of a Co-rich matrix (alpha phase) plus interdendritic and grain boundary carbides or interdendritic Co plus Mo-rich sigma intermetallic and Co-based gamma phase. The ratio of the alpha and carbide phase should be around 85% and 15% respectively. However due to nonequilibrium cooling, a 'cored' microstructure may be developed. In this case, the interdendritic regions become solute (Cr, Mo, C) rich and contain carbides, while the dendrites become depleted in Cr and richer in Co. This is an adverse electro-chemical situation, but solution anneal heat treatment can be used to alleviate this situation [100].

The second is a relatively large grain size. This is also undesirable as it reduces the yield strength through a Hall-Petch relationship between yield strength and grain diameter.

The third is casting defects. The particles of the ceramic mould may break off and embed into the femoral components while the alloys are solidifying. This inclusion can result in accelerated fatigue fracture of the implant in vivo due to stress concentration. For similar reasons, macro and microporosity arising from metal shrinkage upon solidification of castings should be avoided as they cause stress concentration sites.

Powder metallurgical techniques can be applied to avoid the above problems and to improve the microstructure and mechanical properties of the alloys. For instance, in hot isostatic pressing, a fine powder of F75 alloy may be compacted and sintered together under a proper pressure and temperature condition and then forged to final shape [91].

(2) ASTM F90

ASTM F90, also known as Haynes Stellite 25, is a wrought alloy based on CoCrW₂Ni. W and Ni are added to improve the properties of machinability and fabrication. When the F90 is in the annealed state, its mechanical properties are approximately the same as F75 alloy, but when cold works to 44%, the properties are more than double. The different properties of F90 in the annealed condition and work-hardened state mean that great attention must be paid into to ensure the homogenous and thorough deformation of the component. Otherwise, the property change may lead to an unexpected failure of the implant due to internal stress concentrations.

(3) ASTM F562

F562, known as MP35N, is a wrought CoNiCrMo alloy which was originally used as a high performance aerospace fastener alloy. The 'MP' in the name refers to the multiple phases in its microstructure. This alloy can be processed by thermal treatment and cold working to make a controlled microstructure and a high strength alloy.

When cobalt is alloyed to produce MP35N, it needs to be processed by 50% cold work which will increase the driving force for the transformation of the FCC (Face-Centre Cubic) to the HCP (Hexagonal Closed-Packed) phase. The HCP phase appears as fine platelets within FCC grains. Since the FCC grains are small (0.01-0.1 μ m) and HCP platelets further hinder dislocation motion, the generated structure is greatly strengthened. It can be further strengthened by an aging treatment at 430-650⁰C, which produces Co₃Mo precipitates on the HCP platelets. Consequently, this alloy is strengthened from the combination of a cold-worked matrix phase, solid solution strengthening and precipitation hardening and can be described as truly multiphasic. The mechanical properties of MP35N alloy are the strongest among the implant alloys via this processing [102].

(4) ASTM F799

ASTM F799 is a modified F75 alloy which has been mechanically processed by hot forging after casting. This alloys also known as thermo-mechanical CoCrMo alloy and has a slightly different composition from F75. It has a more worked grain structure than F75 and a HCP phase formed from a shear induced transformation of FCC matrix to HCP platelets [103].

(5) Other cobalt based biomaterials

F563 is a wrought CoNiCrMoWFe alloy. It is available in the form of bars, wires and forgings. Similar to F562, this alloy also can be strengthened by cold work or cold work plus aging. The mechanical properties of F562 is shown in Table 2.2 [104].

Table 2.2: Mechanical properties of typical cobalt based alloys

ASTM designation	Condition	Young's modulus (GPa)	Yield strength (MPa)	Tensile strength (MPa)	Fatigue endurance at 10 ⁷ cycles (MPa)
F75	Cast/annealed	210	448-517	655-889	207-310
	P/M HIP (a)	253	841	1277	725-950
F90	Annealed	210	448-648	951-1220	N/A
	44% cold worked	210	1606	1896	586
F562	Hot Forged	232	965-1000	1206	500
	Cold Worked, aged	232	1500	1795	689-793
F799	Hot Forged	210	896-1200	1399-1586	600-896

ASTM F1058 is a wrought CoCrNiMoFe alloys which is available in two grades. Both of these two alloys are strengthened by cold working plus aging. Both grades can be formed in wire and strip. F1058 grade 1, whose elastic modulus is 190GPa, is known as Gligloy and commonly used for artificial heart springs. F1058 grade 2, whose chemical composition is in accordance with the composition limited in ISO 5832-7, is often being employed in devices of neurosurgery and vascular surgery [105].

2.4.1.2 Titanium and titanium based alloys

Due to its low density element (approximately 60% of the density of iron), excellent biocompatibility and corrosion resistance, little reaction with tissue surrounding the implant, titanium and its alloys are widely used in the implant devices [104]. In addition, the increased use of titanium alloys as biomaterials is also attributed to their low modulus (106GPa) which is beneficial for the reduction of stress shielding [106]. Stress shielding is a mechanical phenomenon occurring around the rigidly fixed implants [107]. A femur normally carries its external loads all by itself. When a stem insert into the femur, it shares the load-carrying

capacity with the implant. The load first carried by one structure and now carried by two, the stem and the bone. Consequently, the bone is subjected to reduced stresses, hence stress shielded. The earliest use of titanium as a material for medical, surgical and dental devices was based on the advance of titanium manufacturing processes for aerospace and military requirements after World War II [108]. Compared to stainless steel and cobalt based alloys, titanium and titanium alloys are relatively new biomaterials for medical devices.

Titanium undergoes an allotropic transformation at around 885⁰C, varying from an HCP crystal structure (α phase) to BCC (body-centred cubic) structure (β phase). The mechanical properties of titanium can be changed by controlling its composition and thermo-mechanical processing techniques. The addition of aluminium, tin, carbon, oxygen and nitrogen can stabilize the α phase which will increase the transformation temperature and expand the α phase area in the equilibrium diagram. Molybdenum, niobium, vanadium, chromium, and iron are added to stabilize the β phase, which will decrease the transformation temperature and increase the β phase area in the equilibrium diagram [86]. Titanium and its alloys are divided into four categories as unalloyed grades (CP Ti), α and near- α alloys, α - β alloys and β alloys. The details of titanium and its alloys will be discussed in the following section.

(1) Pure titanium

Table 2.3: Chemical composition of CP titanium (wt %)

Element	Nitrogen	Carbon	Hydrogen	Iron	Oxygen	Titanium
Grade 1	0.03	0.10	0.015	0.20	0.18	Balance
Grade 2	0.03	0.10	0.015	0.30	0.25	
Grade 3	0.05	0.10	0.015	0.50	0.35	
Grade 4	0.05	0.10	0.015	0.50	0.40	

There are four grades of commercially pure (CP) titanium for the application of surgical implants. The chemical compositions of these four grades titanium are shown in table 2.3 [85]. As shown in table 2.3, commercially pure titanium still includes small amounts of nitrogen, carbon, hydrogen, iron, and oxygen, but oxygen, iron and nitrogen should be carefully controlled. The main difference between grades is the oxygen and iron content. The increase of both will increase the strength of titanium. Increasing the purity of titanium decreases the strength, the hardness and the transformation temperature.

The typical microstructure of CP titanium is a single α phase (HCP), which has low strength and high ductility and corrosion resistance. The applications of CP titanium include pacemakers, ventricular-assist devices, implantable infusion drug pumps, dental implants, maxillofacial and craniofacial implants, and screws and staples for spinal surgery [104]. The most commonly used CP titanium is designated as ASTM F67, which is grade 4 of CP Ti.

(2) Titanium alloy [104]

Generally, titanium alloys have either an HCP phase (α), a BCC phase (β) or a combination of both phases. The relative amount of the two phases and their phase morphology in titanium alloys can be controlled by chemical and thermo-mechanical treatment. Take the Ti-6Al-4V alloy for example, aluminium is added to stabilize the α phase and vanadium is used to stabilize the β phase.

(a) α and near α titanium

α alloys, which contain aluminium, tin and/or zirconium, are widely used in high temperature and cryogenic applications. When at high temperature, α -rich alloys are more resistant to creep than α - β or β alloys. When used at cryogenic temperatures, these alloys also retain excellent ductility and toughness. α alloys cannot be greatly strengthened by heat treatment, but they can be annealed or recrystallized to remove residual stresses resulted from cold working. Due to their insensitivity to heat treatment, α alloys have a very good weldability.

When the β stabilizers are added into α alloys, the alloys become the near- α alloys or super- α alloys. Although they consist of small amount of β phase, these alloys mainly contain α phase and perform more like conventional α alloys than α - β alloys. Because of their low ambient temperature strength, α and near- α alloys have not been used for medical applications so far.

(b) α - β titanium alloys

α - β alloys are the alloys which consist of one or more α stabilizers or α -soluble elements together with one or more β stabilizers. They can be strengthened by solution treatment as well as aging. Solution treatment is usually processed at high temperature in the two-phase α - β field followed by quenching in water, oil or other suitable quenchant. After quenching, the β phase generated at the solution treatment temperature is possibly retained, or partly or fully transformed during cooling. Following solution treatment, aging is normally at 480 °C to 650

$^{\circ}\text{C}$ to precipitate α phase and create a fine mixture of α and β in the retained or transformed β phase. Solution treatment and aging can strengthen α - β alloys by 30% to 50%.

There are currently four ASTM standardized α - β alloys applied for medical implants, i.e., F136 (Ti-6Al-4V ELI), F1472 (Ti-6Al-4V), F1295 (Ti-6Al-7Nb) and F2146 (Ti-3Al-2.5V). F136 and F1472 are the most commonly used α - β alloys, which are widely employed for hip and knee prostheses. F1295 is metallurgically similar to Ti-6Al-4V and has been used for hip stems, fracture fixation plates, spinal components, fasteners, nails, rods, screws and wire. F2146 alloys, whose tensile properties are 20% to 50% higher than all CP Ti alloys, are famous for their excellent cold formability and are usually used for tubing and intramedullary nails. The mechanical properties of α - β titanium alloys are displayed in table 2.4 [104].

Table 2.4: Mechanical properties of α - β titanium alloys

Alloy designation	Elastic modulus	0.2% yield strength	Ultimate tensile strength	Elongation (%)
Ti-6Al-4V	110 Gpa	860 Mpa	930 Mpa	10-15
Ti-6Al-7Nb	105 Gpa	795 Mpa	860 Mpa	10
Ti-5Al-2.5Fe	110 Gpa	820 Mpa	900 Mpa	6
Ti-3Al-2.5V	100 Gpa	585 Mpa	690 Mpa	15

(c) β titanium alloys

Compared to α - β alloys, β alloys have more β stabilizers but less α stabilizers. As the β phase is completely retained on air cooling of thin sections or water quenching of thick sections, β alloys can be characterized as having high hardenability, excellent forgeability, and good cold-rolling capability. In these alloys, α phase particles are finely distributed among the retained β phase. The main defects of β alloys compared with α - β alloys are higher density, lower creep strength and lower tensile ductility in the aged condition. However, in the solution-treated condition, β alloys have good ductility and toughness, relatively low strength, and excellent formability.

The β alloys have lower elastic modulus and enhanced biocompatibility in comparison with Ti-6Al-4V and other α - β alloys. The dominating elements in these alloys are niobium, zirconium, molybdenum, tantalum and iron, all of which enhance the biocompatibility.

Moreover, β alloys are vanadium free, which is important, as the element has been reported to be toxic and instigates adverse reactions to soft tissue surrounding implants [104].

2.4.1.3 Stainless steel

Table 2.5: Composition of 316L stainless steel

Element	Composition (wt %)
Carbon	0.03 Max
Manganese	2.00 Max
Phosphorus	0.03 Max
Sulphur	0.03 Max
Silicon	0.75 Max
Chromium	17.00-20.00
Nickel	12.00-14.00
Molybdenum	2.00-4.00
Iron	Balance

Table 2.6: Mechanical properties of 316L stainless steel for implants

Condition	Ultimate tensile strength	Yield strength (0.2% offset)	Elongation 2 in (50.8mm) (%)	Rockwell Hardness
Annealed	485 Mpa	172	40	95HRB
Cold-worked	860 Mpa	690	12	----

Stainless steels are iron based alloys which contain more than 10.5% of chromium, resulting in the formation of a protective chromium-oxide film (< 2 nm thick) at the surface. Other elements added to stainless steel include nickel, molybdenum, carbon, silicon, manganese, and nitrogen (table 2.5 [85]). The use of stainless steel in surgical applications started from 1920s with the development of 18-8-Mo stainless steel. Later 18-8s-Mo stainless steel (known as type 316 stainless steel) which contained a small amount of molybdenum to improve the corrosion resistance was introduced. In 1950s, the carbon content of 316 stainless steel was decreased from 0.08 to a maximum of 0.03% for a better corrosion resistance and hence type 316L stainless steel emerged. 316L (18Cr-14Ni-2.5Mo) stainless

steels are the most widely used in surgical implants among all stainless steel alloys. The ‘L’ in the designation 316L indicates low carbon content.

Table 2.7: Comparison of some of the features of metallic biomaterials

	Stainless steel	Co-based alloys	Ti and Ti-based alloys
Designation	ASTM F138 (316L)	ASTM F75 ASTM F90 ASTM F799 ASTM F562 (Cast and wrought)	ASTM F67, ASTM F136 ASTM F1295 (Cast and wrought)
Primary alloying elements (wt %)	Fe (Balance) Cr (17-20) Ni (12-14) Mo (2-4)	Co (Balance) Cr (19-30) Mo (0-10) Ni (0-37)	Ti (Balance) Al (6) V (4) Nb (7)
Merits	Cost, availability, processing	Wear resistance, corrosion resistance, fatigue strength	Biocompatibility, corrosion, minimum modulus, fatigue strength
Demerits	Long-term behaviour, high modulus	High modulus, biocompatibility	Low wear resistance, low shear strength
Main applications	Temporary devices (fracture plates, screws, hip nails); used for THR stems in UK (Nitrogen strengthened stainless steel)	Dentistry castings, prostheses stems, load-bearing components in total joint replacement (Wrought alloys)	Used in THRs with modular (CoCrMo or ceramic) femoral heads; long term, permanent device (nails, pacemakers)
Polishability	Stainless steel is polishable. The polishability of stainless steel implants depends on the shape of the devices.	All CoCr alloys implants can be polished.	All Ti and Ti alloys are polishable.

Under ASTM specifications, 316L stainless steel is a single-phase austenitic (FCC). There should be no free ferritic (BCC) or carbide phases in the microstructure. In addition, the steel should be free of inclusions or impurity phases such as sulphide stringers. Plastic deformation within grain is another distinct microstructural characteristic of 316L. As cold-worked metals have a significantly increased yield strength, tensile strength and fatigue life as compared to the annealed state, these alloys are often used in a 30% cold-work state [100]. This alloy is

non-magnetic and has better corrosion resistance than any other alloys. The addition of molybdenum can enhance resistance to pitting corrosion in salty water. Nickel is added to stabilize the austenitic phase (FCC) at room temperature and enhance corrosion resistance. The austenitic phase formation can also be affected by both nickel and chromium content.

Table 2.6 shows the mechanical properties of 316L stainless steel [85]. A wide range of properties can be obtained by heat treatment (annealing to obtain softer materials) or cold working (to obtain greater strength and hardness). Selection of the material type is critical as 316L stainless steel is likely to corrode inside the body under certain conditions in a highly stressed and oxygen depleted region, for example the contacts under the screws of the bone of fracture plate. Therefore, these alloys are confined to temporary devices such as fracture plates, screws and hip nails. For the improvement of corrosion resistance, wear resistance and fatigue of 316L alloys, surface modification methods such as anodization, passivation and glow-discharge nitrogen implantation are widely applied [109].

Three metallic biomaterials for orthopaedic implants have been reviewed in this section, i.e., cobalt based alloys, titanium and titanium based alloys and 316L stainless steel. Each metallic biomaterial has distinct merits and drawbacks. Table 2.7 displays some feature comparisons of these alloys [104].

2.4.2 Polymers

Although there are a large amount of polymers used as biomaterials, only 10 to 20 polymers are primarily used in medical devices, two of which are most widely applied in orthopaedic implant, namely PMMA and UHMWPE. This section will review the basic properties of these two polymers.

2.4.2.1 Polymethyl methacrylate (PMMA)

PMMA, is extensively applied as bone cement, is a linear-chain polymer which was popularized by Charnley, who introduced it from the field of dentistry [110]. It is primarily used to secure both the stem of femoral component in the medullary cavity of bone and acetabular component in place, achieving more uniform stress distribution from the implant to the bone. As biomaterials used in orthopaedic, PMMA has excellent biocompatibility wear resistance, creep resistance and yield strength.

Bone cement is supplied in two components, a dry powder and a liquid, to be mixed together in the operating room. The dry powder consists of a PMMA powder, barium sulphate, and benzoyl peroxide and the liquid contains methyl methacrylate monomer, an initiator and a stabilizer. Fillers and fibres are also used to strengthen the cement. For example, the addition of hydroxyapatite (HA) matrix can greatly improve the mechanical and biological activity of PMMA. In addition, ion beam processing has also been applied to improve the bond characteristic of PMMA bone cements. The basic mechanical properties of PMMA are given in table 2.8 [100].

Table 2.8: Mechanical properties of polymers for orthopaedic devices

Biomaterials	Elastic modulus (GPa)	Yield strength (MPa)	Ultimate strength (MPa)	Fatigue strength (MPa)	Hardness HVN	Elongation at fracture (%)
PMMA	1.8-3.3	35-70	38-80 (tension)	19-39	100-200	2.5-6
UHMWPE	0.5-1.3	20-30	30-40 (tension)	13-20	60-90	130-500

2.4.2.2 Ultra high molecular weight polyethylene (UHMWPE)

UHMWPE is a linear polyethylene that has an extremely high average molecular weight (approximate 4×10^6 g/mol) [86]. It has excellent physical and mechanical properties, chemical inertness, lubricity, impact resistance and abrasion resistance [111]. Since being adopted by Sir John Charnley for one of the articulating surface components in the hip joint prosthesis in 1962, UHMWPE has played a central role in joint arthroplasty. As mentioned in the annual report of the NJR [1], the majority of total hip replacements use UHMWPE as the bearing surface, accounting for more than 70% in total. The main constituents in the polymerization of UHMWPE include ethylene, hydrogen, and a catalyst (titanium tetrachloride).

The cyclic articulation motion between bearing components of UHMWPE and metal will result in the creation of sub-micrometer wear particles. The biological interaction of these particles with the body immune system may cause osteolysis and mechanical loosening, which necessitates an expensive and painful prosthesis replacement or revision. In order to improve oxidation and wear resistance of UHMWPE bearing materials, highly cross-linked UHMWPE was developed in the late 1980s and early 1990s. Generally, UHMWPE can be achieved by subjecting the polymer to ionizing radiation or by using peroxide or silane chemistries which instigates cross linking between the polyethylene molecular chains [112,

113]. This is a more prevalent polymer bearing material on the current market of total joint replacements. Wear tests by simulator studies have shown that the wear resistance of highly cross-linked UHMWPE has been greatly improved [114]. Although this new highly cross-linked polymer has superior mechanical properties to previous UHMWPE, there are still insufficient long term performance data. To maximize the performance characteristics of highly cross-linked UHMWPE, it should be cross-linked prior to fabrication into its final form. For example, an extruded bar of polyethylene is cross-linked using conventional gamma irradiation and then heat treated to reduce residual free radicals [115].

2.4.3 Ceramics

Due to its outstanding biocompatibility and wear resistance, alumina ceramic was firstly adopted for the articulating components by Dr Boutin in the 1970s [43]. However, the breakage of several heads resulting from the considerable brittleness of the ceramic material restricted the spread of this initial component. In 1990s, ceramic became prevalent again when the higher purity and better mechanical property ceramic was introduced. The improved ceramics had finer grain size, increased density and more homogeneous structure. At present, ceramic bearing surfaces have played a significant role in the field of THR and TKR. The most commonly used ceramic materials are alumina (Al_2O_3) and zirconia (ZrO_2). These two types of ceramic will be reviewed respectively in the following sections.

2.4.3.1 Alumina (Al_2O_3)

Table 2.9: Physical and mechanical properties of alumina ceramic

Alumina content, %	≥ 99.5
Density, g/cm^3	3.94
Median grain size, μm	≤ 4.5
Vickers hardness, GPa	18
Compressive strength, GPa	4
Flexural strength, MPa	400
Elastic modulus, GPa	380
Weibull modulus	8

High purity ($>99.5\%$), high density alumina ceramics are extensively used in total joint replacements. Impurities such as SiO_2 , metal silicates, and alkali oxides must be minimized to less than 0.1 wt%, because these contaminants can form a glassy phase around grain

boundaries, which has low chemical stability and may greatly impair the fracture, flexure and fatigue strength of the material. High purity alumina ceramics should be produced by using fine particle powders (typically $<1\mu\text{m}$) to achieve the requirement of fine grain size and strength levels after thermal densification. Increased mechanical properties are gained from processing the ceramic by hot isostatic pressing. The strength, fatigue resistance and fracture toughness of polycrystalline alumina depend on its grain size and purity. Alumina with an average grain size of $<4\mu\text{m}$ and $>99.7\%$ purity manifests excellent flexural strength and compressive strength. The basic physical and mechanical properties of ceramic are shown in table 2.9 [104]. A small amount of MgO ($<0.5\text{ w } \%$) is used to aid sintering and limit grain growth during sintering. However, this amount should be strictly controlled because sintering aid remained in the grain boundaries may degrade the fatigue resistance. Alumina ceramics can be polished to a very high surface finish which will be beneficial for the tribological property of bearing surfaces.

2.4.3.2 Zirconia (ZrO_2)

Zirconia ceramic is also applied as the bearing surface in total joint replacements. Compared to alumina ceramic, zirconia has a smaller grain size which means it has a higher strength and a higher wear resistance. The addition of magnesium oxide (MgO) or yttrium oxide (Y_2O_3) is used to stabilize the crystalline structure of zirconia. The stabilized zirconia is stronger than alumina in general and can provide a greater degree of protection against fracture [116]. However, a phase transformation can occur in the environment of high temperature and moisture such as autoclave. This will weaken the material, resulting in roughening of the surface and degradation of wear properties. These problems are thought to have led to the fracture of ZrO_2 femoral heads in vivo [117, 118], leading to the mass recall of ZrO_2 femoral heads in 2001. This event shook the confidence in zirconia as a feasible biomaterial and as a result alumina ceramic has become the most widely used ceramic material for the fabrication of total joint replacement components.

2.4.4 Composites

Composites are the materials that consist of two or more chemically distinct constituents on a scale larger than the atomic scale [100]. They usually contain one or more discontinuous phases embedded within a continuous phase. The discontinuous phase, which is called reinforcement or reinforcing material, is harder and stronger than the tough continuous phase that is termed the matrix. The composite properties are strongly affected by the properties of

the constituent materials, their distribution and content, and the interaction among them. The most extensively used composite materials in implants include carbon fibre reinforced UHMWPE [119], carbon fibre reinforced Polyetheretherketone (PEEK) [120], hydroxyl-apatite ceramic, and tricalcium phosphates [100].

2.5 Manufacturing process for CoCr alloy components of arthroplasty

CoCr alloys are the most commonly used biomaterial in the field of artificial implants. Polishing of CoCr alloys forms the core of this thesis, therefore in the following sections the manufacturing processes for such alloys as they are processed into orthopaedic devices are reviewed. The review will pay particular emphasis on the finishing stages for THR and TKR. The general processes for manufacturing of CoCr alloy components consist of investment casting and machining [121]. Following machining, the components must be sterilized before they can be packaged and delivered to surgeons for implantation.

2.5.1 Investment casting

The investment casting is the most common metalworking process used to manufacture the desired shape of an implant (spherical femoral head or freeform knee component). The first step of the process is to make a wax model close to the final dimension of the desired implant. A ceramic material is used to coat the wax mould. After several ceramic coating stages, the wax model is removed by heating the mould. The final prosthesis is formed by pouring the molten CoCr alloy into the mould. Finally, when metal is solidified into the shape of the desired implant, the ceramic mould is broken away to release the “as cast” prosthesis. The rough shape of prosthesis has now been created and it is ready for final sizing and finishing. The details of investment casting process can be found in [122]. The machining processes can be divided into rough machining (such as grinding) and finishing (such as polishing).

2.5.2 Rough machining

The most widely used rough machining process for CoCr alloys prostheses after investment casting is grinding. Grinding is a conventional machining process that employs bonded abrasives to obtain the desired shape as well as to improve the surface finish of prostheses [123-126]. In the grinding process the abrasives are bonded into a wheel, both the abrasive and bond will encounter the surface of workpiece. As the abrasive grits are bonded into a wheel randomly, individual grain may contact the surface of workpiece with a negative,

positive or zero rake angle. Material is removed in the form of micro chips produced from suitably orientated and sharp abrasive grains. Worn or unfavourably orientated grains either rub or plough the workpiece surface. A typical grinding process for a femoral knee components is shown in figure 2.17 [127]. In grinding temperature increase is a significant factor which can adversely affect the surface qualities. With the temperature variation, the deformation or cracking of a workpiece may take place. This will cause loss of dimensional accuracy of the workpiece and subsurface damage [128]. Another important element that will affect the shape and accuracy of the ground surface must be considered is the wear of grinding wheel, however this is usually corrected by employing suitable grinding wheel dressing and truing. Apart from grinding, milling can also be used as a rough machining process for prostheses (figure 2.18 [129]).



Figure 2.17: Grinding process for knee femoral components [127]



Figure 2.18: Milling process for knee femoral components [129]

2.5.3 Final finishing

The aim of final finishing is to improve the surface topography produced by grinding/milling and to remove the scratches and surface defects left by rough machining then to reduce the surface roughness to a specified low level. The surface quality of the bearing surface is essential to increasing the longevity of prostheses to a great extent [130]. One of the most commonly used finishing technology is polishing, including manual polishing, semi-automatic and automatic polishing. Manual polishing which is labour intensive and time-consuming work and is only performed by experienced craftsmen. Semi-automatic polishing includes some manual involvement by the use of electro-mechanical device such as motorized polishing tools, robotic tools, etc. Automatic polishing began in the 1950s and was only applied for simple geometries, for example flats, spheres, and cylinders in the early stages. In 1980s when the computer numerical control (CNC) was introduced to polishing, automatic polishing has been extended to cover more complicated geometries. Currently, finishing of freeform knee femoral components is still carried out by hand or semi-automatically, however it is the contention of the author that CNC polishing, which is the focus of this thesis, will replace it in the future. The details of polishing technologies will be discussed in the next chapter.

2.6 Surface metrology

Metrology which comprises the measurement of surface finish and geometry is of paramount importance in the manufacture of artificial joints. Surface finish assessment is focused on measuring small-scale topographical features of surfaces and in this work it will be used to evaluate the effect of the polishing process. Geometrical metrology includes assessment of dimension and evaluation of form i.e., sphericity and cylindricity, etc.

2.6.1 Geometrical specification standards for artificial joints

(1) Surface finish

The standard BS ISO7206-2:2011 specifies the roughness average (Ra) for articulating surfaces of total hip joint prostheses. This standard specifies the requirements for the bearing surfaces of total and partial hip joint implants. According to the standard, the surface finish of femoral components of a total hip joint prosthesis should be not greater than $0.05\mu\text{m } Ra$ for metal components and not greater than $0.02\mu\text{m } Ra$ for ceramic components [2]. The standard

of BS ISO7206-2:2011 stipulates that the articulating surfaces of metallic or ceramic knee joint prostheses should have an Ra value not greater than $0.1\mu\text{m}$ [131]. Consequently all surface finish of artificial joints after final finishing must be at a lower level than the above mentioned values.

(2) Geometry

According to the standard BS ISO7206-2:2011, the departure from sphericity of the spherical bearing surface of a femoral head (i.e. a sphere) should be not greater than $10\mu\text{m}$ [2]. The sphericity is assessed by sphericity error which is the sum of maximal and minimal deviations from the least-squares sphere [6]. Roundness error is an indicator used to evaluate the sphericity by obtaining circular traces of the implants [7]. However, there is no specification for freeform knee femoral components in ISO7207-2: 2011. This is may be the reason that the surface of knee prostheses is too complicated. Therefore, it is stringent to develop a feasible polishing and metrology process for freeform knee femoral components.

2.6.2 Instrumentation

To date, several types of instruments are normally used for measuring the surface finish and form error of implant devices. There are many classification systems in existence which distinguish between the various measurements techniques. The simplest system differentiates measurement methods based on whether they are either contact or non-contact [132]. Contacting instruments typically use a mechanical probe while non-contacting systems such as optical techniques based on the reflection of a light from the component surface. The following two instruments are considered optimal for monitoring surface finish and form deviation and are almost exclusively used during this research, the Talysurf phase grating interferometer (PGI) is a contact stylus device, the coherence correlation interferometer (CCI) and 4D laser interferometer are non-contact optical interferometric instruments.

(1) Talysurf phase grating interferometer (PGI)

The Talysurf PGI is a contact stylus instrument where the mechanical stylus, in the work reported in this thesis, has a $2\mu\text{m}$ radius 60° conical tip. The mechanical stylus is pulled across the surface to be measured and the vertical movement (z direction) of the stylus is amplified optically and is directly related to the surface roughness. If the lateral actuation speed (x direction) of the stylus is carefully controlled then the representative profile of a surface topography can be recovered. If a further perpendicular actuation (y direction) of the

stylus is introduced then a topographical map of the surface can be obtained. The vertical measurement system in the PGI Talysurf uses a grating interferometer with a curved diffraction grating carried on a pivotal support arm of a probe for contacting a surface. As measurement occurs, the stylus traverses across the surface and the vertical displacement is converted into an electrical signal which is amplified and then transformed into a digital signal. Then the digital signal is fed into a computer where numerical analysis of the raw topographic data occurs. Historically, an inductive transducer was used to amplify the vertical stylus movement during data collection, however for high resolution (<10nm) over large measurement ranges (>5mm) optical amplification using the phase grating technique is preferred. A further development of the method is based on Doppler principle of the amplification laser and it uses a reflective cylindrical holographic diffraction (RCHD) grating as shown in figure 2.19. As shown in the figure, light is emitted from a laser diode and passes through a beam splitter. Part of the light is reflected from a fixed mirror and part from a mirror mounted on the stylus arm. Fringes created by the recombined beams can be counted. The shift in the fringe pattern is proportional to the displacement of the moving mirror, namely the displacement of stylus [133].

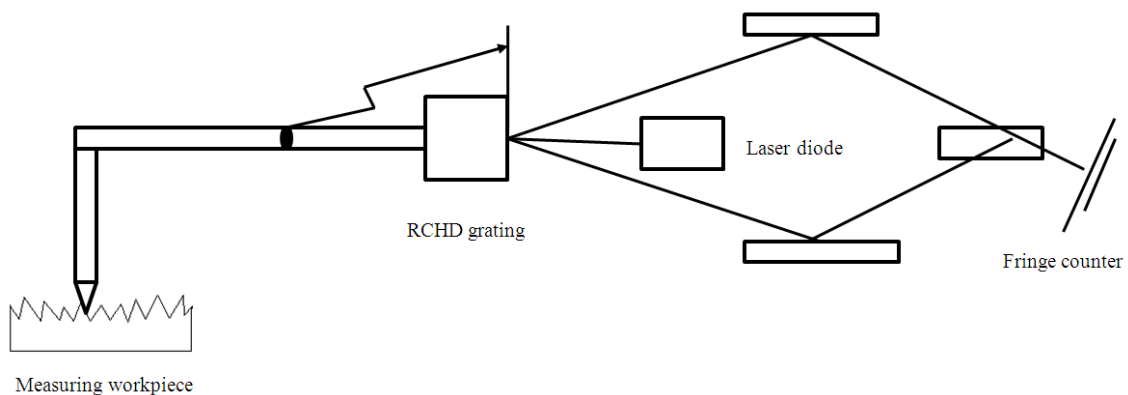


Figure 2.19: The principle of RCHD grating transducer [134]

Due to its nature, the stylus may scratch or damage the surface of a workpiece, especially for the softer material workpiece. Another limitation is that the physical size of the stylus may prevent it from penetrating small pits on the surface. Additionally, stylus wear resulting from long time utilisation could also affect the measurement result. The Talysurf PGI Series 2 (Taylor Hobson Ltd, UK) is based on the RCHD grating method, figure 2.19 [134]. This instrument can measure surface texture, form and contour simultaneously. The excellent resolution throughout its gauge range makes it the most powerful gauging system currently available on any form and surface texture stylus instruments. The typical specifications of

Talysurf PGI are given in table 2.10. The Talysurf PGI is calibrated through carrying out a measurement on a hemisphere of known form and texture. The calibration artefact is from an accredited source to ensure the effective correction of the instrument.



Figure 2.20: Talysurf PGI Series 2

Table 2.10: The typical specification of Talysurf PGI Series 2

Specifications	Values
Vertical resolution	12.8nm
Lateral resolution	0.25 μ m
Vertical range	10mm
Lateral range	120mm
Traverse speed	0.5mm/s or 1.0mm/s
Stylus force	1mN

(2) The Coherence Correlation Interferometer (CCI)

A typical manifestation of an optical measurement is based on the principle of interference of two beams of light where one is reflected by the workpiece surface and the other by a reference mirror. There are two kinds of interferometry which are commercially available, phase shifting interferometry (PSI) and vertical scanning interferometry (VSI). PSI is associated with a high resolution and high measurement speed and is more commonly used for relatively smooth surfaces. The downside of PSI is that the vertical range is usually restricted to about 650nm. VSI, whose resolution is inferior to PSI technique, is preferred for rougher surfaces due to the higher vertical range of topography. The primary disadvantage of

interferometric measurement is that it is only suitable for the surfaces with a reasonable reflectivity and with a gradual slope change. If the surface can not reflect the light, there will be no interference hence no fringes. Rapid slope changes on surface are sometimes very difficult to measure because of insufficient returned light. In addition, when using the interferometers, the instrumentation must be vibration isolated to allow stable interference fringes to be monitored.

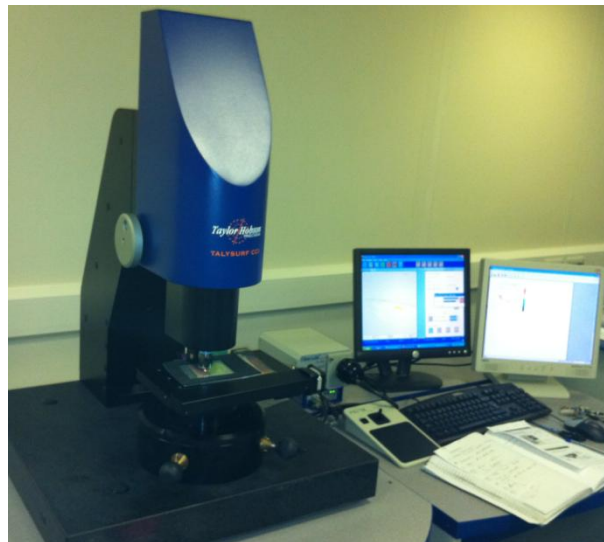


Figure 2.21: Talysurf CCI

Table 2.11: Typical specifications of Talysurf CCI

Specifications	Values
Vertical resolution	0.01nm
Maximal lateral resolution	0.36 μ m
Vertical range	100 μ m
Maximal measurement area	7.2 \times 7.2mm ²
Data points	1024 \times 1024 pixel array
Root mean square repeatability	3pm
Typical measurement time	10-20 seconds

The Talysurf CCI (Taylor Hobson Ltd, UK) is a typical optical interferometer (figure 2.21). It uses an innovative, patented correlation algorithm to find the coherence peak and phase position of an interference pattern produced by a precision optical scanning unit. The basic principle of CCI is schematically shown in figure 2.22. A beam of white light is directed by the beam splitter 2 towards beam splitter 1 where it is separated into two parallel beams. The first beam is directed towards the surface of workpiece and the second beam is directed towards an internal reference mirror. The two beams then recombine and give a local interference image, which is sent to the charge coupled devices (CCD) detector. When the

measuring head is moved vertically by the piezo-electric actuators (PZTs), the vertical position at which maximal intensity interference takes place can be detected for each pixel of the CCD system based on the coherence correlation algorithm. During the process, the position of the objective lens can be tracked. As a result, the topography of workpiece is acquired over the measurement area which is defined by the numerical aperture of the objective lens. CCI can measure all types of material sample including glasses, metals, polymers and composites with a reflectivity between 0.3% and 100%. Furthermore, it has an anti-vibration system and can provide different kinds of automated stages. The typical specifications of CCI are given in table 2.11. Calibration for PSI and VSI is slightly different, both use a reference artefact obtained from an accredited source to check the accuracy of the system. For PSI the artefact is an optical flat mirror but for VSI a step height gauge is applied.

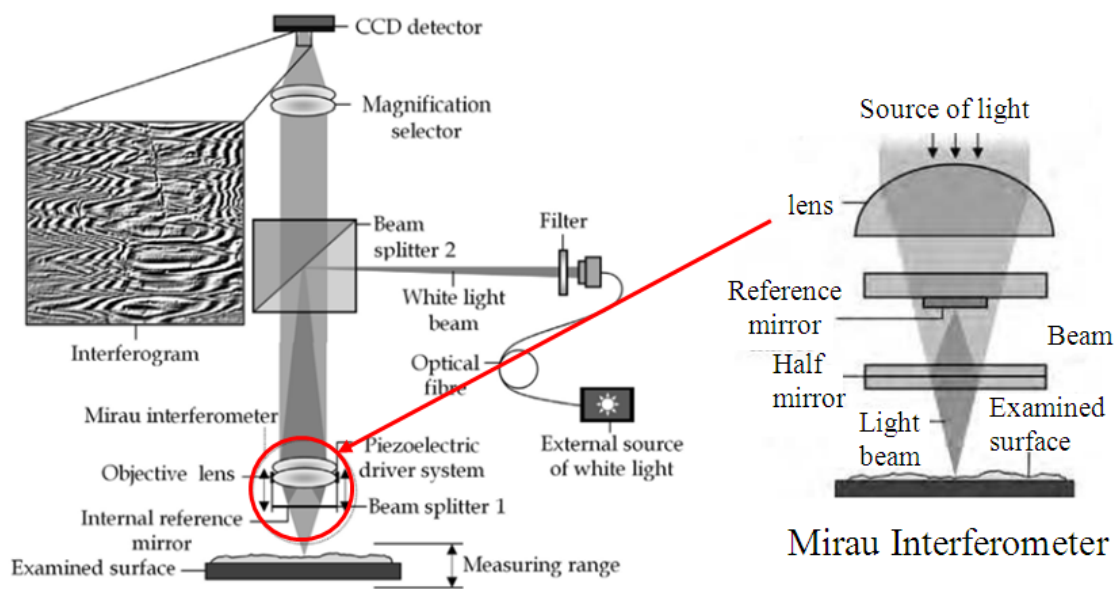


Figure 2.22: The principle of Talysurf CCI [135]

(3) 4D laser interferometer

The main limitation of PSI for optical measuring is that it is very sensitive to the environmental vibration and air turbulence. A method called dynamic interferometry technology which can reduce the environmental effects has been proposed by Millerd et al. [136, 137]. It takes all the phase shifted frames simultaneously as shown in figure 2.23. As shown in the figure 2.23, the illumination system consists of a short coherence laser source and an optical delaying device which splits the source beam into two orthogonally polarized components and applies a controllable optical path difference between the two beams. This output, which is imaged via an afocal imaging system onto a pixedlated mask sensor, is used

as the illumination source for a standard Fizeau interferometer arrangement. The half wave plate in front of the laser source is applied to adjust the intensity ratio between the two beams. Mirror M1 is fixed on a stage and allows the optical path length of the exiting p-polarized beam to be adjusted relative to that of the s-polarized beam which results from mirror M2. Both the s and p-polarized beams illuminate and are reflected by the test and reference surfaces. The returning beams reflect at the non polarizing beam splitter and are imaged via an afocal imaging system onto the pixelated mask sensor. The quarter wave plate, QWP, is used to convert the linearly polarized test and reference beams into right and left circular polarizations. Because the source has a very short coherence length, about $250\mu\text{m}$, only those short beams whose optical paths, from the source to the camera, have been matched will interfere. No interference will take place between the other beam pairs.

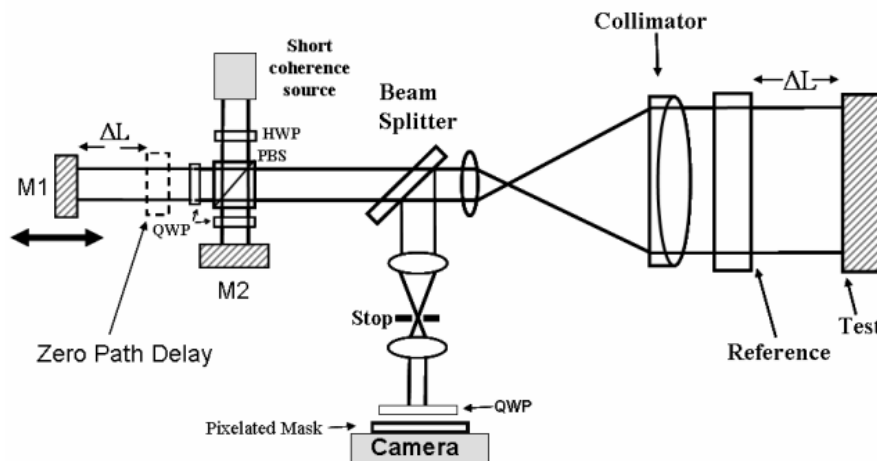


Figure 2.23: The principle of 4D laser interferometer [137]

Dynamic laser interferometer has overcome many barriers to conventional PSI, including vibration, air turbulence and space constraints. It has a wide range of applications such as large optics, general optics, data storage, optical storage pickup heads, etc. A comparison of the instruments mentioned in this section is shown in table 2.12.

Table 2.12: The comparison of instruments

Instruments	Measurement methods	Application
PGI	Contact measurement	Surface roughness and form
CCI	Non-contact measurement	Surface roughness
4D laser interferometer	Non-contact measurement	Surface form

2.7 Summary

At present, nearly all seriously damaged joints of human body can be replaced by suitable artificial implants. Hip replacement and knee replacement are the most prevalent. This chapter has reviewed the background of hip replacement and knee replacement, mainly concentrating on the manufacturing and metrology issues.

In hip replacement, there are mainly two fixation methods, cemented and uncemented. The NJR data indicates that the trend in use of cemented fixation is decreasing while the use of uncemented implants is increasing. Before 2008, the cemented fixation was dominant but after 2008, the use of uncemented fixation has greatly increased. There are six bearing surface combinations of hip replacement, including MoP, MoM, CoC, CoM, CoP and resurfacing. The advantages and disadvantages of each bearing combination have been discussed in detail. Among these combinations, MoP is still the most commonly used, accounting for more than 55% in total hip replacements. Another phenomenon to be noted is the increasing trend in the use of CoC due to an advance of bio-ceramic.

Different from hip replacement, more than 80% of knee replacements apply cemented fixation and only about 5% use uncemented fixation, both of which show little change from 2003 to 2011. The bearing surface combinations for knee replacement are not as abundant as for hip replacement. Most TKRs use a metal femoral component with polyethylene tibial insert. The geometry of TKR components is not standardised (freeform) compared with THR components whose geometry are essentially spherical. Each TKR must be chosen according to the requirement of the patient and conformity and mobility of the bearing. As a result, little attention has been paid to changing material combinations for TKR, but much attention has been paid to the improvement of the mobility and design.

Biomaterials are those materials which must meet the requirement of biocompatibility, sterilizability, manufacturability and reliability. The biomaterials can be categorized into four groups, metals and alloys, polymers, ceramics and composites. There are mainly three metallic biomaterials used for artificial implants, cobalt based alloys, pure titanium and titanium alloys, and stainless steel. The most commonly used metallic biomaterials for THR and TKR is cobalt based alloys, including cast CoCrMo ally (F75), wrought CoCrWNi alloys (F90), wrought CoNiCrMo ally (F562) and wrought CoNiCrMoWFe (F799). The properties and chemical combinations of each alloy have been reviewed in detail in the above sections.

Compared to cobalt based alloys, titanium and titanium alloys are relatively new biomaterials for medical devices and have superior biocompatibility, corrosion resistance and mechanical strength but inferior tribological properties. Because stainless steel is likely to corrode inside the body, therefore, these alloys are only confined to temporary devices such as fracture plates, screws and hip nails. In addition, the commonly used polymers (including PMMA and UHMWPE), ceramics (including alumina and zirconia) and composites are also reviewed.

Because this thesis concentrates on the machining process of cobalt based alloys for artificial joint, especially the final finishing for bearing surface, the manufacturing process of prostheses is reviewed. All cobalt based prostheses must undergo the process of investment casting or forging, rough machining, final finishing, sterilization and package before implantation. CNC final finishing, for example polishing, is of the most interest in this thesis, thus the details of polishing are discussed in the next chapter.

The last section of this chapter briefly reviews surface metrology for the THR and the TKR manufacture, consisting of surface finish, geometrical measurement and instrumentation considerations. The ISO7206-2:2011 standard specifies that the surface finish of bearing surface for artificial joints must be better than 50nm for metals and 20nm for ceramics. The geometry of prosthesis must be precisely controlled as well during machining. In the case of hip implant, the sphericity of femoral head should be superior to 10 μ m. However, there is no specification for freeform knee femoral components in ISO7207-2:2011 standards due to their complexity. In this research, the PGI and CCI instrument are almost exclusively used to evaluate the surface finish and geometry of the polished surface. Therefore, the basic principles of these devices are also reviewed.

3. POLISHING TECHNOLOGIES FOR BEARING SURFACES OF ARTIFICIAL IMPLANTS

3.1 Introduction

Ultra-precision polishing is one of the most commonly used final finishing technologies [138]. The bearing surfaces of prostheses must be polished to nanometre scale surface texture and micrometer scale form tolerance before implantation to ensure optimum functionality [9, 130]. Currently, the final finishing for artificial joints is still mainly performed manually or semi-automatically by experienced and skilled workers or crude robot control. The application of fully automated CNC polishing has not yet been achieved and manual polishing is still significant for freeform knee femoral components for example. The CNC bonnet polishing is an attempt to address this technology gap using automatic controlled finishing. This technique has been successfully applied in the area of optics [139]. The application of this technology to other areas such as artificial prostheses is still developing. The aim of this thesis is to develop a feasible finishing process for cobalt based implants.

This chapter will review the related technologies of ultra-precision polishing. Firstly, polishing technologies are introduced, including polishing tools, polishing slurry, polishing abrasives and polishing pads/clothes. Secondly, the material removal process of polishing are discussed. Thirdly is the investigation of surface roughness improvement. After that is the process of form correction. Different types of polishing technologies which are potentially used for artificial joints in the future are also reviewed and special attention is paid to the bonnet polishing technology in the last section.

3.2 Polishing

Polishing is a machining process that applies free abrasives with conformable pads or soft cloths to create smooth and shiny surfaces [124]. During polishing processes, material is primarily removed by plastic deformation (microchips) instead of brittle fractures [124]. All polishing systems generally consist of the following four components, i.e., polishing tool, slurry, abrasives and workpiece [140]. The workpiece is the objective of polishing, including almost all types of materials, such as metals, glasses, quartz, silica, etc. In this research, most investigations were carried out on cobalt based alloys. The other three components are discussed respectively in the following sections.

3.2.1 Polishing tool

The polishing tool is usually a conformable substrate covered with a pad or cloth that is used to impose the relative motion between the workpiece and abrasives. Slurry can be distributed evenly and swarf can be transported by the polishing tool during the polishing process. Traditionally, the substrate can be usually made of cast iron plates or relatively soft metals [140]. Currently, other substrates such as rubber or plastic have been developed. Figure 3.1 shows a typical rubber substrate with and without a polishing pad.



Figure 3.1: Polishing tool (Left: without pad, right: with pad)

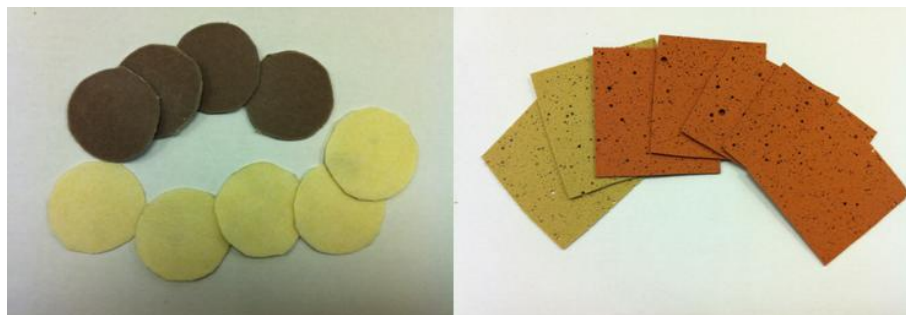


Figure 3.2: Polishing cloth (left) and polishing pad (right)

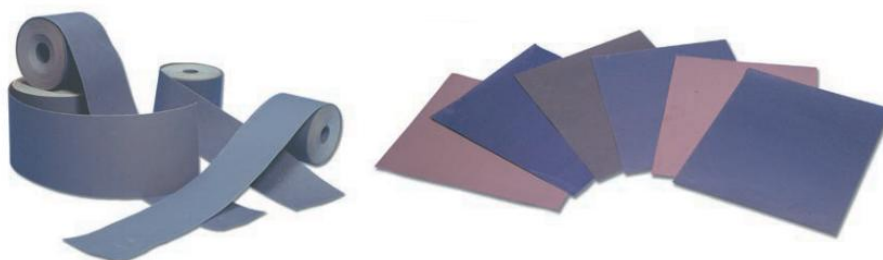


Figure 3.3: Fixed-abrasive polishing cloths [141]

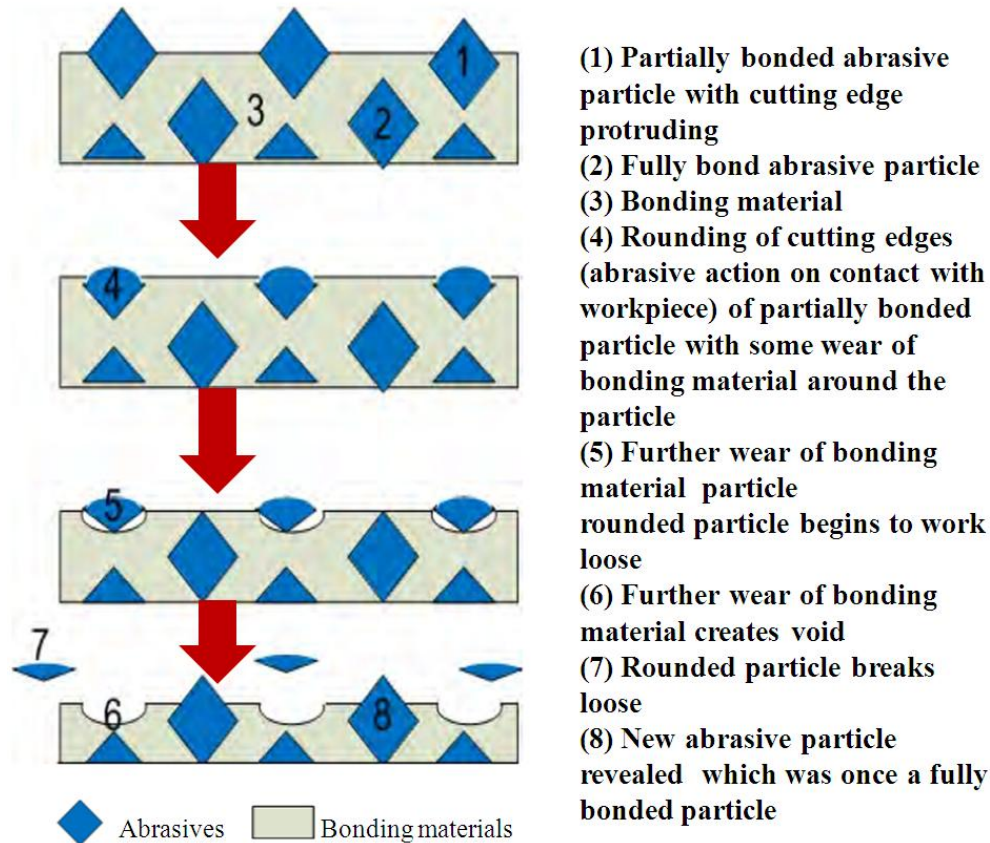


Figure 3.4: Self-sharpening process [142]

A variety of different cloths and pads have been used in polishing. Polishing cloths can be categorized into three groups: woven, flocked and non-woven. Woven cloths are made of different fibres and weave sizes. They are all laminated at the back to avoid penetration of the abrasives and diluents into the abrasive layer. The woven cloths are usually used in the stage of rough polishing. Non-woven cloths are the mixtures of various fibres impregnated with plastic, elastomer, latex, etc and often undergo mechano-chemical treatments. They are used on very hard materials and for finishing of light alloys in mechano-chemical polishing [143]. Flocked cloths are made using different type, length, density and grade of flock, as well as different flock support and bonding. Only flocked cloths provide a super-polished finish on metallic materials. When using a flock cloth, the polishing duration should be as short as possible to avoid inclusion extraction [141]. A selection of polishing cloths is shown in figure 3.2 (left). Polishing pads usually refer to polyurethane foam pads (figure 3.2 (right)). The pad may contain a variety of grooved configurations and porosities, which can greatly improve the pad performance, enabling the transport of swarf and slurry to and from the interface surface more efficiently. Polishing pads can be available to unfilled or abrasive-filled with cerium oxide or zirconium oxide according to the application purpose [144]. In addition,

polishing pads may have different horizontal and vertical elastic and plastic behaviours which can affect material removal rates and surface finish. The wear of pad is usually noted during polishing, because it can change the form and surface texture of pad, resulting in a change of contact mechanics, fluid films, temperature distribution, etc [124].

The polishing cloths and pads discussed above are usually related to loose-abrasive polishing. A further derivative of the polishing cloth, which is related to fixed-abrasive polishing, will be introduced in the following of this section. The term of fixed-abrasive indicates that the abrasives used in these types of polishing cloth are bonded into the papers or cloths (figure 3.3). Silicon carbide is the most common abrasive for fixed-abrasive cloths. The advantage of the fixed-abrasive cloth is that when the cutting edges of the ambient abrasives are worn away, the internal abrasives will expose new shape edges. This process is known as self-sharpening (figure 3.4). In this research, when polishing is referred, it implies loose-abrasive polishing.

3.2.2 Polishing slurry

Slurry consists of the abrasives (grains) and polishing medium (fluid or paste) and is a critical component of the polishing process [124]. The ratio of abrasives in the slurry is termed the volumetric concentration, also called grain concentration. The grit size and concentration of abrasives are two key factors in slurry specification and performance. The selection of the optimal slurry is normally determined experimentally as it is dependent on the properties of the workpiece and polishing cloth/pad. During the polishing process, the slurry is supplied into the gap between the polishing cloth/pad and the workpiece. The types of abrasive, the grit size and concentration may affect the material removal rate and surface finish. The most commonly used polishing fluid is water (deionised) with added agents. The added agents are usually used to control the physical properties of the polishing slurry such as viscosity, density and thermal conductivity, etc [140].

The commonly used polishing paste includes diamond paste and silicon carbide paste (figure 3.5 (Left)). Apart from the abrasives, other compositions for the paste may consist of some of the following substances: stearic acid, fatty acid, paraffin wax, lanolin, glycerin monostearate (GMS), vaseline, rosin, iron oxide, etc. The exact composition of fluid slurry is usually the commercial secret. However, for some generally used fluid slurry, such as alumina slurry, the main compositions are known [141]. Apart from alumina powder and water, it also includes glycerine and carbomer, etc (figure 3.5 (Right)). Paste is generally used to improve the

surface finish. During the polishing process, the amount of paste is consuming quickly and hence the material removal rate decreases with the time elapse [145]. Fluid slurry is preferred when applying to form correction in metals. The material removal rate is assumed to be constant during the fluid slurry polishing. This is beneficial for the calculation of dwell time and considerations of models for material removal rates.



Figure 3.5: Paste slurry (left) and fluid slurry (right) [141]

3.2.3 Abrasives

The abrasives used in polishing processes are of paramount importance. Polishing abrasives may be hard or soft according to the desired material removal rates [124]. Hard abrasives are applied for rough polishing slurry compositions while soft abrasives are employed for fine polishing slurry compositions. Both natural minerals and synthetic products can be used as abrasives. Generally, the abrasive has to be harder than the workpiece to be machined. The option of abrasives for a specific utilization may be based on durability tests including impact strength, fatigue compression strength, dynamic friability, and resistance to spalling [123]. As to a particular application the shape of abrasive grains, its grain size distribution and its material characteristics should be considered. The shape of the grains is essentially affected not only by the material properties such as cleavability and fracture toughness, but also by the manufacturing process. The grain size of abrasives is generally characterized by the specification of the average equivalent diameter of the sphere (called average grain diameter or equivalent diameter) and its standard deviation [146]. The grain size is usually a random value with a characteristic distribution function. Generally, the larger grain size of abrasive should be used for rough polishing and the finer abrasive should be used for final finishing [140]. Accordingly, material removal rate will reduce with the decrease of grain size.

The most commonly used polishing abrasives include diamond, silicon carbide, aluminium oxide, cerium oxide, and colloidal silica, etc. The basic properties of these abrasives will be summarized in the following.

(1) Diamond

Diamond has the highest hardness (Mohs: 10, Knoop scale: 7000Kg mm^{-2}) in nature and is regarded as one of the two super-abrasives (the other one is cubic boron nitride). Both natural diamond and synthetic diamond are available for polishing but synthetic diamond dominates the current market for polishing. Being the hardest known material, diamond is naturally selected for polishing the hardest and most difficult materials and material removal rate is higher comparing to the same grain size of other abrasives. Therefore, despite its high price, the use of diamond is economically efficient in many cases because of the reduced machining times in comparison with other softer abrasives. Since diamond is a form of carbon, it can interact with ferrous materials, creating a specific compound such as Fe_3C which can result in premature wear and pull-out of diamond grits. Chemical reaction has also been found when diamond polishing cloth was applied to cobalt chrome alloys (figure 3.6) [142]. As clearly shown in the figure, the new cloth shows sharp diamonds while the used cloth shows obtuse diamonds due to graphitisation. This phenomenon should be noted when using the diamond abrasives to polish the cobalt chrome alloys.

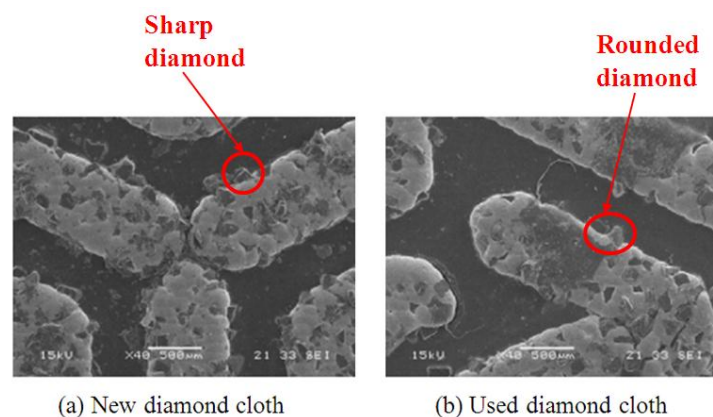


Figure 3.6: Graphitisation of diamond [142]

(2) Silicon carbide (SiC)

SiC has a high hardness (Mohs: 9, Knoop scale: 2700 Kg mm^{-2}) and sharp crystal cutting edges. It is one of the most generally used polishing abrasives and can be used to polish almost all materials. Silicon carbide is quite friable, but impurity within the abrasives can

increase toughness to some extent. When the temperature is higher than 760⁰C, SiC reveals a chemical reactivity towards metals with an affinity for carbon such as iron or nickel [147].

(3) Aluminium oxide (Al₂O₃)

Aluminium oxide, also called corundum, is widely used as an abrasive for polishing steel and other metals. The Mohs hardness and Knoop scale for aluminium oxide are 9 and 2500 Kg mm⁻², respectively. Alumina abrasive is a mixture of α -Al₂O₃ and other metals and oxides. The abrasive properties of alumina are created during the operation of furnace treatment and crushing but the subsequent processes affect the feature of grains very slightly. Alumina abrasives can be obtained by electrofusion, chemical precipitation and/or sintering [124].

(4) Cerium oxide (CeO₂)

Cerium oxide has been widely used in glass polishing and semiconductor fabrication. The Mohs hardness of CeO₂ is 6~6.5. When using cerium oxide for polishing glass, the material is removed not only by mechanical processes but also by chemical reactions. The material removal rate is significantly higher than other abrasives. The details of the interaction between CeO₂ and the polished materials are discussed in [148, 149].

(5) Colloidal silica

Colloidal silica is the suspension of fine amorphous, nonporous and typically spherical particles in a liquid phase. It is suitable for polishing ferrous and nonferrous materials, titanium, semiconductors and ceramics. The high pH of colloidal silica is useful for enhancing the material removal rate chemically [140].

Other common polishing abrasives include chromium oxide (Cr₂O₃), iron oxide (Fe₂O₃), boron carbide (B₄C), and zirconium oxide (ZrO₂), etc. Before deciding to use a particular abrasive, all aspects of material properties such as hardness or chemical properties should be taken into account. In addition, the cost and availability of the abrasives are another factors that needs to be considered [124].

3.3 Material removal in polishing

3.3.1 Material removal mechanism

Polishing has been recognised as a critical technology for achieving the surface finish at the nanometre scale. When machining by polishing, the abrasives are mixed with a polishing

fluid or paste to be supplied to the polishing zone. Due to the fact that they are suspended in the fluid or paste, the abrasive particles interact with the workpiece surface in two modes: (1) they may penetrate into the polishing pad or stick to the polishing pad and become fixed (2) roll and slide freely between the pad and workpiece. If material is removed by the former mode it is classified as two-body abrasion and if the material is removed by the latter it is classified as three-body abrasion. Polishing therefore is a combination of two-body and three-body abrasion [125]. In the case of two-body abrasion material removal is caused by micro-ploughing or micro-cutting of the surface, while three-body abrasion leads to micro-fatigue and micro-fracture (figure 3.7). Micro-chips can only be produced by two-body abrasion rather than by three-body abrasion. Depending on the material combinations, chemical reactions may take place in the contact zone which may be unavoidable and may affect the material removal rate. Excluding chemical reaction the micro cutting mode is recognised as the most efficient material removal mode.

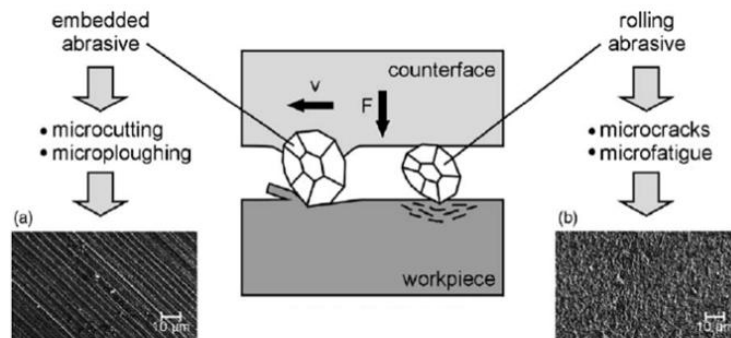


Figure 3.7: Material removal mechanism by polishing [150]

Historically, the material removal mechanism of polishing has been the subject of several theories [151]. The earliest view held by Hooke, Newton and Herschel was that fine abrasive particles cut away the asperities in an abraded surface, replacing them with a set of finer ones (Mechanical mechanism). In the early of 20th century this simple view was superseded by the theory of Sir George Beilby who believed that polishing took place by material being smeared over the surface to fill in pre-existing depressions (Flow mechanism) [152]. He proposed that a rough surface could be covered by an amorphous layer of material whose surface is infinitely smooth. Bowden et al. [153] advanced the mechanism of smearing process by hypothesising that very high temperatures were attained at the points where the abrasive particles rubbed past the asperities in a rough surface. The asperities could be heated up to their melting points, so the heated areas would either melt or become highly plastic and

be easily transported into adjoining depressions by the shearing forces imposed by the abrasive points. They further supposed that the Beilby layer was formed by the transported material of amorphous-like structure due to rapid chilling. However, this plausible concept has been proved false by the modern surface metrology and microscopy techniques. In addition, modern analyses of the transient local temperatures indicate that there is no possibility of temperatures approaching the melting points of metals in general abrasive polishing [154, 155]. As a result, Samuels [151] asserted that mechanisms of the type proposed by Beilby did not occur during metallographic polishing. It is now generally believed that material is removed during polishing rather than being gross smearing. Samuels supposed that material was removed by slurry erosion mechanism, delamination mechanisms, chemical mechanical mechanisms, and micromachining by the abrasives entangled or embedded in the fibre of polishing cloth and abrasives contained in a carrier paste. Nevertheless, these mechanisms are essentially the same as the mechanisms of two-body abrasion and three-body abrasion together with chemical reactions which are widely accepted in the field of polishing.

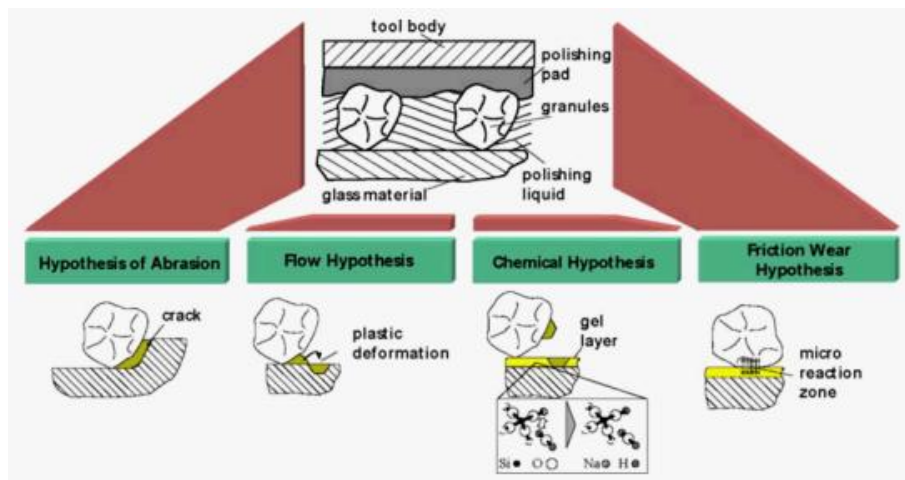


Figure 3.8: The four hypotheses of material removal for mechanical-chemical glass polishing [140]

The above material removal mechanisms can explain the most cases of polishing processes, except for specific materials such as glass, in this case the material removal mechanism is more complicated. Evans et al. [140] summarized four hypotheses for mechanical-chemical glass polishing. These hypotheses include the abrasion hypothesis, flow hypothesis, chemical hypothesis, friction wear hypothesis (figure 3.8). Generally, one hypothesis cannot explain all aspects of glass polishing. Consequently, hybrid hypotheses using certain mechanisms from all available hypotheses have been developed. Komanduri et al. [138, 156] also investigated

extensively the material removal mechanism for brittle materials (glass, SiC, silicon, etc). The research described in this thesis focuses on metal polishing, so the brittle material removal mechanisms are not discussed in detail.

3.3.2 Material removal model

(1) Models based on the Preston equation

As the above mentioned, the material removal mechanism in polishing can be generally classified as two-body abrasion and three-body abrasion as well as certain chemical reactions. It is considered that two-body abrasion is the main material removal mechanism if the abrasives are fixed by a bonnet/lap and three-body abrasion is the primary material removal if the abrasives are freely rolling or sliding in the slurry. Other factors that may impact on the material removal are normal load, particle size and material, concentration of abrasives, hardness of the workpiece and bonnet/lap properties. The mass amount of material removal (MRR) dz can be expressed by the Preston equation [12]:

$$\frac{dz}{dt} = K_p P v_r \quad (3.1)$$

Where P is the contact pressure, v_r is the relative speed between the polishing tool and the workpiece, t is polishing time (dwell time), and K_p is the Preston coefficient which indicates the summation of grain size, concentration of abrasives, materials of polishing tool and the workpiece. Therefore, the Preston coefficient K_p has to be determined by experiments for each polishing system. The MMR is defined as the ratio of dz and dt .

The Preston equation is extensively used to create the MRR model in the various polishing processes. In chemical mechanical polishing (CMP), Wang et al. [157] proposed a model to describe the relationships between polishing parameters and the MRR. Experimental verification showed that this model could predict MRR more accurately than existing models.

In Magnetorheological finishing (MRF), Schinhaerl et al. [158, 159] predicted the distribution of MRR within the influence function. The predicted model was based on the Preston's equation and used to predict influence functions. This model was suitable for planar and convex workpieces and enabled the utilization of the influence function with very high removal rates which reduced the processing time during polishing. Aslo in MRF, Shorey [160] proposed a model to describe the MRR, where the Preston coefficient contains the chemistry

of the carrier fluid, abrasive type and glass type. He used the shear stress to replace the pressure or the frictional force and showed that the material removal increased with the addition of cerium oxide, alumina oxide and diamond. With the consideration of near surface mechanical properties, modified Preston's equation, abrasive size and concentration, glass chemistry and durability and glass average single bond strength, DeGroot et al. [161] used a peak MRR to substitute the MRR and created a considerably more complex model. This model was validated term by term firstly and then combined together to examine mechanics, fluid properties and chemistry in MRF material removal processes. Lambropoulos et al.'s [162] model shows the volume removal rate had a linear relationship with the workpiece's Young's modulus, an inversely proportional relationship with the fracture toughness and the square of Knoop hardness. Through introducing the mechanical properties of workpiece, the Preston's model can be more accurately modified according to different material of the workpiece. With the consideration of the effects of processing parameters, Mao et al. [163] modified the model proposed by Shorey. There were four major process parameters were taken into account in this new equation, including nanodiamond concentration in the MR fluid, penetration depth, magnetic field strength and relative velocity between the rotating wheel and the workpiece. This model was shown to improve the understanding of material removal process in MRF and provided a direct estimation of MRR for glass under a specified experimental conditions.

Jin et al. [164] created an MRR model for bonnet polishing on the basis of the Preston equation and distributions of linear velocity and contact stress in the circular contact area between the polishing tool and the workpiece. This model was based on the assumption that the contact area was circular. In the equation the velocity was deduced by kinematics principles and the contact stress was based on the Hertz contacting theory. Another MRR model for bonnet polishing was established by Cheung et al. [165]. In Cheung's model, the distribution of pressure of the polishing tool was assumed to be Gaussian shape. So a modified Gaussian function was applied to create the pressure distribution. The relative velocity was derived from kinematics theory which was similar to the method applied by Jin. Both Jin and Cheung's models appeared to estimate the MRR for bonnet polishing, but neither of them considered the process parameters during the creation of their models.

(2) Models based on tribological theory

From a tribological point of view, wear volume can be expressed using Archard's Law [125]:

$$V = C_p \times F_n \times L / H_v \quad (3.2)$$

From the Archard equation, it can be seen that that abraded wear volume V is proportional to the normal force F_n and the sliding distance L and inversely proportional to the hardness H_v of the abraded surface, C_p is wear coefficient.

If the material removal mechanism of polishing is assumed to be analogous to a wear mechanism, then certain tribological theories can be directly applied to polishing. Zhang et al. [166] investigated the material removal of fixed abrasives polishing and developed a method to calculate the material removal rate based on the wear index. In this model the pressure distribution in the contact area of the workpiece and polishing tool was assumed to be Hertzian. According to the model, it was found that the shape of material removal profile was parabolic and the material removal was related to the following factors: the normal polishing force, the geometry of polishing tool and the workpiece, the spindle speed and federate of the polishing tool, the materials of the workpiece and the polishing tool.

Based on Rabinowicz's energy equation, Wang et al. [167] developed a mathematical model to describe the material removal rate. This model indicated that the material removal rate was related to the surface energy which implied that for the same conditions a surface with lower surface energy had a higher material removal rate. Furthermore, this investigation also showed that the hardness effect of a ductile material had a negligible influence on the material removal rate.

(3) Others

Apart from theoretical research, investigations of material removal mechanism have also been carried out experimentally. The investigation results of Brinksmeier et al. [150] indicated that abrasives were able to roll between the polishing tool and the workpiece when at low speeds but they were impossible at higher relative velocities. At lower speeds, the material removal was caused by micro-fatigue or micro-cracking while at higher speed it was caused by micro-cutting and micro-ploughing because the faster rotating polishing tool enabled the abrasives embed into the polishing tool. This is the same as higher pressure condition. In other words, for polishing at low pressure and speed, three-body abrasion was the primary material removal mechanism; two-body abrasion was to be found at high pressure and large relative velocities; at intermediate polishing pressure and speed a mixture

of two-body and three-body abrasion was observed. Xie et al. [168] investigated the relationship between the wear rate and polishing parameters such as particle size, polishing pad and nominal contact pressure. The results showed that the material removal rate increased with the increase of particle size, hardness of polishing pad and polishing pressure but decreased with the rise of elastic modulus of polishing pad. It was suggested that it was better to utilize the diamond abrasives to polish hard material so that to obtain a higher removal rate and smoother surfaces. Accepting the aforementioned factors, the material removal rate increased with the increase of abrasive concentration [169, 170]. In addition, abrasive particle characteristics (for example hardness, shape, toughness and angularity) and tool surface irregularities are also relevant to the material removal rate of polishing [171, 172].

3.4 Surface roughness improvement

Traditionally, polishing is mainly applied to improve the surface roughness, therefore how to produce and then quantify the ultra-smooth surface produced by polishing has become of the greatest interest to researchers. Much work has been carried out to investigate the technique of surface roughness improvement. Brinksmeier et al. [150] showed that the surface roughness reduced with smaller relative velocities. Kasai et al. [173] investigated the relationship between the roughness and polishing parameters indicating that the roughness was proportional to abrasives diameter and hardness of tool and inversely proportional to the hardness of workpiece. This research also showed that the surface roughness was proportional to the height of irregularity of polishing tool and inversely proportional to the elastic deformation of the polishing tool. Xie et al. [168] showed the same result as [173], surface roughness increased with the increase of abrasive particle size and the hardness of polishing tool but nominal contact pressure had less effect on the surface roughness. Huang et al. [169] showed that surface roughness could be improved by using a higher rotating speed, smaller particle size and lower concentration.

In order to construct the relationship between the surface roughness and polishing parameters, a predictive model of surface roughness based on Reye's wear model which supposes that the material removal per unit area was proportional to the work due to the friction force was proposed by Savio et al. [174]. In this research, the effects of polishing parameters such as polishing tool deformation, the relative velocity, the tool radius, the Young modulus of tool, and the feedrate on surface roughness were assessed. This model correlated the surface

parameters S_a , S_q , S_v , S_z and polishing parameters. According to [175], these parameters can be expressed as follows:

The arithmetic mean height:

$$S_a = \frac{1}{A} \iint_A |z(x, y)| dx dy \quad (3.3)$$

The root mean square height:

$$S_q = \sqrt{\frac{1}{A} \iint_A z^2(x, y) dx dy} \quad (3.4)$$

The maximum pit height:

$$S_v = |\min(z(x, y))| \quad (3.5)$$

The maximum height of scale limited surface:

$$S_z = |\max(z(x, y))| + |\min(z(x, y))| \quad (3.6)$$

Where $z(x,y)$ is the height of surface coordinate at the position of (x,y) and is acquired by using filtration techniques [176]. Hertz contact theory and Reye's wear hypothesis were also used in the process of creating a predictive model of surface roughness. Based on the assumption of a random distribution of abrasive grits in polishing tool and the force balance by contact grains, Xi et al. [177] developed a model for predicting surface roughness. The predicted results showed good agreement with the experimental results over the range of conditions tested.

3.5 Form correction

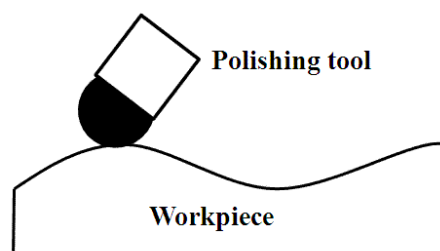


Figure 3.9: Schematic of form correction

With the development of precision technology, the form accuracy of a component has become increasingly important in the areas of aerospace, medicine and energy. Form correction is a technology that is used to correct the form error of a component by mainly controlling the dwell time (the time for the polishing tool to slow down and speed up should also be noted). In other words assuming a constant material removal rate, the longer the polishing tool dwells, the more material will be removed (figure 3.9). The relationship between the amount of material removal and dwell time can be expressed as follows [178]:

$$\Delta z(x, y) = t(x, y) * r(x, y) \quad (3.7)$$

This equation indicates that the amount of material removal $\Delta z(x, y)$ is the convolution of the dwell time function $t(x, y)$ and the influence function $r(x, y)$. The amount of material removal $\Delta z(x, y)$ is the difference of surface figure before and after polishing. According to the equation (3.7), the desired material removal and influence function should be already known, so the dwell time function can be calculated by a deconvolution process. Fourier transformation is the most widely used to perform the deconvolution operation [179]. In Fourier transformation, convolution of two functions in the spatial domain can be expressed as the product of them in the frequency domain, so after Fourier transformation equation (3.7) can be expressed as:

$$\Delta z(f_x, f_y) = T(f_x, f_y) * R(f_x, f_y) \quad (3.8)$$

Where, $\Delta z(f_x, f_y)$, $T(f_x, f_y)$ and $R(f_x, f_y)$ are two dimensional Fourier transformation of $\Delta z(x, y)$, $t(x, y)$ and $r(x, y)$, respectively. Then,

$$T(f_x, f_y) = \frac{\Delta z(f_x, f_y)}{R(f_x, f_y)} \quad (3.9)$$

So the dwell time can be obtained by inverse Fourier transformation of equation (3.9).

$$t(x, y) = F^{-1} \left(\frac{\Delta z(f_x, f_y)}{R(f_x, f_y)} \right) \quad (3.10)$$

Where, F^{-1} implies inverse Fourier transformation. Equation (3.7) is continuous, but the actual measurement surface figure of a workpiece is a set of discrete grid points. Therefore, the continuous Fourier transformation is usually applied to the theoretical analysis while the

discrete convolution method is actually used in real polishing [180]. Equation (3.7) can be discretized as:

$$\Delta z(x, y) = \sum_i \sum_j r(x - x'_i, y - y'_j) t(x'_i, y'_j) \Delta x'_i \Delta y'_j \quad (3.11)$$

The material removal, influence function and dwell time function can then be expressed by the matrix,

$$\Delta z = R * T \quad (3.11)$$

Where, Δz and R are the discrete matrix of $\Delta z(x, y)$ and $r(x, y)$ respectively, namely $\Delta Z_{i,j} = \Delta z(x_i, y_j)$, $R_{i,j} = r(x_i, y_j)$. T is the dwell time matrix, $T_{i,j} = t(x_i, y_j) \Delta x'_i \Delta y'_j$. The dwell time matrix can be resolved by discrete convolution. In addition, iterative methods and a matrix algebraic approach are also used to solve the dwell time map [181, 182].

3.6 Types of polishing

In this section, some common types of polishing technologies which could be potentially used for finishing the bearing surface of artificial joints are reviewed, including elastic emission machining, magnetorhological finishing, ion beam figuring and bonnet polishing. Bonnet polishing is the focus of this section.

3.6.1 Elastic emission machining

The Elastic emission machining (EEM) process (also referred to Hydrodynamic polishing, HDP) was considered to be an ultra-precision machining process and was first developed by Mori et al. [183, 184]. As shown in figure 3.10, the EEM system includes a soft spherical rotating tool, slurry and the workpiece. The workpiece and rotating tool are both immersed in the slurry that consists of abrasives and water. The rotating tool which is made of polyurethane always stays at 45 degrees from the tangent line of the workpiece. EEM uses extremely fine size abrasives to polish the workpiece by dragging the moving slurry. The abrasive particles are accelerated by the flow of slurry but progressively leave the slurry flow to shear the workpiece surface. As stated by inventors, when polishing a silicon workpiece, material removal was not achieved by mechanical scratching by the rotating tool but by utilizing the chemical activities of particle surfaces, therefore the sub-surface of workpiece did not sustain any damage [185].

The EEM method has been applied successfully to create smooth mirror-like surfaces as the amount of material removal at a given point can be controlled by dwell time, hence the complex surface geometry of a component can be manufactured. Compared with the traditional machining methods, EEM has the following advantages:

- (1) The rigidity demand of machine structure of EEM methods is much less than traditional methods.
- (2) The machining performance of the EEM is less sensitive to temperature variation or system vibration than its traditional counterparts.

However, the material removal in EEM is realized by the flow of slurry, the material removal rate is relatively low comparing to other contact polishing. In addition, this method is unsuitable for large workpiece for the reason that the workpiece must be immersed in the slurry during polishing.

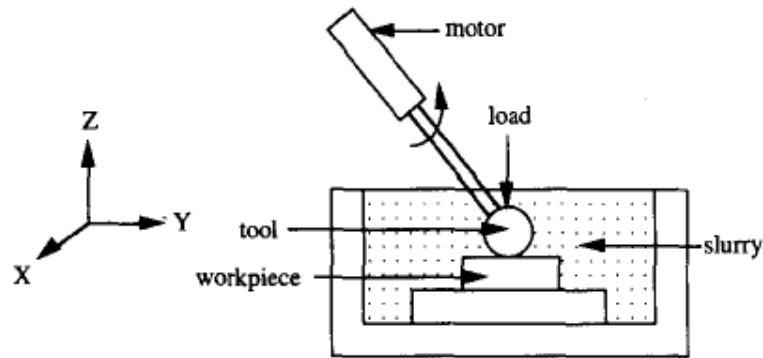


Figure 3.10: Schematic of EEM process [183]

3.6.2 Magnetorheological finishing

Magnetorheological finishing (MRF), which was invented in the mid-1980s by Kordonski et al. [186], is a revolutionary technology that utilizes Magnetorheological (MR) fluid to polish optics surfaces such as glass, SiC, silicon and so on. The MR fluid which consists of deionized water, iron particles, abrasives and stabilizing agents is controlled by computer. Different from traditional rigid lap polishing, the MR fluid acts as a compliant polishing lap, whose shape and stiffness can be magnetically manipulated and controlled in real time. MRF is applicable to quite complicated surfaces as it allows a surface to be selectively finished by using the variability of the MR fluid's yield stress through an external magnetic field. In addition, MRF is a non-direct contact finishing process which can obtain high precision in surface shape with relatively little sub-surface damage.

Figure 3.11 shows the MR fluid delivery system. After being loaded into the closed-loop fluid delivery system, the MR fluid is drawn out of the conditioner and extruded onto a

rotating spherical wheel in a thin ribbon that will contact the optical surface. The ribbon is then suctioned by pump and comes back to the conditioner. Below the polishing wheel, there is an electromagnet which exerts a strong local magnetic field gradient over the upper side of the wheel. When the MR fluid passes through the magnetic field, it stiffens in milliseconds, and then recovers its original fluid state as it leaves the field. This precisely controlled MR fluid becomes the polishing tool. If an optical surface is placed into the fluid in this zone, the stiff fluid ribbon results in shear stress and the material removal occurs. MRF can obtain a very stable influence function which indicates that the MRF is a highly deterministic process. This is an excellent advantage for corrective polishing. MRF can polish most materials except those with magnetism. Unfortunately, some biomaterials (such as stainless steel, etc) as used for artificial joints are magnetic. These kinds of biomaterial cannot be finished by MRF.

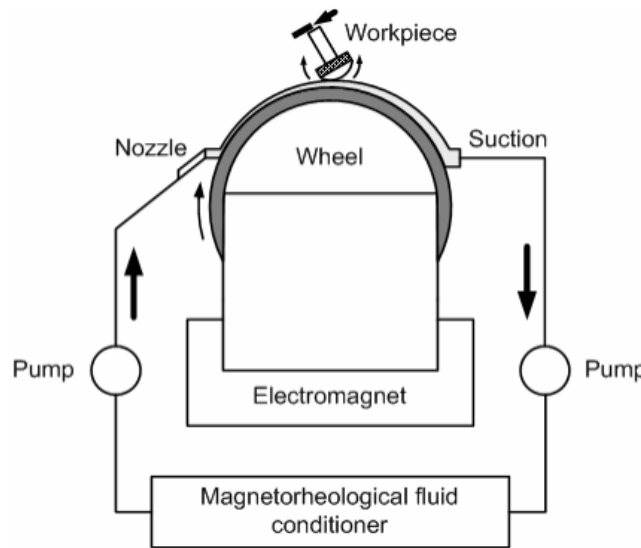


Figure 3.11: MR fluid delivery system [187]

3.6.3 Ion beaming figuring

Ion beam figuring (IBF), first demonstrated by Wilson et al. [188], is a corrective process based on Computer Controlled Optical Surfacing (CCOS) with the application of ion sputtering effects. IBF is an emerging advanced optical fabrication technology capable of deterministic figuring of optical surfaces. Following other mechanical polishing methods, IBF is usually performed as the final figuring of high precision optics [189]. In the process a stable beam of accelerated ions bombards a target component in a predictable and controlled way, and the surface materials are selectively sputtered and removed in molecular units [190] (figure 3.12). Dissimilar to conventional methods of polishing, problems associated with edge effects, tool wear and force load of the workpiece can be avoided because IBF is a noncontact

technique to remove material. IBF has been demonstrated an effective process to machine both large and small precision optics.

The advantage of IBF is that it can achieve very high accuracy of both surface roughness and form. However, the high temperature during figuring process limits its usage for metal finishing. The high temperature will result in the deformation as well as phase transformation, both of which must be avoided. In addition, the very low material removal rate is another significant disadvantage of IBF, because of this deficit it is difficult for IBF to meet the requirement of rapid growth of joint replacements.

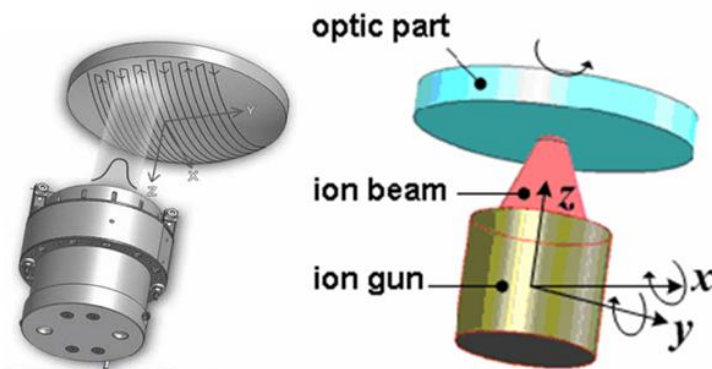


Figure 3.12: Schematic of IBF [190]

3.6.4 Bonnet tool polishing

3.6.4.1 The development of bonnet polishing

Bonnet tool polishing is a technology that uses a spinning bulged bonnet with internal pressure as a polishing tool to polish the workpiece [191]. The bonnet is flexible and covered with polishing cloths or polishing pads. When polishing, the inflated bonnet can conform to the variable curvature of curved surface of a component by controlling the air pressure. The advantage of the bonnet polishing is that it has a flexible and conformal polishing tool so that it can achieve a good surface roughness as well as high precision local form of a workpiece.

The bonnet polishing technology was developed for meeting the growing requirement of both axially symmetric and non-axially symmetric lenses and mirrors as well as prosthetic joints by Walker et al. at the University College London (UCL) and later in collaboration with Zeeko Ltd in 2000 [192]. The innovation of this technology is that the effective size of contacting area and the polishing pressure can be changed independently by adjusting the

axial position of the tool with respect to the workpiece surface and the internal pressure. The basic features of this polishing technology are summarized as follows.

(1) Precession process

In order to avoid the zero central speed of polishing tool, the developers introduced a ‘Precession’ process which dictates that the polishing tool is oblique rather than perpendicular to the surface of the workpiece (figure 3.13) [193]. Figure 3.14 shows the influence function obtained with non-precession process (‘pole-down’) and precession process. As displayed in the figure, the influence function obtained with non-precession process is ‘W’ shape and obtained with precession process approximates to Gaussian shape. The near-Gaussian shape influence function is quite convenient for calculating the toolpath by using deconvolution or global optimization methods. Apart from the influence function, the precession process can also have a profound effect on surface texture. Figure 3.15 shows the results of surface texture polished by non-precession process and precession process [193]. It is clearly shown that non-precession process leaves many scuff marks on the workpiece surface while precession process leaves a surface free of such marks.



Figure 3.13: Precession tool concept [193]

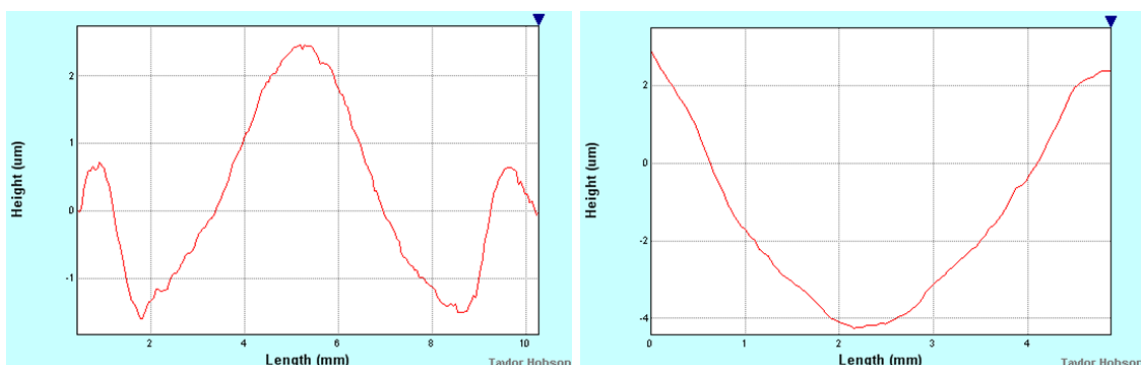


Figure 3.14: Influence function obtained with non-precession process (left) and precession process (right)

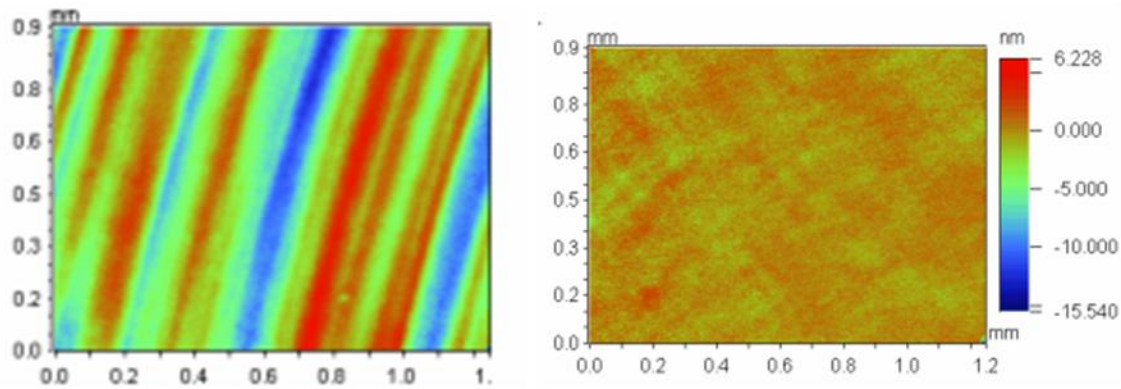


Figure 3.15: Surface texture obtained with non-precession process (left) and precession process (right) [193]

(2) Dwell time method

When the experimental conditions are kept constant, the material depth removed at each point is proportional to the dwell time. This process is called dwell time method. On most of normal tasks, Walker et al. [192] use this method. The use of dwell-time as the basis of control provides a predictable process, giving linearly-responding, arbitrarily deep, local removal of the substrate material. They used a numerical optimization rather than the usual Fourier deconvolution to calculate the dwell time. This algorithm can find the best of many possible solutions while deconvolution can only find one solution. In addition, the numerical optimization algorithm also optimizes the slope error and height error of the optical surface as well as limits the requirement of accelerations in the machine and minimizes the total polishing time.

(3) Tool path

Initially, Walker et al. [194] applied two polishing toolpaths for form preserving pre-polishing, namely raster and spiral (figure 3.16). In both cases, the polishing tool advances towards the workpiece until the load cell detects the contact, then advances further by a pre-calculated distance to give the required spot-size. During the pre-polishing process, the spot-size is kept constant. The polishing tool then tracks the form of workpiece in either a raster on a stationary workpiece or a spiral on a rotating workpiece. The raster toolpath can avoid the problem of controlling the centre, but it needs to accelerate and decelerate the machine traverse at rates within the machine capacity, which not only costs process time but also may cause the locally enhanced removal due to longer dwell time implied. In spiral toolpath, the rotating polishing tool performs a spiral path polishing by traversing the diameter of the

workpiece several times with the workpiece is rotating at a specified speed. The spiral tool path always leaves a central depression due to the spot overlapping centre. The spiral path is especially suitable for rotationally-symmetric workpieces.

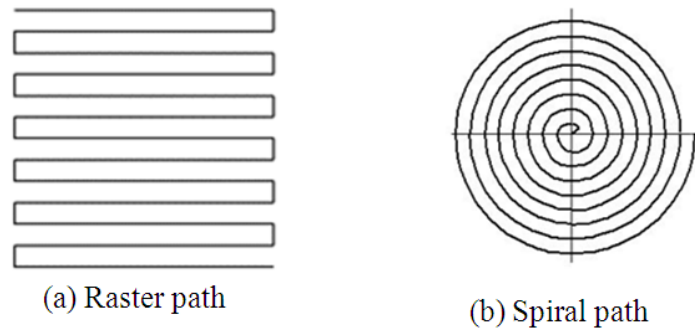


Figure 3.16: Polishing path

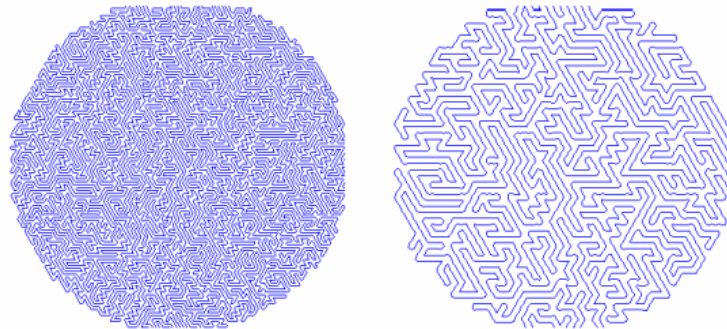


Figure 3.17: Random toolpath [195]

In order to avoid the repetitive signatures left in the workpiece surface by both raster path or spiral path, Dunn et al. [195] have developed a pseudo-random toolpath in 2008 (figure 3.17). The pseudo-random toolpath travels over the workpiece without crossing. It can be used for any continuous region, including those with one or more interior perforations. The density of the pattern can be altered which is similar to the change of the spacing of raster or spiral path. Once the generation algorithm is run, a completely different random pattern will be created. This pattern can be used directly with a dwell time map to perform a prescriptive corrective polishing because it never crosses itself.

(4) Edge control

The edge control for large telescope optics is challenging. Several strategies have been attempted to control the edges of optics components, including [196]:

(a) The use of a waster piece to temporarily cement around the edges of components prior to polishing and detached at the end. This method risks cementing stresses being released at the waster removal, distorting the components.

(b) The use of over-size segments to manufacture optics component then process by edging down. This process will re-distribute the internal material stresses, resulting in distortion as well.

(c) The use of optimization of the intrinsic polishing process to actively control the edges.

Zeeko applied the method of (c) with (a) as a fall-back to control the edge and has conducted a series of experiments to validate this method. The influence function also changes when the polishing tool contacts the edge. Based on the measured influence functions data from interferometers and profilometers, Li et al. [197] created a model which could be used to accurately predict the edge profile. Experimental results were in agreement with the proposed model. With the assistance of this model, it is said that more effective optimization could be achieved and the machining time can be reduced. In 2012, Walker et al. [198] reported a new approach to control the edges through polishing of the entire surface of a workpiece which had been pre-machined to its final external dimensions. This method deployed a compliant bonnet that delivered influence functions of variable diameter and was complemented by a small pitch tool size to accommodate aspheric mis-fit. They also described the experimental results in preparation for full size prototype segments for the European Extreme Large Telescope. Recently, Li et al. [198] proposed a new model to predict the edge influence function. Different from the model presented in reference [198], this model was based on surface-speed profiles and pressure distributions over the polishing spot at the edge of the part.

3.6.4.2 Zeeko polishing technologies and machines

Under the development over 10 years, Zeeko has developed a series of polishing technologies, including [199]:

- Zeeko-Classic: This is the traditional bonnet polishing. The polishing tool comprises an inflated membrane, covered with a standard polishing cloth or polishing pad. It needs a pump to circulate the slurry.
- Zeeko-Grolish (loose-abrasive): Different from Classic, in this case the ‘polishing cloth’ cemented on the bonnet is hard, typically a metal such as aluminium or copper foil. The

loose abrasive slurry is usually carborundum or diamond and applied locally rather than by a circulation pump.

- Zeeko-Grolish (fixed-abrasive): In this case, the bonnet is covered with a flexible backing carrying bound diamond pellets such as 3M Trizact™ product. This process is always run within a containment vessel on the machine turntable so that the workpiece and the polishing tool can be submerged into the coolant.
- Zeeko-Jet: Here, slurry is pumped at high pressure through jets and removes material by direct impact with the surface of the workpiece. This process is usually accommodated into a bonnet polishing machine.



(a) IRP200



(b) IRP600



(c) IRP1200

Figure 3.18: IRP series polishing machine [200-202]

Zeeko has developed a series of Intelligent Robotic Polisher (IRP) machines in accordance with the proposed polishing technologies. IRP200 is the first generation of IRP machines (figure 3.18 [200]). Other machines have been reported including IRP400 [201], IRP600 (figure 3.19 [202]), IRP1000 [203] and IRP1200 (Figure 3.20 [201]), etc.

In addition, Zeeko has also developed three software to control the polishing process, namely, Tool Path Generator (TPG), PrecessionsTM, and Metrology Toolkit [204].

- TPG: This software is used to generate simple and complex tool paths for Zeeko IRP series of polishing machine, including integrated surface designer, tool path modules, on-machine geometry compensation, form correction module (Moderation), etc.
- Precession: Precession software is capable of optimising simple and complex tool paths to efficiently reduce surface form deviations within little iteration. It is usually used in cooperation with TPG software.
- Metrology Toolkit: The Metrology Toolkit is able to read data from a wide variety of metrology instruments, to process and analyse it. This software can also export surface deviation maps.

As the first generation of IRP series machine, IRP200 has combined all the superiorities of both hardware and software proposed by Zeeko. The first IRP200 machine was constructed in November 2000 [200]. This machine was designed to polish flat, spherical, aspheric and free-form surface [192, 201, 203]. It has 7-axis: X, Y, Z are linear axes and A, B, C, H are rotational axes. The machine axes can be used for traditional spiral polishing or raster polishing within a total envelope size of 300×260×130mm. This machine uses a spinning, bulged and compliant tool covered with a suitable polishing cloth as the lap medium in combination with water based polishing slurries. The inflated bonnet can be modulated to vary the polished spot size. The mechanical movement is controlled by CNC machine tool principles, moving the polishing tool relative to workpiece surface in three linear axes (X, Y and Z) and three rotational axes (A,B and C). With the control software, excellent surface texture with almost no directional properties can be obtained across the machined surface. In addition, because the influence function of this machine is Gaussian-like, symmetrical and it is able to change the polishing pressure and spot size, IRP200 is also suitable for figuring flats, spheres, aspherics and free-form surfaces.

Because of the above mentioned advantages, all polishing experiments of this research were carried out by using Zeeko IRP200. Especially for free-form surface polishing, IRP200 can

import the CAD (computer aided design) model into the accessory software and implement polishing. This is quite useful for polishing artificial knee joints. To achieve high accuracies of form and surface texture, several machine parameters need to be adjusted. These parameters include precess angle, head speed, tool offset, tool air pressure (head pressure), point spacing, track spacing and surface feed and will be outlined in the following.

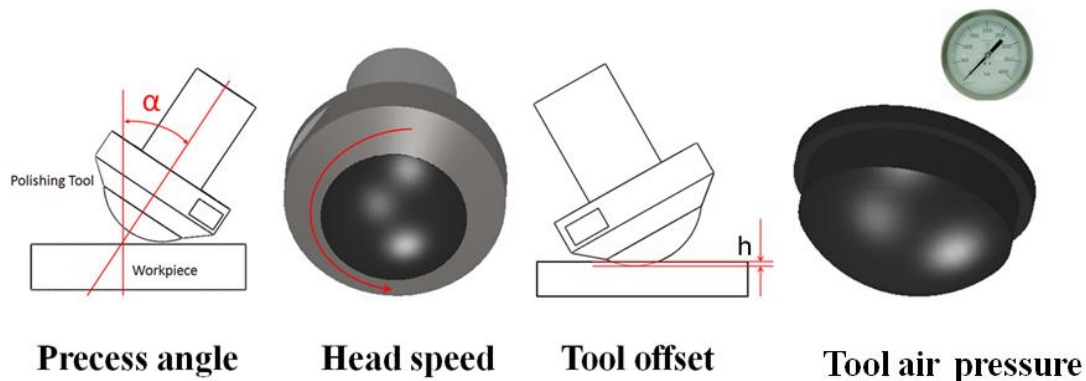


Figure 3.19: Process parameters of bonnet tool polishing

(1) Precess angle: This parameter describes the angle of the centre line of bonnet and the perpendicular line of the workpiece. The unit of precess angle is degrees (figure3.19).

(2) Head speed: This parameter relates to the speed of the rotation of polishing tool. The unit is measured in revolutions per minute (figure 3.19).

(3) Tool air pressure: This is the pressure of bonnet which inflates the bonnet into a spherical shape. The pressure is measured in bar.

(4) Tool offset: This parameter relates to the deformation deep of bonnet when the bonnet touched the workpiece. The unit of tool offset is millimetres (figure 3.19).

(5) Point spacing and track spacing: The parameters of point spacing and track spacing can also be described as X spacing and Y spacing. The point spacing is related to the spacing of polishing points along the X-direction while the track spacing depicts the spacing of polishing points along the Y-direction. Both of these parameters are measured in millimetres.

(6) Surface feed: This parameter depicts the feedrate of the polishing tool. The unit of surface feed is millimetres per minute.

The first four parameters are deemed as the most significant during bonnet polishing process. In this research, these parameters are usually used to investigate the effects of process parameters on both surface finish improvement and form correction. The other parameters are deemed as less important and remained constant during investigation.

3.7 Summary

This chapter has reviewed the final finishing technologies for load-bearing surfaces of artificial joints. Polishing is one of the most commonly used finishing technologies. A polishing system usually consists of the workpiece, the polishing tool, polishing slurry, polishing abrasives and polishing pads/cloths. Workpiece is the objective of polishing, including all types of materials. The polishing tool is typically a conformable substrate covered with pads or cloths used to impose the relative motion between the workpiece and abrasives. The slurry is composed of abrasives and a medium of fluid or paste. The paste slurry is unsuitable for form correction. Generally, the abrasives used in polishing process have to be harder than the workpiece to be machined. The option of abrasive for a specific utilization may be based on durability tests including impact strength, fatigue compression strength, dynamic friability, and resistance to spalling. The common abrasives include diamond, SiC, alumina, cerium oxide, and colloidal silica, etc.

In section 3.3, the material removal in polishing process, including material removal mechanism and material removal modelling, has been discussed. The material removal mechanism of polishing has undergone several years' development and various hypotheses have been proposed. Nevertheless, some hypotheses have been demonstrated that are wrong or not accurate. Currently, the material removal mechanism of polishing is deemed as the combination of two-body abrasion and three-body abrasion as well as some chemical reactions. Because of the complexity, material removal rate modelling is rather difficult comparing to other traditional machining processes such as turning or milling. The efforts of material removal modelling based on the Preston equation, tribological theory and experimental investigations are also discussed in this section.

Initially, polishing was usually used to improve the surface finish rather than form error. Therefore, how to acquire the ultra-smooth surface with polishing has become the greatest interest of researchers. Much work carried out to investigate the technique of surface roughness improvement has been introduced in section 3.4.

With the increasing importance of form accuracy, the use of ultra-precision polishing to correct the form error of a workpiece has become possible. Form correction by polishing is achieved by controlling the dwell time. Namely, when all polishing parameters are kept constant, the longer the polishing tool dwells, the more material will be removed. Section 3.5 introduced the calculation process of dwell time in detail. The commonly used calculation method is deconvolution process.

Section 3.6 introduces several types of polishing technologies potentially applied for the bearing surfaces of prostheses, including EEM, MRF, IBF and bonnet tool polishing. Each technology has its own advantages and disadvantages. For example, the advantages of EEM include less rigidity requirement of machine structure and less sensitive to temperature variation or system vibration; the disadvantages of EEM are low material removal rate and unsuitable for large workpiece. Bonnet polishing is proposed and developed by Walker et al. at the UCL. The advantage of the bonnet polishing is that it has a flexible and conformal polishing tool so that it can achieve a good surface roughness as well as high precision local form of a workpiece. In addition, the related technologies, including the precession process, optimization of dwell time method, tool path and edge control have been introduced in this section. Finally, other polishing technologies derivatives such as Groish polishing and fluid jets proposed by Zeeko, IRP series polishing machines, software supported for IRP polishing machines and related polishing parameters have also been introduced.

4. OPTIMIZATION OF PROCESS PARAMETERS FOR SURFACE ROUGHNESS IMPROVEMENT

4.1 Introduction

Research has shown that an artificial joint system has a longer lifespan if it is fabricated with an ultra-smooth surface [205]. Most failures of prosthetic implants originate from surface imperfections [206]. Therefore it is of paramount importance that the surface finish should be of the highest quality with minimal defects. This chapter outlines an optimisation methodology for the process parameters to obtain the best combination of roughness parameters so that an optimal approach will be found to improve the surface finish.

This chapter uses the Taguchi method to optimize the process parameters with the consideration of interaction effects to improve the surface roughness. The Taguchi method which was developed by Dr. Genichi Taguchi is a valuable tool for improving the quality of products [207]. The philosophy of the Taguchi method is completely different from conventional experiments design which emphasizes the inspection whereas the Taguchi method focuses on experimental design. The design of experiment (DOE) is a method of defining and investigating all possible conditions in an experiment. The DOE using the simplified and standardized Taguchi approach enables any engineers running the experiments to employ similar designs hopefully giving similar results. Compared to conventional factorial and fractional factorial designs of experiments, the Taguchi method needs fewer tests when a large number of variables need to be considered while more precise information can be extracted efficiently. Taguchi created a set of standard Orthogonal Arrays (OA) to lay out the experiments. The OA facilitates the experimental design process. To design an experiment encompasses the selection of a suitable OA and assigning the factors to the appropriate columns. The combination of the individual experiments is called the trial conditions. The procedure of analysing experimental results has also been standardized not only based on statistical calculations such as average and analysis of variance (ANOVA), but also mixed with the deviation from the target instead of absolute values, which leads to improved quality.

Many investigations based on Taguchi's methods have been performed to investigate the effect of process parameters on surface roughness and material removal rate (MRR) for various polishing technologies. Liu et al. [208] considered polishing factors such as feedrate,

spring constant, rotation speed of the hand grinder, abrasive particle size and type of polishing rings when polishing molds and dies. The experimental results showed that the surface roughness could be reduced by imposing compliance in the tool holder and by rising spring constants. Jiang et al. [209] adopted the Taguchi method for optimizing the finishing conditions in Magnetic float polishing. The surface finish parameters of Ra and Rt were chosen as standards for optimization. The polishing parameters considered were polishing force, the abrasive concentration and the polishing speed. Among these polishing parameters, the most significant factor for surface finish, both Ra and Rt , was polishing force. The conclusion indicated that the Taguchi method could extract information more accurately and more effectively. Tsai et al. [210] employed the Taguchi method to identify the optimal abrasive jet polishing (AJP) parameters. The workpiece used in this research was electrically discharge machined SKD61 mold steel. The optimal AJP parameters were applied to investigate the effects of the additive variety, and the material and diameter of abrasive particle respectively on surface finish. The Taguchi method had been successfully extract the best combination of process paramters for the surface roughness improvement. The Taguchi method was also used to optimize the polishing parameters for polishing ceramic gauge blocks [211]. The experimental results showed that the most important parameters for removal rate was speed, followed by load, concentration, and diamond size. Liao et al. [212] employed the Taguchi method to optimize paramters for chemical mechanical polishing in wafer manufacturing. In this study, the quality targets were material removal rate (MRR) and non-uniformity of surface profiles. 54 tests based on an orthogonal array table were carried out. The experimental results showed that the optimal parameter combination for the chemical mechanical polishing process was using a platen speed of 85rpm, a carrier speed of 100rpm, a back side pressure of 80hpa, a slurry flow rate of 180ml/min and a head down force of 250hpa. Through reviewing the previous research, none of the research that has been found mentioned the interaction effect of process parameters. However, interaction is considerably important in bonnet polishing. In the present study the interaction effect of the process parameters could not be ignored. Unfortunately, the Taguchi method does not provide the guideline to establish such interactions. Therefore, the present author used full factorial experimentation to investigate the interaction first and then used the Taguchi method with the established interaction to optimize the process parameters for surface roughness improvement.

The process parameters of precess angle, head speed, tool offset and tool air pressure were identified as the most critical variables in the creation of best surface finish for a given abrasive (material and size) and workpiece combination in bonnet polishing [213]. Other parameters are regarded as less important and kept constant during the investigation (table 4.1). The 3mm tool overhang is a default value, and the 0.3mm and 0.1mm point spacing are the minimum values for the toolpath of raster and spiral tool movement respectively and 1000mm/min and 600mm/min are also the minimum values of the toolpath surface feed for raster and spiral polishing, respectively. The values of C-axis speed and number of passes have been optimized experimentally.

Table 4.1: The fixed polishing factors

Fixed factors	values
Tool overhang	3mm
Point spacing	0.3mm(Raster) and 0.1mm(Spiral)
Surface feed	1000mm/min(Raster) and 600mm/min(Spiral)
C-axis speed	300rpm
Number of passes	30

4.2 Interaction effects

4.2.1 Experimental design

Table 4.2: Chemical composition of samples (%wt)

Alloy	Cr	Mn	Fe	Co	Ni	Nb	Mo	W
F75	28.0282	0.7867	0.5394	62.9672	0.4695	0.0249	538997	0.2024

Table 4.3: Factor levels for 16-run experiment

Factor \ Level	Precess angle (degs)	Head speed (rpm)	Tool offset (mm)	Tool air pressure (bar)
Low	5	800	0.1	0.5
High	10	1200	0.2	1.0

The term interaction is used to describe a condition in which the influence of one factor upon the result is dependent on the condition of another. Two factors A and B are said to interact when the effects of changes in the level of A affects the level of factor B and vice versa. In

bonnet polishing, the effect of one factor may be affected by the level of another. The Taguchi method does not give any guidelines for detecting and measuring such interaction effects among factors. Therefore, full factorial designs was used to evaluate the interaction of process parameters [214]. All specimens were polished using a raster toolpath first and then spiral toolpath with the same parameters except point spacing (0.3mm for raster and 0.1mm for spiral) and surface feed (1000mm/min for raster and 600mm/min for spiral). The samples used in the experiments were flat-end cylindrical CoCr alloy (F75) with 23mm diameter and the chemical composition measured by XRF (X-ray fluorescence) is shown in table 4.2. The polishing medium was 1 μ m diamond paste on a Microcloth polishing cloth. The samples were measured with a Taylor Hobson CCI optical interferometer and the surface finish parameter *Sa* was chosen as the criterion for process evaluation. The CoCr samples were polished manually with 320 grits, 800 grits and 1200 grits abrasive papers and 6 μ m diamond paste in sequence before experiments to establish a reasonable baseline surface topography. In this investigation, each process parameter had two levels as displayed in table 4.3.

With the above given 2-level factors, a full 16-run experimental design was implemented as shown in table 4.4.

Table 4.4: Design matrix for 16-run experiments

Runs	A(Precess angle)	B(Head speed)	C(Tool offset)	D(Tool air pressure)
1	5	800	0.1	0.5
2	5	800	0.1	1.0
3	5	800	0.2	0.5
4	5	800	0.2	1.0
5	5	1200	0.1	0.5
6	5	1200	0.1	1.0
7	5	1200	0.2	0.5
8	5	1200	0.2	1.0
9	10	800	0.1	0.5
10	10	800	0.1	1.0
11	10	800	0.2	0.5
12	10	800	0.2	1.0
13	10	1200	0.1	0.5
14	10	1200	0.1	1.0
15	10	1200	0.2	0.5
16	10	1200	0.2	1.0

4.2.2 Experimental results

The parameter Sa of surface roughness was selected as the assessment criterion. The experimental results are given in table 4.5 and response table with all interaction terms is given in table 4.6. In table 4.6, the ‘effect’ means the influence of each process parameters and the value of the ‘effect’ is the difference of the average value for two levels of process parameters.

Table 4.5: Experimental results for interaction effects

Trial number	Sa before polishing (nm)	Sa after polishing (nm)	Difference (nm) $\Delta Sa = Sa_{\text{before}} - Sa_{\text{after}}$	Improvement Percentage (%)
1	28.8	13.53	15.27	53
2	30.2	11.89	18.31	60.6
3	28.2	11.97	16.23	57.6
4	32.2	11.7	20.5	63.7
5	30.4	13.88	16.52	54.3
6	32.6	13.15	19.45	59.7
7	34.2	13.73	20.47	59.9
8	31.2	11.2	20	64.1
9	30.9	14.2	16.7	54
10	32.75	12.9	19.85	60.6
11	29.5	12.16	17.34	58.8
12	32.8	11.9	20.9	63.7
13	34.4	13.82	20.58	59.8
14	31.8	11.76	20.04	63
15	33	11.51	21.49	65.1
16	31.2	9.45	21.75	69.7

Table 4.6: Response table with all interaction terms

Trial number	Response observed values Y	A		B		C		D		AB	
		5	10	800	1200	0.1	0.2	0.5	1.0	1	2
1	0.53	0.53		0.53		0.53		0.53		0.53	0.53
2	0.606	0.606		0.606		0.606		0.606		0.606	0.606
3	0.576	0.576		0.576		0.576		0.576		0.576	0.576
4	0.637	0.637		0.637		0.637		0.637		0.637	0.637
5	0.543	0.543		0.543		0.543		0.543		0.543	0.543
6	0.597	0.597		0.597		0.597		0.597		0.597	0.597
7	0.599	0.599		0.599		0.599		0.599		0.599	0.599
8	0.641	0.641		0.641		0.641		0.641		0.641	0.641
9	0.54		0.54		0.54		0.54		0.54		0.54
10	0.606		0.606		0.606		0.606		0.606		0.606
11	0.588		0.588		0.588		0.588		0.588		0.588
12	0.637		0.637		0.637		0.637		0.637		0.637
13	0.598		0.598		0.598		0.598		0.598		0.598
14	0.63		0.63		0.63		0.63		0.63		0.63
15	0.651		0.651		0.651		0.651		0.651		0.651
16	0.697		0.697		0.697		0.697		0.697		0.697
Total	9.68	4.73	4.95	4.72	4.96	4.65	5.03	4.63	5.05	4.75	4.93
No of values	16	8	8	8	8	8	8	8	8	8	8
Average	0.605	0.591	0.619	0.59	0.62	0.581	0.628	0.578	0.631	0.594	0.616
Effect		0.028		0.030		0.047		0.053		0.022	

Table 4.6: Continued

Trial number	AC		AD		BC		BD		CD	
	0	2	1	2	1	2	1	2	1	2
1		0.53		0.53		0.53		0.53		0.53
2		0.606		0.606		0.606		0.606		0.606
3	0.576		0.576		0.576		0.576		0.576	
4	0.637		0.637		0.637		0.637		0.637	
5		0.543		0.543		0.543		0.543		0.543
6		0.597		0.597		0.597		0.597		0.597
7	0.599		0.599		0.599		0.599		0.599	
8	0.641		0.641		0.641		0.641		0.641	
9	0.54		0.54		0.54		0.54		0.54	
10	0.606		0.606		0.606		0.606		0.606	
11		0.588		0.588		0.588		0.588		0.588
12		0.637		0.637		0.637		0.637		0.637
13	0.598		0.598		0.598		0.598		0.598	
14	0.63		0.63		0.63		0.63		0.63	
15		0.651		0.651		0.651		0.651		0.651
16		0.697		0.697		0.697		0.697		0.697
Total	4.83	4.85	4.86	4.82	4.81	4.87	4.88	4.80	4.85	4.82
No of values	8	8	8	8	8	8	8	8	8	8
Average	0.603	0.606	0.607	0.602	0.601	0.609	0.610	0.601	0.607	0.603
Effect	0.003		-0.005		0.008		-0.009		-0.003	

Table 4.6: Continued

Trial number	ABC		ABD		ACD		BCD		ABCD	
	0	2	1	2	1	2	1	2	1	2
1	0.53		0.53		0.53		0.53		0.53	0.53
2	0.606		0.606		0.606		0.606		0.606	0.606
3		0.576	0.576			0.576		0.576		0.576
4		0.637		0.637	0.637		0.637			0.637
5		0.543		0.543	0.543		0.543		0.543	0.543
6		0.597	0.597		0.597		0.597		0.597	0.597
7	0.599			0.599		0.599		0.599		0.599
8	0.641		0.641		0.641		0.641		0.641	0.641
9		0.54		0.54		0.54		0.54		0.54
10		0.615	0.615		0.615		0.615		0.615	0.615
11	0.588			0.588	0.588		0.588		0.588	0.588
12	0.637		0.637		0.637		0.637		0.637	0.637
13	0.598		0.598		0.598		0.598		0.598	0.598
14	0.63		0.63		0.63		0.63		0.63	0.63
15	0.651		0.651		0.651		0.651		0.651	0.651
16	0.697		0.697		0.697		0.697		0.697	0.697
Total	4.83	4.85	4.84	4.85	4.83	4.85	4.82	4.86	4.83	4.85
No of values.	8	8	8	8	8	8	8	8	8	8
Average	0.604	0.606	0.6045	0.606	0.603	0.606	0.603	0.607	0.603	0.606
Effect	0.002		-0.0015		0.003		0.004		0.003	

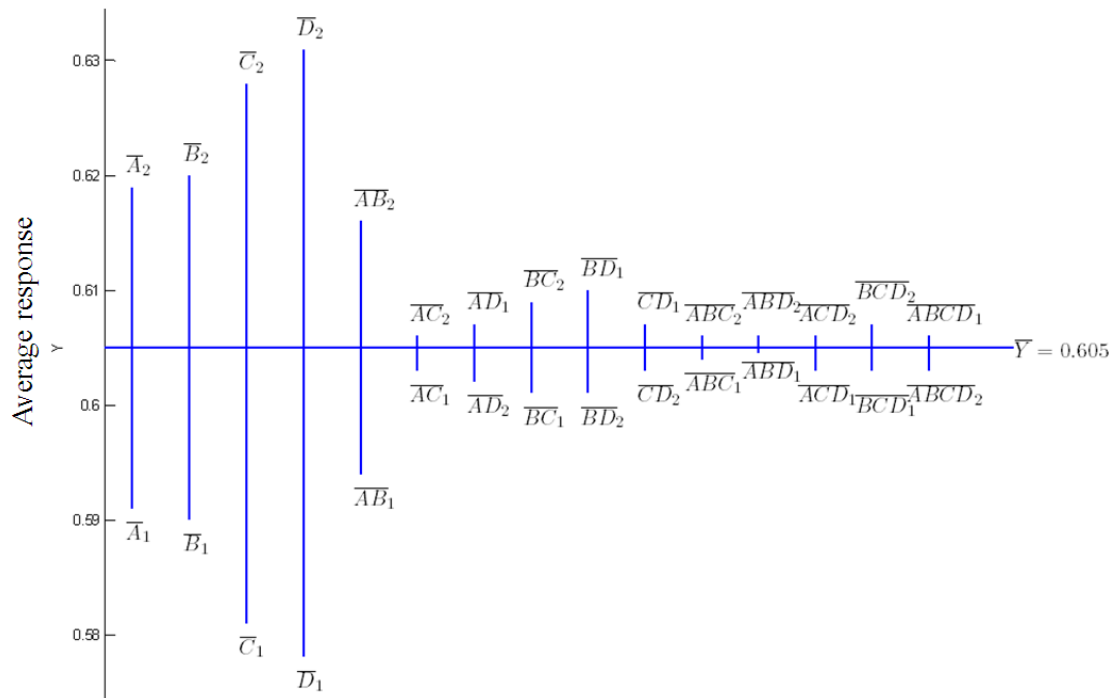


Figure 4.1: Graphical displays of process parameter effects

Figure 4.1 shows the main effects of process parameter on the surface roughness. As can be seen in this figure, the primary factors affecting surface roughness are A, B, C, D (as expected), and AB while the effects of other factor interaction appear negligible. The experimental results indicate that precess angle and head speed would interact each other while other interactions are insignificant. With the above experimental results, the use of Taguchi approach to further optimise the process parameters was carried out. In the following investigation, interaction of precess angle and head speed was considered. Through reviewing the previous research, very few were found relating to interaction of factors when the Taguchi approach was used to optimise the process parameters which in the opinion of the present author indicated these results were not as robust as they should be. In the next section reports how the Taguchi approach was used to optimise the process parameters including the consideration of interaction.

4.3 The application of Taguchi method to optimise process parameters

The samples used in this investigation were F75 CoCr alloy, the same with the previous sections'. The polishing medium was 1 μ m diamond paste charged on a Microcloth polishing cloth. Surface finish parameter *Sa* was chosen as the criterion for process evaluation. The CoCr samples were polished manually with 320 grits, 800 grits and 1200 grits abrasive

papers and 6 μ m diamond paste in sequence before experiments. The fixed process parameters are shown in table 4.1 and the variable process parameters with their three levels are displayed in table 4.7. All specimens were polished using raster toolpath first and then spiral toolpath with the same parameters except point spacing and surface feed as shown in table 4.1.

Table 4.7: Process parameters with their three levels

Parameters \ Levels	1	2	3
A: Precess angle (degs)	5	10	15
B: Head speed (rpm)	800	1200	1600
C: Tool offset (mm)	0.1	0.2	0.3
D: Tool air pressure (bar)	0.6	1.2	1.8

4.3.1 Experimental design

The experimental design was based on the Taguchi approach with the consideration of interaction. In this investigation each of the four factors was to be studied at three levels, therefore, each factor has a DOF (Degree of freedom) of 2. The DOF for the interaction is calculated by multiplying the DOF of each of the interaction factors. Thus, the DOF for A×B is 4. The total DOF for 4 factors and 1 interaction in this case is 12. Therefore, the suitable OA (Orthogonal array) for this experimental design should be L27 (3^{13}) as shown in table 4.8. This array has 27 rows and each row represents a run condition with parameter levels indicated by the numbers in the row. The vertical columns relates to the parameters specified in the investigation. A×B indicates the interaction of precess angle and head speed.

Table 4.8: L27 Orthogonal array

Factors Runs	A: Precess angle (deg)	B: Head speed (rpm)	(A×B) ₁	(A×B) ₂	C: Tool offset (mm)	D: Tool air pressure (bar)
1	5	800	1	1	0.1	0.6
2	5	800	1	1	0.2	1.2
3	5	800	1	1	0.3	1.8
4	5	1200	2	2	0.1	1.2
5	5	1200	2	2	0.2	1.8
6	5	1200	2	2	0.3	0.6
7	5	1600	3	3	0.1	1.8
8	5	1600	3	3	0.2	0.6
9	5	1600	3	3	0.3	1.2
10	10	800	2	3	0.1	1.8
11	10	800	2	3	0.2	0.6
12	10	800	2	3	0.3	1.2
13	10	1200	3	1	0.1	0.6
14	10	1200	3	1	0.2	1.2
15	10	1200	3	1	0.3	1.8
16	10	1600	1	2	0.1	1.2
17	10	1600	1	2	0.2	1.8
18	10	1600	1	2	0.3	0.6
19	15	800	3	2	0.1	1.2
20	15	800	3	2	0.2	1.8
21	15	800	3	2	0.3	0.6
22	15	1200	1	3	0.1	1.8
23	15	1200	1	3	0.2	0.6
24	15	1200	1	3	0.3	1.2
25	15	1600	2	1	0.1	0.6
26	15	1600	2	1	0.2	1.2
27	15	1600	2	1	0.3	1.8

4.3.2 Experimental results and analysis

The experimental results were assessed using the surface finish parameter Sa . Table 4.9 presents the initial and final surface roughness Sa , variation, S.R. ratio and S/N ratio. Each specimen was measured at points across the surface by optical interferometry (Taylor Hobson

CCI) one point was in the centre and the other four points randomly distributed around the periphery. The values shown in the table are the mean roughness value, Sa , of the five points. The variation is the difference of initial value and final value. S. R ratio is the proportion of variation and initial value. The last column is the S/N ratio calculated by S.R ratio using the equation (4-1). S/N ratio signifies the Signal to Noise Ratio the concept of which has been applied in the area of acoustics, electrics, mechanics and other engineering disciplines over many years [207].

$$S / N = -10 \log_{10}(MSD) \quad (4.1)$$

Where MSD is mean squared deviation. MSD has different values as it in the different cases. In the case of ‘smaller the better’:

$$MSD = (Y_1^2 + Y_2^2 + \dots + Y_n^2) / n \quad (4.2)$$

Where Y is the experimental results, n is the number of repetition.

In the case of ‘nominal the better’:

$$MSD = ((Y_1 - Y_0)^2 + (Y_2 - Y_0)^2 + \dots + (Y_n - Y_0)^2) / n \quad (4.3)$$

Where, Y_0 is the nominal value.

In the case of ‘larger the better’:

$$MSD = (1/Y_1^2 + 1/Y_2^2 + \dots + 1/Y_n^2) / n \quad (4.4)$$

For use in orthopaedic industries, the surface roughness of prosthetic joints should be as smooth as possible with large variation (table 4.9). Therefore, this investigation is the case of ‘larger the better’. The S. R ratio is Y in this case.

Table 4.9: The experimental results of *Sa* parameter

Runs	Initial (nm)	Final (nm)	Variation	S.R. ratio	S/N ratio
1	32.6	13.3	19.3	0.592	-4.55
2	30.5	12.25	18.25	0.598	-4.46
3	29.6	9.7	19.9	0.672	-3.45
4	26.2	10.9	15.3	0.584	-4.67
5	35.09	10.2	24.89	0.709	-3.60
6	32.2	13.8	18.4	0.571	-4.86
7	35.6	8.6	27	0.758	-2.40
8	36.4	9.5	26.9	0.739	-2.63
9	35.2	13.9	21.3	0.605	-4.36
10	25.3	11.67	13.63	0.539	-5.37
11	34.5	7.44	27.06	0.784	-2.11
12	27.6	11.54	16.06	0.582	-4.70
13	33.8	11.17	22.63	0.669	-3.48
14	29.8	8.2	21.6	0.725	-2.79
15	30.4	13.75	16.65	0.548	-5.23
16	35.8	8.92	26.88	0.751	-2.48
17	36.6	9.85	26.75	0.731	-2.72
18	31.8	10.19	21.61	0.679	-3.36
19	24.8	9.09	15.71	0.633	-3.96
20	28.27	13.79	14.48	0.512	-5.81
21	23.2	13.87	9.33	0.402	-7.91
22	25.7	7.51	18.19	0.708	-3.02
23	25.6	6.99	18.61	0.727	-2.77
24	30.1	7.45	22.65	0.752	-2.47
25	23.2	12.08	11.12	0.479	-6.39
26	30.2	9.01	21.19	0.702	-3.08
27	25.8	10.9	14.9	0.578	-4.77

4.3.3 The main effects of S/N ratio

The main effect of *S/N* ratio is to calculate the average effects of each parameter and the calculation results are displayed in table 4.10. The main effects of *S/N* ratio for each parameter are given in figure 4.2. As shown in figure 4.2, the optimal experimental condition

using Microcloth with 1m diamond paste is $A_2B_1C_2D_3$, i.e. 10^0 precess angle, 800rpm head speed, 0.2mm tool offset and 1.8bar tool air pressure.

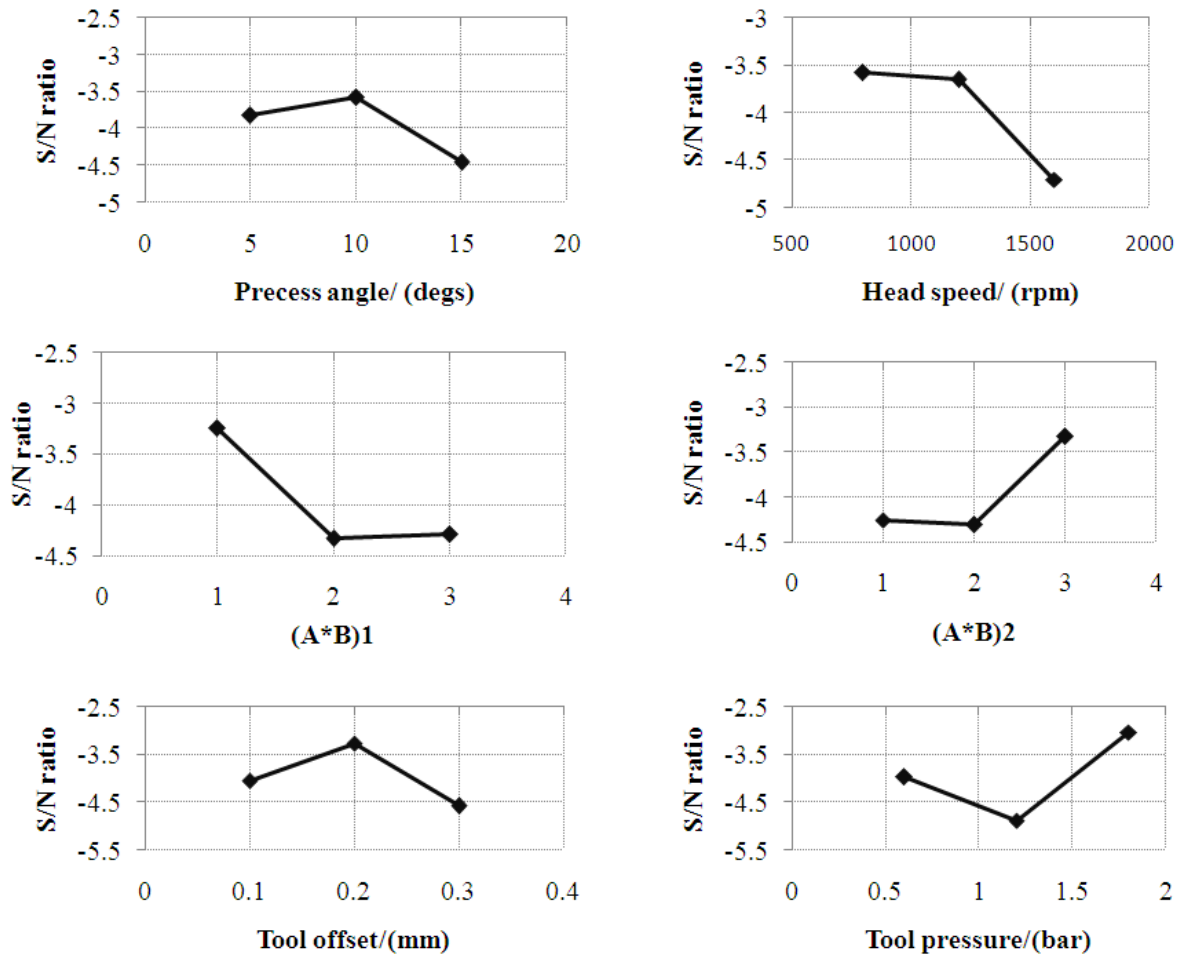


Figure 4.2: The main effects of S/N ratio

Table 4.10: The main effects of S/N ratio

Parameters	Level1	Level2	Level3
A: Precess angle	-3.88	-3.58	-4.46
B: Head speed	-3.57	-3.65	-4.70
A×B ₁	-3.25	-4.39	-4.29
A×B ₂	-4.24	-4.37	-3.33
C: Tool offset	-4.04	-3.33	-4.56
D: Tool air pressure	-3.96	-4.88	-3.10

4.3.4 ANOVA

Analysis of Variance (ANOVA) is a statistical method which is used to analyze the variance of experimental results. The main objective of ANOVA is to find the percentage of contribution of individual factor related to the total output. In the analysis of variance, several quantities were calculated and organized in a standard table.

(1) DOF

Degree of Freedom (DOF) is used to uniquely determine the amount of information from a given set of experiments. DOF for experiments relating to a parameter equals to one less than the number of levels. In this study each parameter has 3 levels, so the level of each parameter is 2. The DOF for interaction of precess angle and head speed is calculated by multiplying the DOF of each of the interacting factors. Thus, the DOF for A×B is 4. The total DOF of these experiments equals to the product of the number of trials and repetitions subtracted by 1. In this case, the total number of trial is 27 and the repetition is 1, so the total DOF is 26. The error DOF is the difference of the total DOF and the sum of all parameter's DOF. Each DOF is given in table 4.11.

(2) Sum of squares

The sum of square is the deviation squared of experimental data from the average value of the data. The total deviation of experimental results equals to the sum of squared deviation:

$$S_T = \sum_{i=1}^n (Y_i - \bar{Y})^2 \quad (4.5)$$

Where S_T is the total deviation, Y_i is the i th experimental data, \bar{Y} is the average value of Y_i .

(3) Variance

Variance distributes the average of the experimental data:

$$V = S / f \quad (4.6)$$

Where S is the sum of square of each parameter, f is DOF of each parameter.

(4) F-value

The F-value, commonly called F statistic, is the ratio of variance due to the effect of a factor and variance due to the error term. This value is used to determine the importance of the parameter under investigation with respect to the variance of all the parameters included in the error term:

$$F = V / V_e \quad (4.7)$$

Where V_e is the variance of error, $V_e = S_e / f_e$.

(5) Pure sum of squares

Pure sum of squares means the sum of square without the effect of noise and can be calculated using the following equation:

$$S'_i = S_i - f_i \times V_e \quad (4.8)$$

(6) Percent contribution

The percent contribution is to calculate the contribution of each parameter using the following equation:

$$P_i = S'_i \times 100 / S_T \quad (4.9)$$

Table 4.11: ANOVA

Variables	DOF	Sum of squares	Variance	F-value	Pure sum of squares	Percent contribution	Rank
A: Precess angle	2	3.58	1.79	4.54	2.79	5.5%	5
B: Head speed	2	7.14	3.57	9.05	6.35	12.5%	4
(A×B) ₁	4	7.16	1.79	4.54	5.58	10.9%	3
(A×B) ₂	4	7.07	1.78	4.48	5.49	10.8%	
C: Tool offset	2	6.94	3.47	8.79	6.15	12.1%	2
D: Tool air pressure	2	14.19	7.09	17.99	13.40	26.4%	1
Error	12	4.73	0.39	1	10.26	20.2%	
Total	26	50.8	1.95				

All the above mentioned quantities were calculated and assigned in table 4.11. As can be seen in table 4.11, the greatest contribution for surface roughness is tool air pressure, accounting for 26.4%, followed by head speed (12.5%), interaction of precess angle and head speed (10.9% and 10.8%), tool offset (12.1%) and precess angle (5.5%).

4.3.5 Confirmatory experiment

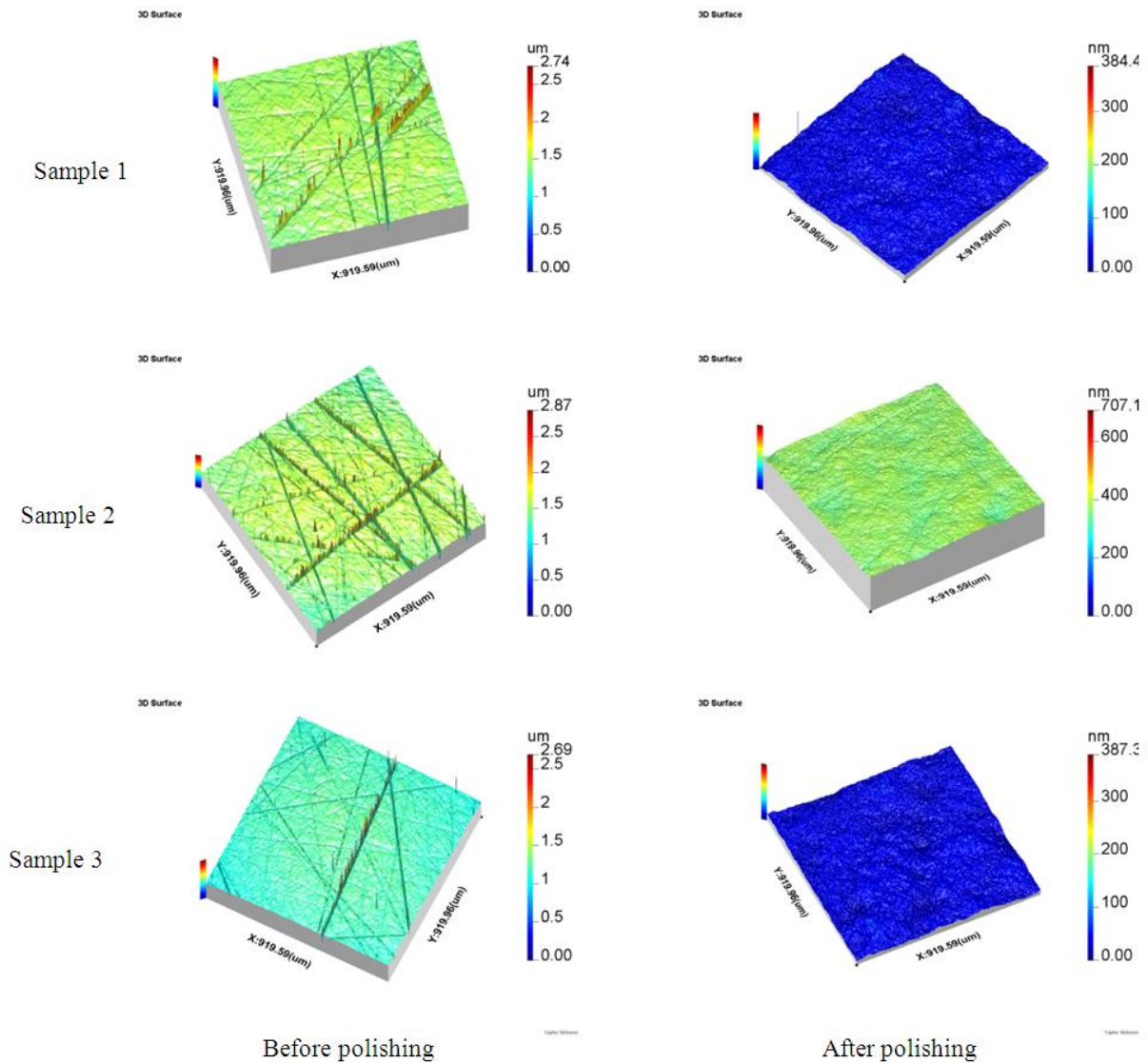


Figure 4.3: Surface roughness before and after polishing under the optimal condition

As can be seen in Figure 4.2, in the case of “the larger the better” the optimal combination of factors is: $A_2B_1(AB_1)_1(AB_2)_3C_2D_3$. The estimated reduction ratio at the optimum condition was $Y_{\text{expected}}=0.823$ as shown in table 4.12. To verify the reliability of the Taguchi experimental results, three confirmatory experiments were conducted under the optimal factor level combination acquired from the Taguchi trials. The corresponding results are

given in table 4.12. It is clear that a slight discrepancy exists between the estimated ratio and surface roughness improvement ratio. Figure 4.3 shows the 3D maps of the samples before and after polishing. As can be seen in Figure 4.3, the surface roughness of the sample has been improved greatly polished by the optimal experimental condition.

Table 4.12: The results of confirmatory experiment

Sample No	Before polishing (nm)	After polishing (nm)	S.R. ratio	Estimated reduction ratio
1	36	8.2	77.2%	82.3%
2	39.2	8.9	77.3%	
3	30.3	7.8	74.3%	

4.4 Summary

Based on the Taguchi method, this chapter has investigated the parameters optimization for surface roughness improvement in bonnet polishing of CoCr alloys. The investigation has considered the interaction effects. Unfortunately, the Taguchi method does not provide guidelines to detect the interaction effects. Therefore, a full factorial experiment design was used to study the interaction effects of the four significant process parameters, namely, precess angle, head speed, too offset and tool air pressure. In the full factorial experiments, all parameters had two levels and the number of total runs was 16. The full factorial experimental results indicate that precess angle and head speed interacts with each other most. Then the Taguchi method was used to optimize the process parameters for surface roughness improvement with the consideration of interaction effects.

In the investigation of Taguchi method, each of the four factors has three levels, which can basically cover the low and high level of each parameter. With these four factors and their three levels and one interaction, a L27 (3^{13}) OA (Orthogonal array) was selected to design the experiments. This array had 27 runs in total. After the experiments, the Sa values were selected as the criterion; the variations of the initial and final value of Sa were calculated and then converted into S/N ratio. The main effects of S/N ratio were then calculated, indicating that the optimal experimental condition were 10^0 precess angle, 800rpm head speed, 0.2mm tool offset and 1.8bar tool air pressure. In order to find the percentage contribution of individual factor related to the total output, the method of Analysis of Variance (ANOVA) was applied. In ANOVA, several quantities, including DOF, sum of squares, variance, F-value, pure sum of squares and percent contribution were calculated. The ANOVA results

indicate that the greatest contribution for surface roughness is tool air pressure, accounting for 26.4%, followed by head speed (12.5%), interaction effect (about 11%), tool offset (12.1%), and precess angle (5.5%). Theoretically, the experimental results at the optimal conditions were estimated as 82.3%. To verify the reliability of the Taguchi experimental results, three confirmatory experiments were conducted under the obtained optimal factor level combination. The corresponding results display only a slight discrepancy between the estimated ratio and real experiment results, which means the Taguchi method with the consideration of interaction effect is fairly robust.

However, it needs to be noted that some results of the full factorial experiments are not completely in agreement with Taguchi experiments. For example, in the full factorial experiments, the main factors affecting the surface roughness improvement are tool air pressure, followed by tool offset, head speed, precess angle and interaction effect, while in Taguchi experiments, the sequence is tool air pressure, head speed, interaction effect, tool offset and precess angle. The primary reason is that any experimentation exist the noise which is difficult to be avoided. This has been demonstrated in Taguchi experiments whose error contribution is 20.2%. Nevertheless, it is considered that the Taguchi method is still a very strong experimental design tool and has attracted more and more researchers to apply it in various experimental designs.

5. THE EFFECTS OF POLISHING CONDITIONS ON SURFACE TOPOGRAPHY

5.1 Introduction

The results presented in chapter 4 established the optimal experimental conditions for improving surface roughness in bonnet polishing of CoCr alloys. However, the evolution of surface topography with the change of experimental conditions (such as polishing cloth, grit size of abrasives, etc) and the effects of the combination of polishing cloths/pads and abrasives on surface topography are still not obvious. The objective of this chapter is to fully investigate the effects of experimental conditions on areal parameters of surface topography so that a better solution can be found to improve the surface topography in bonnet polishing of CoCr alloy.

Comparing to 2D characterization, the advantages of areal characterization are obvious (figure 5.1). As can be seen in figure 5.1, considering the image on the right of this figure, it is impossible to identify what topographic features exist in these areas. However, using areal characterization of surface topography can present a clear identification of the functionally important pits and scratches. Furthermore, areal characterization not only can identify the surface features qualitatively but can also calculate the sizes, shapes and volumes of the features quantitatively [64, 215]. Areal surface topography characterisation can provide new and meaningful parameters to understand the manufacturing process and the function of a particular surface.

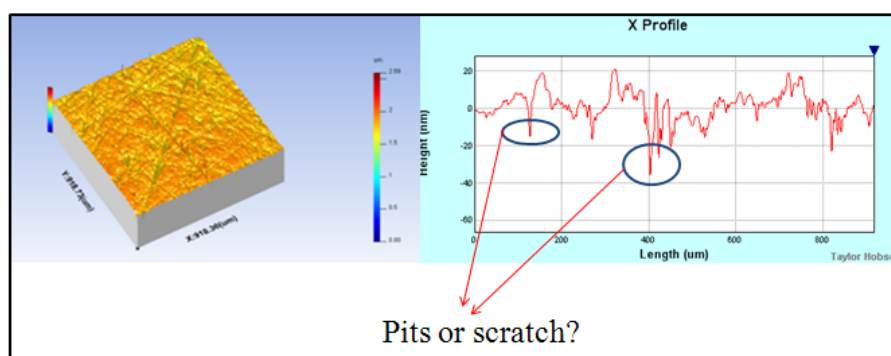


Figure 5.1: Comparison of 2D and areal measurement

As indicated by Blunt et al. [176], numerical parameters for surface roughness are the communication link between design, manufacture and functional performance, and provide a means of communication between supplier and customer. However, only a few of the areal

parameters are commonly used to assess the quality of machined surface. The most commonly used parameter is arithmetical mean height, S_a . However, S_a can only depict the arithmetical average of the absolute of the height. This is just one property of a surface. Other properties, such as surface departures, surface deviations, height distributions, etc, need other parameters to describe them. This investigation attempts to completely investigate the evolution of all areal parameters during changes in polishing conditions and the effects of the combination of polishing pads/cloths with polishing abrasives on surface topography. All of these 3D parameters are classified into two groups: S -parameter set and V -parameter set. The S -parameter set consists of 15 parameters and V -parameter contains 9 parameters. These parameters will be introduced briefly in the following. The definitions of these parameters are based on reference [176].

(1) Amplitude parameters

S_q : root-mean-square, this is defined as the root mean square value of the surface departures within a defined area.

S_{sk} : skewness of topography height distribution, this is to measure the asymmetry of surface deviations relative to the mean/reference plane.

S_{ku} : kurtosis of topography height distribution, this is a parameter to measure the peakedness or sharpness of the surface height distribution.

S_p : the maximum surface peak height, this is the largest height value relative to the mean/reference surface within the definition area.

S_v : the lowest valley of the surface, this is the deepest value of valley from the mean/reference surface within the definition area.

S_z : maximum height of the topographic surface, this is the sum of absolute value of S_p and S_v within the definition area.

(2) Spacing parameters

S_{ds} : density of summits of the surface, this is the number of summits of a unit sampling area.

S_{al} : the fastest decay auto-correlation length, this is defined as the horizontal distance of the AACF that has the fastest decay to 0.2.

Str: texture aspect ratio of the surface, this is used to identify texture strength i.e. uniformity of the texture aspect.

(3) Hybrid parameters

Ssc: arithmetic mean summit curvature of the surface, this is defined as the arithmetic mean of the principal curvatures of the summits within the definition area.

Sdq: root-mean-square slope of the assessed topographic surface, this is defined as the root-mean-square value of the surface slope within the definition area.

Sdr: developed interfacial area ratio, this is the ratio of the increment of the interfacial area of a surface within the definition area.

(4) Linear areal material ratio curve parameters (*Sk* family parameters)

Sk, core roughness depth, this is defined as the vertical height between the left and right intercepts of the line through the ends of the minimum *Htp* 40% window.

Spk, reduced peak height, this is an estimated value of the small peaks above the main plateau of the surface.

Svk, reduced valley height, this is an estimated depth of valleys that retain lubrication in a functioning part.

Smr1, peak material component, this is the fraction of the surface which contains small peaks above the main plateau.

Smr2, peak material component, this is the fraction of the surface which will carry the load during the practical lifetime of the part.

(5) Material/void volume parameters of the topographic surface

Vmp, peak material volume of the topographic surface, this is to describe the material volume enclosed in the 10% material ratio and normalised to unity.

Vmc, core material volume of the topographic surface, this is the material volume enclosed from 10% to 80% of surface material ratio and normalised to the unit definition area.

Vvc, core void volume of the surface, this is the void volume enclosed from 10% to 80% of surface material ratio and normalised to the unit definition area.

V_{vv} , valley void volume of the surface, this is defined as a void volume in the valley zone from 80% to 100% surface material ratio in the unit definition area.

(6) Other parameters

$S5z$: ten point height of the surface, this is an extreme parameter defined as the mean value of the absolute heights of the five highest peaks and the depths of the five deepest pits or valleys within the definition area.

Std : this parameter is used to determine the most pronounced direction of the surface texture with respect to the y-axis within the frequency domain, in other words, it gives the lay direction of the surface.

Sa : arithmetic mean of the absolute value of the height within a definition area.

As the aim of polishing technology is to improve the surface roughness, in other words, to smooth the surface, the amplitude parameters seem to have the most importance among all surface topography parameters.

5.2 The evolution of surface topography during polishing

To better understand the evolution of surface topography during polishing process, a series of experiments were carried out. Areal parameters of surface roughness were used to quantitatively evaluate the surface topography of samples. The samples were polished according to the following steps and four samples were polished for each step:

Table 5.1: The experimental conditions

Parameters	Precess angle (degs)	Head speed (rpm)	Tool offset (mm)	Tool air pressure (bar)	Tool Overhang (mm)	Point Spacing (mm)	C axis speed (rpm)	Surface Feed (mm/min)
Values	10	800	0.2	1.8	3	0.3(Raster) 0.1(Spiral)	300	1000(Raster) 600(Spiral)

320# SiC abrasive papers;

800# SiC abrasive papers;

1200# SiC abrasive papers;

6 μ m diamond paste;

1 μ m diamond paste;

After each step, all specimens were measured at 5 points randomly using an optical interferometer (Taylor Hobson CCI) and then areal parameters of surface roughness were calculated using a self-developed software *SurfStand*. The specimens were cylindrical CoCr alloys (F75) which are the same with chapter 4. The polishing cloth for 6 μ m diamond paste was Texmet 1500 and for 1 μ m diamond paste was Microcloth. The machine settings used in this investigation are the optimised conditions established in Chapter 4 (Table 5.1).

5.2.1 Amplitude parameters

Figure 5.2 shows the evolution of amplitude parameters during polishing process. As shown in the figure, root mean square parameter Sq decreases greatly with the decrease of abrasive size. Since Sq is a dispersion parameter, polishing can effectively reduce the standard deviation height of the workpiece surface. The skewness of the topography height distribution parameter Ssk increases slightly first and then drops sharply to -5.9 after 6 μ m diamond polishing and finally increases to 0.3. The Ssk is usually used to describe the shape of the topography height distribution. If the skewness of a surface is zero, the shape of the surface height distribution is symmetrical, which indicates it is a Gaussian type surface. If the skewness of a surface is not zero, it means the surface height distribution is asymmetrical. When the skewness is positive, such as produced by rough polishing (320#, 800# and 1200# SiC abrasive paper), it means the distribution has a longer tail at the upper side of the mean/reference plane indicating a peak dominated surface. Fine polishing of 6 μ m diamond has changed the distribution to the lower side of the mean/reference plane and the skewness is negative, which means fine polishing can effectively remove the ‘spiky’ features producing a valley dominated surface. After final polishing, the skewness is near zero, which means the height distribution of the polished surface is a Gaussian shape more random surface. The kurtosis parameter Sku increases steadily from 6.2 during polishing process. This parameter is used to characterise the spread of the height distribution. All values of Sku are greater than 3 which mean the peakedness or sharpness of the polished surface is centrally distributed. The maximum surface peak height parameter Sp decreases slowly during rough polishing (320#, 800# and 1200# SiC abrasive paper) and sharply during fine polishing (6 μ m and 1 μ m diamond), which means that the peak height is decreasing after polishing. This is in agreement with the principle that the smoother the surface, the lower the peak height. The

lowest valley of the surface parameter S_v fluctuates during polishing process. This is because some scratches left by previous machining are too deep to be removed. But if the whole layer material of the workpiece is removed, S_v will decrease. The maximum height of the topographic surface parameter S_z is the sum of the S_p and S_v , therefore the variation trend of S_z are affected by both S_p and S_v . In this investigation, it has the same variation trend with S_p .

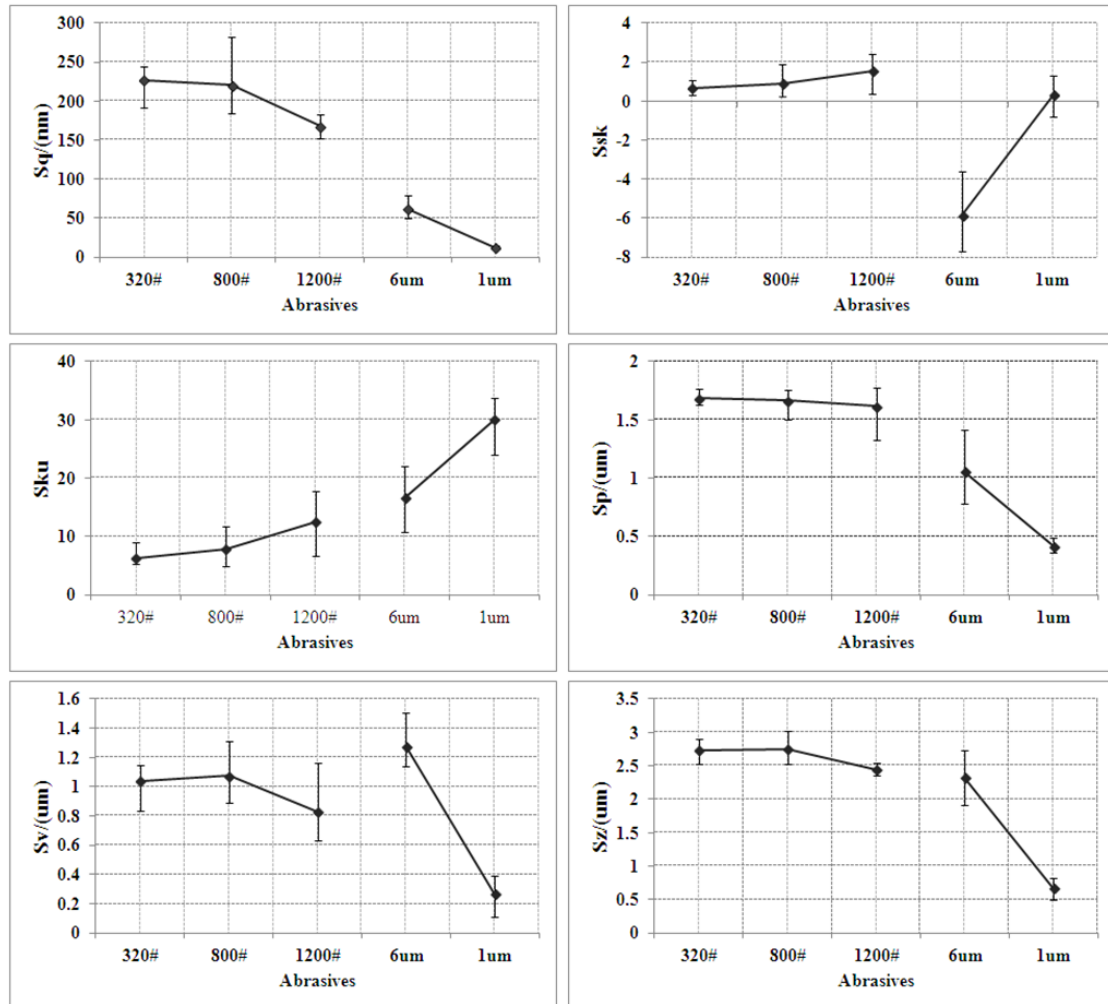


Figure 5.2: The evolution of amplitude parameters

5.2.2 Spacing parameters

Figure 5.3 shows the evolution of spacing parameter during polishing. The spacing parameter includes density of summits of the surface parameter S_{ds} , the fastest decay auto-correlation length parameter S_{al} and texture aspect ratio of the surface parameter S_{tr} . As displayed in the figure, S_{ds} decrease steadily during polishing process which indicates that the density of summits of a polished workpiece reduces with the decrease of abrasive size. It should be noted however that this parameter is highly dependent on the summit definition in this case the S_{ds} was used. The S_{tr} shows little change during rough polishing and then decreases

sharply to about 0.25 during fine polishing. The Str is still almost not changed during fine polishing which is due to the transfer from directional finishing (abrasive papers) to non-directional finishing (machine polishing). The Sal increases slightly during rough polishing and 6 μ m diamond polishing then increases sharply after 1 μ m diamond polishing. A small value of Sal denotes that the surface is dominated by high frequency (or short wavelength) components. The results indicate that in fine or final polishing, the surface is dominated by low frequency (or long wavelength) components often referred to as mid-spatial frequencies [194].

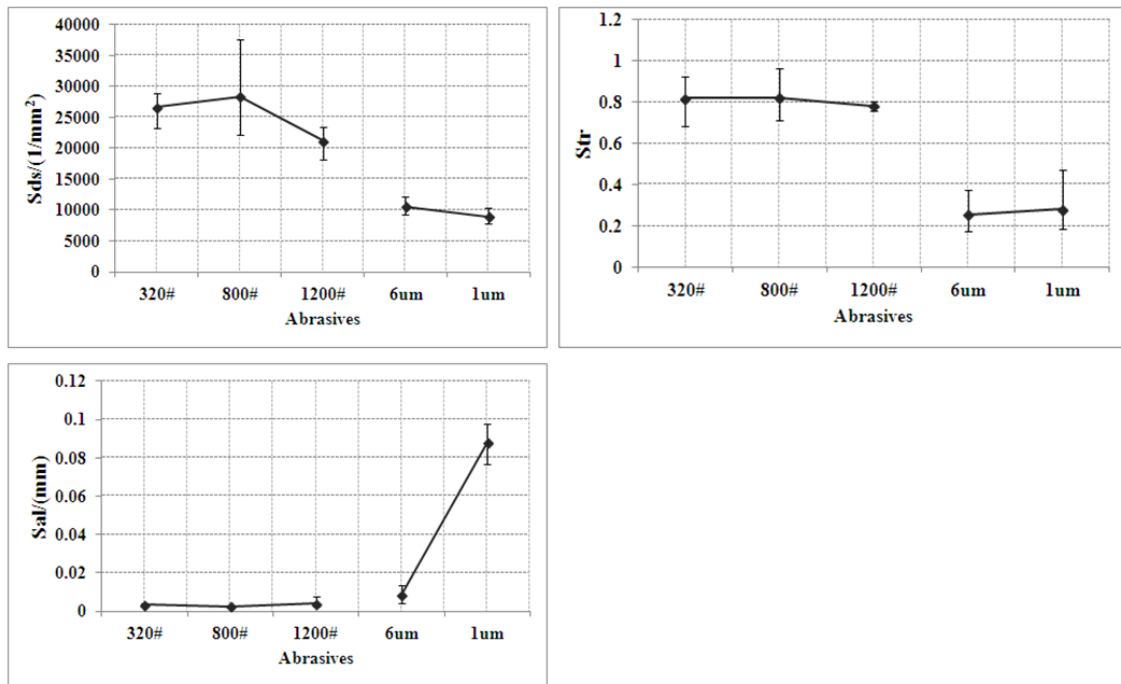


Figure 5.3: The evolution of spacing parameters

5.2.3 Hybrid parameters

The hybrid parameters, including the arithmetic mean summit of curvature of the surface parameter Ssc , root-mean-square slope of the assessed topographic surface parameter Sdq and developed interfacial area ratio parameter Sdr , are based on both amplitude and spatial information. These parameters are used to numerically define the hybrid topography features such as the slope of the surface, the curvature of high spots and the interfacial area. Any changes in either amplitude or spacing may affect the hybrid feature. Figure 5.4 displays the evolution of hybrid parameters during polishing process. As shown in the figure, all hybrid parameters have nearly the same variation trend during polishing process, namely, increase slightly first and then decrease steadily. After final polishing, all hybrid parameters are at low

values. The decrease of Ssc indicates that the principle curvatures at the summits within the sampling area reduces with the decrease of abrasive size. It should be noted however that this parameter is highly dependent on the summit definition in this case the Ssc was used. The decrease of Sdr denotes that either the amplitude or the spacing or both is becoming insignificant during polishing process. The results indicate a general smoothing of the surface.

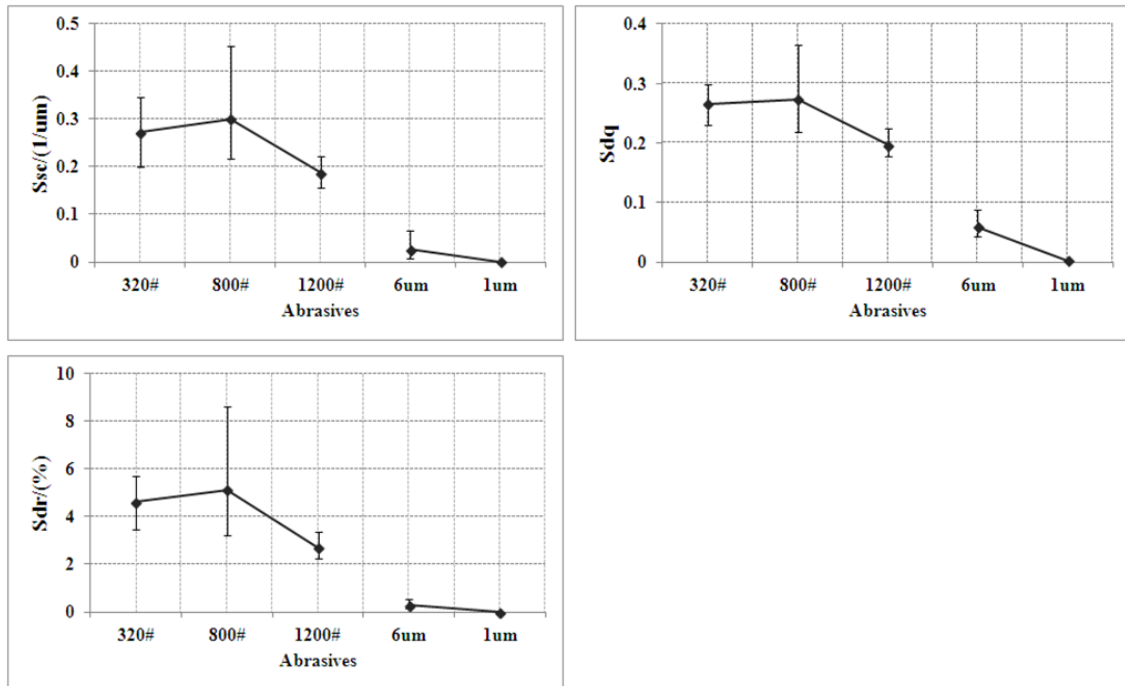


Figure 5.4: The evolution of hybrid parameters

5.2.4 Sk family parameters

Sk family parameters, also called linear areal material ratio curve parameters, are the parameters designed specially for highly stressed surface texture. The Sk family parameters are constructed by deriving three sections of the areal material ratio curve, the peaks above the main plateaus, the plateaus themselves and the deep valleys between plateaus. The Sk family parameters consist of core roughness depth parameter Sk , reduced peak height parameter Spk , reduced valley height parameter Svk , peak material component parameter $Smr1$ and peak material component parameter $Smr2$. As shown in figure 5.5, Spk has only a slight variation during rough polishing then decrease greatly after fine polishing by 6µm diamond polishing and there is little change after 1µm diamond polishing. This means that the reduced peaks can only be polished off in the latter stages of processing. Sk reduces steadily with the decrease of abrasive size. Sk correlates with the depth of the working/core part of the surface, which carries the load and contacts the bearing surface, a critical factor in

orthopaedic surfaces. The decrease of Sk is in agreement with the principle of wear. From tribological point of view, the polishing process is a kind of wear process. Svk also decreases steadily during polishing process, which means the depth of valleys decreases. The peak material component $Smr1$ and $Smr2$ keep quite stable during the polishing process as the relative parameters (calculated as a relative contribution to the surface topography) rather than absolute.

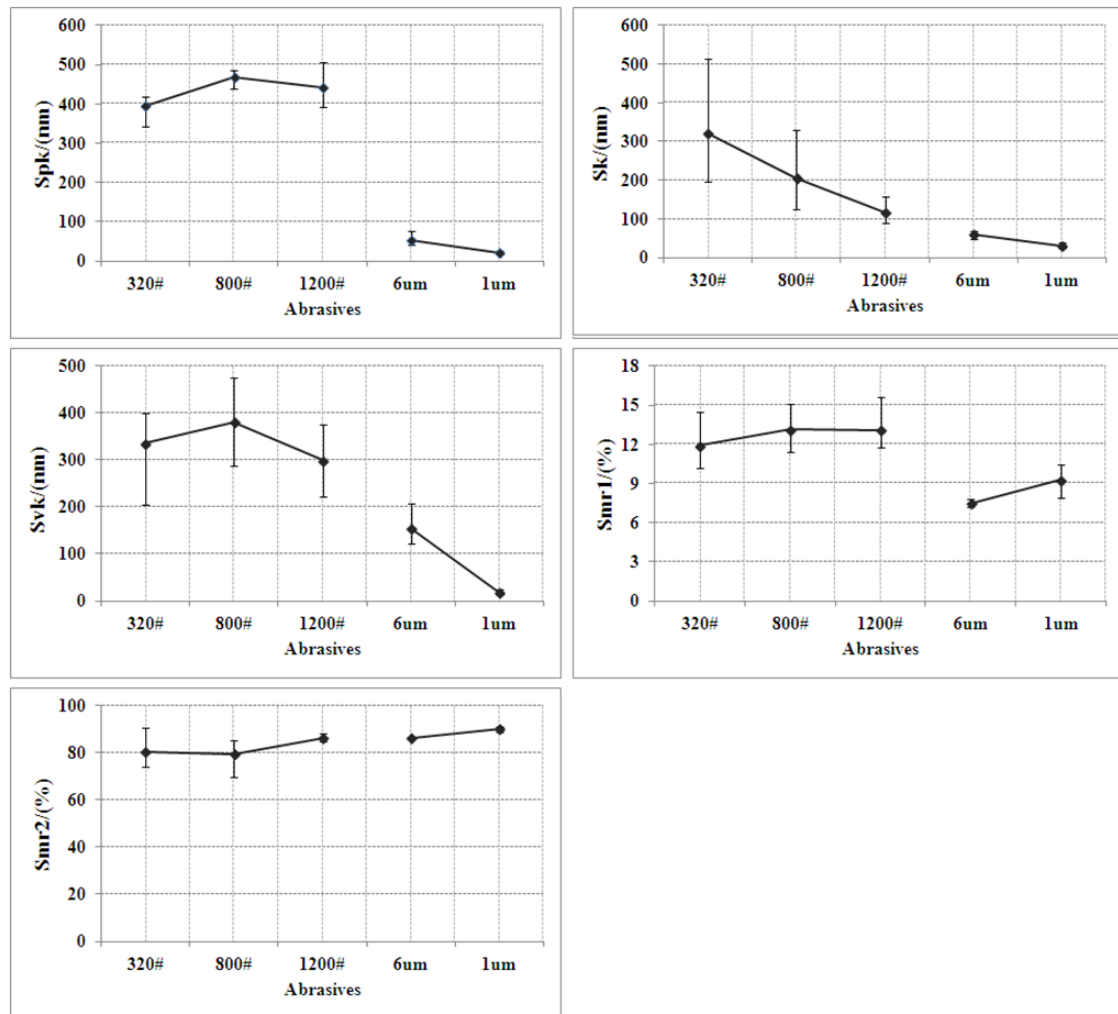


Figure 5.5: The evolution of Sk family parameters

5.2.5 Material/void volume parameters

Figure 5.6 gives the evolution of material/void volume parameters of the topographic surface. These parameters are derived from the volume information of areal material ratio curves of the topographic surface and can characterise the common functional properties of surface as well as interpret wear and tribological properties in a running-in procedure. Material/void volume parameters include peak material volume of the topographic surface parameter Vmp ,

core material volume of the topographic surface parameter V_{mc} , core void volume of the surface parameter V_{vc} and valley void volume of the surface parameter V_{vv} . As displayed in the figure, V_{mp} increases slightly during rough polishing and then drops sharply after fine polishing. There is not big difference during fine polishing for V_{mp} . The V_{mc} and V_{vc} decrease gradually with the decrease of abrasive size. The V_{vv} parameter increases slightly during rough polishing and then decreases steadily during fine polishing. This parameter is used to represent the fluid retention ability of a contacting surface. The large value of V_{vv} indicates the surface is ‘spiky’ with relatively large isolated valleys.

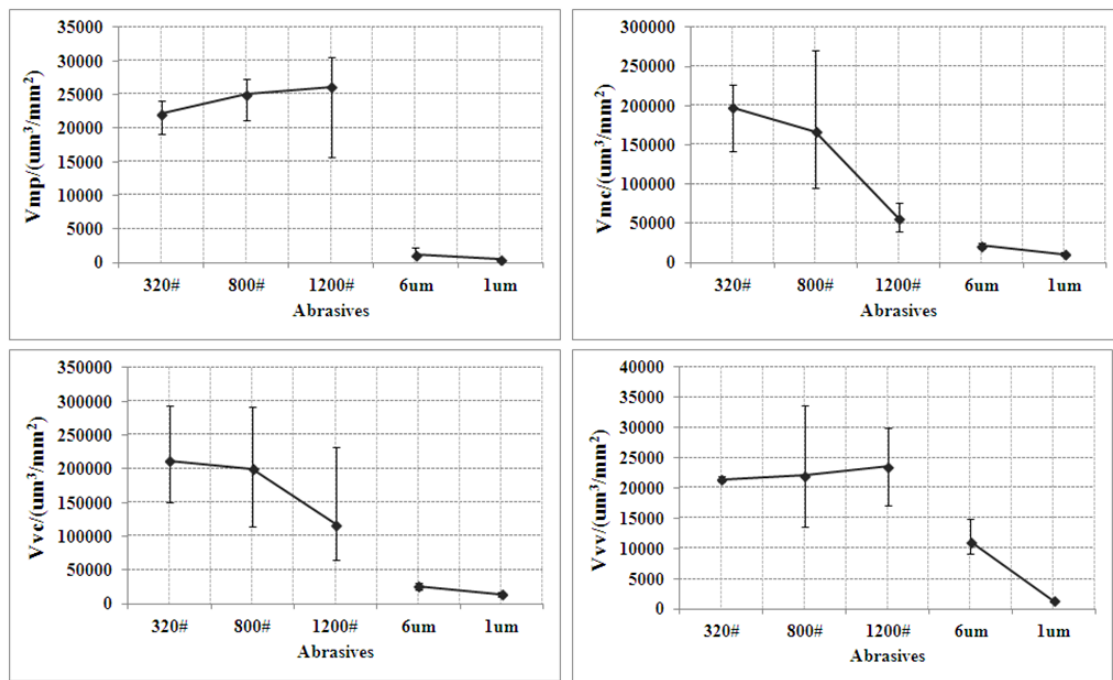


Figure 5.6: The evolution of material/void volume parameters

5.2.6 Other parameters

Figure 5.7 shows the evolution of other parameters during polishing process. Other parameters are those which are excluded in the above mentioned groups, including texture direction of the surface parameter Std , ten point height of the surface parameter $S5z$ and arithmetical average of the surface parameter Sa . Std is given by an angle. As displayed in the figure, Std only changes slightly when the abrasive size decreases. $S5z$ reduces steadily during the polishing process. This denotes the number of highest peaks decreases for a polished surface. Sa is the most commonly used parameter. This parameter is corresponding to Ra in the case of 2D measurement. The variation trend of Sa is usually similar to Sq . In

this investigation, Sa decreases gradually with the reduction of abrasive size. After final polishing, Sa decreases to about 9nm.

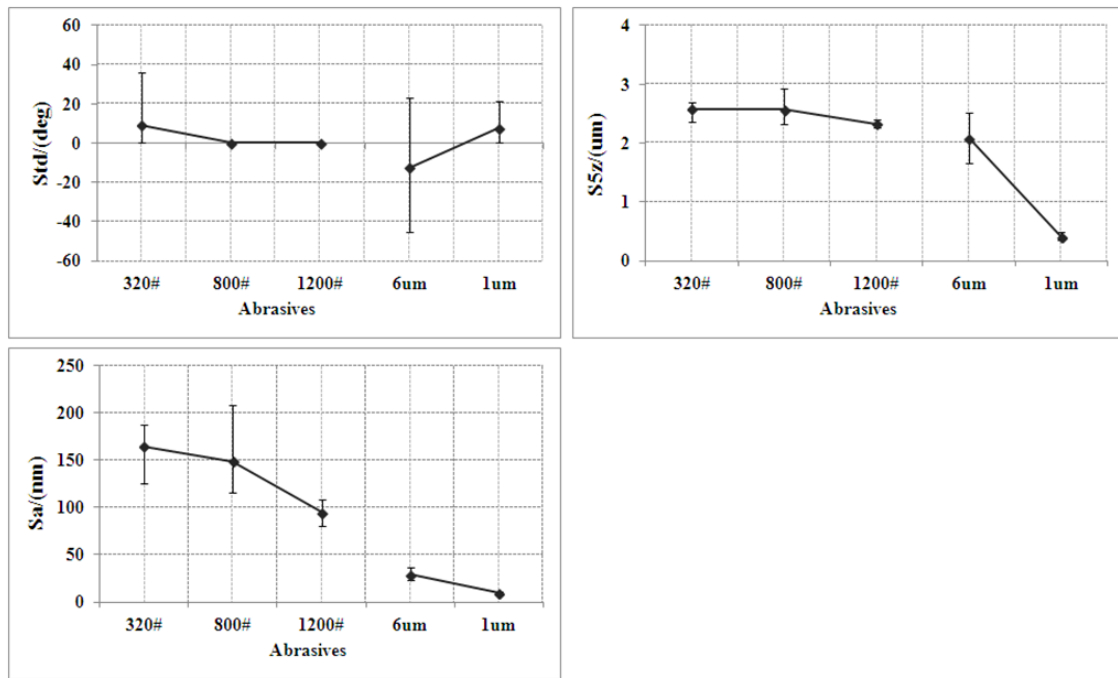


Figure 5.7: The evolution of other parameters

5.3 The effects of the combination of polishing cloths/pads and polishing abrasives on surface topography

It is well known that both polishing cloths/pads and abrasive can affect surface topography. However, the effects of the combination of them are still obscure. The aim of this investigation was to study the effects of the combination of polishing cloths/pads and abrasives on surface topography and try to understand which one of the polishing pads/cloths and abrasives would affect surface topography more. The samples used here are the same with section 5.2, and the machining settings are shown in table 5.1.

The first investigation was for the combination of LP13 and 6 μ m diamond paste. In this investigation, 3 samples were polished. Table 5.3 displays the surface topography of these three samples before and after polishing. As displayed in table 5.3, most topography parameters varied slightly after polishing except for Ssk , Sp and Sv , all of which had a relatively great change comparing to other parameters. The experimental results indicate that the combination of LP13 polishing pad and 6 μ m diamond paste affects surface topography only slightly.

Table 5.2: The effects of the combination of LP13 and 6 μ m diamond paste on surface topography

Parameters	Sample 1		Sample 2		Sample 3	
	Before polishing	After polishing	Before polishing	After polishing	Before polishing	After polishing
Sq (nm)	65.5	69.1	59.2	67.5	61.6	68.1
Ssk	-0.32	-0.63	-0.29	-0.60	-0.35	-0.59
Sku	3.9	3.9	3.5	3.8	3.9	3.8
Sp (nm)	319.9	226.7	302.2	220.5	280.5	242.4
Sv (nm)	444.4	506.8	328.1	433.6	430.9	425.7
Sz (nm)	764.2	733.6	630.3	654.1	711.4	668.1
Spacing parameters						
Sds (1/mm ²)	1983.4	1892.8	1980.2	1896.4	1994.6	1862
Str	0.91	0.86	0.79	0.79	0.88	0.77
Sal (mm)	0.012	0.012	0.011	0.012	0.012	0.012
Hybrid parameters						
Sdq	0.014	0.014	0.012	0.013	0.013	0.014
Ssc (1/ μ m)	0.003	0.003	0.003	0.003	0.003	0.003
Sdr (%)	0.009	0.009	0.007	0.009	0.008	0.009
Curves parameters						
Vmp (μ m ³ /mm ²)	2944.8	2374	2645	2431.8	2689	2419.4
Vmc (μ m ³ /mm ²)	57222	61502	52172	59574	54020	60430
Vvc (μ m ³ /mm ²)	74314	74560	67242	73170	69546	73988
Vvv (μ m ³ /mm ²)	8450.4	9810.8	7568.8	9605.4	7980	9626.6
SK family						
Spk (nm)	60.83	45.61	54.83	47.15	55.04	47.26
Sk (nm)	162.4	170.90	148.69	164.42	153.96	168.41
Svk (nm)	82.3	96.2	71.34	92.78	77.24	92.8
Smr1 (%)	8.96	7.18	8.64	7.82	8.6	7.5
Smr2 (%)	88.9	87.5	89	87.36	88.82	87.64
Other parameters						
Std (deg)	0	0	0	0	0	0
S5z (nm)	622.95	614.57	549.44	592.93	577.21	580.86
Sa (nm)	51.2	54.2	46.5	52.7	48.1	53.5

Table 5.3: The effects of the combination of LP13 and 1 μ m diamond paste on surface topography

Parameters	Sample 1		Sample 2		Sample 3	
	Before polishing	After polishing	Before polishing	After polishing	Before polishing	After polishing
Sq (nm)	69.1	70.9	67.5	67.5	68.1	77.9
Ssk	-0.63	-0.65	-0.60	-0.59	-0.59	-0.68
Sku	3.9	3.8	3.8	3.8	3.8	3.8
Sp (nm)	226.7	208.5	220.5	243.1	242.4	218.6
Sv (nm)	506.8	467.3	433.6	424.2	425.7	517.7
Sz (nm)	733.6	675.8	654.1	667.3	668.1	736.3
Spacing parameters						
Sds (1/mm ²)	1892.8	1811.8	1896.4	1876.8	1862	1713.8
Str	0.86	0.86	0.79	0.73	0.77	0.90
Sal (mm)	0.012	0.013	0.012	0.012	0.012	0.013
Hybrid parameters						
Sdq	0.014	0.014	0.013	0.013	0.014	0.015
Ssc (1/ μ m)	0.003	0.003	0.003	0.0028	0.003	0.0028
Sdr (%)	0.009	0.010	0.009	0.009	0.009	0.011
Curves parameters						
Vmp (μ m ³ /mm ²)	2374	2385.6	2431.8	2390.8	2419.4	2467.4
Vmc (μ m ³ /mm ²)	61502	63372	59574	60056	60430	70000
Vvc (μ m ³ /mm ²)	74560	75820	73170	74104	73988	83396
Vvv (μ m ³ /mm ²)	9810.8	10227.8	9605.4	9379.4	9626.6	11256
SK family						
Spk (nm)	45.61	44.86	47.15	46.77	47.26	45.5326
Sk (nm)	170.90	173.59	164.42	168.3	168.41	193.0916
Svk (nm)	96.2	98.71	92.78	90.57	92.8	108.97075
Smr1 (%)	7.18	7.1	7.82	7.58	7.5	6.7
Smr2 (%)	87.5	86.96	87.36	87.96	87.64	87.14
Other parameters						
Std (deg)	0	0	0	0	0	0
S5z (nm)	614.57	593.25	592.93	587.72	580.86	632.47
Sa (nm)	54.2	55.7	52.7	52.9	53.5	61.42

Table 5.4: The effects of the combination of Microcloth and 1 μ m diamond paste on surface topography

Parameters	Sample 1		Sample 2		Sample 3	
	Before polishing	After polishing	Before polishing	After polishing	Before polishing	After polishing
Sq (nm)	68.1	10.8	54.6	12.2	54.7	15.5
Ssk	-0.59	-0.22	-2.19	-2.74	-1.24	-1.16
Sku	3.8	4.4	13.8	7.3	6.9	12.1
Sp (nm)	242.4	45.2	174.7	48.9	165.1	52.7
Sv (nm)	425.7	73.9	621.2	216.9	482.9	203.6
Sz (nm)	668.1	119.1	795.7	265.9	647.9	256.3
Spacing parameters						
Sds (1/mm ²)	1862	443.3	921.3	391.1	1197.8	383.3
Str	0.77	0.17	0.45	0.41	0.57	0.29
Sal (mm)	0.012	0.035	0.016	0.057	0.014	0.035
Hybrid parameters						
Sdq	0.014	0.0008	0.008	0.001	0.009	0.0013
Ssc (1/ μ m)	0.003	0.0001	0.0008	0.0001	0.0013	0.0001
Sdr (%)	0.009	0.000035	0.003	0.00006	0.005	0.00009
Curves parameters						
Vmp (μ m ³ /mm ²)	2419.4	552.2	1478.4	629.3	1653.2	679.9
Vmc (μ m ³ /mm ²)	60430	9346.6	39124	8638.2	45534	12166
Vvc (μ m ³ /mm ²)	73988	12514	44152	12168	53352	15728
Vvv (μ m ³ /mm ²)	9626.6	1241.5	10110	1378.2	8848	2179.5
SK family						
Spk (nm)	47.26	11.03	29.88	12.49	31.58	13.5
Sk (nm)	168.41	26.52	99.11	24.36	121.18	34.4
Svk (nm)	92.8	11.6	107.03	16.61	90.55	24.4
Smr1 (%)	7.5	10.3	7.02	11.2	7.14	9.12
Smr2 (%)	87.64	89.78	83.98	90.3	85.7	89.02
Other parameters						
Std (deg)	0	18	-1.8	36	-12.6	36
S5z (nm)	580.86	92.72	675.76	140.65	552.78	178.9
Sa (nm)	53.5	8.4	37.99	8.6	41.27	11.4

The second investigation was for the combination of LP13 and 1 μ m diamond paste. Three samples were polished in this study. Table 5.3 shows the experimental results. As shown in the table, only S_v and S_z for sample 1 decreased significantly, all other parameters for sample 1 and all topography parameters for both sample 2 and sample 3 varied only slightly after polishing. These experimental results mean that the combination of LP13 and 1 μ m diamond paste has a little effect on surface topography.

The third investigation was for the combination of Microcloth (Buehler) and 1 μ m diamond paste. Three samples were polished in this investigation. As shown in table 5.4, all parameters of surface topography for three samples varied greatly after polishing, indicating that this combination of polishing cloth and abrasive affects surface topography greatly.

Comparing the above three investigations, it was found that both polishing cloths/pads and abrasive can affect surface topography significantly. When the polishing cloths/pads are the same, the decrease of the abrasive size only affects the topography slightly. When the abrasive size is kept constant, changing the polishing cloths/pad will greatly influence the surface topography. These experimental results indicate that both the polishing cloths/pads and abrasives, and the combination of them must be determined experimentally for the improvement of surface topography. Poor selection of the combination of polishing abrasives and cloths/pad may result in little roughness improvement.

5.4 Summary

This chapter firstly investigated the evolution of the surface topography during polishing process and then the effects of the combination of polishing cloths/pads and abrasives on the surface topography. The surface topography parameters include the following groups: amplitude parameters, spacing parameters, hybrid parameters, material/void volume parameters (or curves parameters), Sk family parameters and other parameters.

In the first investigation, the following conclusions have been obtained:

(1) Amplitude parameters

During the polishing process, the amplitude parameters of S_q , S_p and S_z decrease steadily; S_{ku} increases gradually; S_{sk} and S_v fluctuate. The decrease of S_q means that the standard deviation of the surface can be reduced by polishing. The decrease of S_p denotes that the peak height is decreasing after polishing, which is in agreement with the polishing principle

that the smoother the surface, the lower the peak height. All values of Sku are greater than 3 which mean the peakedness or sharpness of the polished surface is centrally distributed. Although the Ssk fluctuates to positive or negative during polishing process, its value is near zero after final polishing, which indicates that the final polished surface is random in nature with Gaussian shape roughness distribution. If the scratches left by previous machining can be completely removed, the value of Sv can be effectively reduced by polishing. Sz relates to both Sp and Sv , because Sz is the sum of the Sp and Sv . In this study, Sz has the same variation trend with Sp .

(2) Spacing parameters

The spacing parameters of Sds and Str decrease gradually while the Sal increases slightly first and then sharply during the polishing process. The decrease of Sds means that the density of summits of a polished surface reduces with the decrease of abrasive size. Only if the abrasive size decreases greatly, the Str will vary greatly as well. Otherwise, Str only changes slightly if abrasive size varies slightly. The increase of Sal indicates that the final polished surface is dominated by low frequency (or long wavelength) components.

(3) Hybrid parameters

All three hybrid parameters nearly have the same variation trend, namely, increase very slightly first and then decrease to low values. Since the hybrid parameters are based on amplitude and spatial information, any changes in either amplitude or spacing or both may affect the hybrid property. The decrease of Ssc indicates that the principle curvatures at the summits within the sampling area reduces with the decrease of abrasive size. The decrease of Sdr denotes that either the amplitude or the spacing or both is becoming unimportant during polishing process.

(4) Sk family parameters

Sk family parameters of Spk and Svk increase slightly and then decrease gradually; Sk decreases steadily; $Smr1$ fluctuates and $Smr2$ increases very slightly. The variation trend of Spk means that the reduced peaks can only be polished off if the size of abasive are changing greatly. The decrease of Svk indicates that the depth of valleys decreases during the polishing process. The decrease of Sk denotes that the depth of the working part of the surface decreases. The stabilization of $Smr1$ and $Smr2$ indicate that the small peaks above the main

plateau are not too many for whatever the roughly polished surface or the finely polished surface.

(5) Material/void volume parameters

The parameters of V_{mp} and V_{vv} increase slightly and then decrease; the V_{mc} and V_{vc} decrease gradually during polishing process. V_{mp} keeps relatively stable during fine polishing. The decrease of V_{vv} indicates that fluid retention ability of a contacting surface decreases. A small value of V_{mc} indicates that the polished surface has a good load bearing capability, which denotes that polishing technology can improve the load bearing capability and lubrication property.

(6) Other parameters

Other parameters include Std , $S5z$ and Sa . In this investigation, Std varies slightly; $S5z$ and Sa decrease steadily. The decrease of $S5z$ means that the number of highest peaks decreases after polishing. Sa is the most commonly used topography parameter to assess the surface quality after machining. The variation tendency is usually corresponding to Sq .

In the second investigation, the effects of the combination of polishing cloths/pads and abrasive on surface topography has been investigated. The investigation results indicate that both polishing cloths/pads and abrasives can affect surface topography. When the polishing cloths/pads are the same, the change of abrasive size affects the surface topography only slightly. When the abrasive size is kept constant, changing the polishing cloths/pad will result in great effect on the surface topography. In addition, the combination of polishing cloths/pads and abrasive should be determined by experiments so that a better combination can be found for the surface topography improvement.

6. MATERIAL REMOVAL INVESTIGATION

6.1 Introduction

The characteristic to defining material removal is termed the influence function (IF) which was defined by Walker et al. [193] as the contour of a dimple (also called polishing spot) produced by a spinning polishing tool exerting a load on a location of the workpiece surface. The influence function is closely related to the information pertaining to the material removal characteristic of the polishing tool involving the geometric size and the distribution of the material removal of the polishing tool [158]. In Computer numerical control (CNC) polishing an influence function is of vital importance for quantifying a polishing procedure. Obtaining an influence function is a critical step in corrective polishing. However, the effects of polishing pads, workpiece hardness and process parameters (such as precess angle, head speed, tool offset and tool air pressure) on influence functions are still unknown for polishing CoCr alloys. This chapter seeks to find the effects of the process parameters on influence functions and to create the model of the material removal rate based on the experimental data. In order to better understand the material removal mechanism, this chapter also investigates the effects of process parameters on polishing forces, including normal force and tangential force.

The specimens used in this chapter were the same with the chapter 4 and chapter 5, i.e., F75 CoCr alloys. As discussed in chapter 3, polishing slurry is beneficial for obtaining a stable MRR. Therefore, this investigation applied a 3 μ m alumina slurry whose specific gravity was 1.025 to polish the influence function. The polishing pad used in the investigation was polyurethane GR35, LP66 and LP13. All experiments were carried out on the Zeeko IRP200 polishing machine. After spots were polished, the 3D maps of the influence functions were measured by a contacting stylus Somicronic Surface profilometer. The volumetric material removal rates (MRR) were calculated by using the Precession software which was developed by Zeeko Ltd. The process parameters are shown in table 6.1.

Table 6.1: The polishing factors used during experiments

Factors	Precess angle	Head speed	Tool offset	Tool air pressure	Dwell time
Value	15degs	1200rpm	0.15mm	1bar	300s

6.2 The effects of process parameters on material removal

6.2.1 The effect of dwell time

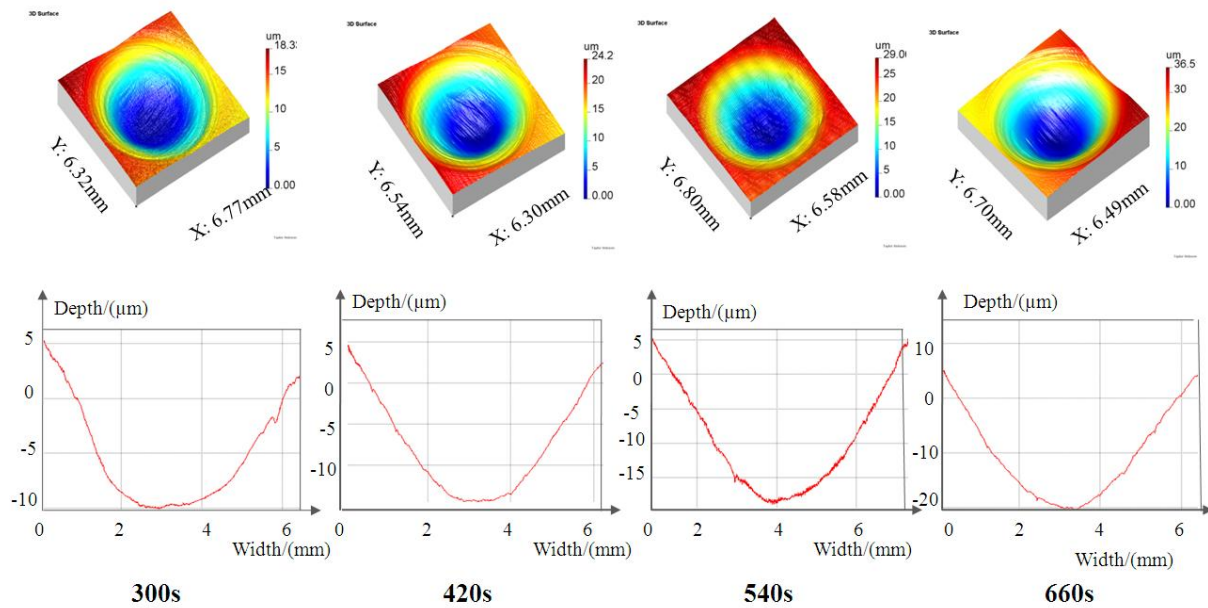


Figure 6.1: Measurements of the IF and profile V.S. dwell time

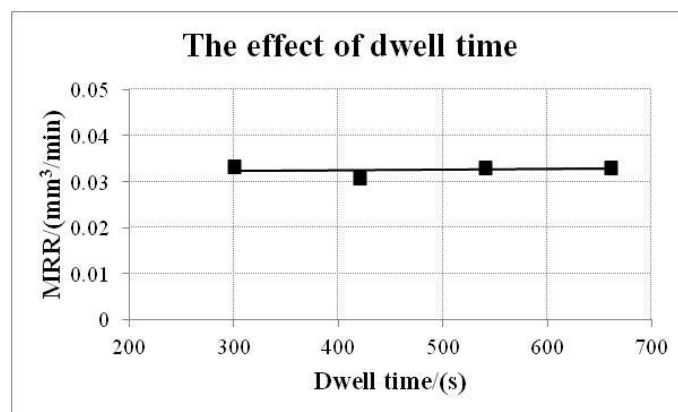


Figure 6.2: The effect of dwell time on the MRR

In this set of experiments, all process parameters were kept constant as shown in table 1. Dwell time was increased from 300s to 660s in increments of 120s during the experiments. According to the Preston equation [12], if polishing conditions are determined, the material removed by polishing is linearly proportional to dwell time. The longer the dwell time lasts, the deeper the polishing spot is. As can be seen in figure 6.1, with the increase of dwell time from 300s to 660s, the widths of the influence functions are nearly the same. Figure 6.2 is the fitting line of the experimental results. The fitting line is parallel to the X-axis which means that the MRR is constant with the increase of dwell time. The dwell time experiments

indicate that if all experimental conditions are fixed, the MRR will keep constant. This is very important in deterministic corrective polishing process which demands a stable MRR.

6.2.2 The effect of precess angle

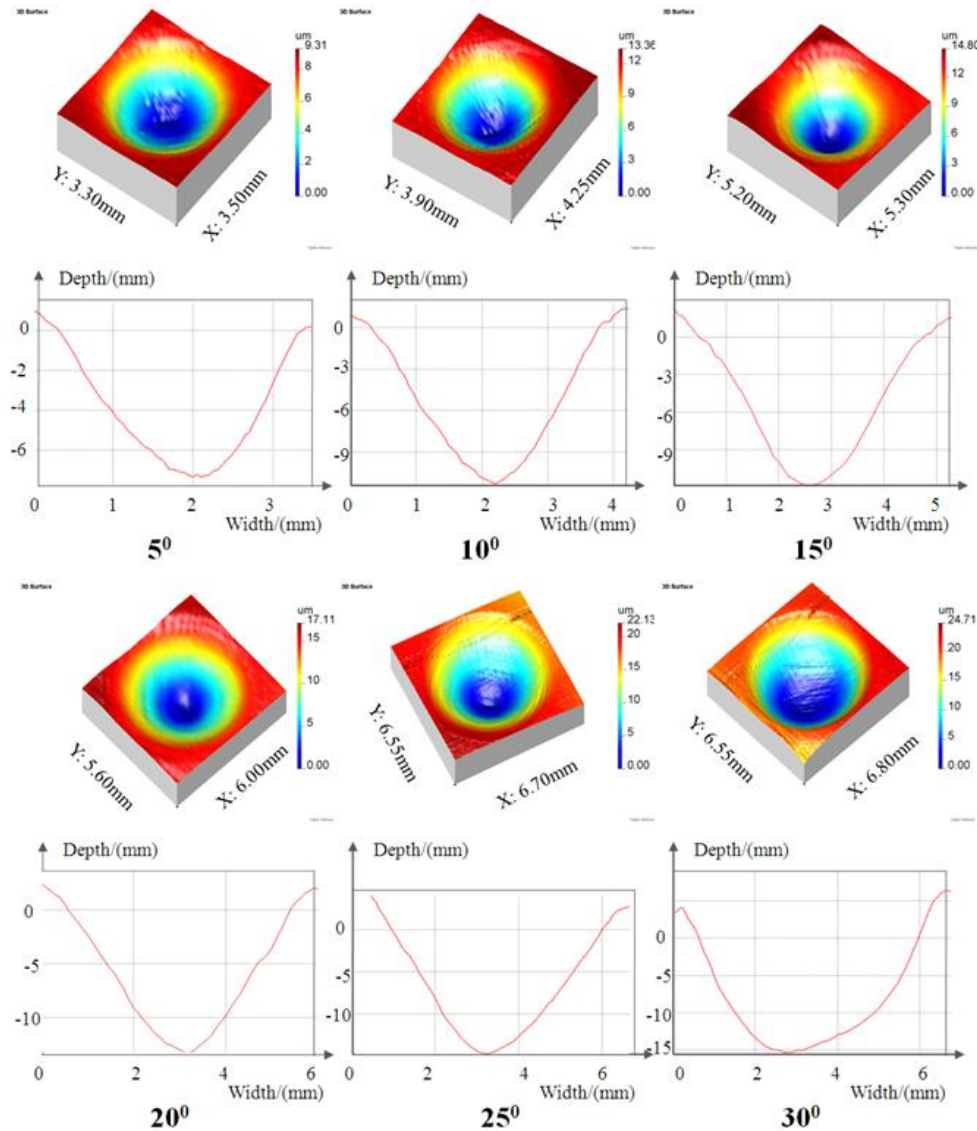


Figure 6.3: Measurement of the IF and profile V.S. precess angle

In this investigation the precess angle was increased from 5° to 30° in increments of 5° . Other parameters were kept constant and given in table 1. The measurements of the influence function are displayed in figure 6.3. As can be seen in figure 6.3, all influence functions are circular and the precess angle clearly affects the width of the influence functions (The diameter of the influence function increases from 3.5mm to 6.5mm). The width and the maximal depth of the influence function increases significantly with the increase of precess angle when the precess angle increases from 5° to 30° . The reason for this is that when the

precess angle is small, the contacting area of the polishing tool is near the centre of the bonnet. In this situation, the polishing speed as well as the contact area is small and the MRR is therefore low. As the precess angle increases the polishing speed and contact area increases which leads to the increase in the width and the maximal depth of the influence function. All influence functions comply broadly with a Gaussian shape and are uniform. Viewing all the 2D profiles, when precess angle is 5° , 10° , 15° , 20° and 25° , the profiles are regular while in 30° the profile is irregular.

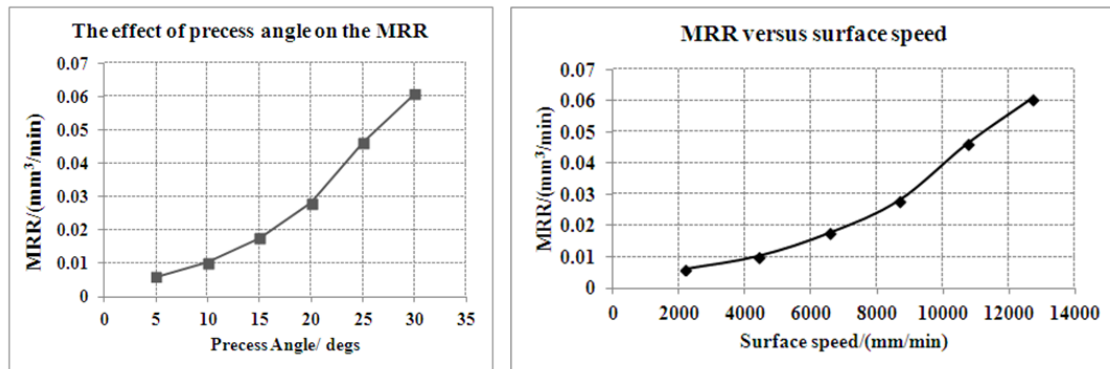


Figure 6.4: The effect of precess angle on the MRR and MRR versus surface speed

Figure 6.4 gives the relationship of MRR and precess angle. As can be seen in figure 6.4, the MRR increases with the increase of precess angle. When the precess angle is 5° , the MRR is lowest ($0.0059\text{mm}^3/\text{min}$). Then the MRR increase sharply with the increase of precess angle up to the highest ($0.061\text{mm}^3/\text{min}$). The exact relationship of MRR and precess angle appears clearly non-linear but probably relates to the non-linear increase in polishing speed as a function of the precess angle. This set of experiments indicates that the precess angle is one of the main parameters affecting the MRR and the consequent width and maximal depth of the influence function. The effect of surface speed on the MRR is also plotted in figure 6.4. As shown in figure 6.4, the variation trend of MRR versus surface speed is the same with the effect of precess angle on the MRR.

6.2.3 The effect of head speed

According to the Preston equation, the MRR is linearly proportional to the polishing speed. A higher speed will always result in more material removal in the same period of time. In bonnet polishing, the polishing speed is the velocity of bonnet revolution (Unit: rpm). This investigation tries to confirm if this relationship of head speed and MRR is applicable to bonnet polishing of CoCr. The experimental conditions are given in table 6.1. The polishing speeds range from 300rpm to 1800rpm in increments of 300rpm. Figure 6.5 shows the

influence function changes with the increase of polishing speed. As can be seen in figure 6.5, the width of the influence function does not change obviously while the maximal depth of the influence function increases greatly with the increase of head speed. All influence functions comply broadly with Gaussian shape. Therefore, polishing speed affects the shape of the influence function only slightly. Figure 6.6 shows the fitting results of polishing speed and MRR. The fitted line of the polishing speed and MRR shows that the relationship is fairly linear. This investigation indicates that polishing speed does not affect the shape of the influence function but greatly affects the MRR linearly in line with the Preston equation. When the head speed is too high, an aquaplaning may occur between the polishing tool and the workpiece as this is the reason why the trend of MRR decreases with the increase of head speed.

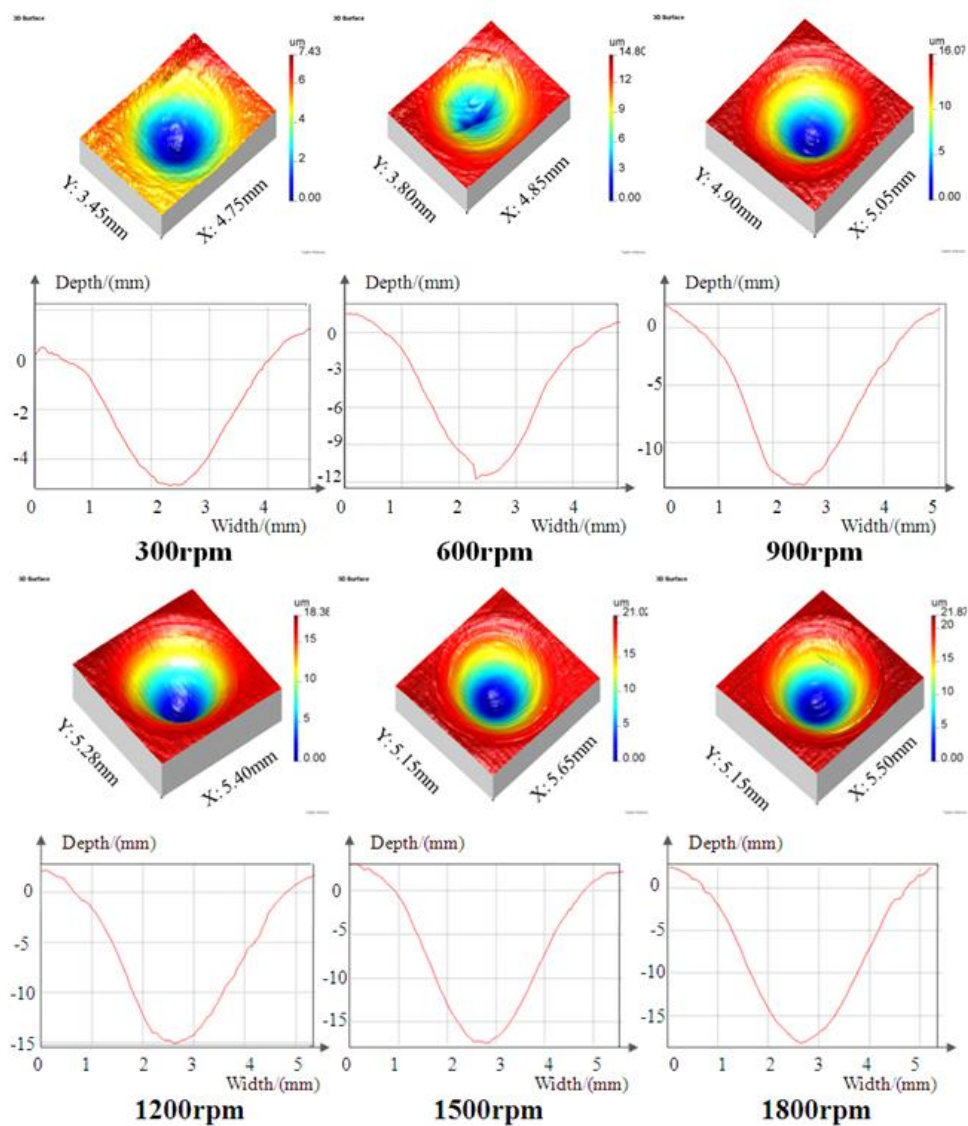


Figure 6.5: Measurements of the IF and profile V.S. head speed

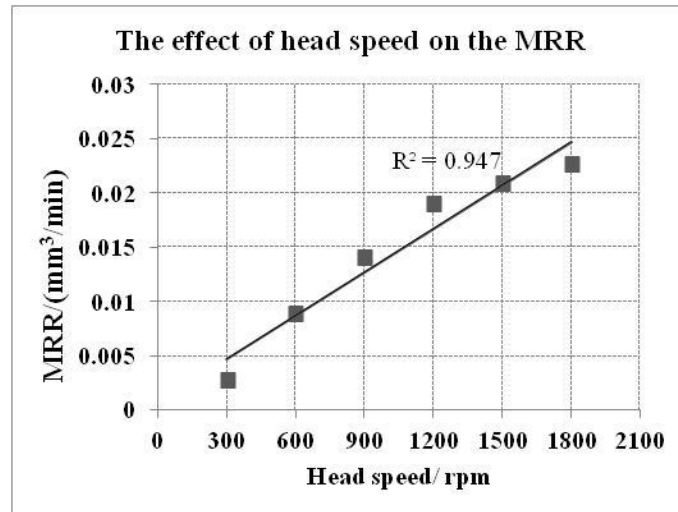


Figure 6.6: The effect of head speed on the MRR

6.2.4 The effect of tool offset

Tool offset is the deformation depth of the bonnet when it contacts on the surface of a workpiece in polishing. Obviously, different tool offsets generate different contacting areas and contacting pressure during polishing process. Contacting zones hold the abrasives which remove the material of the workpiece during polishing process. Therefore, when tool offset varies, the width and the maximal depth of the influence function should change as well. However, how much tool offset affects the influence function needs to be investigated. In this investigation, tool offset increased from 0.1mm to 0.6mm in increments of 0.1mm while other experimental conditions remained unchanged and are given in table 6.1.

Figure 6.7 shows measurements of the influence functions when the tool offsets are changed from 0.1mm to 0.6mm. As shown in Figure 6.7, the width of the influence function increases significantly with the increase of the tool offset, which clearly indicates that the tool offset affects the width of the influence function greatly. It can also be seen from figure 6.7 that from 0.1mm to 0.3mm, the influence functions are broadly Gaussian in shape, but from 0.4mm to 0.6mm, the influence functions are not Gaussian shape and are related to the distortion of the bonnet tool. This phenomenon results in the maximal depth of the influence function increasing first and then decreasing. With the increase of the tool offset, the rubber bonnet deforms predictably (increasing contact area) when the tool offset is less than 0.3mm, but when the tool offset is greater than 0.4mm, the bonnet warps slightly (figure 6.8, FEA simulation). In this situation, the centre of contacting area departs from the surface of the workpiece. Consequently the material of the workpiece in this area is not removed. Therefore,

a protrusion is created in the centre of the polishing spot. This phenomenon is harmful for deterministic corrective polishing and should clearly be avoided.

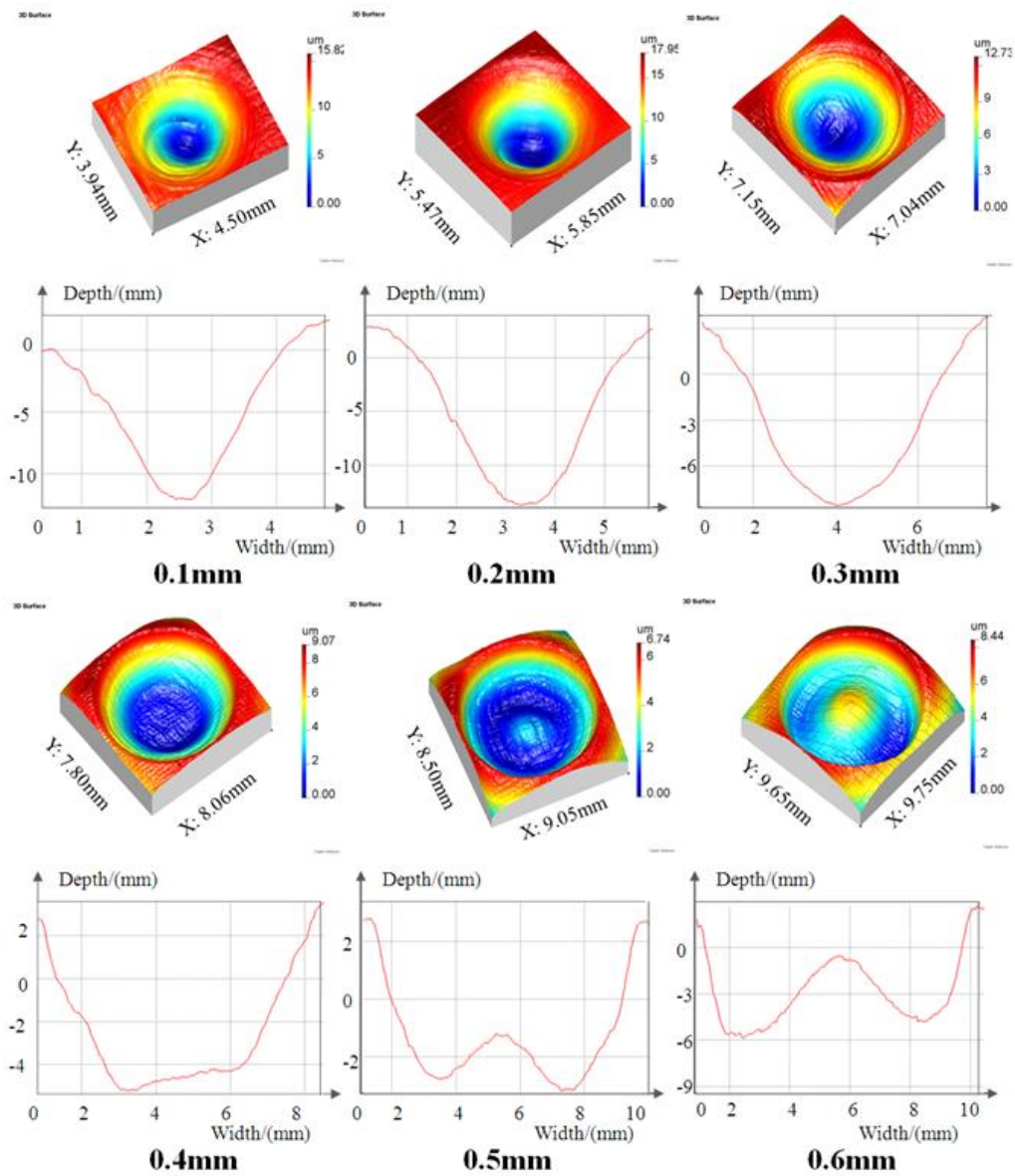


Figure 6.7: Measurements of the IF and profile V.S. tool air pressure (1.0bar tool air pressure)

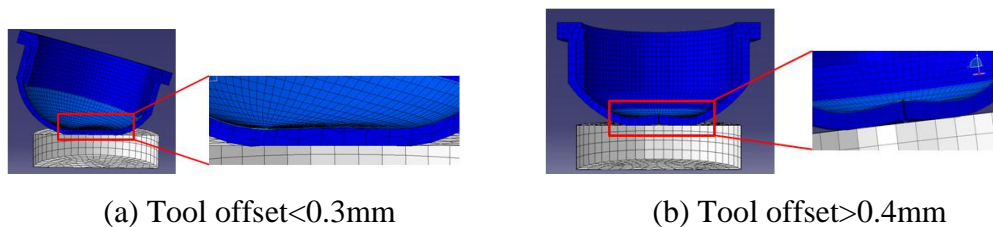


Figure 6.8: The deformation of bonnet (FEA simulation, Abaqus 6.90)

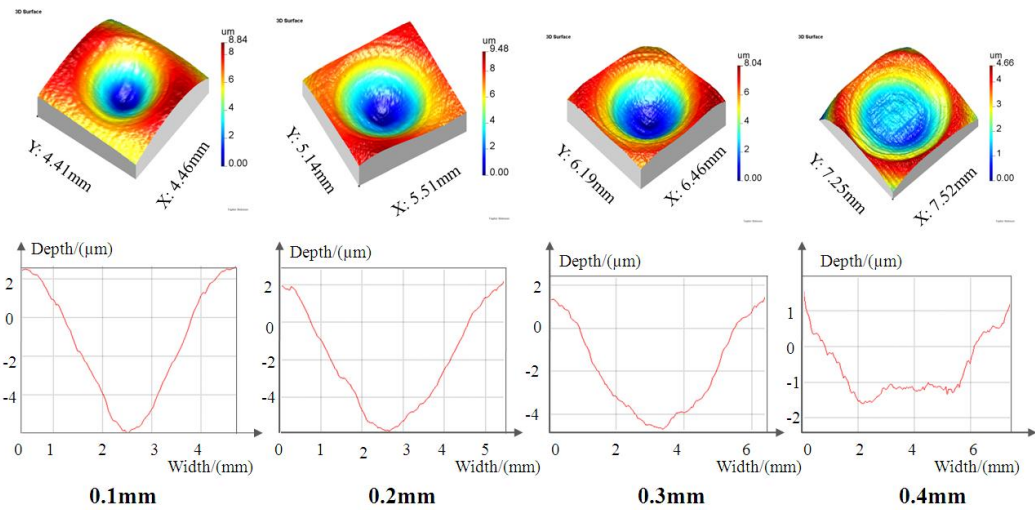


Figure 6.9: Measurements of the IF and profile V.S. tool offset (0.5bar tool air pressure)

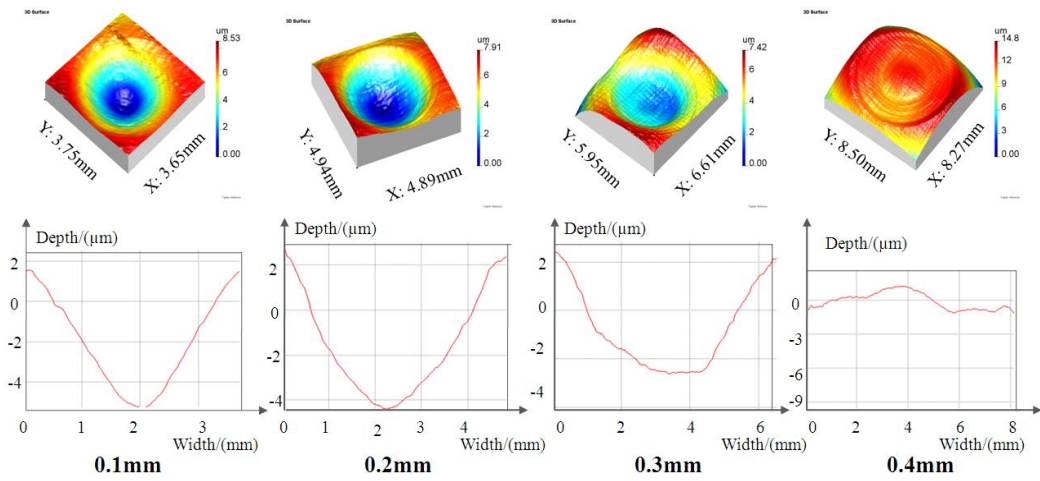


Figure 6.10: Measurements of the IF and profile V.S. tool offset (1.5bar tool air pressure)

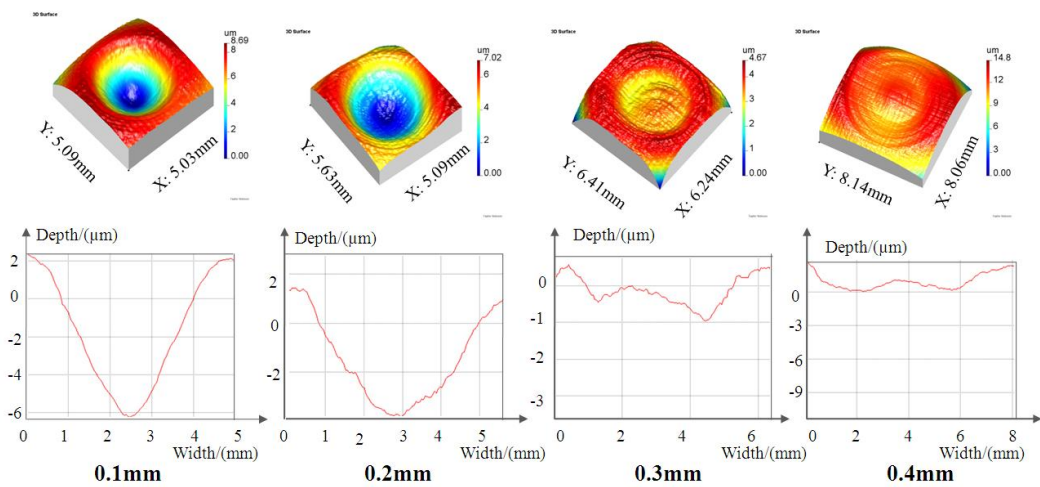


Figure 6.11: Measurements of the IF and profile V.S. tool offset (2.0bar tool air pressure)

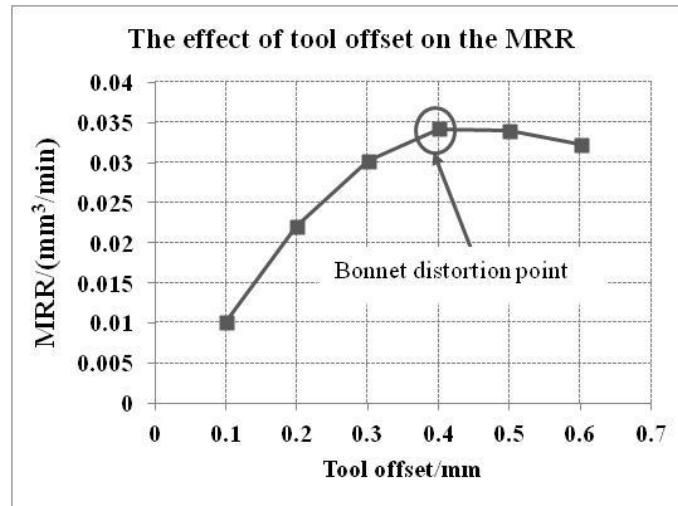


Figure 6.12: The effect of tool offset on the MRR

In order to further investigate the threshold for the bonnet warping phenomenon under the different tool air pressure conditions, a further three sets of experiments were carried out where the tool air pressure was changed to 0.5bar, 1.5bar and 2.0bar, and the other conditions are given in table 6.1. The experimental results for threshold of tool offset under the different tool air pressure shows that when tool air pressure is 0.5bar and 1bar, the threshold for tool offset is 0.3mm; when tool air pressure is 1.5bar and 2bar, the threshold for tool offset is 0.2mm (figure 6.9-6.11). These results are very important for corrective polishing which always needs a stable and deterministic MRR.

Figure 6.12 shows the relationship of tool offset and the MRR when tool air pressure is 1bar. As can be seen in figure 6.12, the MRR increases with the increase of tool offset from 0.1mm to 0.4mm greatly, from 0.4mm to 0.6mm, the MRR decreases slightly. When tool offset increases from 0.1mm to 0.3mm, the increase of MRR is nearly linear and after 0.3mm, the slope decreases. The slope starts to become negative from 0.4mm with a small slope. The results indicate for a given set of abrasives and workpiece material that there is an upper limit to the tool offset.

6.2.5 The effect of tool air pressure

As discussed above, tool air pressure in bonnet polishing is not the contacting pressure on the workpiece. This pressure relates to the “hardness” of the polishing tool. If the tool offset is constant, the increase of pressure will result in the increase of contacting pressure and vice versa. Hence in bonnet polishing, the contacting pressure relates to both the tool offset and tool air pressure. The tool offset was kept constant at 0.15mm in this investigation and the

tool air pressure was changed from 0.4bar to 2.0bar in increments of 0.4bar. Other polishing parameters are given in table 6.1.

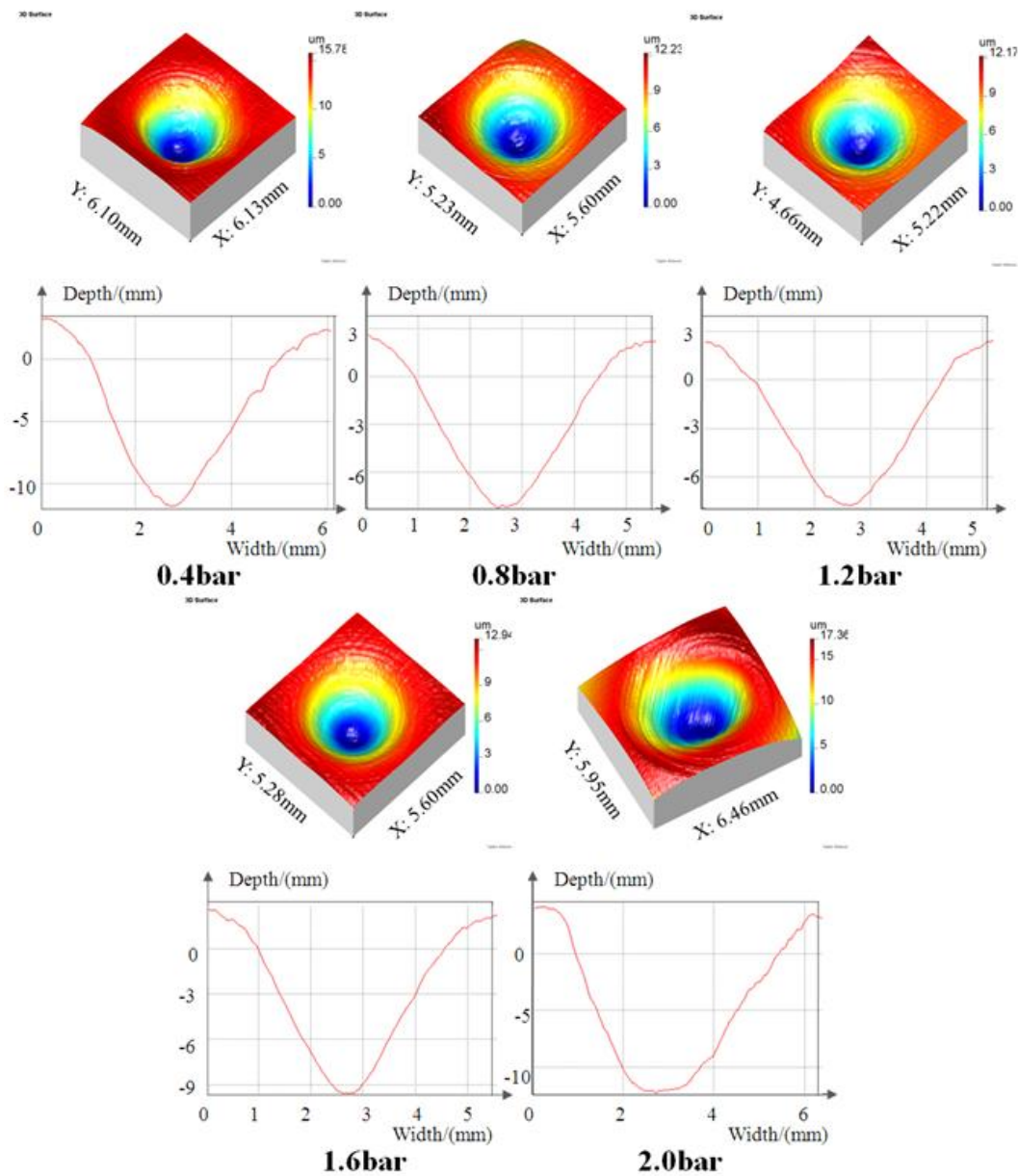


Figure 6.13: Measurements of the IF and profile V.S. tool air pressure

Figure 6.13 shows the measurement of the influence function varies with the increase of tool air pressure. It can be seen in figure 6.13 that the width and the maximal depth of the influence function remain fairly constant with the increase of tool air pressure. This figure also shows that when the tool air pressure increases, the influence function always remains broadly Gaussian in shape. Figure 6.14 shows the effects of tool air pressure on the MRR. The MRR increases with the increase of tool air pressure slightly compared to other process parameters. This indicates that if precess angle, head speed and tool offset are kept constant,

tool air pressure has only a small effect on the MRR. The reason for the weak effect of tool air pressure is that the geometry of bonnet polishing tool changes slightly when tool air pressure increase because of a reinforced cloth inside the rubber.

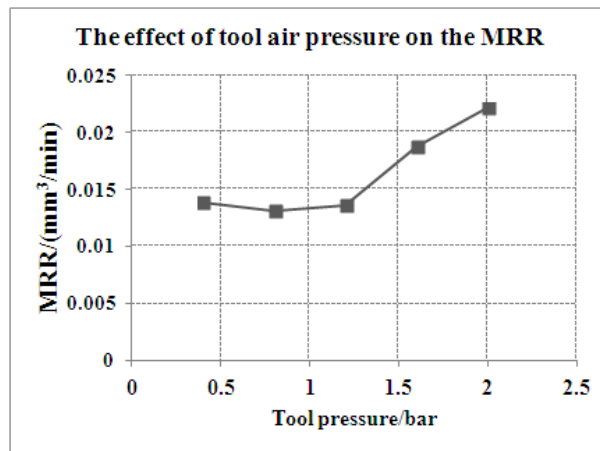


Figure 6.14: The effect of tool air pressure on the MRR

6.3 The effects of workpiece hardness

To meet the different requirements of function, the biomaterial of an artificial joint can be manufactured by several routes, e.g. forming, casting and machining. Therefore the hardness of the resultant samples is likely to be different. This study tries to establish the relationship of the workpiece hardness and the MRR. Here three different hardness samples were tested and their hardness is given in table 6.2. All of them were F75 which had nearly the same chemical composition. In this investigation, we only changed the head speed from 300rpm to 1800rpm and other parameters are given in table 6.1.

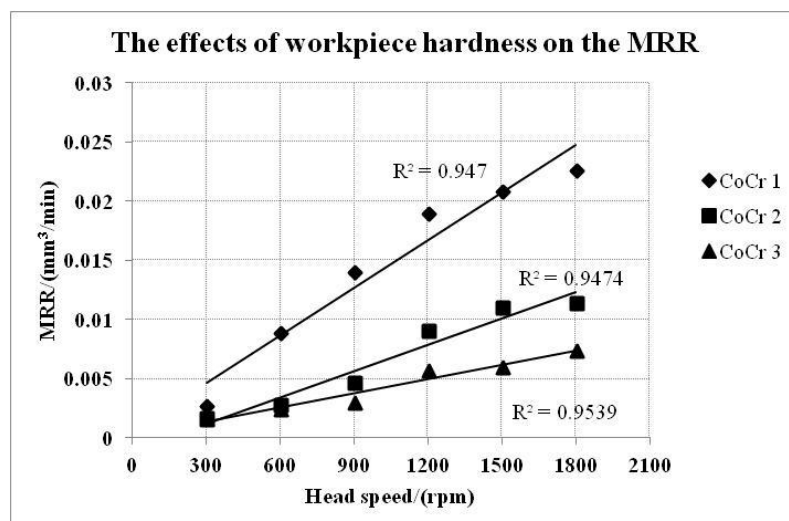


Figure 6.15: The effects of workpiece hardness on the MRR

Table 6.2: Hardness of samples

Samples	Hardness (GPa)
CoCr1	4.21~4.67
CoCr2	5.42~5.77
CoCr3	6.11~6.35

Figure 6.15 shows the experimental results of the workpiece hardness on the MRR. As can be seen in figure 6.15, the harder the workpiece is, the lower the MRRs are. This indicates that the MRR is inversely proportional to the hardness of workpiece, an expected result. The figure also shows when the head speed is slow, the discrepancy of MRR of these three samples is small, and this discrepancy increases with the increase of the head speed.

6.4 The effects of the hardness of polishing pads

In order to understand how the hardness of polishing pads affects the MRR in bonnet polishing of CoCr alloy. An investigation which consists of three sets of experiments was carried out. The experimental conditions were the same with “the effect of the head speed”. The polishing pads for each set of experiments were: GR35, LP66 and LP13 and their Shore hardness was 90, 78 and 66 respectively.

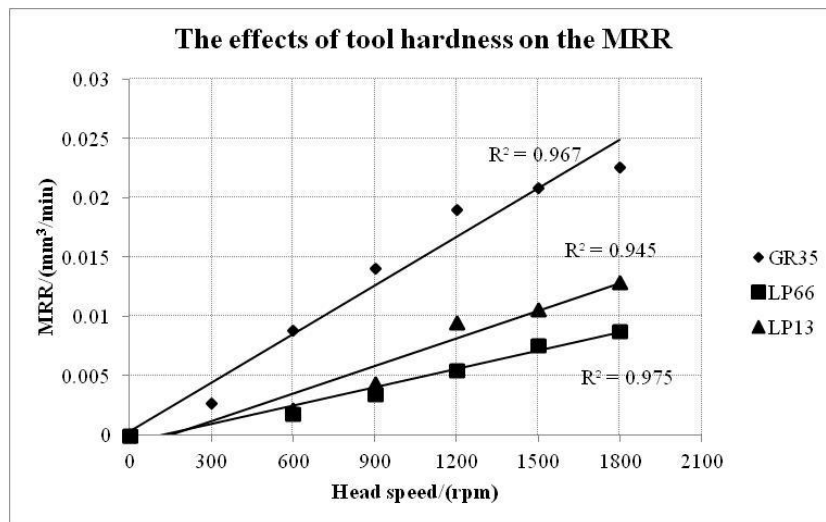


Figure 6.16: The effects of tool hardness on the MRR

Figure 6.16 shows the effects of tool hardness on the MRR. As shown in figure 6.16, at the same head speed, the MRR of GR35 is always higher than LP66 and LP13; when the head speed is at 600rpm and 900rpm, the MRRs of LP66 and LP13 are nearly the same; when the head speed is higher than 1200rpm, the MRR of LP13 is a slightly higher than LP66. The

experimental results indicate that the harder the polishing pads, the higher the MRR. In addition, the fillers of polishing pad can also affect the MRR. GR35 and LP13 are filled with zirconium oxide; LP66 is filled with cerium oxide. The hardness of zirconium oxide is higher than cerium oxide.

6.5 The effects of process parameters on polishing forces

To further understand material removal mechanisms for the bonnet polishing of CoCr alloys, several experiments were carried out to investigate the relationship between the process parameters and polishing forces. In the previous investigation, it was established that the precess angle and tool offset greatly affected the width and maximal depth of the influence function while the head speed affected the maximal depth of the influence function but had only a slight influence on the width of the influence function. The tool air pressure had a small effect on both the width and maximal depth of the influence function. From the material removal rate point of view, precess angle, head speed and tool offset had obvious effects on MRR but the tool air pressure had little effect on MRR. How the above mentioned process factors affect the influence function and the MRR is still not very clear. The aim of this investigation was to find what kinds of force (normal force or tangential force) affects the influence function during bonnet polishing of the CoCr specimens. The experiments were carried out on the Zeeko IRP200 polishing machine. A special fixture was designed to fix the force sensor (figure 6.17). The slurry used in the experiments was $3\mu\text{m}$ alumina whose specific gravity was 1.025 and the samples used in this investigation were the same with the section 6.2.

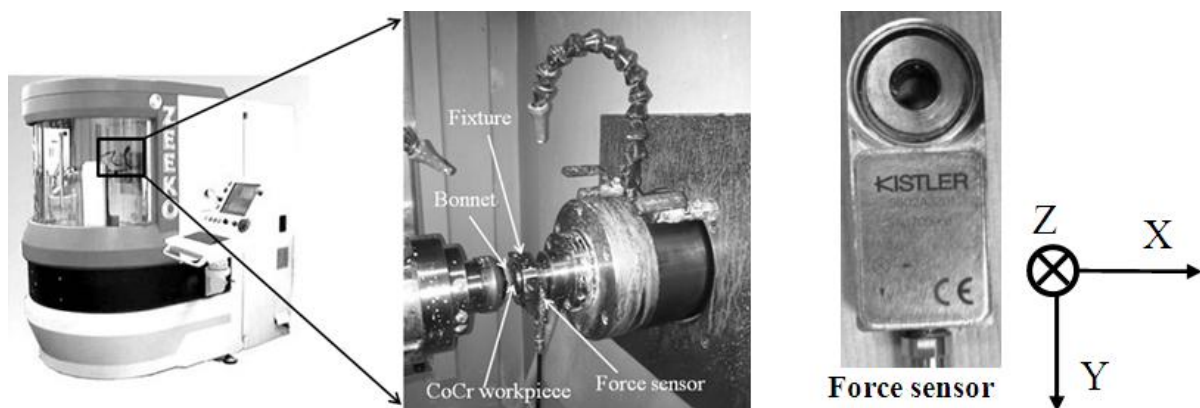


Figure 6.17: Experimental setup with force sensor

6.5.1 Calibration of force sensor

The force sensor produces an analogue signal, therefore it needs to be calibrated so that the relationship between voltage and force can be calculated. The force sensor and sample must be in the same condition during the calibration and the following experiments. After the sample and sensor were fixed, they could not be dismantled. For calibration, dead mass method in the three direction of the sensor was used (F_x , F_y and F_z , figure 6.17). A 0.5kg mass was used in the first calibration and then increased to 2.5kg with increment of 0.5kg. The data collected is shown in figure 6.18. As can be seen in this figure, when the weight of one axis direction (for example, X-axis) was increased, only the relevant voltage of this axis increases and the other two were kept nearly constant. This result means that the calibration results are stable. The calibration results are shown in figure 6.19. The relationship between voltage and three directions of force are given in follows.

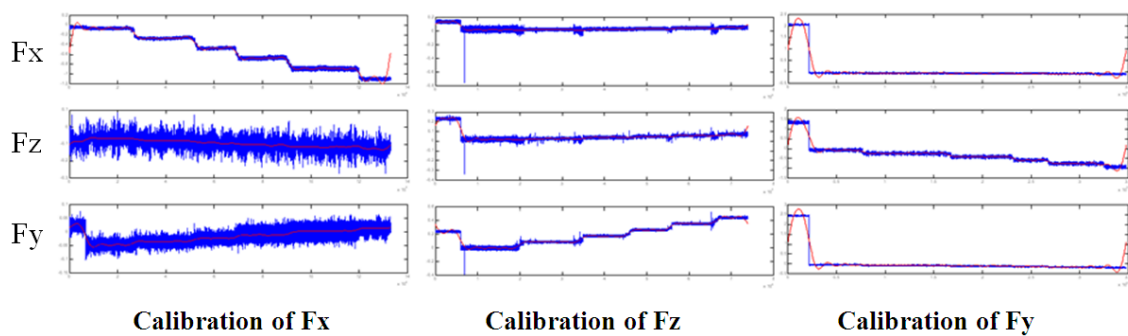


Figure 6.18: The data collection

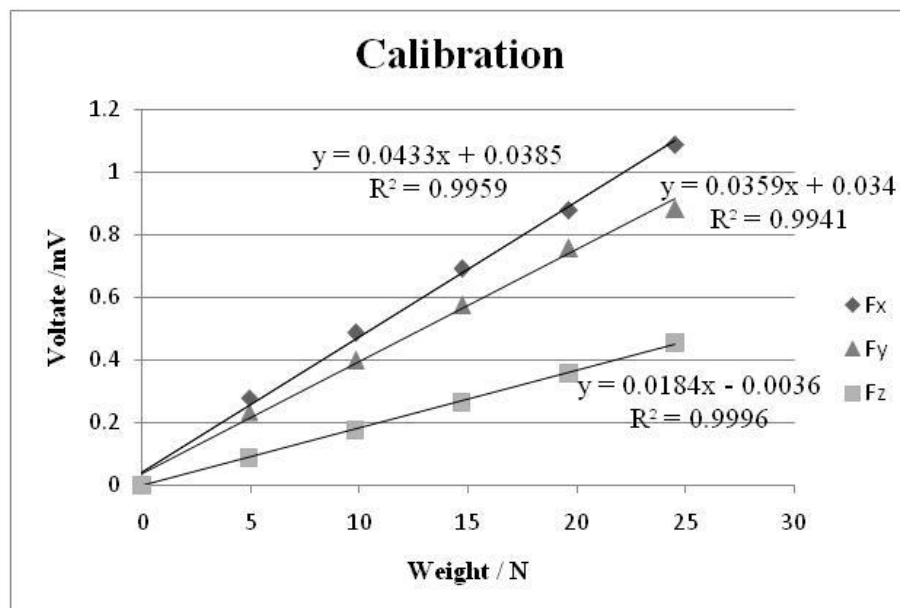


Figure 6.19: Calibration results

$$F_x = 43.3 \text{ mV/N}$$

$$F_y = 35.9 \text{ mV/N}$$

$$F_z = 18.4 \text{ mV/N}$$

6.5.2 Force acquisition

A Labview interface was designed to acquire F_x , F_y and F_z force signal simultaneously (figure 6.20). The output signal displayed on the Labview was voltage which was proportional to the force acting on the workpiece. The data was collecting in real time as long as the bonnet was contacting the workpiece during polishing (around 10 seconds). After data acquisition, the noise was filtered out by using a specially designed Matlab programme and then the averaged voltage was selected as the required data. Finally, the voltage signal was transferred into force units by using the calibration results.

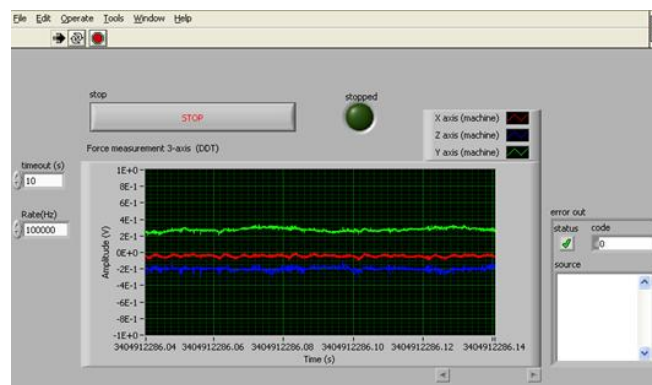


Figure 6.20: Labview interface for data acquisition

6.5.3 The variation of polishing force

During the experiments, once the workpiece materials, polishing pads and slurry were fixed the four factors (precess angle, head speed, tool offset and tool air pressure) affecting the material removal rate were analysed. When investigating one factor, the other three factors were kept constant as shown in table 6.1. Dwell time was fixed at 10s during the experiments.

(1) Precess angle

Figure 6.21 shows the polishing force as a function of the precess angle. As shown in the figure, all polishing forces F_x , F_y and F_z increase with the increase of precess angle nonlinearly. The increasing tendency of three polishing forces is nearly the same and in line with the effects of precess angle on the MRR. The increase of normal force results from the

increase of relative speed which is the result of the precess angle increase. The increase of the tangential force is due to the increase of the contact area as described in section 6.2. Figure 6.21 also shows normal force is always slightly higher than tangential force F_x and F_y which indicates that the material removal is dominated by normal force in the precess angle experiments.

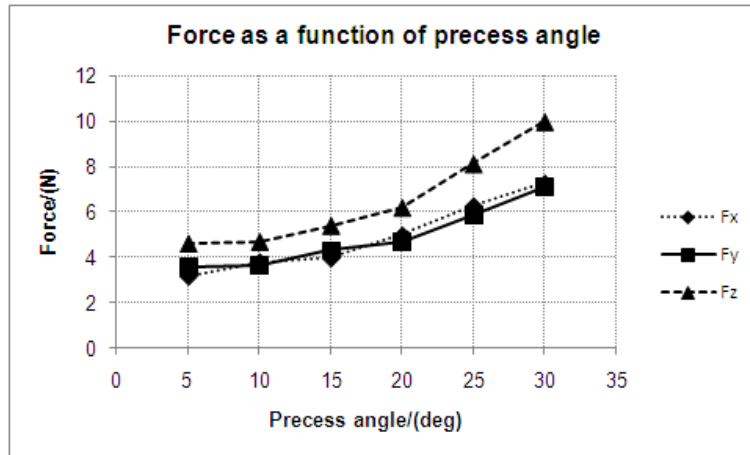


Figure 6.21: Force as a function of precess angle

(2) Head speed

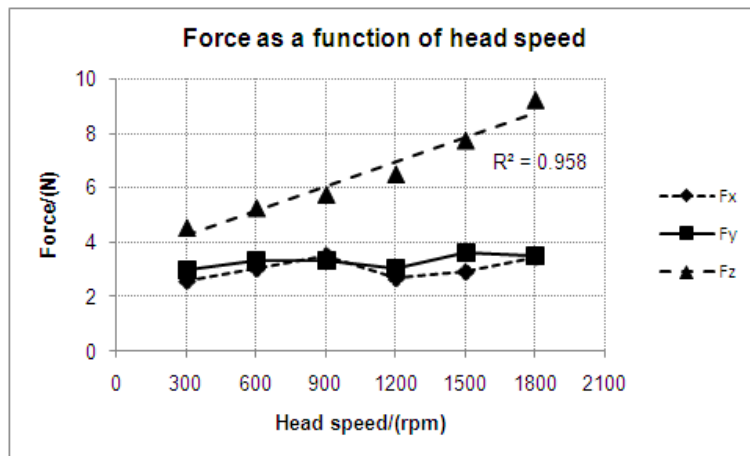


Figure 6.22: Force as a function of head speed

Figure 6.22 shows the variation of polishing forces when the head speed increased from 300rpm to 1800rpm. As shown in figure 6.22, tangential force F_x and F_y are smaller than normal force F_z . There are no apparent changes in both F_x and F_y with the increase of head speed. Normal force increases linearly when the head speed increases from 300rpm to 1800rpm. When the head speed increases, only the normal force increases while the tangential force keeps stable, implying that the increase of normal force is caused by the

increase of relative speed. The increasing tendency of normal force is in agreement with the relationship of the MRR and the head speed.

(3) Tool offset

With the above investigation, it was already shown that when the tool air pressure is 1bar, the maximal tool offset is 0.3mm. Therefore, only the polishing forces when the tool offset was smaller than 0.3mm were measured. In order to obtain more data concerning polishing forces, additional measurements of polishing force when the tool offset was 0.05mm, 0.15mm and 0.25mm were performed as well. The experimental results are given in figure 6.23. As shown in figure 6.23, all polishing forces increase linearly with the increase of the tool offset. Normal force is greater than tangential force F_x and F_y . When the tool air pressure is kept constant, the increase of the tool offset leads to an increase in contact pressure, hence the increase in normal force. The increase of tangential forces F_x and F_y probably results from the larger contacting area, because the greater the tool offset, the larger the contacting area and more abrasives go through larger contacting area during polishing which can result in more material removal and therefore larger tangential forces.

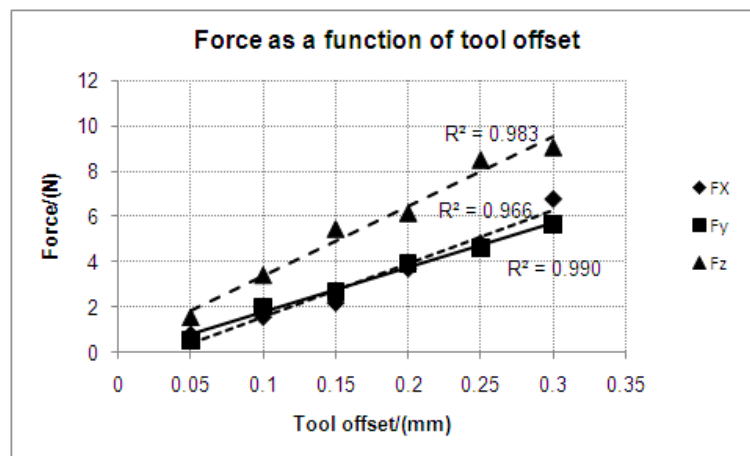


Figure 6.23: Force as a function of tool offset

(4) Tool air pressure

Figure 6.24 shows the polishing forces as function of the tool air pressure. As can be seen in figure 6.24, all polishing forces are randomly distributed between 3N and 6N when the tool air pressure varies from 0.4bar to 2.0bar. Normal force is slightly higher than tangential force F_x and F_y . When comparing the value of polishing forces, only a little discrepancy is seen during these experiments. The deviation is smaller than other experimental results which

indicates that all polishing forces have no obvious change when tool air pressure increases. The polishing force results are in agreement with the relationship of the MRR and the tool air pressure.

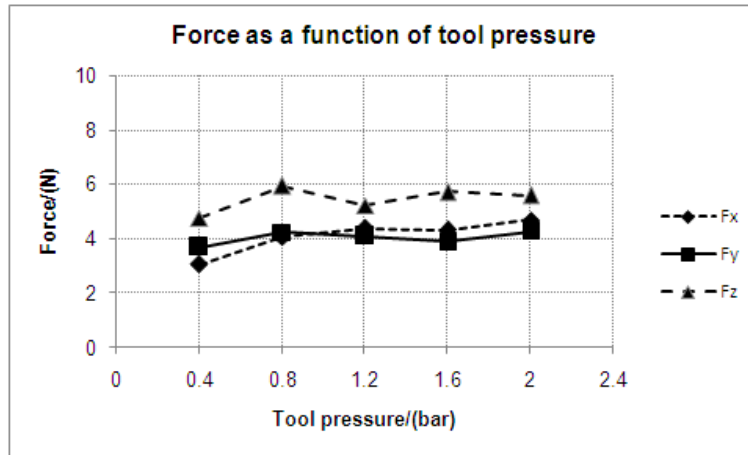


Figure 6.24: Force as a function of tool air pressure

6.6 Material removal rate modelling

This section used the above experimental data to create a material removal rate model based on the Preston equation. All Ifs are symmetrical in shape. As described in Chapter 3, the Preston equation can be expressed as follows:

$$MRR = K \times P \times V \quad (6.1)$$

Where, K is the Preston coefficient, including the effects of abrasive size and material, slurry concentration, workpiece material, polishing cloths/pads, etc; P is the contact pressure between the polishing tool and the workpiece; V represents the velocity of the polishing tool relative to the workpiece. In this section, the author used the theory of contact mechanics to build the links between the process parameters and the contact pressure P and then applied kinematics theory to establish the relationship between the process parameters and the relative velocity V .

6.6.1 Contact pressure P

In this research, the polishing tool is made up of a hollow spherical rubber tool covered with a polyurethane polishing pad (Chapter 3, section 3.2.1). When the polishing tool comes to contact the workpiece, it can be considered as an elastic deformable sphere pressed against a rigid flat (figure 6.25). In order to precisely establish the relationship of the process

parameters and the influence function, the plot of the relationship of the width W and the maximal depth h of the influence function and process parameters is shown in figure 6.26-6.29.

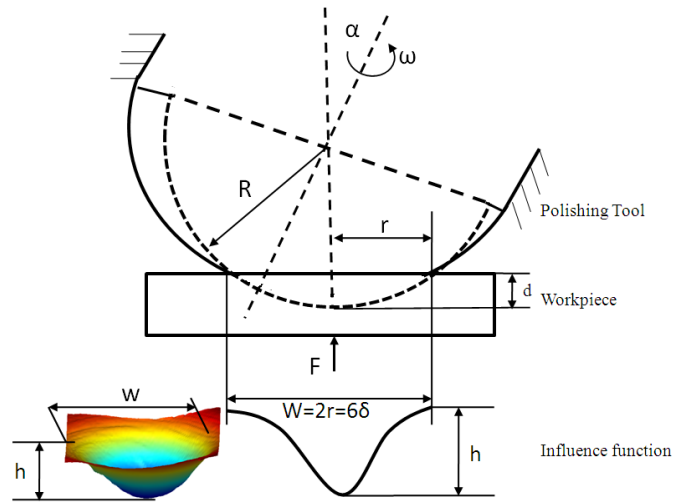


Figure 6.25: Schematic of the contact between polishing tool and workpiece

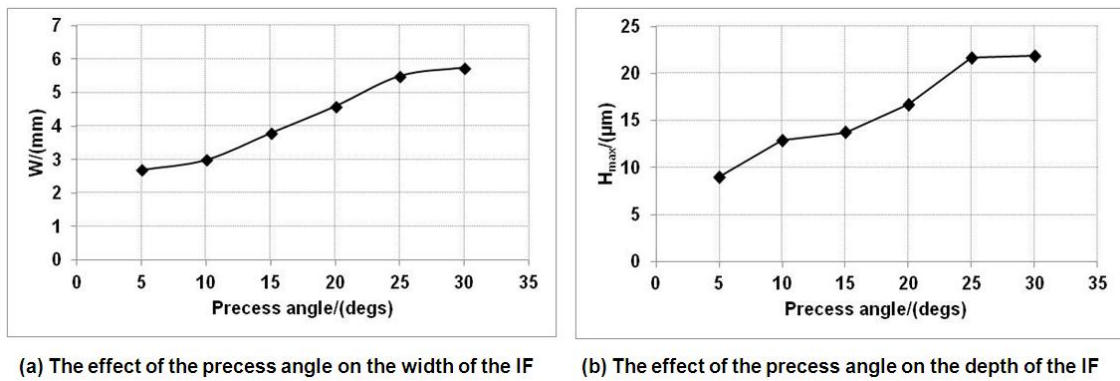


Figure 6.26: The effect of precess angle on the IF

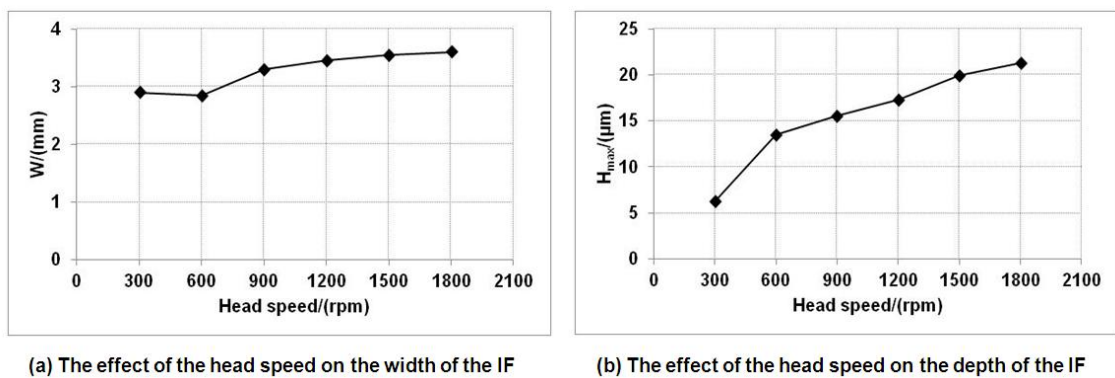
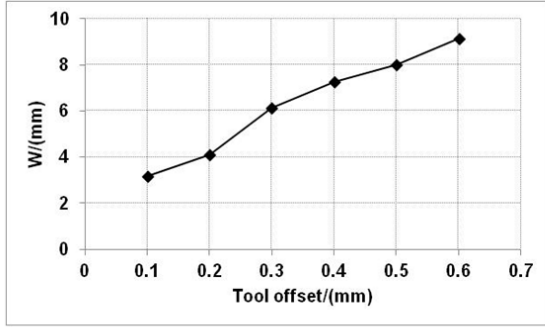
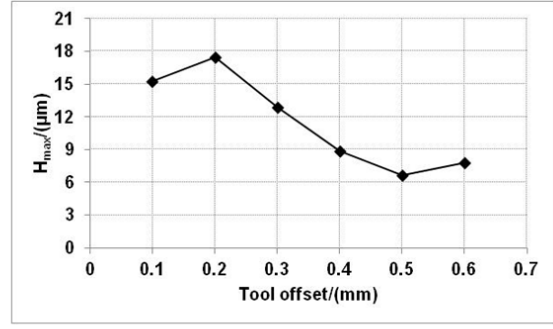


Figure 6.27: The effect of head speed on the IF

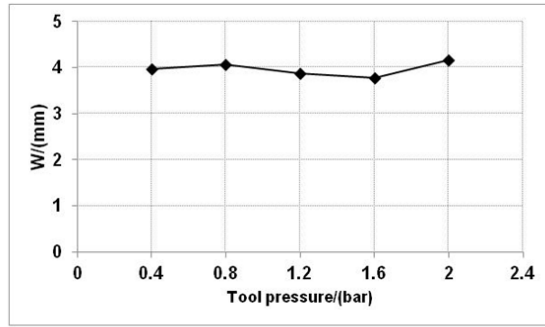


(a) The effect of the tool offset on the width of the IF

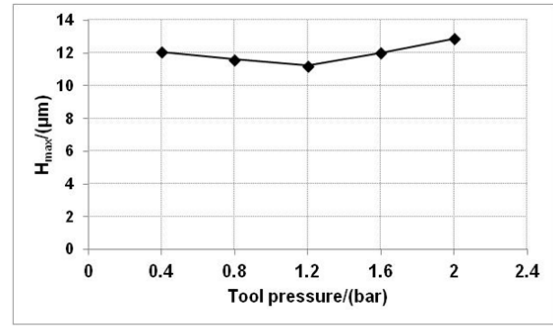


(b) The effect of the tool offset on the depth of the IF

Figure 6.28: The effect of tool offset on the IF



(a) The effect of the tool pressure on the width of the IF



(b) The effect of the tool pressure on the depth of the IF

Figure 6.29: The effect of tool air pressure on the IF

As shown in figure 6.25, when the polishing tool contacts the workpiece, the radius of the contact area r can be calculated as equation (6.2) according to Hertz solution [216].

$$r = \sqrt{Rd} \quad (6.2)$$

Where, R is the radius of the polishing tool and d is the depth of the tool offset. However, equation (6.2) is only suitable for ideally elastic contact. In this case, because the bonnet is fixed to a duralumin frame, the radius of the contact area is also highly affected by the precess angle α (figure 6.26) and slightly affected by the head speed ω (figure 6.27) and tool air pressure (figure 6.29). In order to simplify the model, the slight effects of the head speed and the tool air pressure on the width of the influence function are ignored. Therefore, equation (6.2) can be modified as:

$$r = P_a(\alpha) \times \sqrt{Rd} \quad (6.3)$$

Where, $P_a(\alpha)$ is the effect of the precess angle on the width of influence function and can be deduced by regression analysis using figure 6.26 and figure 6.28.

$$P_a(\alpha) = -2 \times 10^{-6} \alpha^4 + 5 \times 10^{-5} \alpha^3 + 0.002 \alpha^2 - 0.016 \alpha + 0.777 \quad (R^2 = 0.999) \quad (6.4)$$

So, the contact area A can be expressed as:

$$A = \pi r^2 = \pi P_a^2(\alpha) R d \quad (6.5)$$

Again, according to the Hertz solution when the polishing tool contacts the workpiece, the contact load F is given by:

$$F = \frac{4}{3} E R^{1/2} d^{3/2} \quad (6.6)$$

Where, E is the Hertz elastic modulus and can be defined as:

$$E = \left(\frac{1-\nu_1^2}{E_1} + \frac{1-\nu_2^2}{E_2} \right)^{-1} \quad (6.7)$$

Where, E_1 , E_2 , ν_1 , ν_2 are Young's moduli and Poisson's ratios of the polishing tool and the workpiece, respectively. As discussed in section 6.2.4, when the tool offset is increased, the bonnet polishing tool presents a warping phenomenon. The inception of warping point d_c can be calculated by:

$$d_c = \left(\frac{\pi m H}{2E} \right)^2 R \quad (6.8)$$

Where, H is the hardness of the polishing tool related to the tool air pressure and m is the hardness coefficient. The onset of warping is changeable with the variation of the tool air pressure.

Substitute equation (6.8) into equation (6.6), gives:

$$F = \frac{2}{3} \pi m H R d^{3/2} d_c^{-1/2} \quad (6.9)$$

Therefore the contact pressure P between the polishing tool and the workpiece is given by:

$$P = \frac{F}{A} = \frac{\frac{2}{3} \pi m H R d^{3/2} d_c^{-1/2}}{\pi P_a^2(\alpha) R d} = \frac{2}{3} m H d^{1/2} P_a^{-2}(\alpha) d_c^{-1/2} \quad (6.10)$$

If the radius of the polishing tool is 20mm, when the tool air pressure is greater than 1.5bar, $d_c=0.2\text{mm}$; when the tool air pressure is less than 1.5bar, $d_c=0.3\text{mm}$.

6.6.2 Relative velocity V

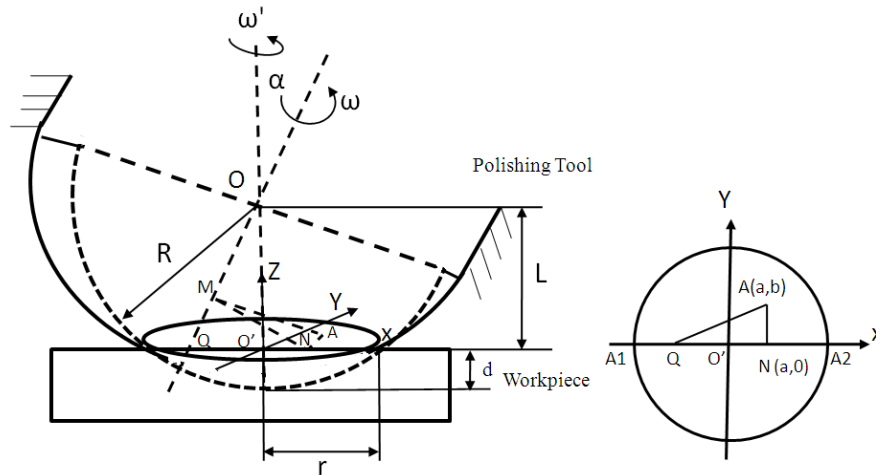


Figure 6.30: Schematic of velocity distribution

Figure 6.29 schematically shows the details of the velocity distribution of a random point $A(a, b)$ ($a^2 + b^2 \leq r^2$) in the contact area when the polishing tool is rotating with the speed of ω . As shown in the figure 6.29, O is the centre of the polishing tool, O' is the centre of contact area, OQ is the centre line of polishing tool and Q is in the contact area. Therefore,

$$|OQ| = (R - d) / \cos \alpha \quad (6.11)$$

Then,

$$|QO'| = |OQ| \sin \alpha = (R - d) \tan \alpha \quad (6.12)$$

And,

$$|QN| = (R - d) \tan \alpha + a \quad (6.13)$$

Also,

$$|MN| = |QN| \cos \alpha = [(R - d) \tan \alpha + a] \cos \alpha \quad (6.14)$$

So in the triangle ΔMNA ,

$$|MN|^2 + |NA|^2 = |MA|^2 \quad (6.15)$$

So,

$$|MA| = \sqrt{a^2 \cos^2 \alpha + 2a(R-d) \sin \alpha \cdot \cos \alpha + (R-d)^2 \sin^2 \alpha + b^2} \quad (6.16)$$

Therefore, the relative velocity V can be expressed as follows:

$$V = \omega \cdot |MA| = \omega \cdot \sqrt{a^2 \cos^2 \alpha + 2a(R-d) \sin \alpha \cdot \cos \alpha + (R-d)^2 \sin^2 \alpha + b^2} \quad (6.17)$$

When $a=0$, $b=0$, the average of the contact area can be obtained as:

$$V = \omega \cdot (R-d) \cdot \sin \alpha \quad (6.18)$$

During the polishing process, the polishing tool moves in a precession mode which means the polishing tool is rotating as well as revolving around OO' with the speed of ω' . However, the revolution speed is very slow compared with the rotating speed. The effects of revolution on material removal rate can be neglected. The revolution only affects the shape of the influence function, creating the rotationally symmetrically Gaussian shape.

So the Preston equation can be reconstituted as:

$$MRR = KPV = \frac{2}{3} KmH \omega d^{1/2} P_a^{-2}(\alpha) d_c^{-1/2} \cdot (R-d) \cdot \sin \alpha \quad (6.19)$$

As shown in figure 6.29, the effect of the tool air pressure on the width and the maximal depth of the influence function, and the MRR are very slight. Hence, mH in equation (6.19) can be considered as a constant and combined into the Preston coefficient K . Therefore, the final MRR model can be expressed as:

$$MRR = \frac{2}{3} \underbrace{K}_{term1} \cdot \underbrace{\omega}_{term2} \cdot \underbrace{d^{1/2} \cdot d_c^{-1/2} \cdot (R-d)}_{term3} \cdot \underbrace{\frac{\sin \alpha}{(-2 \times 10^{-6} \alpha^4 + 5 \times 10^{-5} \alpha^3 + 0.002 \alpha^2 - 0.016 \alpha + 0.777)^2}}_{term4} \quad (6.20)$$

In equation (6.20), term 1 represents the modified Preston coefficient, including the effects of abrasive size and material, slurry concentration, workpiece material, polishing cloths/pads and the tool air pressure. The value of K can be experimentally determined.

Term 2 describes the effect of the head speed, which indicates MRR is linearly proportional to the head speed and is in agreement with experimental results as well as the Preston equation.

Term 3 depicts the effect of the tool offset on MRR. When the tool air pressure is less than 1.5bar, d_c is 0.3mm, which means the value of the tool offset d should not be greater than 0.3mm; when the tool air pressure is greater than 1.5bar, d_c is 0.2mm, which indicates that in this case the value of the tool offset d should not be greater than 0.2mm.

Term 4 gives the effects of the precess angle on the MRR. As can be seen in equation (6.20), the MRR increases non-linearly with the increase of the precess angle, which is in agreement with the experimental results.

6.6.3 Verification of the model

Table 6.2: The machine settings for verification experiments

Factors	Precess angle	Head speed	Tool offset	Tool air pressure	Dwell time
Value	8degs	1000rpm	0.12mm	1bar	240s

Table 6.3: Preston coefficient for different materials

Material	Preston Coefficient	Comments
Cobalt chrome (CoCr)	$3.74 \times 10^{-7} \text{ mm}^2/\text{N}$	The authors' calculated value, diamond abrasives with polyurethane pad
Copper	$2.5 \times 10^{-7} \text{ mm}^2/\text{N}$	From Ref [217], silica abrasives with wafer-pad
Hardened steel	$7.59 \times 10^{-7} \text{ mm}^2/\text{N}$	From Ref [218], diamond abrasives with cast iron lapping tool
Borosilicate (BK7)	$8.3 \times 10^{-7} \text{ mm}^2/\text{N}$	From Ref [219], CeO_2 abrasives with polyurethane pad
Fused silica (FS)	$3.3 \times 10^{-7} \text{ mm}^2/\text{N}$	From Ref [220], CeO_2 abrasives with polyurethane pad

In order to confirm the viability of the created model, four sets of experiments were performed to verify the role of precess angle, head speed, tool offset and tool air pressure respectively. The machine settings are shown in table 6.2. The polishing medium was a GR35 polishing pad with $1\mu\text{m}$ diamond slurry whose specific gravity was 1.024. The workpieces were 23mm diameter and 8mm high cylinders of CoCr alloy (F75), of the same material as used in section 6.2. The Preston coefficient calculated from the above polishing medium and workpiece material is shown in table 6.3. To further verify the model, other Preston coefficients for polishing optics and metallic materials are taken from literature and given in table 6.3. The experimental results and the calculated results based on the proposed model

using different Preston coefficients are given in figure 6.31. As illustrated in the figure, the trends of predicted data are well in agreement with the experimental data, which would imply the created model can be used within this range of machine settings to predict the MRR in bonnet polishing of CoCr alloys. In figure 6.31(d), the increase in MRR is thought to result from the decrease of d_c due to the tool air pressure exceeding 1.5bar.

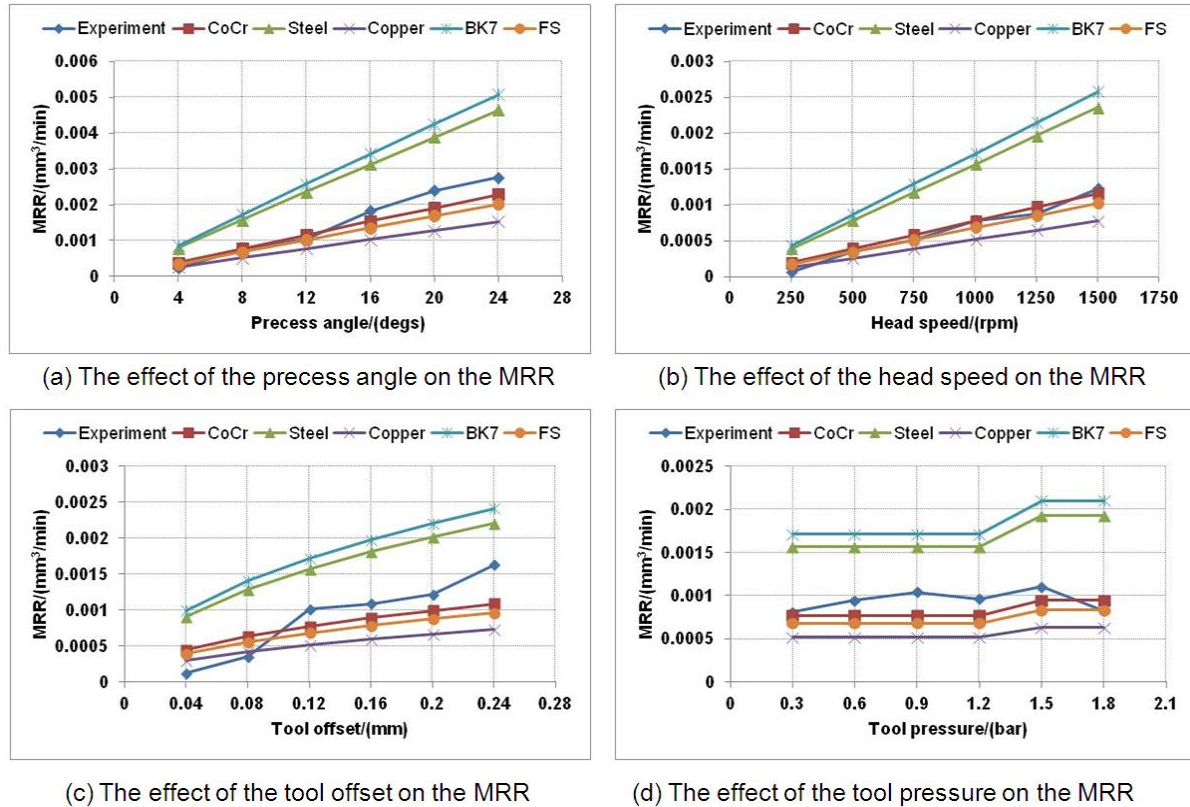


Figure 6.31: The comparison of experimental data and predicted data

6.7 Summary

This chapter has further investigated the material removal in bonnet polishing of CoCr alloys, including the effects of the process parameters on the material removal, the effects of the workpiece hardness and the polishing pad hardness on material removal, the effects of the process parameters on polishing forces and material removal rate modelling.

In section 6.2, the effects of the process parameters on material removal have been experimentally studied. The investigation results indicate that the width of the influence function increases with the increase of both precess angle and tool offset; the depth of the influence function increases with the increase of the head speed, increases first and then decreases with the increase of the tool offset. The MRR increases with an increase in precess

angle non-linearly, with the increase of the head speed linearly, and increases first then decreases with the increase of the tool offset because of the bonnet distortion. The tool air pressure has only a slight effect on the influence function. However, the tool air pressure can affect the optimal depth of the tool offset. If the tool air pressure is less than 1.5bar, the tool offset should be less than 0.3mm; if the tool air pressure is greater than 1.5bar, the tool offset should be less than 0.2mm.

Section 6.3 and 6.4 investigates the effects of workpiece hardness and polishing pad hardness on the MRR. The MRR is inversely proportional to the hardness of the workpiece but proportional to the hardness of polishing pads. The results indicate that higher MRR can be achieved by using harder polishing pads.

Section 6.5 studies the effects of the process parameters on polishing forces. The following results can be concluded during the investigation: normal force F_z is always greater than tangential force F_x and F_y and the tangential force F_x and F_y are always nearly the same; the effect of the precess angle on polishing force has nearly the same increasing tendency with the change of the MRR; normal force F_z increases linearly with the increase in head speed but tangential force F_x and F_y shows no change; all polishing forces increase almost linearly when the tool offset increases and all polishing forces show little change in tool air pressure experiments. In addition, through comparing all experimental data it would seem normal force has a significant effect on the maximal depth of the influence function while the tangential forces seem to dominate the width of the influence function, and both normal force and tangential force can contribute to the MRR.

On the basis of experimental data and the theory of contact mechanics, an MRR model resulting from the Preston equation has been created in section 6.6. The contact pressure was deduced by using a Hertz solution and the relative velocity was derived by the kinematics theory. The final MRR model is a function of the modified Preston coefficient, precess angle, head speed and tool offset. The created model has been verified by the experiments. The predicted results are in good agreement with the experimental results, which indicate the model can be used to predict the MRR in bonnet polishing under the conditions used here.

7. FORM CORRECTION

7.1 Introduction

With the introduction of CNC controlled technology, ultra-precision polishing is not only capable of the improvement of surface roughness but also capable of form correction. Form correction, also called corrective polishing, is usually achieved by dwell time control, namely, when the polishing tool dwells longer on the workpiece, more material on the local zone of the workpiece will be removed. The critical process of form correction is the application of the designed surface, the created influence function and the error map to calculate the dwell time map. The dwell time map is then translated into CNC code to control the polishing process. The designed surface can be plane, sphere, asphere, or freeform and convex or concave. The influence function can be obtained by practical polishing or by a model based on the experimental data. The error map is usually obtained by the subtraction of the surface of the component to be corrected away from the desired surface. The interface of the form correction process used in this investigation is displayed in figure 7.1.

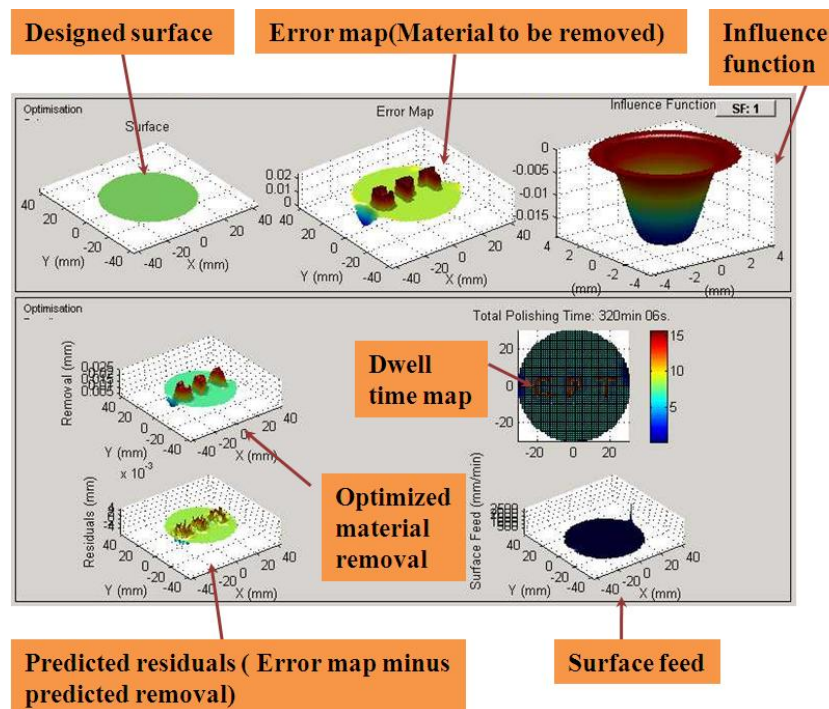


Figure 7.1: The interface of form correction process

This chapter performed a series of studies related to the form correction, including the effect of the tool path on the form correction, polishing of a multi-radius femoral head of a hip prosthesis and polishing of a freeform knee femoral component. The workpiece material for

the effect of the tool path on the form correction and CPT letters polishing was polycrystalline copper; for the multi-radius femoral head polishing and the freeform knee femoral component polishing were CoCr alloys.

7.2 The effect of the tool path on form correction

7.2.1 Tool path

Tool path is a series of movement trajectories on the surface of a machined workpiece made by a polishing tool. The basic demand for a polishing tool path should be that the polished surface is able to be completely covered during a machining cycle. Over the decades, many tool paths have been developed: raster path, spiral path [221], Hilbert path [222], Peano path [223], Lissajous path [222], etc (figure 7.2). Two of the most commonly used tool paths are raster path and spiral path. In this section, the author has investigated the effects of the raster path and the spiral path tool movements on surface roughness and form error. The workpieces polished in the experiments were two polycrystalline copper specimens, both of which were 65mm diameter and one was 12mm thick (for raster path) and the other was 8mm thick (for spiral path). The polishing medium was 3 μ m diamond with GR35 polyurethane. The polishing parameters are displayed in table 7.1 according to the previous investigation results.

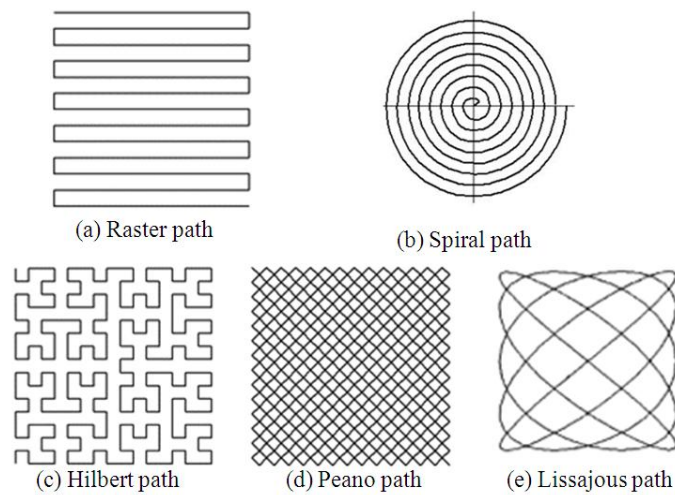


Figure 7.2: Polishing tool path

Table 7.1: Process parameters for tool path investigation

Parameters	Precess angle	Head speed	Tool offset	Tool air pressure
Values	15degs	1800rpm	0.2mm	1.0bar

7.2.2 Raster polishing

In raster path polishing (also known as scanning path or zigzag path) the polishing tool moves backward and forward to travel across the surface of a workpiece with a specific spacing size between the adjacent paths (figure 7.2(a)). The algorithms for raster polishing are simple comparing to other tool paths. Tam et al. [224] depicted an algorithm for raster tool path in detail. In this study, both x, y spacing size were set as 1mm. In the present work, both raster polishing and spiral polishing used the same influence function whose MRR was $0.172\text{mm}^3/\text{min}$ (figure 7.3). Before polishing, the surface roughness of the workpiece was $0.3\mu\text{m}$ Ra (figure 7.4) and the form error was $12.9\mu\text{m}$ PV (peak to valley) and $2.73\mu\text{m}$ RMS (root mean square) (figure 7.5).

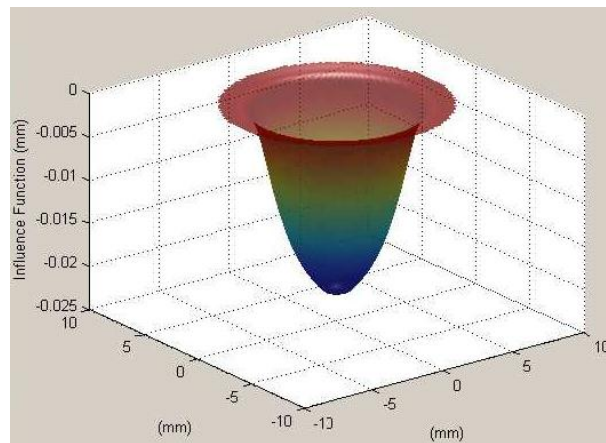


Figure 7.3: Influence function for tool path investigation

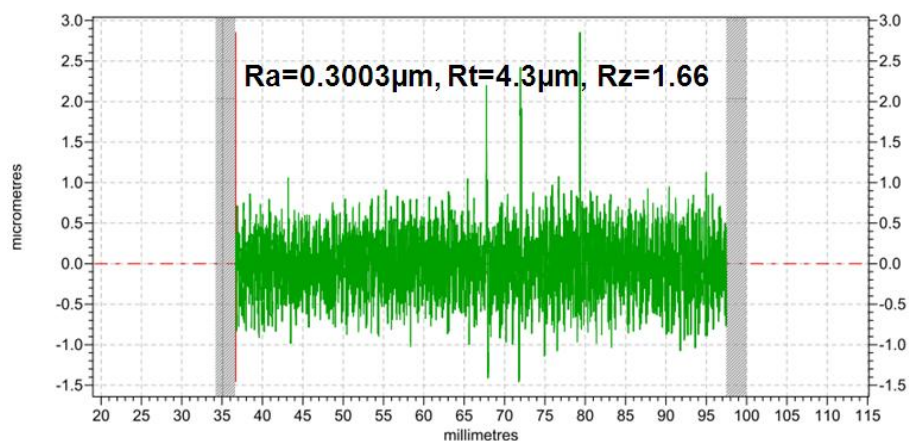


Figure 7.4: Surface roughness of 12mm thick copper before polishing

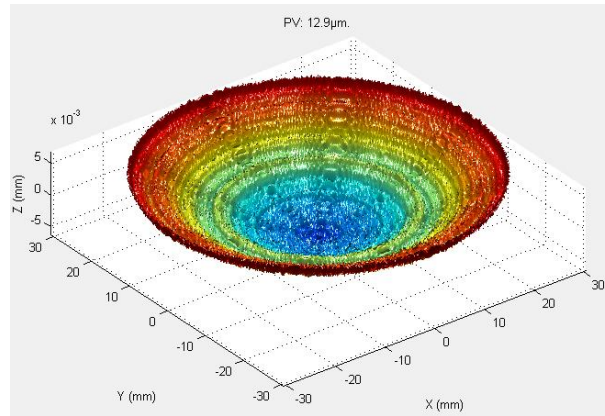


Figure 7.5: Form error of 12mm thick copper before polishing

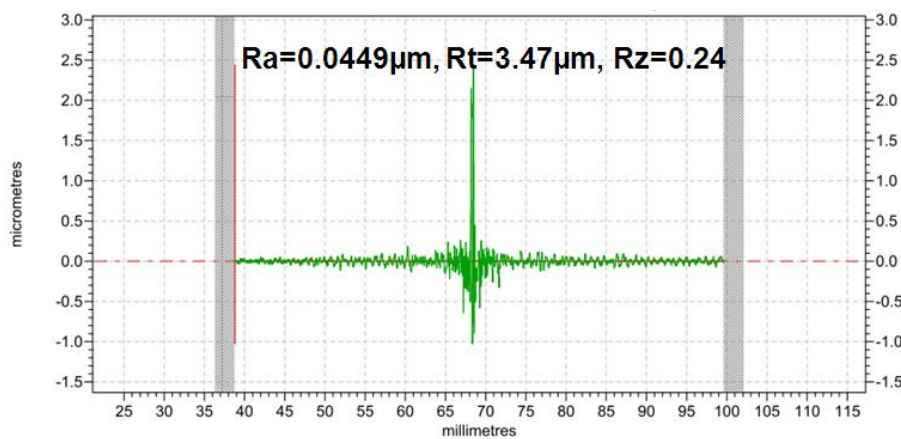


Figure 7.6: Surface roughness of 12mm thick copper after the first diamond polishing

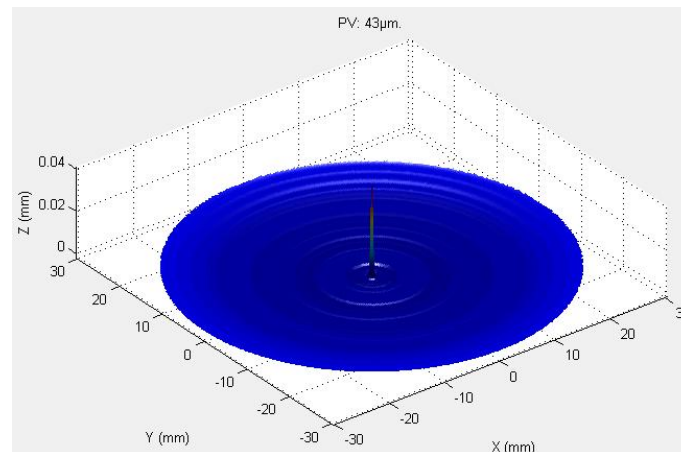


Figure 7.7: Form error of 12mm thick copper after the first diamond polishing

After first polishing, the surface roughness and form error are shown in figure 7.6 and figure 7.7 respectively. The surface roughness was reduced to 44.9nm but form error of PV value was increased to 43μm and RMS value was decreased to 1.38 μm because a small peak left by turning was not removed during polishing.

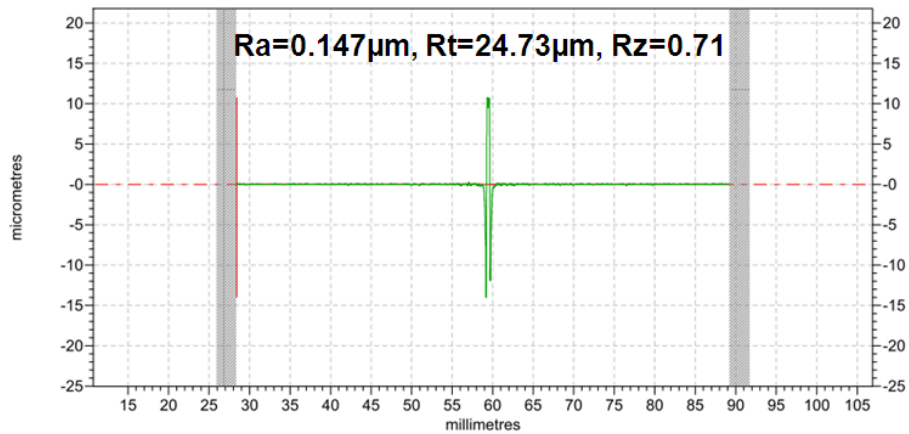


Figure 7.8: Surface roughness of 12mm copper after second diamond polishing

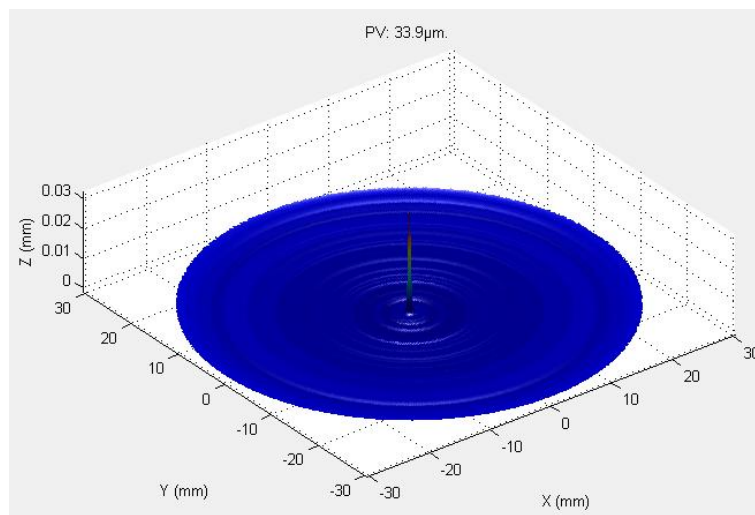


Figure 7.9: Form error of 12mm thick copper after second diamond polishing

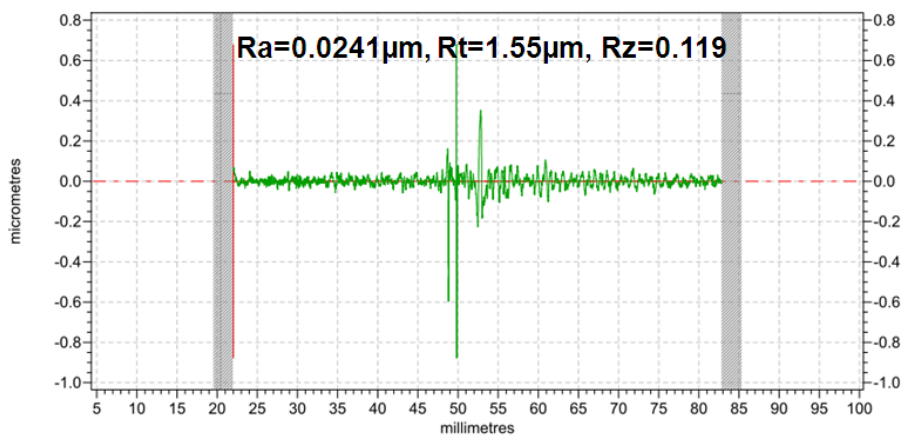


Figure 7.10: Surface roughness of 12mm thick copper after third diamond polishing

The results of the second diamond polishing for 12mm thick copper are shown in figure 7.8 and figure 7.9. The results indicate that this polishing could not remove the central peak

effectively which led to the increase in surface roughness ($R_a=0.147\mu\text{m}$) comparing to the last polishing. Form error only decreased slightly to $33.9\mu\text{m PV}$ and $0.74\mu\text{m RMS}$.

In order to remove the peak in the centre of the workpiece, the third diamond polishing was carried out. The surface roughness was reduced to $R_a 24.1\text{nm}$ (figure 7.10) and form error was decreased to $11.75\mu\text{m PV}$ and $0.08\mu\text{m RMS}$ (figure 7.11) but the central peak were still not completely removed.

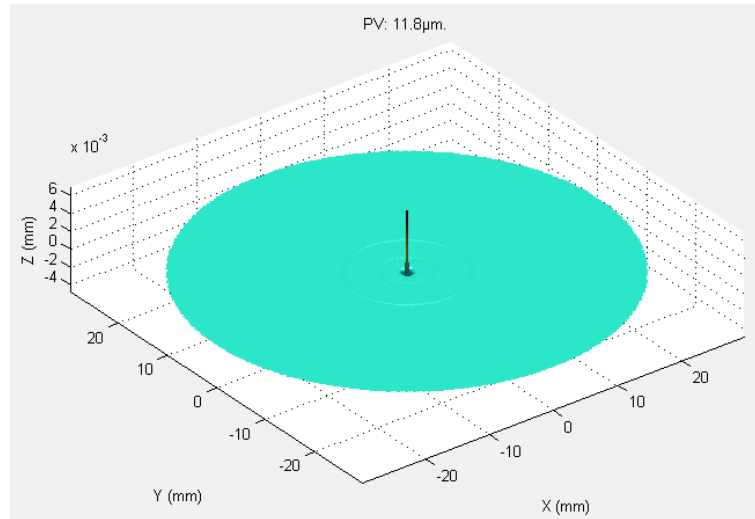


Figure 7.11: Form error of 12mm thick copper after third diamond polishing

7.2.3 Spiral polishing

In spiral path the polishing tool starts at the centre of workpieces and moves outwards spirally toward the edge of the workpieces or vice versa (figure 7.1 (b)). Spiral path is especially suitable for rotationally- symmetric workpieces. The basic algorithm for the spiral path can be described as follows [225]:

$$P_i = (P_{i-1}^2 + \frac{L \cdot S}{2\pi})^{1/2};$$

$$\theta_i = \theta_{i-1} + \frac{2L}{P_i + P_{i-1}};$$

$$\text{If } K = 1, R_i = P_i;$$

$$\text{If } K \neq 1, R_i = \frac{P_i}{(K^2 \sin^2 \theta_i + \cos^2 \theta_i)^{1/2}};$$

$$X_i = R_i \cdot \cos \theta_i;$$

$$Y_i = R_i \cdot \sin \theta_i;$$

Where, S is the path separation (“+” for spiral out and “-” for spiral in);

L is the length of each path step;

P_i is the radial position for the i th point on a circular spiral;

θ_i is the angular position for the i th point on the spiral;

K is ratio of the major radius to the minor radius for ellipse;

R_i is the radial position for the i th point on the spiral;

X_i and Y_i are the coordinates of the i th point on the elliptical spiral with the major axis of ellipse along the X axis.

In this investigation, the spacing of the tool path was 1mm. Before polishing, the 8mm thick copper’s surface roughness was $0.306\mu\text{m}$ Ra and form error was $34.9\mu\text{m}$ PV and $33.7\mu\text{m}$ RMS shown in figure 7.12 and figure 7.13.

After first diamond polishing, both surface roughness and form error were reduced greatly (figure 7.14 and figure 7.15). The surface roughness was decreased to 30.2nm Ra and form error was $15.9\mu\text{m}$ PV and $1.38\mu\text{m}$ RMS. But similar to raster polishing, the central peak left by turning was still not removed.

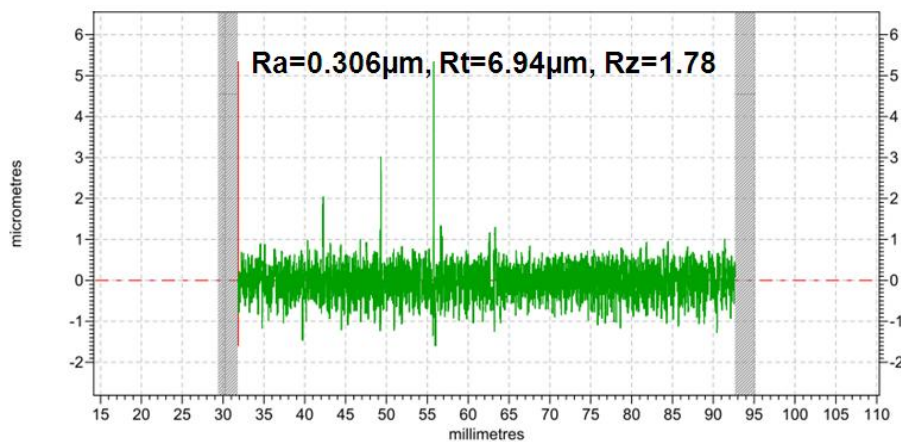


Figure 7.12: Surface roughness of 8mm thick copper before polishing

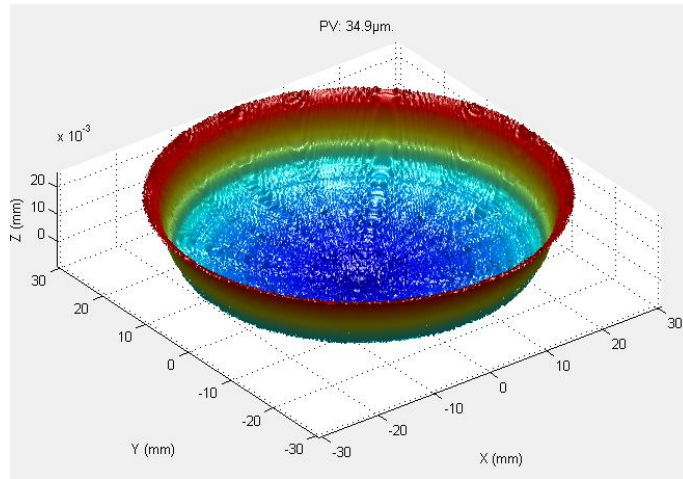


Figure 7.13: Form error of 8mm thick copper before polishing

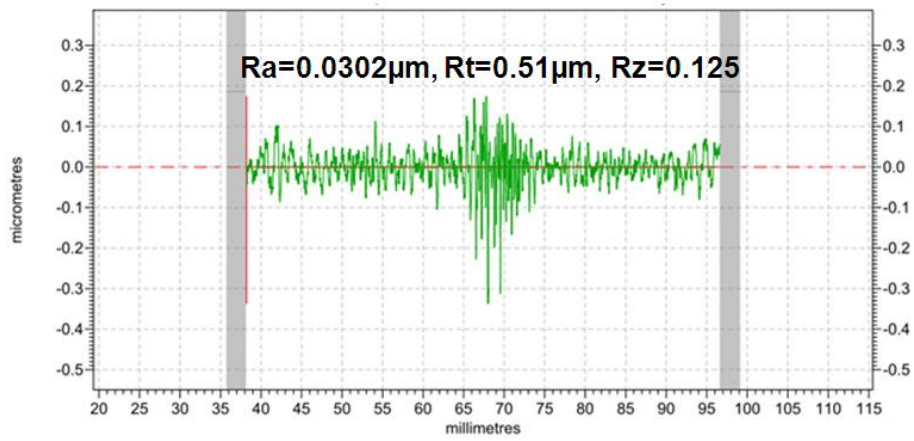


Figure 7.14: Surface roughness of 8mm thick copper after first polishing

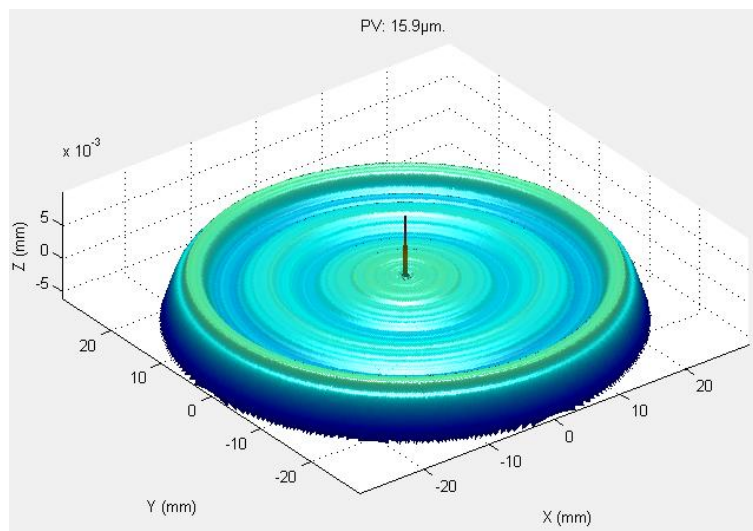


Figure 7.15: Form error of 8mm thick copper after first polishing

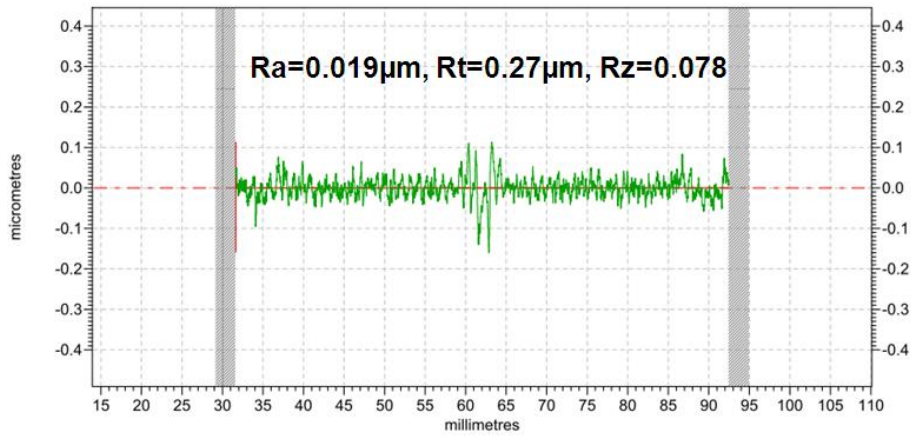


Figure 7.16: Surface roughness of 8mm thick copper after second polishing

To further improve the surface quality of the copper, the second diamond polishing was carried out. The experimental results are shown in figure 7.16 and figure 7.17. The surface roughness was 19.4nm Ra and form error was 4.84µm PV and 1.43µm RMS. The peak in the centre was completely removed after the second diamond spiral polishing.

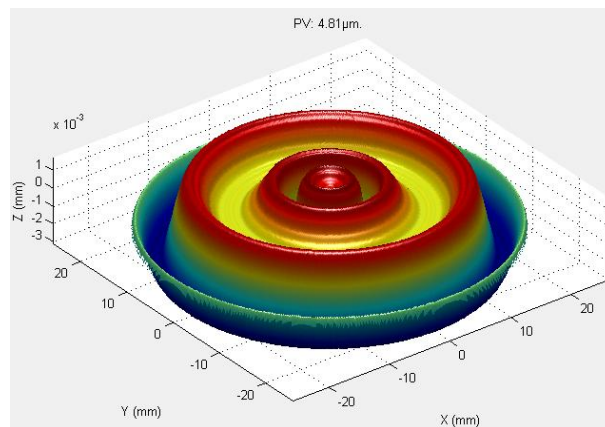


Figure 7.17: Form error of 8mm thick copper after second polishing



Figure 7.18: The copper before polishing (left) and after polishing (right)

The experimental results show that both raster path and spiral path can effectively improve the surface quality of a workpiece. However, they are suitable for different shapes of the workpiece. For rotationally-symmetric workpieces, spiral path is better while for non-rotationally-symmetric or free-form surface workpieces, raster path is more useful. In order to precisely correct the form error, it is better to use 3D error map which is measured by interferometers or stylus instruments (the stylus instrument can only measure the squared workpieces or part of the circular workpieces). But for spiral polishing, the profile of a workpiece can be applied to create a 3D error map which will save a lot of time in measurement. In addition, if the spacing size of the tool path is too large (for example 2mm) the trajectory of the tool path can be clearly seen on the surface. Therefore, for final polishing the spacing size should be as small as possible. But the selection of the spacing size should also consider the polishing time. Generally, the smaller the spacing size, the longer the polishing time. The copper photographs before and after polishing are shown in figure 7.18.

7.3 Polishing of multi-radius femoral head of hip prostheses

As the gold standard combination of the THR MoP has been found to produce large numbers of polyethylenes wear particles and debris which have been found to be fundamental in the premature failure of hip prostheses [36]. As a result, MoM hip replacement has been introduced to avoid the polyethylene wear particles [226]. Compared to the MoP THR's, MoM prostheses can significantly improve the lifespan of hip implants, but they produce a huge number of nanometre size of wear particles, resulting in the patients with higher levels of metal ions in the serum, urine and red blood cells which may cause hypersensitivity, tissue toxicity or carcinogenesis [227-229]. This is especially severe in the initial phase of running-in or bedding-in for the current spherical femoral head against a hemispherical acetabular cup [230]. After the running-in wear phase, there is a lower wear rate phase called steady-state phase. In this phase, the two bearing surfaces of hip implants have been modified to form the more conforming bearing surfaces within the worn area [231]. It is reported that the conformity of the worn geometry is more favourable to fluid film lubrication, which indicates that the current spherical bearings are not optimal for MoM hip implants [232]. Therefore, a new geometrical design of bearing surface, termed multi-radius, also called aspherical or non-spherical femoral head, has been introduced [10, 11]. The new design of MoM hip implant has a radius of curvature in the articulating zone larger than the radius of curvature elsewhere. Such a multi-radius geometry design has been demonstrated to generate extremely low wear

rates and minimise the release of metal ions due to the better lubrication performance compared with the typical single radius bearing surface [233].

In this investigation, the form correction of bonnet polishing to manufacture an R19mm multi-radius femoral head through changing the radius of the articulating zone of an R18mm single radius femoral head is reported. By using this technology, it is possible to obtain an improved clearance between femoral head and acetabular cup for MoM hip implants, where clearance has been identified as a key factor affecting the lubrication performance [234]. The workpiece material was CoCr alloy which is the most widespread material in artificial implants. The polishing medium was 3 μ m alumina slurry with GR35 polyurethane.

7.3.1 Experimental procedure

In this investigation, form correction to remove the undesired material in the articulating zone is applied to a basic spherical component. When using the form correction, it is critical to establish the influence function and the amount of material removal to calculate the dwell time function and then translate this into a feed-rate for the process control. In order to match the practical polishing as close as possible, the influence function should polish on a surface which has the similar form and material to the desired workpiece to be corrected. The workpiece for the influence function polishing was a spherical CoCr alloy femoral head with a 16mm radius. Based on the principle of higher material removal rate, the values of process parameters were set as table 7.2. Figure 7.19 displays the polished influence function. This influence function is Gaussian shape with a 0.083mm³/min material removal rate.

Table 7.2: Process parameters for polishing multi-radius head

Parameters	Precess angle	Head speed	Tool offset	Tool air pressure
Values	15deg	2000rpm	0.2mm	1.0bar

Different from the general corrective polishing which the error map is established via measurement, the error map used in this investigation is artificially generated. As given in figure 7.20, an R19mm CoCr multi-radius femoral head was manufactured. The generated error map is the difference of the R18mm map and R19mm map (the hatched zone in figure 7.20). The radius of the articulating zone is $x=8$ mm. The R19 map was created by a Matlab program. The PV of the initial error map was 103 μ m and the RMS was 29.65 μ m (figure 7.21) and the initial radius measured by Talysurf PGI was 18.04mm (figure 7.22).

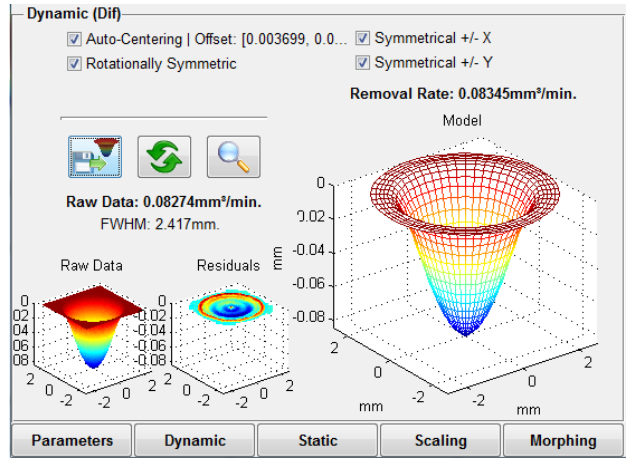


Figure 7.19: Influence function for multi-radius femoral head polishing

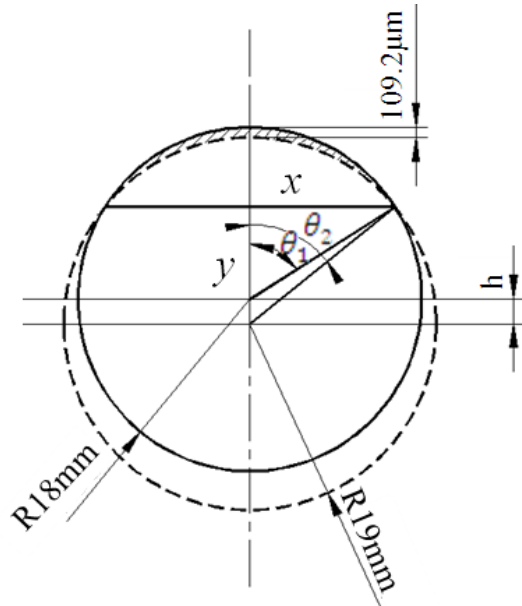


Figure 7.20: Schematic of the polishing zone

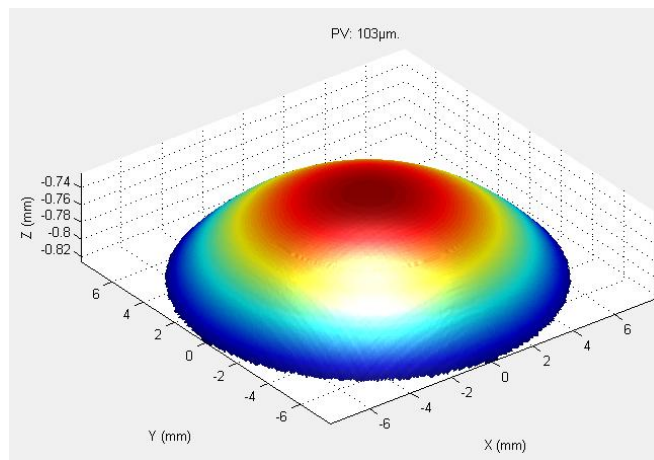


Figure 7.21: Error map before polishing

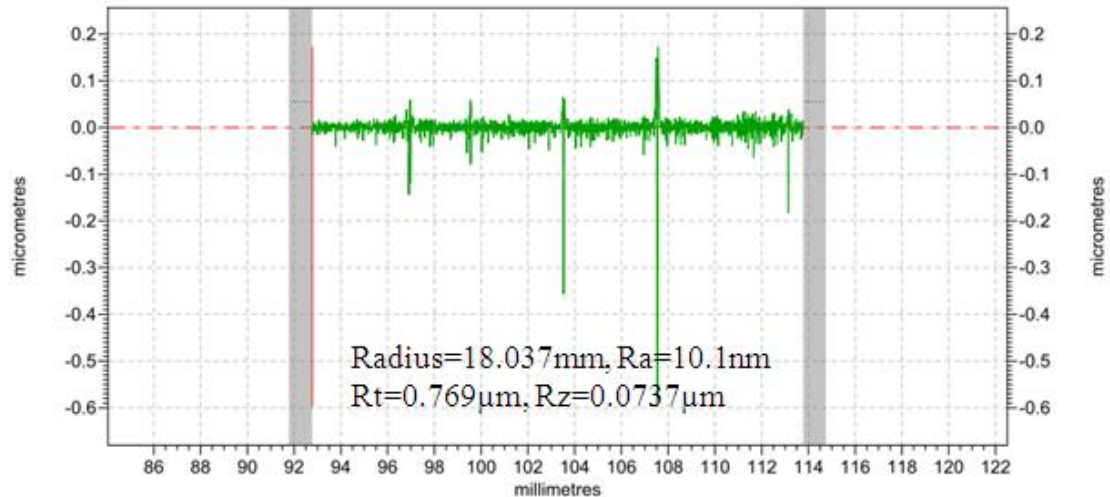


Figure 7.22: Form Talysurf measurement before polishing

7.3.2 Experimental results and discussion

The finished sample of the desired radius was created using only a two stages of polishing process. After each polishing, the sample was evaluated by both Talysurf PGI and a Zeiss coordinate measuring machine (CMM). The measurement result of the PGI was imported into the Zeeko Precession software to create the 3D map and then subtracted by the desired map to generate the error map. After the first polishing run, the error map was reduced to $37.7\mu\text{m}$ PV and $8.85\mu\text{m}$ RMS (figure 7.23 (a)) and the radius was increased to 18.7mm (figure 7.24 (a)). After the final polishing, the error map was reduced to $1.36\mu\text{m}$ PV and $0.318\mu\text{m}$ RMS (figure 7.23 (b)) and the radius was increased to 18.985mm (figure 7.24 (b)). After final polishing, the surface roughness of the sample was 12.6nm Sa (figure 7.25 (c)). Figure 7.25 (a) and (b) also give the surface roughness of unpolished area and the boundary area. As clearly illustrated in the figure, there are a lot of peaks in the unpolished area, reduced peaks in the boundary area and no peaks in the polished area. Figure 7.26 gives the CMM measurement result before polishing and after final polishing. The red area in the figure 7.26 (a) is the polished zone. In the figure 7.26 (b), the green zone is the material that has been removed during polishing. Before polishing, the radius of sample measured by the CMM was 18.001mm and after polishing, the radius of the polished area was 19.017mm . The final results indicate that the form correction of bonnet polishing is able to manufacture the multi-radius femoral head up to the desired accuracy. Figure 7.27 gives the photograph of the machined multi-radius femoral head.

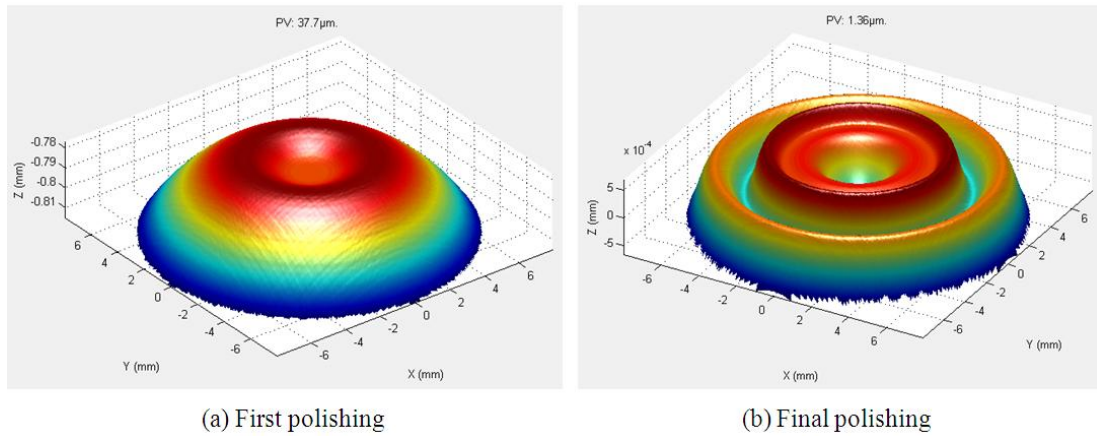
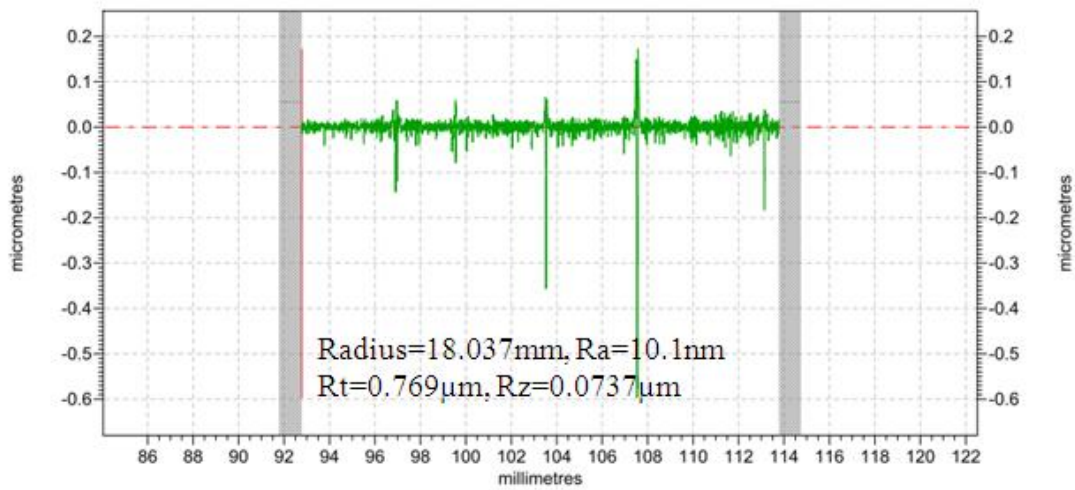
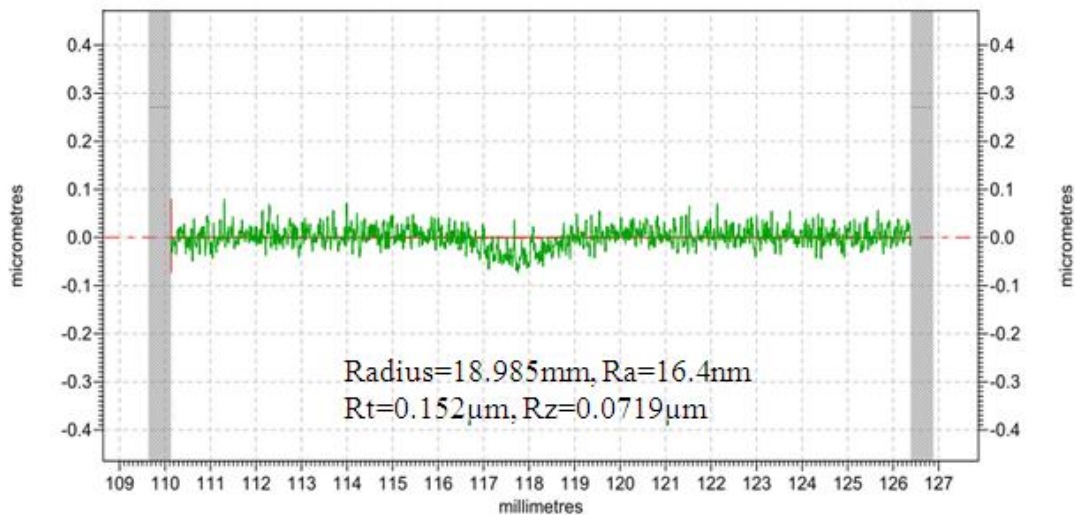


Figure 7.23: Error map after polishing

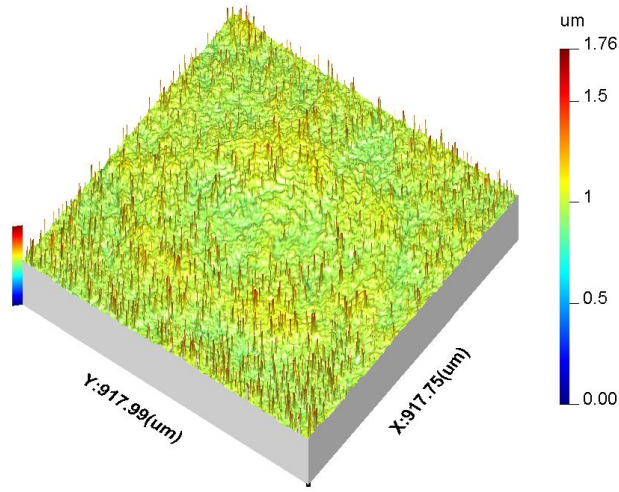


(a) First polishing

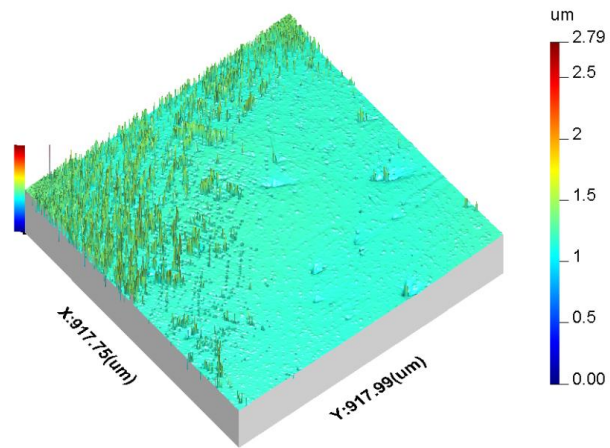


(b) Final polishing

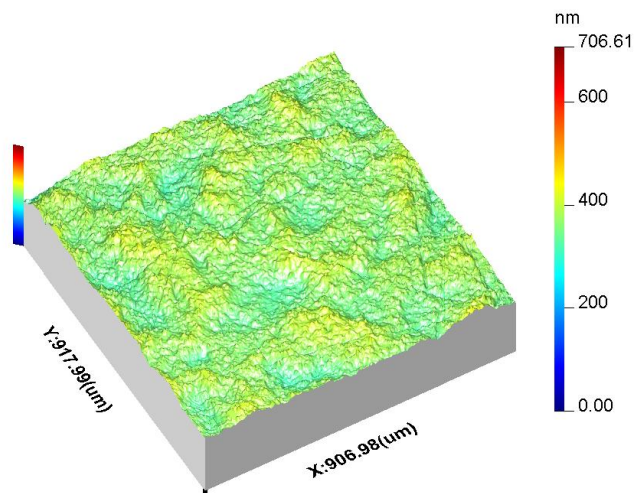
Figure 7.24: Form Talysurf measurement after polishing



(a) Unpolished area ($S_a=35\text{nm}$)



(b) Boundary area ($S_a=29\text{nm}$)



(c) Polished area ($S_a=12.6\text{nm}$)

Figure 7.25: The surface roughness of the unpolished area, boundary and polished area

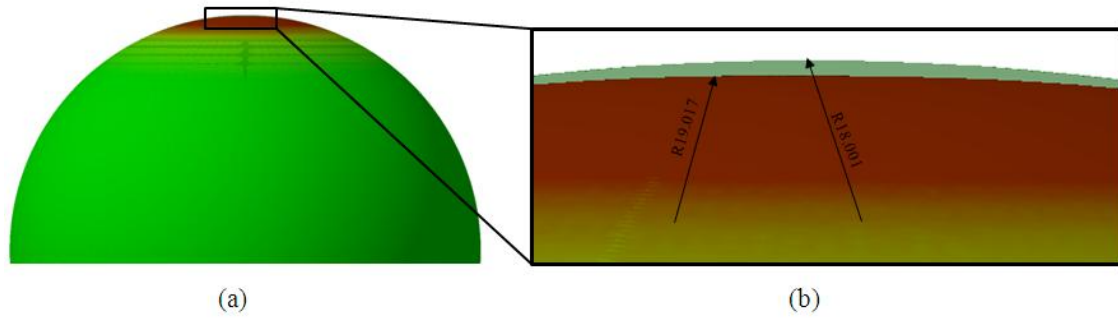


Figure 7.26: CMM measurement (Displayed by CATIA)

(R18.001 was the radius before polishing, and R19.017 was the radius after final polishing)



Figure 7.27: Photograph of the machined multi-radius femoral head

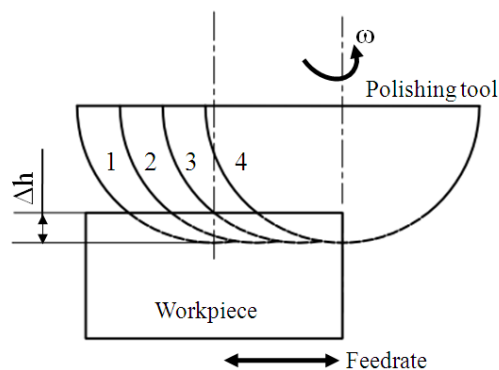


Figure 7.28: The motion of the workpiece and the polishing tool

In this investigation, the spiral tool path was used, namely, when polishing is in progress, the polishing tool is rotating as well as the workpiece reciprocating (figure 7.28). If the tool

offset Δh is big relative to the surface to be polished, when the polishing tool moves from position 1 to position 3, the polishing tool is always contacting the centre of the sample. In other words, the centre of the sample is being over polished during this process, which is undesired and must be avoided, creating the spot in the middle of the error map (figure 7.23 (a) and (b)). This phenomenon can be reduced by decreasing the tool offset or the size of polishing tool. Therefore, smaller tool offset and smaller polishing tool is beneficial for the form correction of multi-radius femoral heads of hip prostheses.

In the study, the PGI and CMM, both of which are contact measurements were used to measure the form, as well as the CCI which is a non-contact instrument was used to measure the 3D topography of the manufactured multi-radius head. Compared with the contact measurement methods, non-contact measurements are more reliable for the following reasons:

1. It is more convenient to obtain the 3D map of samples and generate more accurate error maps for form correction compared to contact measurement which has to use the 2D profiles to create the 3D map.
2. Non-contact measurements also can reduce contamination and damage of the workpiece surfaces.

In addition, the so called “error map” of this investigation before polishing was obtained by design which is different from conventional corrective polishing whose error map results from measurement. The concept of designing an error map is worth notice. In the case of irregular surfaces, such as structured surfaces, surface measurement prior to polishing is difficult. In this case it is feasible to design a pseudo error map and then carry out the form correction process. In order to verify the validity of the designing the error map, an experiment which the ‘CPT’ letters were polished into a copper part was carried out.

7.3.3 Verification of designing error map

In this investigation, the method of designing error map by polishing ‘CPT’ letters on the flat surface of a copper was verified. The letters were polished into an R32.5mm poly-crystalline copper. The polishing medium was a GR35 polyurethane pad with $3\mu\text{m}$ alumina slurry whose specific gravity was 1.025. As mentioned in section 7.2, the better tool path for this polishing was raster. The influence function used in the polishing is shown in figure 7.3. The values of the process parameters are given in table 7.1. The designed error map is shown in figure 7.29. As shown in figure 7.29, the diameter of the error map is 50mm and the depth of the CPT

letters is $60\mu\text{m}$ which means the depth of the letters on the surface after polishing should be around $60\mu\text{m}$ if the polishing process is accurately controlled.

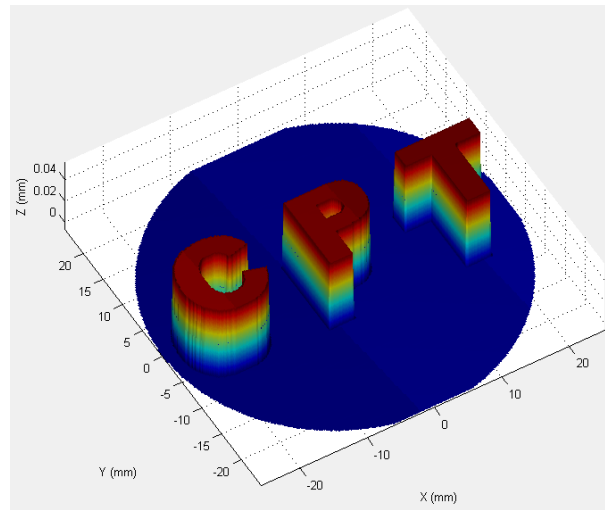
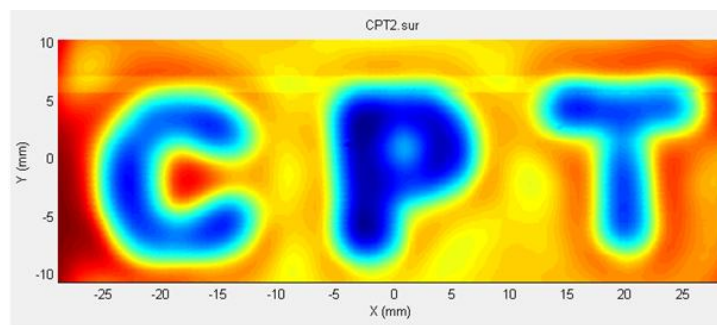
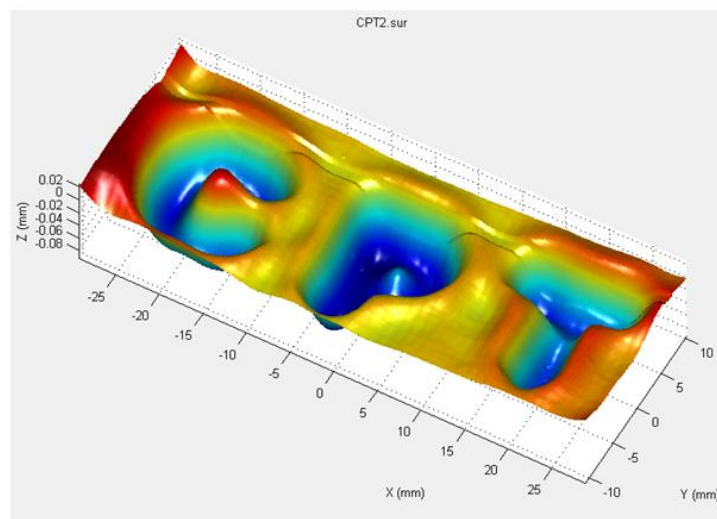


Figure 7.29: Error map of CPT



(a) The front view of the measured CPT letter



(b) The 3D map of the CPT letter

Figure 7.30: The measurement of CPT letters (Mirrored)



Figure 7.31: The photograph of the polished CPT letters

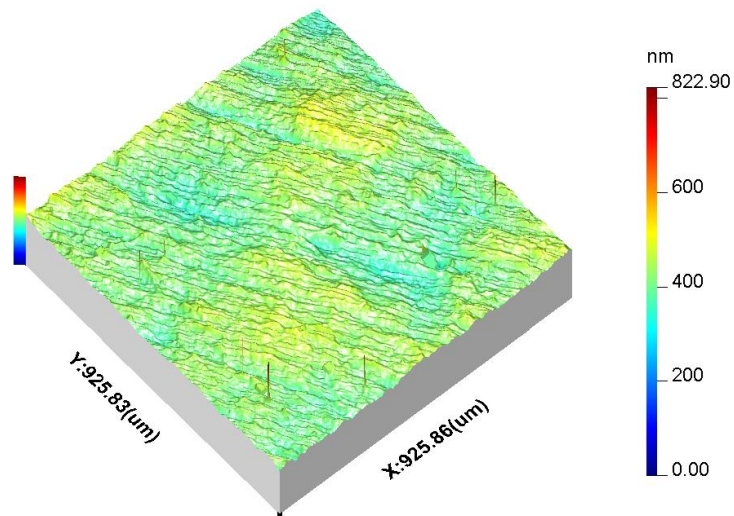


Figure 7.32: Surface roughness of the polished CPT letters

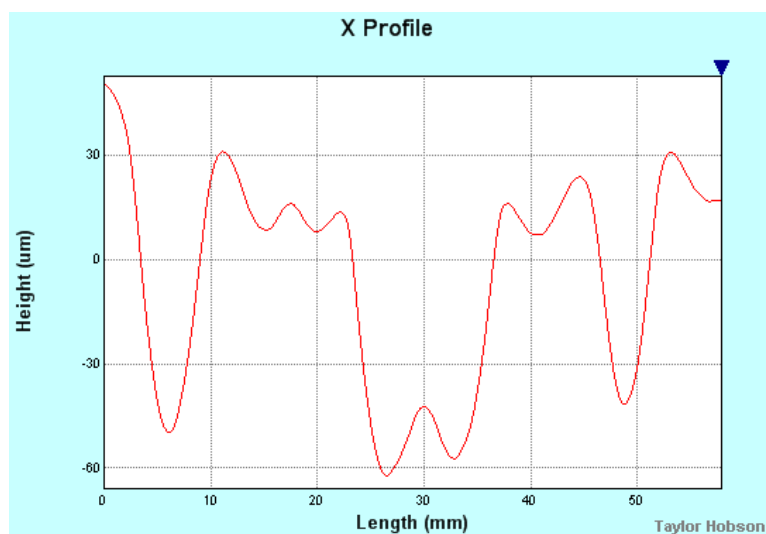


Figure 7.33: The average depth of polished CPT letters

The experiment was deemed successful. After polishing, the CPT letters were clearly formed into the workpiece (figure 7.30 and figure 7.31). The average depth of the CPT letters is about $60\mu\text{m}$ (figure 7.33) which basically achieves the expected value. The error produced during polishing process was mainly due to the reason that the workpiece used in the investigation was only roughly turned, which means the surface before polishing was not ideally flat. The surface roughness of the workpiece after polishing is 12.9nm Sa .

7.4 Polishing of freeform knee femoral components

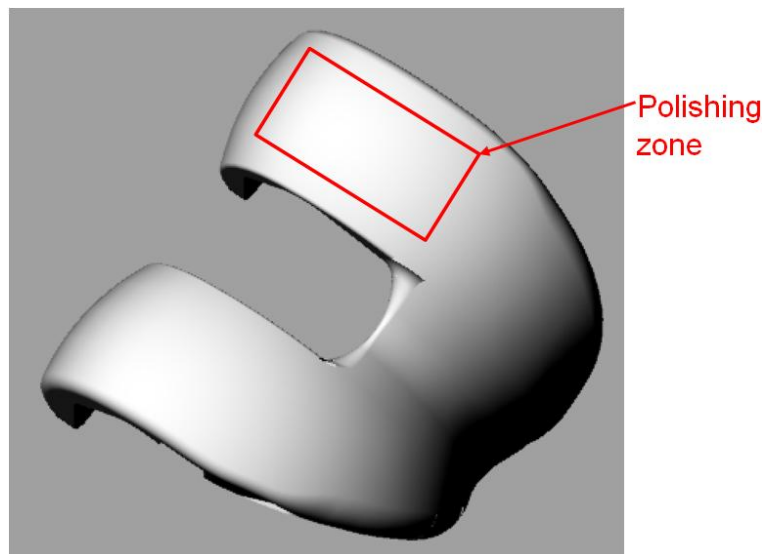


Figure 7.34: CAD model of knee femoral component

According to ISO17450-1, freeform surfaces, also called sculptured or curved surfaces, can be defined as a complex surface which has no invariance degree [235]. Unlike conventional surfaces, freeform surfaces are non rotationally-symmetric. Freeform surfaces are of great interest in many areas such as automobile (car bodies, 3D-cams, seals and gears), aerospace (turbine blades, impellers, fluid-dynamic ducts and aerodynamic parts), household appliances (water pumps and fans), consumer products (mobile phones and cameras), optical parts (computational imaging, compact projection displays and document security), prosthesis (knee joints) etc [236]. Many freeform surfaces need to be fabricated with micrometer level form error and nanometer scale surface roughness. However, the machining of freeform surfaces to such scale is still the most challenging task in the current industry. This section illustrates the development of a polishing process for finishing the surfaces of freeform knee prostheses. The CoCr alloy sample used in the investigation was a part of a freeform knee prosthesis roughly machined by grinding. Because of the stroke limitation of the machine, the available polishing area was $16\text{mm}\times 18\text{mm}$ (figure 7.34). The polishing medium was a

polyurethane GR35 pad with $3\mu\text{m}$ diamond slurry whose specific gravity was 1.024. The influence function for the freeform knee joint polishing is given in figure 7.35. The machine settings are displayed in table 7.2 based on the previous work. Before polishing, the form error and surface roughness are given in figure 7.35 and 7.36 respectively. The PV of the error map was $43.9\mu\text{m}$ and RMS was $3.49\mu\text{m}$. The surface roughness was 85.5nm Ra . The surface before polishing was not shiny enough, so it was impossible to measure the workpiece by using the CCI.

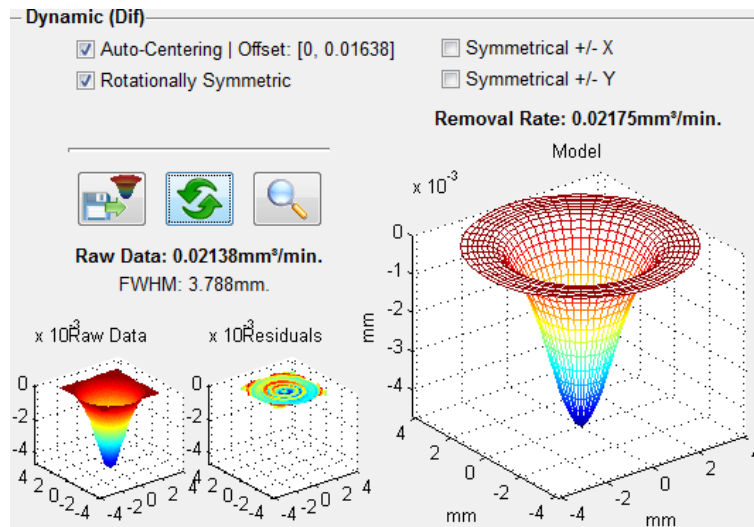


Figure 7.35: The influence function for knee femoral component

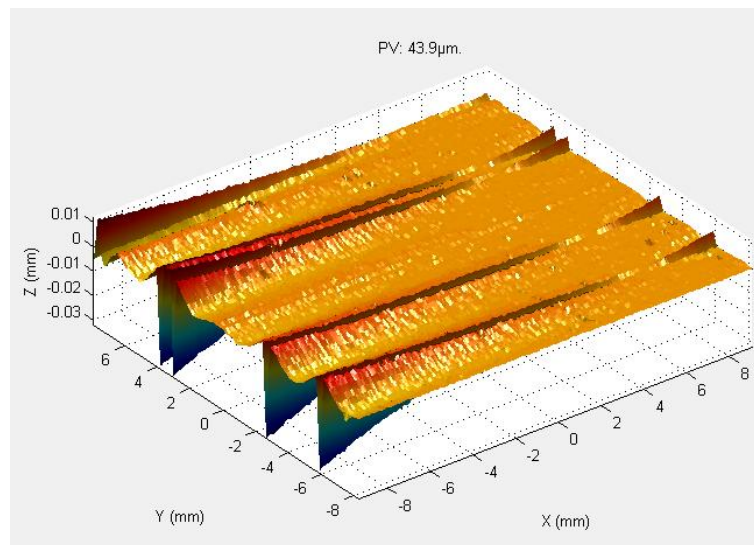


Figure 7.36: Error map of knee femoral component before polishing
(PV= $43.9\mu\text{m}$, RMS= $3.49\mu\text{m}$)

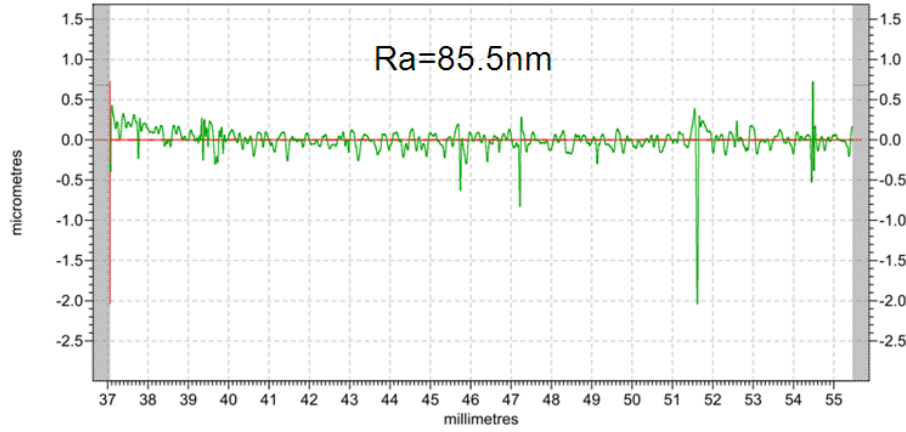


Figure 7.37: Surface roughness of knee femoral component before polishing

7.4.1 Description and creation of freeform surfaces based on NURBS

The geometry of freeform surfaces are commonly defined by a CAD model and described by a parametric surface representation [237]. Non Uniform Rational B-Spline (NURBS) surfaces are the most commonly employed parametric surface, others employed include are Bézier, B-spline. A NURBS surface can be described by [238]:

$$S(x, y) = \frac{\sum_{j=1}^S \sum_{k=1}^T N_{j,m}(x) N_{k,n}(y) w_{j,k} P_{j,k}}{\sum_{j=1}^S \sum_{k=1}^T N_{j,m}(x) N_{k,n}(y) w_{j,k}}, \quad 0 \leq x, y \leq 1 \quad (7.1)$$

Where, m and n indicate the surface degree in the x and y direction, respectively. $\{N_{j,m}(x)\}$ and $\{N_{k,n}(y)\}$ are the basis functions in the x and y directions. S and T are the number of control points along the x and y direction. $P_{j,k}$ are the control points and $w_{j,k}$ are the weights.

The advantage of NURBS can be summarized as follows [239, 240]:

- ❖ NURBS is able to construct very complicated curves and surfaces;
- ❖ Control points which are provided by NURBS can easily determine the shape of the curve and surface;
- ❖ Changing one control point will not affect the shape of the whole surface but only the local surface shape near the control points;
- ❖ NURBS are invariant under transformation such as translation, rotation and scaling, etc;

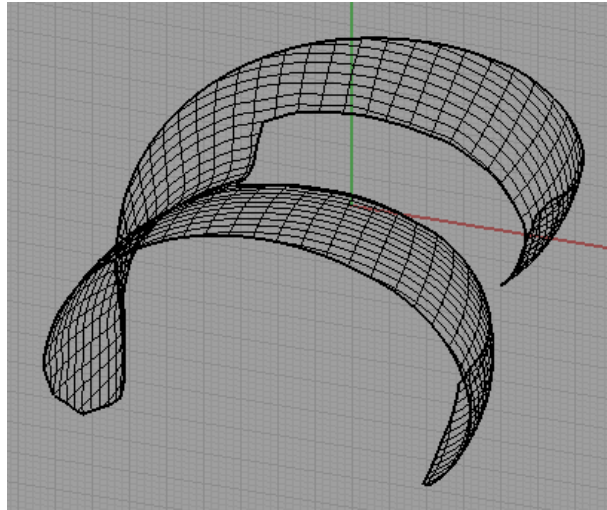


Figure 7.38: The created NURBS surface by Rhinoceros 4.0

And the disadvantages of NURBS are as follows:

- ❖ The interpolation matrix probably leads to rank deficiency or a poorly conditioned problem;
- ❖ The selection of knots will influence the quality of surface construction if the data or surface displays different behaviors in different areas.

A CAD model cannot be directly imported into the polishing machine as the nominal surface. It must be converted into a NURBS surface with the .obj format by the Rhinoceros software as shown in figure 7.38.

7.4.2 Evaluation of the freeform knee femoral components

There are several types of instruments that can be used to measure the freeform surfaces: CMMs, interferometers and profilometers. CMMs, which can be equipped with both contact and non-contact scanning system, are considerably flexible. Another advantage of CMMs is that they can measure large scale and complex workpieces. The most salient feature of interferometry technology is fast measurement and high accuracy. It is easy to measure regular surfaces, such as flat and spherical surfaces, but interferometry can only measure small areas of complex surfaces which can be approximated to sphere and have low slope values. Complex surfaces can be measured by sub-aperture stitching methods, i.e., measure the surface several times until all sub-apertures cover the whole surface and then stitch the sub-apertures together [241]. This is complex and subject to specimen handling inaccuracies. The contact profilometer employs a mechanical stylus to move across the measured surface

as well as the vertical displacement of stylus is measured by a transducer. The greatest merit of the profilometer is that it can measure surface texture, form and contour simultaneously. Limitations are the contacting force may scratch or damage the surface, especially for polished surfaces which are highly smooth and mirror-like. In this investigation, the Talysurf PGI, a kind of profilometer, was used to evaluate the quality of the polished surface.

For planes and spheres, the form error after measurement can be easily assessed. However, for freeform surfaces, an extra process to evaluate the form error is needed. The procedure used in this investigation was developed by Zhang [240], including matching and comparison. Matching, also called alignment, registration, best-fitting or localization, is a process that minimizes the average square distance of the related position of the measurement data and reference data (CAD model) through transformation of translation and rotation [240],

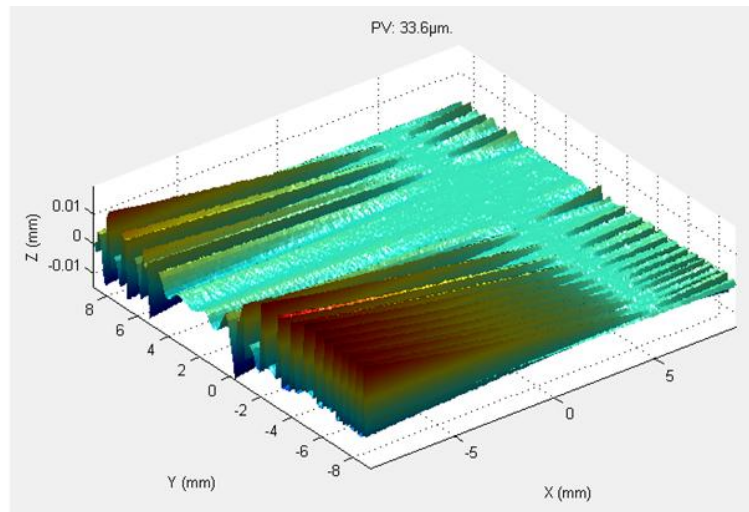
$$D = \frac{1}{M} \sum_{i=1}^M \|R\mu_i + t - v_i\|^2 \quad (7.2)$$

Where, v_i is the corresponding reference point of an arbitrary measured point μ_i . t is the translation vector and R is the rotational matrix as shown in follows:

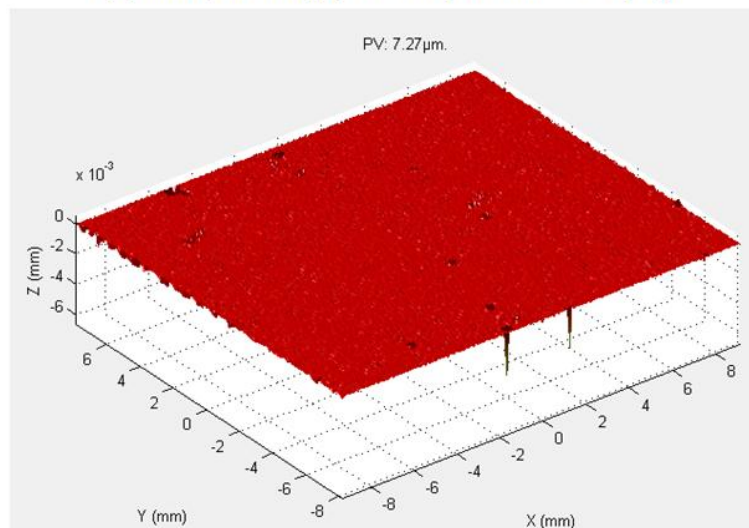
$$R = R_x(\alpha_x)R_y(\alpha_y)R_z(\alpha_z) = \begin{bmatrix} 1 & 0 & 0 \\ 0 & \cos \alpha_x & \sin \alpha_x \\ 0 & -\sin \alpha_x & \cos \alpha_x \end{bmatrix} \begin{bmatrix} \cos \alpha_y & 0 & -\sin \alpha_y \\ 0 & 1 & 0 \\ \sin \alpha_y & 0 & \cos \alpha_y \end{bmatrix} \begin{bmatrix} \cos \alpha_z & \sin \alpha_z & 0 \\ -\sin \alpha_z & \cos \alpha_z & 0 \\ 0 & 0 & 1 \end{bmatrix} \quad (7.3)$$

Generally, two matching steps, initial matching and fine matching, are needed to complete a freeform surface metrology process. The aim of the initial matching is to find the rough position of the measured data related to its nominal data. So far, several rough matching algorithms have been developed based on different features such as global features, manufactured features, local features and surface geometry while other methods are based on image or graph. After finishing the initial matching, mathematical algorithms are used for fine matching. These algorithms include parameter based algorithms and iterative closet point (ICP) methods [242]. After matching, comparison is then carried out to calculate the distance between the measured surface and the designed CAD model and form error is then obtained.

7.4.3 Experimental results and discussion



(a) First polishing (PV=33.6µm, RMS=3.26µm)

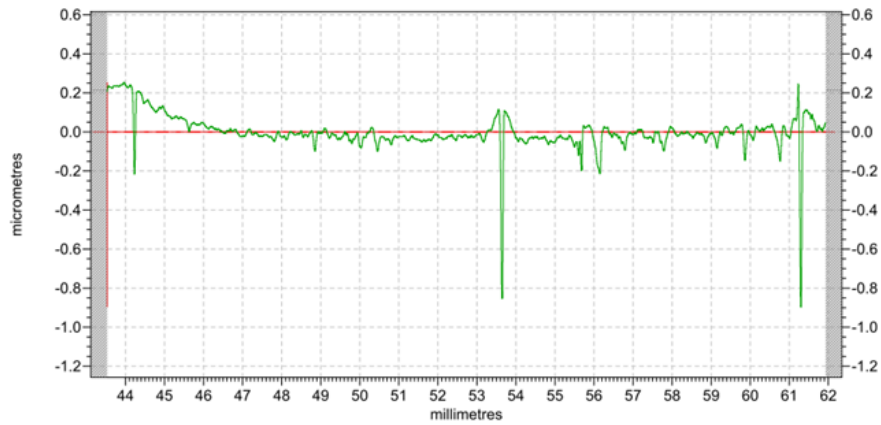


(b) Final polishing (PV=7.27µm, RMS=1.09µm)

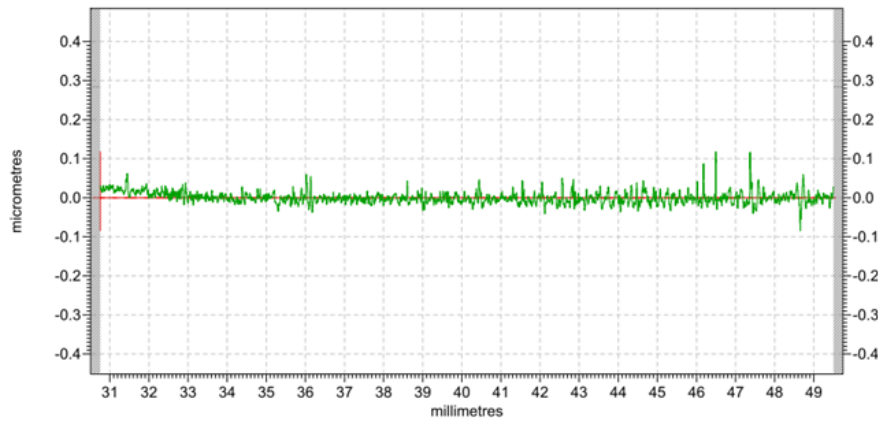
Figure 7.39: Error map of knee femoral component after polishing

The sample was subject to two polishing stages and the polishing results are shown in figure 7.39-7.41. As shown in figure 7.39, the form error was reduced to 33.6µm PV and 3.26µm RMS after first polishing and reduced to 7.27µm PV and 1.09µm RMS after final polishing. After the first polishing, the trajectories left by the previous machining can be clearly seen and after final polishing these trajectories have been effectively removed. Figure 7.40 and 7.41 show the surface roughness of the sample after first polishing and final polishing as measured by Talysurf PGI and CCI. As can be seen in figure 7.40, after the first polishing the surface roughness measured by PGI was decreased to 49.2nm Ra and after final polishing was decreased to 11nm Ra. Figure 7.41 shows the surface roughness measured by CCI,

indicating that Sa was decreased to 28nm Sa after the first polishing and decreased to 10.9nm Sa after the final polishing. Figure 7.42 shows photographs of the sample before and after polishing.

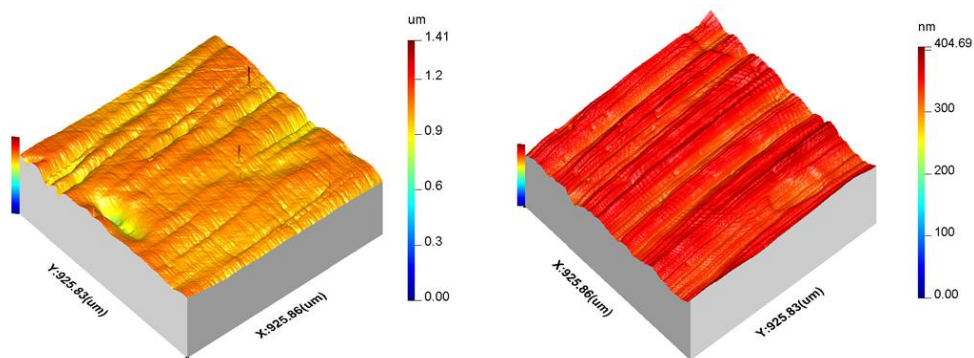


(b) First polishing, Ra=49.2nm



(c) Final polishing, Ra=11nm

Figure 7.40: Surface roughness of knee femoral component after polishing measured by PGI



(a) After first polishing, Sa=28nm

(b) After final polishing, Sa=10.9nm

Figure 7.41: Surface roughness of knee femoral component after polishing measured by CCI



Figure 7.42: The photograph of knee femoral component before and after polishing

As shown in figure 7.41, the trajectories left by previous grinding process after final polishing still can be seen. This indicates that an ultra-precision sample does not just depend on the final finishing, but also the previous machining, especially the grinding process which greatly affects the form error of a workpiece. In addition, positioning of the sample is another issue that needs to be noted in freeform surface correction. Sometimes a special fixture which can be used to locate the origin of the sample and create the link between the coordinates of the workpiece and the machine may be necessary.

7.5 Summary

This chapter has investigated some issues related to form correction, including the effect of tool path on form correction, multi-radius femoral head polishing and freeform knee femoral component polishing. The investigation of the tool path indicates that both raster path and spiral path can effectively improve the surface roughness and form error of a sample, but these two general paths are applied to different shapes of the workpiece. For rotationally-symmetric workpieces, a spiral path is more suitable while for non-rotationally-symmetric workpieces or freeform surfaces, raster path processing is more useful. When using raster polishing, it is better to use a 3D form error which is measured by an interferometer or a stylus instrument (the stylus instrument can only measure a squared workpiece or a part of the circular workpiece). However, when using the spiral polishing, users can employ the profile of a workpiece to create a 3D form error to save a lot of time in measurement.

In section 7.3, the form correction technology of the bonnet polishing was used to manufacture the next generation multi-radius femoral head of a hip prosthesis. This new design femoral head can greatly improve the lubrication performance but suffers from manufacturing challenges. This investigation has successfully machined a R19mm CoCr multi-radius femoral head by using an R18mm single radius femoral head. Post polishing measurement of the radius of the articulating zone was 18.98mm and 19.017mm (measured through Taylor Hobson PGI and Zeiss CMM respectively), in an attempt to test the design for the desired value R19mm. Also, the PV of the error map was reduced from 103 μ m to 1.36 μ m and RMS was reduced from 29.65 μ m to 0.318 μ m. The experimental result confirms that the bonnet polishing could potentially be a viable choice to finish the new design multi-radius femoral head. The machined surface roughness obtained through the process was 16.4nm Ra and 12.6nm Sa. In this investigation, the concept of designing error map was also proposed. This concept is very useful for polishing structured surfaces. To verify the validity of this concept, an experiment to polish the CPT letters on a flat copper was carried out. The expected depth of the letters was 60 μ m and the actual polished depth was 62 μ m which indicates that the experiment was largely successful.

The metrology and finishing of freeform surfaces is still a challenge in the field of machining. In section 7.4, the polishing of a freeform knee femoral component was investigated. The material of the sample was a CoCr alloy. Because of the stroke limitation of the polishing machine, only a limited squared area of 16mm \times 18mm was polished. Different from the polishing of regular surfaces such as plane or sphere, the freeform surfaces cannot be designed directly and must be imported by using a CAD model to allow the machine to carry out the polishing process. After polishing, the PV of the form error was decreased from 43.9 μ m to 7.27 μ m and RMS was decreased from 3.26 μ m to 1.09 μ m. The surface roughness after final polishing was 10.9nm Sa measured by CCI and 11nm Ra measured by PGI.

8. OVERALL DISCUSSION

As introduced in chapter 1, both surface finish and form tolerance can greatly affect the wear of bearing surfaces of artificial joints, i.e., insufficient surface finish and inadequate form tolerance can significantly lead to premature failure of the implanted prostheses. In order to improve the longevity of the prostheses, this research attempted to address this issue by using the CNC controlled ultra-precision bonnet polishing technology to improve both the surface finish and form tolerance of bearing surfaces for hip and knee prostheses. The discussions presented in this chapter consist of the following contents:

- ◆ Surface roughness improvement
- ◆ The effects of experimental conditions on surface topography
- ◆ Material removal investigation
- ◆ Form correction

8.1 Surface roughness improvement

It has been recognized that polishing technology is one of the most effective approaches to improve the surface roughness of a workpiece if the processing conditions are well controlled. The processing conditions include polishing pads/cloths, polishing slurry, material properties of workpieces and process parameters. The effects of polishing pads/cloths, material properties of workpieces and polishing slurry on surface roughness have been widely investigated [168, 169, 173]. Generally, surface roughness is not only correlated with the grit size and hardness of abrasives, hardness of polishing pads/cloths and slurry concentration but also related to the hardness of workpieces, elastic deformation amount of the polishing tool, etc. These conclusions have been extensively accepted across various polishing methods by other authors [168, 169, 173]. However, the effects of process parameters on surface roughness are not well established, and sometimes contradictory for different polishing systems. Take the polishing speed for example, Brinksmeier et al. [150] showed surface roughness was decreased by a smaller relative velocity while Jiang et al. [167] and Huang et al. [208] regarded a higher polishing speed was beneficial for the improvement of surface roughness. Therefore, it is necessary to investigate the effect of each process parameter on surface roughness for different polishing methodologies so that a deterministic and highly efficient process can be obtained.

In this thesis, the effects of the main process parameters in bonnet polishing system for the rapid improvement of surface roughness have been investigated. The process parameters considered in the study consisted of precess angle, head speed, tool offset and tool air pressure. Different from other research which did not take into account the interaction effects [209, 210, 243-245], this work considered the interaction effects. Due to the fact that the Taguchi method does not give guidelines for measuring the interaction effects among factors, full factorial design was used to evaluate the interaction effects when using the bonnet polishing system. The results presented in the study showed that precess angle and head speed interacted each other during surface roughness improvement. As shown in chapter 7 and figure 8.1, the relative velocity $V = \omega \cdot (R-d) \cdot \sin\alpha$, when the precess angle $\alpha = 0$, the relative speed V is 0; when the precess angle $\alpha \neq 0$, the increase of α could lead to an increase of relative speed V . Therefore, the variation of precess angle is essentially the change of relative speed.

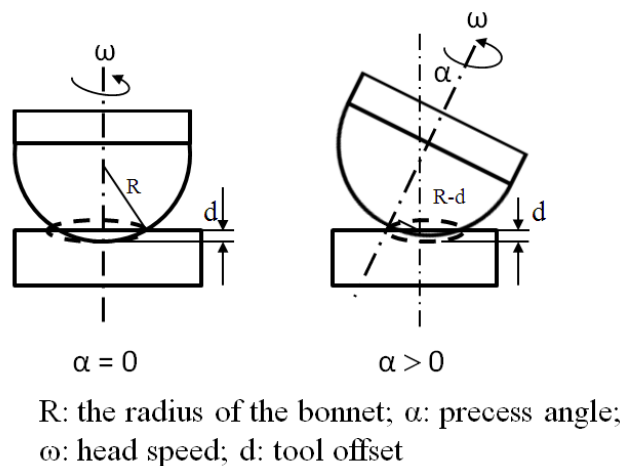


Figure 8.1: The precess angle variation

When considering the interaction effects, the Taguchi approach was used to optimize the process parameters for surface roughness improvement. The optimized values for process parameters were 10^0 precess angle, 800rpm head speed, 0.2mm tool offset and 1.8bar tool air pressure, which implied that precess angle and tool offset were set at the medium levels, head speed were set at low levels and tool air pressure was set at the high levels. As described above, when the precess angle was 0, the relative polishing speed was 0, which indicated that the material in the centre of contact area was not removed. But when precess angle was too large, the polishing area was too close to the edge of the polishing tool (figure 8.1, right figure), which may cause the edge of the polishing tool to contact the workpiece during

polishing process. A small value of head speed meant at the finishing stage, a slow head speed would not lead to the damage of the generated surface. Tool offset and tool air pressure worked together to create the contact pressure of the bonnet polishing. The experimental results indicated that medium tool offset and higher tool air pressure were beneficial for the surface roughness improvement.

When comparing the Taguchi experiments with the full factorial experiments, it was found that the results obtained were not completely in agreement. In the full factorial investigation the primary factors affecting surface roughness improvement were tool air pressure, followed by tool offset, head speed, precess angle and interaction effects, while in Taguchi experiments, the influence sequence was tool air pressure, head speed, interaction effects, tool offset and precess angle. The main reason for the difference appeared that the Taguchi experiment showed high noise, accounting for up to 20.2% of the total contribution and this was difficult to avoid. As noise is adverse to the experimental precisions, it could be reduced by changing the environmental conditions, such as controlling the temperature or reducing the vibration of the machine, etc.

8.2 The effects of experimental conditions on surface topography

It is well-known that surface topography parameters have numerous advantages compared with 2D profile parameters. Surface topography parameters include amplitude parameters, spacing parameters, hybrid parameters, Sk family parameters, material/void volume parameters and other parameters [176]. In the present study the evolution of all surface topography parameters during polishing processes was investigated.

Amplitude parameters used to describe amplitude-related properties of a surface are dependent on the height deviations, including six parameters, Sq , Ssk , Sku , Sp , Sv , Sz . The experimental results were fairly predictable and indicated that when the grit size of abrasives decreased, Sq , Sp and Sz decreased steadily, Sku increased gradually, Ssk and Sv fluctuated, which implied that smoother surfaces had smaller values of Sq , Sp and Sz , higher values of Sku . The change of the amplitude parameters indicated that after polishing, the standard deviation and the peak height of the surface were reduced; the peakedness or sharpness of the polished surface was centrally distributed indicating that the polished surface was a Gaussian shape and the peaks height and scratches depth gradually decreased.

Spacing parameters are used to depict the spatial properties of surfaces and mainly depend on the information in the x-y plane. The spacing parameters consist of density of summits of the surface parameter Sds , the fastest decay auto-correlation length parameter Sal and texture aspect ratio parameter Str . The decrease in Sds indicated that the density of summits of a polished workpiece was reduced by decreasing the grit size of abrasives. Str was smaller than 0.3 after 6 μ m diamond and 1 μ m diamond polishing which indicated that the directional structure or lay of a final polished surface was increasingly strong. As the surface was polished the strength of the lay should decrease. During polishing process Sal increased indicating that the polished surface was dominated by low frequency (or long wavelength) components.

Hybrid parameters are based on both amplitude and spatial information, including the arithmetic mean summit of curvature of the surface parameter Ssc , the root-mean-square slope of the assessed topographic surface parameter Sdq and the developed interfacial area ratio parameter Sdr . Any changes in either amplitude or spacing can affect on the hybrid features. The investigation results showed that all hybrid parameters decreased with the decrease of grit size of abrasives, which indicated that the principle curvature at the summits of a polished surface and the surface slope decreased with the decrease of grit size of abrasives. The decrease of Sdr denoted that either the amplitude or the spacing or both was becoming insignificant during polishing process and that there was a general smoothing of the surface, as expected.

Sk family parameters result from the peaks above the main plateaus, the plateaus themselves and the deep valleys between plateaus. Sk family parameters include the core roughness depth parameter Sk , the reduced peak height parameter Spk , the reduced valley height parameter Svk , the peak material component parameter $Smr1$ and the peak material component parameter $Smr2$. After final polishing, Spk , Sk and Svk decrease while $Smr1$ and $Smr2$ were relatively stable. The decrease of Spk indicated that the small peaks above the main plateau of the surface were reduced by polishing. The decrease of Sk indicated that the depth of the working part of the surface reduced in depth during polishing process. The decrease in Svk denoted that the depth of valleys of the surface decreased. The relative stability of $Smr1$ and $Smr2$ indicated that the small peaks above the main plateau were relatively few even in rough polishing.

The material/void volume parameters originate from the volume information of areal material ratio curves of the topographic surface, including the peak material volume of the topographic surface parameter V_{mp} , the core material volume of the topographic surface parameter V_{mc} , the core void volume of the surface parameter V_{vc} and valley void volume of the surface parameter V_{vv} . The decrease in V_{mp} showed that the material volume enclosed in the 10% material ratio and normalised to unity reduced after polishing. The small value of V_{mc} indicated that the polished surface had a good load bearing capability and good lubrication retention, which denoted polishing technology could improve the load bearing capability and lubrication properties. V_{vv} is used to describe the fluid retention ability of a contacting surface. V_{vv} decreased after polishing which indicated the relative depth of the lubrication retaining valleys was decreased.

Other parameters consist of texture direction of the surface parameter Std , ten point height of the surface parameter $S5z$ and arithmetical average of the surface parameter Sa . Std changed slightly during polishing which meant that the lay direction of a polished surface changed slightly. The decrease in $S5z$ denoted that the number of high peaks decreased for a polished surface. Sa is the most commonly used parameter. This parameter corresponds to Ra in the case of 2D measurement. The variation trend of Sa was usually similar to Sq in this case showed a general reduction.

In addition, the combination of polishing pads/cloths on surface topography was also investigated. 3 combinations of polishing pads/cloths and polishing paste (LP13+6 μ m diamond paste, LP13+1 μ m diamond paste and soft Microcloth+1 μ m diamond) were used. The first two combinations improved the topography slightly and the last combination improved the surface topography greatly. The investigation results indicated that in order to obtain the best surface topography a polishing pad/cloth should be carefully matched with a polishing paste or polishing slurry.

8.3 Material removal investigation

(1) The effects of process parameters

When the experimental conditions such as the types of polishing slurry, the concentration of slurry, the polishing pads, etc are determined, the primary process parameters affecting material removal include process angle, head speed, tool offset and tool air pressure in bonnet polishing. In the research presented here the effects of these process parameters on material

removal characteristics which is termed influence function (IF) were studied. Investigation results indicated that precess angle clearly affected the width of the IF and the material removal rate (MRR). The reason for the increase of the width of the IF mainly resulted from the increase of contact area between polishing tool and workpiece. Although the bonnet is a part made of spherical rubber, the contact areas in position 1 and position 2 are different if the tool offset is the same because the bonnet is fixed by a duralumin framework (figure 8.2). The increase of the MRR was derived from both the increase of the contact area and the relative velocity (figure 8.1). When the precess angle and tool offset were set, the increase of the head speed could result in the great increase in MRR (figure 6.6) and slight increase of the width of IF (figure 6.27). This result was in agreement with Walker et al. (figure 8.3) [246]. When the precess angle and head speed were fixed, the increase in tool offset led to an increased contact area, hence the increased width of IF (figure 6.28) and MRR (figure 6.12). The investigation results showed that the effect of tool air pressure on both the width of IF and MRR was very slight. However, the interaction of tool offset and tool air pressure on the IF should be noted to avoid the warp of bonnet which can give rise to a protrusion in the centre of IF (figure 6.7, 6.9, 6.10, 6.11).

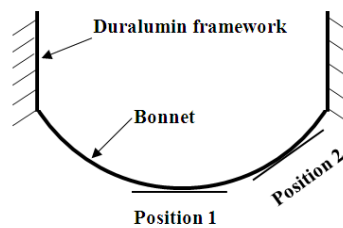


Figure 8.2: The change of contact area resulting from the precess angle

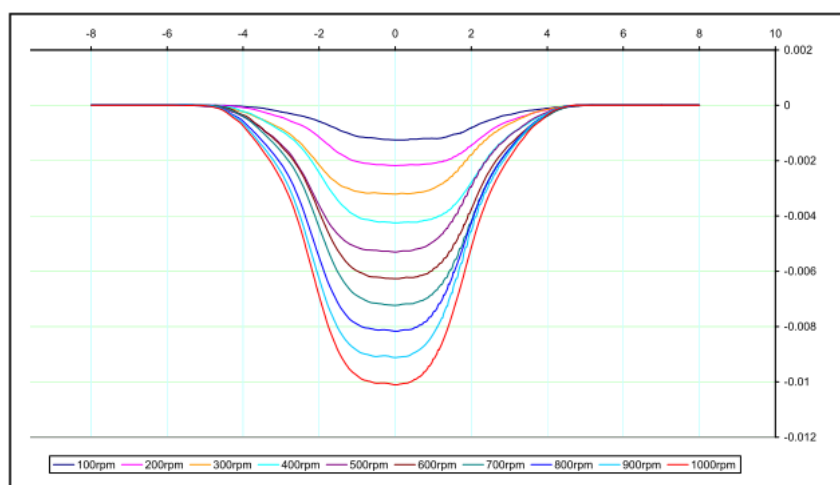


Figure 8.3: The effect of the head speed on the IF [246]

(2) The effects of workpiece hardness and polishing pads hardness

Apart from the investigation of the effects of process parameters on the MRR, the effects of workpiece hardness and polishing pad hardness on the MRR were also studied. The investigation results showed that the MRR was proportional to polishing pad hardness and inversely proportional to the workpiece hardness. In the experiments, only the head speed was increased while the other process parameters were kept constant. When head speed was slow, the discrepancy in MRR of both investigations was small, but this discrepancy increased with increasing head speed. Therefore, a higher head speed was preferred for distinguishing the difference of the effect of the workpiece hardness and the polishing pad hardness. Other experimental conditions such as grit size of abrasive, concentration of polishing slurry also affected the MRR. Generally, larger grit size of abrasives and higher concentration resulted in a higher MRR [246]. The effects of different types of abrasives on MRR are very complicated. If the effects of chemical reactions are not considered, then the higher hardness of abrasive generally results in higher MRR. If the chemical reactions between workpiece and abrasives are considered, the MRR would need further investigation [142].

(3) Polishing force

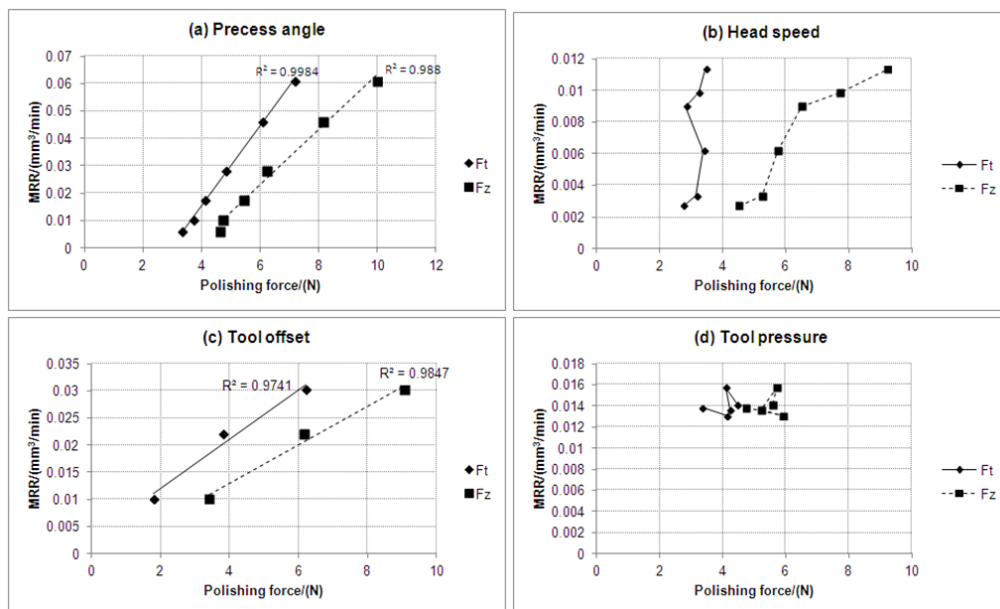


Figure 8.4: The correlation of polishing force and MRR

It was found that polishing forces strongly correlated with the MRR and IF [163, 247]. In this thesis, the effects of process parameters on polishing forces were investigated. The investigation results showed that the normal force was greatly affected by the precess angle, head speed and tool offset but only slightly affected by the tool air pressure; tangential forces were obviously affected by the precess angle and the tool offset but slightly affected by the head speed and the tool air pressure. Comparing the experimental results of section 6.2 and section 6.5, the figures for the correlation of polishing forces including normal force F_z and tangential force F_t (the average of F_x and F_y) and the characteristics of IF with respect to the MRR, the width and the maximal depth of IF were drawn as shown in figure 8.4-8.6. As can be seen in figure 8.4 (a) and (c), both normal force and tangential force had a positive linear relationship with respect to MRR during precess angle and tool offset experiments. During head speed experiments, the increase in MRR was resulted from the increased normal force while tangential force had only a slight contribution to the MRR (figure 8.4 (b)). Both normal force and tangential force had a little effect on the MRR when the tool air pressure increased (figure 8.4 (d)).

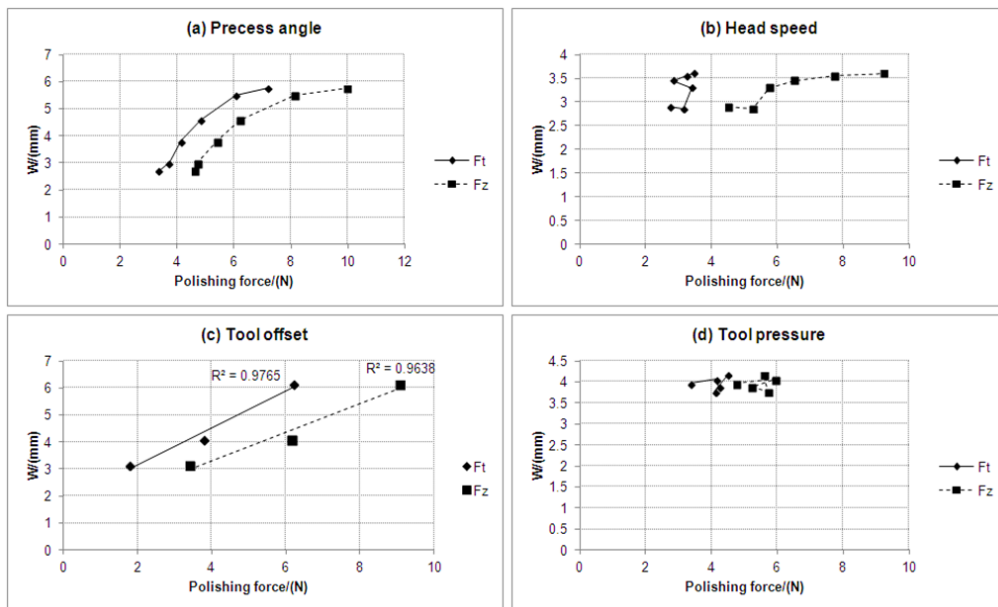


Figure 8.5: The correlation of polishing force and width of IF

Figure 8.5 illustrates the correlation of polishing forces and the width of IF. As shown in figure 8.5 (a), the width of IF increased with the increase of both normal force and tangential force during precess angle experiments. Figure 8.5 (b) illustrates that when the head speed increased the normal force increased, but the tangential force as well as the width of IF

remained fairly stable, which inferred that tangential force was strongly correlated the width of IF. Figure 8.5 (c) shows that both normal force and tangential force had a linear correlation with the width of the IF during the investigation of tool offset effect. In the tool air pressure experiments, both normal force and tangential force had only a minor effect on the width of IF (figure 8.5 (d)).

Figure 8.6 illustrates the effects of polishing forces on the maximal depth of the IF. As can be seen in figure 8.6 (a), both normal force and tangential force changes had a great effect on the maximal depth of the IF during precess angle experiments. In head speed experiments shown in figure 8.6 (b), the maximal depth of IF increased with the increase of normal force while tangential force was quite stable which indicated that the maximal depth of IF was dominated by the normal force. Both normal force and tangential force showed a linear correlation with the maximal depth of IF during tool offset experiments (figure 8.6 (c)). Both normal force and tangential force had little effect on the maximal depth of IF during tool air pressure experiments (figure 8.6 (d)).

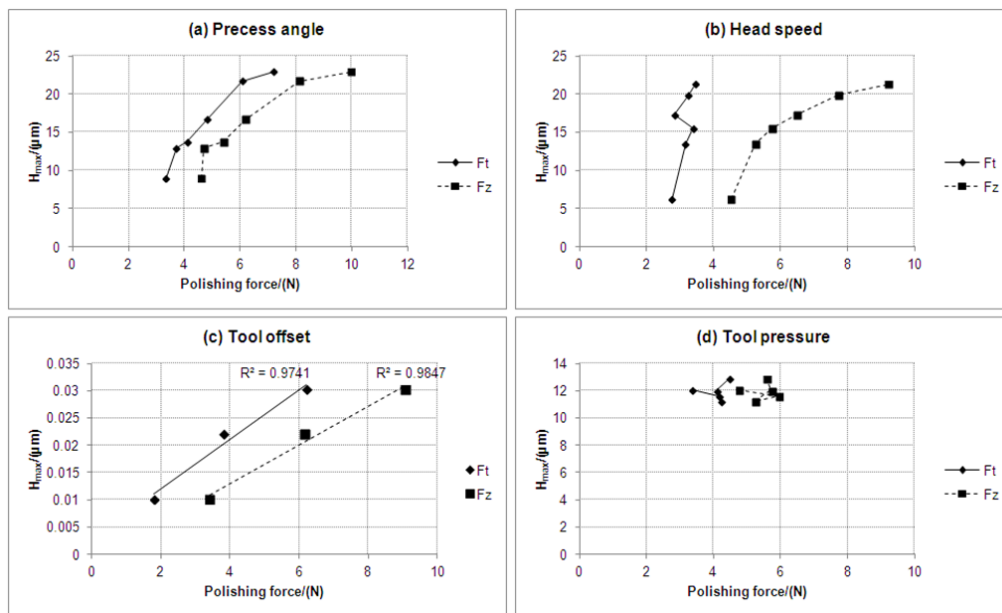


Figure 8.6: The correlation of polishing force and depth of IF

Through comparing the experimental results, it was found that the increase in tangential force resulted from the increase of contact area while the increase of normal force originated from the increase of relative speed and contact pressure. The increase in precess angle could lead to the increase of both the contact area and the relative speed, hence the increased tangential

force and normal force. The increase of head speed resulted in an increase of relative speed, so it only caused the increase in normal force. The change of tool offset generated variation in the contact area and contact pressure, therefore the increased tool offset increased both normal force and tangential force. Tool air pressure had a slight effect on the contact area and contact pressure, consequently it had a little effect on both normal force and tangential force.

(4) Material removal rate modelling

Based on the experimental results, the Preston equation was modified by introducing the process parameters into the equation to create a new MRR model. Although the created model was based on CoCr alloys, it could be used to predict MRR for bonnet polishing of other materials such as stainless steel, copper, ceramic, glass and so on if the Preston coefficient has been determined. Preston coefficient is very complicated to quantify and includes the effects of all experimental conditions. If the value is not known, the Preston coefficient can only be ascertained experimentally. Fortunately, once the experimental conditions have been determined, the Preston coefficient is constant. Hence this developed model can be used to predict the MRR.

8.4 Form correction

In order to facilitate a form correction process, the designed surface, the created influence function and the error map need to be ascertained to calculate the dwell time map. The dwell time map is then translated into CNC code to control the polishing process. Generally, the shapes of the designed surface are flat, spherical, cylindrical, and conical etc. These general surfaces are relative simple and can be designed directly by the commercial software, such as Zeeko TPG. Other complex surfaces, such as freeform surfaces must be described by a CAD model. Unfortunately, not all CAD models can be imported into the polishing machine software. These models must be converted into a specific format for example, .obj format (section 7.4). The influence function can be obtained by practical polishing or by a created model. If the influence function is obtained by practical polishing, the general form of the workpiece for the influence function should be the same as that of the workpiece for form correction. In addition, the process conditions for the influence function must be the same as the process conditions for form correction. If the influence function is obtained by the created model, the Preston coefficient should be acquired precisely by numerous experiments under the same experimental conditions as the form correction. The error map is usually acquired

by the subtraction of the surface of the component to be corrected away from the desired surface. The surface of the component is obtained by measurement. Therefore, the accuracy of the error map is highly dependent on the measurement process. The best measurement for creating error map is via areal measurement which can be achieved by contact measurement such as Talysurf PGI or non-contact interferometer such as Zygo GPI. The contact Talysurf PGI can only measure the squared area and needs significant amount of time to finish an areal measurement and sometimes may even damage the surface if the workpiece is not hard enough. A non-contact system such as a Zygo GPI can measure not only the squared area but also the circle area. In addition, compared to contact measurement, non-contact measurement is normally faster and does not compromise the surface in terms of damage. However, non-contact measurement requires a high standard of environment, such as clean room, anti-vibration and so on. In some circumstances, an error map can be obtained by design as used in section 7.3. The concept of designing an error map is worthy of note. In the case of irregular surfaces which are difficult or impossible to measure before polishing, it is feasible to design a pseudo error map and then perform the form correction process on this designed map.

The most often used polishing tool paths are spiral and raster. These two tool paths are suitable for different shapes of workpiece. Spiral paths are more suitable for rotationally-symmetric workpieces and raster path is better for non-rotationally-symmetric workpieces or free-form surfaces. The disadvantage of these two tool paths is that both tool paths can leave the periodic structure after polishing [195]. In order to avoid introducing the periodic structure, Dunn et al. [195] developed a pseudo-random tool path for bonnet polishing (figure 3.17). It is reported that surface polished by pseudo-random path had no periodic structure and a better surface roughness, which indicated that pseudo-random tool path was more suitable for final smoothing of a workpiece.

Another key factor probably affecting the accuracy of form tolerance is registration. This is especially important for form correction of freeform surfaces. Sometimes, a specific fixture is needed to assist the positioning (section 7.4). Apart from this element, when designing the CAD model, a reference point to match the model to the coordinate of the machine tool should be designed.

9. CONCLUSIONS AND FUTURE WORK

9.1 Conclusions

The aim of this dissertation was to develop a deterministic polishing process for the improvement of both surface finish and form tolerance of articulating surface for hip replacements and knee replacements by using the bonnet polishing technology. The research conclusions completed in the thesis are listed below.

1. Surface roughness improvement

The aim of this investigation was to rapidly obtain the best surface finish of cobalt chrome alloys with a simple polishing process (all samples were polished at the same process time). Prior to the use of a Taguchi approach to optimise the process parameters for surface roughness improvement, a full factorial experiment design was used to detect the interaction effects. The experimental results indicated that precess angle and the head speed interacted each other mostly. Based on this interaction effect, a Taguchi method was used to optimise the main process parameters, including precess angle, head speed, tool offset and tool air pressure. Sa values were selected as the optimization criterion. The optimal experimental conditions for obtaining the best Sa value were 10^0 precess angle, 800rpm head speed, 0.2mm tool offset and 1.8bar tool air pressure. The ANOVA results denoted that the greatest contribution for surface roughness was tool air pressure, accounting for 26.4%, followed by head speed (12.5%), interaction effect (about 11%), tool offset (12.1%), and precess angle (5.5%). The optimal conditions were verified by a set of confirmatory experiments. The corresponding results showed only a slight discrepancy between the estimated ratios and the real experiment results, which indicated that the Taguchi method with the consideration of interaction effect was a robust methodology.

2. The effects of experimental conditions on surface topography

This study investigated the evolution of surface topography during the polishing process and the effects of the combination of polishing cloths/pads and abrasives on the surface topography. Most surface topography parameters decreased during polishing process except a few parameters fluctuated or increased. Amplitude parameters, spacing parameters, hybrid parameters and other parameters related to the smoothness of surface are good reference for

polishing. Sk family parameters and material volume parameters related to bearing surface lubrication are not very useful for polishing process.

3. Material removal investigation

The experimental results have shown that the process parameters with the dominant effect on material removal were precess angle, head speed, tool offset and tool air pressure. The investigation concluded that the MRR increased with the increase of precess angle non-linearly, with the increase of head speed linearly, increased first and then decreased with the increase of tool offset due to the bonnet distortion, and was not affected by tool air pressure. The results showed that if the tool air pressure was less than 1.5bar, the tool offset needed to be less than 0.3mm; if the tool air pressure was greater than 1.5bar, then the tool offset needed to be less than 0.2mm.

The experimental conditions investigation indicated that MRR was proportional to the hardness of polishing pads, but was inversely proportional to the hardness of the workpieces.

The polishing force investigation showed that the normal force was always greater than tangential force; the effect of precess angle on polishing force had nearly the same with its effect on the MRR; normal force increased linearly with the increase of head speed but tangential force displayed no change; both normal force and tangential force increased linearly with the increase of tool offset, but varied only slightly with the change of tool air pressure. The investigation results also showed that normal force had a distinct effect on the maximal depth of the influence function while the tangential force seemed to dominate the width of the influence function and both normal force and tangential force could contribute to the MRR.

Based on the experimental results of the material investigation and the theory of contact mechanics, an MRR model originating from the Preston equation was created. The model included 4 terms, i.e, term 1 depicted the modified Preston coefficient, term 2 represented the effect of the head speed, term 3 described the effect of the tool offset and term 4 accounted for the effect of the precess angle. The created model was a function of the process parameters, apart from the tool air pressure which had only a slightly effect on the MRR and was combined into the Preston coefficient. This MRR model was successfully verified by a set of confirmatory experiments. The predicted results were in good agreement with the

experimental results and those of other materials, indicating that the model could be used to predict the MRR in bonnet polishing.

4. Form correction

The last investigation of this thesis concerned form correction, including the effect of tool path on form correction, multi-radius femoral head polishing and freeform knee femoral component polishing. The tool path investigation indicated that both raster path and spiral path can greatly improve the surface roughness and form tolerance of a workpiece. However, these two tool paths were suitable for different shapes of workpieces. Spiral path was more suited to rotationally-symmetric workpieces while the raster path was more useful for non-rotationally-symmetric workpieces.

In the investigation of multi-radius femoral head polishing, the form correction technology was applied to manufacture a next generation multi-radius femoral head of hip implant. This investigation successfully machined a CoCr multi-radius femoral head through changing the radius of the articulating zone by using a single radius femoral head as a starting sample. The error map used in the multi-radius head polishing was created by design. The concept of designing an error map was verified by an experiment of CPT letters polishing, indicating that this concept is effective for polishing some complicated structure surfaces.

In the final part of the form correction investigation, polishing of a freeform knee femoral component was carried out. The material of the sample was CoCr alloy. However, due to the stroke limitation of the machine tool, only a part of the component was polished. Different from regular surfaces which can be designed directly by the integrated software TPG, freeform surfaces must be designed by a CAD model and the CAD model is then imported into the machine to perform the polishing process. After form correction, the PV of the error map was reduced from $43.9\mu\text{m}$ to $7.27\mu\text{m}$ and RMS was decreased from $3.26\mu\text{m}$ to $1.09\mu\text{m}$. The post polishing measurement of surface roughness was 10.9nm Sa .

9.2 Future work

This dissertation has successfully developed the polishing processes for the improvement of both surface roughness and form error of artificial implants. However, some problems still exist and need to be solved in the future work.

1. In this investigation, the Zeeko IRP200 bonnet polishing machine was used to carry out the experiments. This machine can be widely used to polish the surfaces of flats, spheres, cylinders, cones, etc. When it is applied to polish the freeform surfaces such as knee joints, it is restricted by the range limitation of the machine. Therefore, there is urgent to develop a specific polishing tool and related process for finishing the whole freeform knee implants. In addition, the evaluation metrology for the whole freeform knee femoral component still needs to be improved greatly because the current evaluation methods cannot meet this requirement.
2. In this thesis, the medical grade CoCr alloy polishing has been the main focus. As other bio-materials such as titanium based alloys, stainless steel, and ceramics, etc have been widely applied in the artificial implants, the polishing of these materials should be paid more attention in future work, especially the polishing of hard materials such as ceramics because other machining processes have difficulties to meet the requirements of machining efficiency and accuracy.
3. As the shapes of artificial implants are usually spherical (hip joint) or freeform (knee joint), the effect of curvature on the material removal rate should be the subject of research in future. The created material removal rate model can be modified with the consideration of curvature and consequently improved.
4. When using the polishing cloth to improve the surface roughness, it was found that the polishing cloth was easily damaged under some experimental conditions. Therefore, deterioration of polishing cloths and the effect of the damaged/wear of the polishing cloths on surface roughness need to be further investigated.

REFERENCES

1. NJR, National Joint Registry for England and Wales 9th Annual Report 2012. 2012.
2. ISO7206-2, Implants for surgery — Partial and total hip joint prostheses, in Part 2: Articulating surfaces made of metallic, ceramic and plastics materials. 2011, British Standard: Switzerland
3. Wang, A., et al., Effect of femoral head surface roughness on the wear of ultrahigh molecular weight polyethylene acetabular cups. *Journal of Arthroplasty*, 1998. **13**(6): p. 615-620.
4. Verdonschot, N., E. Tanck, and R. Huiskes, Effects of prosthesis surface roughness on the failure process of cemented hip implants after stem-cement debonding. *Journal of Biomedical Materials Research*, 1998. **42**(4): p. 554-559.
5. Jin, Z., The synovial joint, in *The Leeds Orthopaedic Biomechanics Course*. 2006, University of Leeds: Leeds.
6. Udupa, G., et al., Assessment of surface geometry using confocal scanning optical microscope. *Mechatronics*, 1998. **8**(3): p. 187-215.
7. Murthy, T.S.R., B.R. Rao, and S.Z. Abdin, Evaluation of spherical surfaces. *Wear*, 1979. **57**(1): p. 167-184.
8. Oonishi, H. Studies on the shape and contour of the metal prosthetic head in total hip prosthesis. in *Orthop Surg Trauma Proc 12th SICOT*. 1972.
9. Ito, H., et al., The sphericity of the bearing surface in total hip arthroplasty. *The Journal of Arthroplasty*, 2001. **16**(8): p. 1024-1029.
10. Lippincott , A.L. and J.B. Medley, Low wear ball and cup joint prosthesis. 2000, Wright Medical Technology, Inc: United State Patents.
11. Fisher, J., Acetabular cup, W.I.P. Organization, Editor. 1995: World Intellectual Property Organization.
12. Preston, F.W., The theory and design of glass plate polishing machine. *Journal of the Society of Glass Technology*, 1927. **V11**(p214-256).
13. Adams, B.D., Wrist Arthroplasty. Partial and Total. *Hand Clinics*, 2013. **29**(1): p. 79-89.
14. Rush, S.M. and N. Todd, Salto Talaris Fixed-Bearing Total Ankle Replacement System. *Clinics in Podiatric Medicine and Surgery*, 2013. **30**(1): p. 69-80.
15. Gougoulas, N. and N. Maffulli, History of Total Ankle Replacement. *Clinics in Podiatric Medicine and Surgery*, 2013. **30**(1): p. 1-20.
16. Raiss, P., et al., Results of cemented total shoulder replacement with a minimum follow-up of ten years. *Journal of Bone and Joint Surgery - Series A*, 2012. **94**(23): p. e171.1-e171.10.
17. Joyce, T.J. and A. Unsworth, A test procedure for artificial finger joints. *Proceedings of the Institution of Mechanical Engineers, Part H: Journal of Engineering in Medicine*, 2002. **216**(2): p. 105-110.
18. Joyce, T.J. and A. Unsworth, A literature review of "failures" of the Swanson finger prosthesis in the metacarpophalangeal joint. *Hand surgery : an international journal devoted to hand and upper limb surgery and related research : journal of the Asia-Pacific Federation of Societies for Surgery of the Hand*, 2002. **7**(1): p. 139-146.
19. Tharin, S. and E.C. Benzel, Cervical spine arthroplasty: fact or fiction: the absence of need for arthroplasty. *Clinical neurosurgery*, 2012. **59**: p. 82-90.
20. Wu, J.C., T.H. Tu, and P.V. Mummaneni, Spinal arthroplasty: Differences between the cervical and lumbar spine. *World Neurosurgery*, 2012. **78**(3-4): p. 245-246.
21. Stanton, P. and J.C. Eck, Materials and design characteristics of cervical arthroplasty devices. *Techniques in Orthopaedics*, 2010. **25**(2): p. 93-96.

22. Denaro, V., et al., Cervical spinal disc replacement. *Journal of Bone and Joint Surgery - Series B*, 2009. **91**(6): p. 713-719.
23. Bumpass, D.B. and R.M. Nunley, Assessing the value of a total joint replacement. *Current Reviews in Musculoskeletal Medicine*, 2012: p. 1-9.
24. Hamilton, D., et al., Comparative outcomes of total hip and knee arthroplasty: A prospective cohort study. *Postgraduate Medical Journal*, 2012. **88**(1045): p. 627-631.
25. Charnley, J. and Z. Cupic, The nine and ten year results of the low-friction arthroplasty of the hip. *Clinical Orthopaedics and Related Research*, 1973. **95**: p. 9-25.
26. <http://bonesmart.org>.
27. <http://www.eorthopod.com>.
28. Learmonth, I.D., C. Young, and C. Rorabeck, The operation of the century: total hip replacement. *The Lancet*. **370**(9597): p. 1508-1519.
29. Callaghan, J.J., et al., Results of revision for mechanical failure after cemented total hip replacement, 1979 to 1982. A two to five-year follow-up. *The Journal of bone and joint surgery. American volume*, 1985. **67**(7): p. 1074-1085.
30. Morscher, E.W., Cementless Total Hip Arthroplasty. *Clinical orthopaedics and related research*, 1983. **181**: p. 76-91.
31. <http://www.hipsforyou.com/strykerceramichip.php>.
32. Berry, D.J., et al., Twenty-five-Year Survivorship of Two Thousand Consecutive Primary Charnley Total Hip Replacements Factors Affecting Survivorship of Acetabular and Femoral Components. *The Journal of Bone and Joint Surgery (American)*, 2002. **84**(2): p. 171-177.
33. Cross, M.B., D. Nam, and D.J. Mayman, Ideal Femoral Head Size in Total Hip Arthroplasty Balances Stability and Volumetric Wear. *HSS Journal*: p. 1-5.
34. Berry, D.J., Periprosthetic fractures associated with osteolysis: a problem on the rise. *The Journal of arthroplasty*, 2003. **18**(3): p. 107-111.
35. Vendittoli, P.-A., C. Riviere, and M. Lavigne, et al, Alumina on alumina versus metal on conventional polyethylene: A randomized clinical trial with 9 to 15 years follow-up. *Acta Orthopædica Belgica*, 2013. **79**: p. 181-190.
36. Wroblewski, B., Wear and loosening of the socket in the Charnley low-friction arthroplasty. *Orthop Clin North Am*, 1988. **19**(3): p. 627-30.
37. <http://www.cmprnews.co.uk>.
38. McKee, G. and J. Watson-Farrar, Replacement of arthritic hips by the McKee-Farrar prosthesis. *Journal of Bone & Joint Surgery, British Volume*, 1966. **48**(2): p. 245-259.
39. Cuckler, J.M., et al., Large versus small femoral heads in metal-on-metal total hip arthroplasty. *The Journal of arthroplasty*, 2004. **19**(8, Supplement): p. 41-44.
40. Savarino, L., et al., Ion release in patients with metal-on-metal hip bearings in total joint replacement: A comparison with metal-on-polyethylene bearings. *Journal of Biomedical Materials Research*, 2002. **63**(5): p. 467-474.
41. Haddad, F., et al., Metal-on-metal bearings: The Evidence So Far. *Journal of Bone & Joint Surgery, British Volume*, 2011. **93**(5): p. 572-579.
42. Amstutz, H.C., et al., Metal on Metal Total Hip Replacement Workshop Consensus Document. *Clinical orthopaedics and related research*, 1996. **329**: p. S297-S303.
43. Boutin, P., Total arthroplasty of the hip by fritted aluminum prosthesis. Experimental study and 1st clinical applications [in French]. *Rev Chir Orthop Reparatrice Appar Mot*, 1972. **58**: p. 17.
44. Dorlot, J.M., P. Christel, and A. Meunier, Wear analysis of retrieved alumina heads and sockets of hip prostheses. *Journal of Biomedical Materials Research*, 1989. **23**(S14): p. 299-310.

45. Hasegawa, M., A. Sudo, and A. Uchida, Alumina ceramic-on-ceramic total hip replacement with a layered acetabular component. *Journal of Bone & Joint Surgery, British Volume*, 2006. **88**(7): p. 877-882.
46. Bierbaum, B.E., et al., Ceramic-on-ceramic bearings in total hip arthroplasty. *Clinical Orthopaedics and Related Research*, 2002. **405**: p. 158-163.
47. Bizot, P., et al., Press-fit metal-backed alumina sockets: a minimum 5-year followup study. *Clinical Orthopaedics and Related Research*, 2000. **379**: p. 134-142.
48. Firkins, P., et al., A novel low wearing differential hardness, ceramic-on-metal hip joint prosthesis. *Journal of Biomechanics*, 2001. **34**(10): p. 1291-1298.
49. <http://www.medgadget.com>.
50. Firkins, P.J., et al., A novel low wearing differential hardness, ceramic-on-metal hip joint prosthesis. *Journal of Biomechanics*, 2001. **34**(10): p. 1291-1298.
51. Williams, S., et al., The 2007 Otto Aufranc Award: ceramic-on-metal hip arthroplasties: a comparative in vitro and in vivo study. *Clinical Orthopaedics and Related Research*, 2007. **465**: p. 23-32.
52. Semlitsch, M., et al., New prospects for a prolonged functional life-span of artificial hip joints by using the material combination polyethylene/aluminium oxide ceramic/metal. *Journal of Biomedical Materials Research*, 1977. **11**(4): p. 537-552.
53. <http://evertsmith.com/innovations>.
54. Oonishi H, I.H., Takayama Y, Comparison of wear of UHMW polyethylene sliding against metal and alumina in total hip prostheses. *Bioceramics*, 1989. **1**: p. 278-283.
55. Callaghan J. J, L.S.S., Ceramic on crosslinked polyethylene in total hip replacement: Any better than metal on crosslinked polyethylene. *The Iowa Orthopaedic Journal*, 2009. **29**: p. 1-4.
56. Wroblewski BM, S.P., Low-friction arthroplasty of the hip using alumina ceramic and cross-linked polyethylene. *JBJS-Br*, 2005. **87**: p. 1220-1.
57. Heisel, C., M. Silva, and T.P. Schmalzried, Bearing surface options for total hip replacement in young patients. *Instructional Course Lecturers-American Academy of Orthopaedics Surgeons*, 2004. **53**: p. 49-66.
58. <http://www.mdnews.com>.
59. Smith-Petersen, M., Evolution of mould arthroplasty of the hip joint. *Journal of Bone & Joint Surgery, British Volume*, 1948. **30**(1): p. 59-75.
60. Charnley, J., Arthroplasty of the Hip: A New Operation. *Clinical Orthopaedics and Related Research*, 1973. **95**: p. 4-8.
61. August, A., C. Aldam, and P. Pynsent, The McKee-Farrar hip arthroplasty. A long-term study. *Journal of Bone & Joint Surgery, British Volume*, 1986. **68**(4): p. 520-527.
62. Mont, M.A., et al., Hip resurfacing arthroplasty. *Journal of the American Academy of Orthopaedic Surgeons*, 2006. **14**(8): p. 454-463.
63. <http://www.depuy-asr-hip-recall.com/>.
64. Brown, L.T., The use of 3D surface analysis techniques to investigate the wear of matt surface finish femoral stems in total hip replacement. 2006.
65. Sutherland, C.J., et al., A ten-year follow-up of one hundred consecutive Muller curved-stem total hip-replacement arthroplasties. *The Journal of bone and joint surgery. American volume*, 1982. **64**(7): p. 970-982.
66. Mohler, C.G., et al., Early loosening of the femoral component at the cement-prosthesis interface after total hip replacement. *Journal of Bone and Joint Surgery-A-American Volumes*, 1995. **77**(9): p. 1315-1322.
67. http://en.wikipedia.org/wiki/Knee_replacement.
68. <http://dallasboneandjoint.com/procedures/total-knee-replacement>.
69. <http://www.eorthopod.com>.

70. Hodge, W. and H. Chandler, Unicompartmental knee replacement: a comparison of constrained and unconstrained designs. *The Journal of bone and joint surgery. American volume*, 1992. **74**(6): p. 877.
71. <http://ehealthmd.com/content/different-types-knee-replacements>.
72. Price, A., et al., A mobile-bearing total knee prosthesis compared with a fixed-bearing prosthesis a multicentre single-blind randomised controlled trial. *Journal of Bone & Joint Surgery, British Volume*, 2003. **85**(1): p. 62-67.
73. Bills, P., The development of a geometric methodology for the determination of volumetric wear in total joint replacements and development of a total knee replacement using new and novel measurement techniques. 2007, University of Huddersfield: Huddersfield. p. 288.
74. Walker, P.S., Bearing surface design in total knee replacement. *Engineering in medicine*, 1988. **17**(4): p. 149-156.
75. <http://web.fs.cvut.cz>.
76. Langer, G., Ceramic Tibial Plateau of the 70s, in 7th International BIOLOX Symposium. 2002: Stuttgart.
77. Oonishi, H., H.T., Cementless alumina ceramic total knee prosthesis. *Orthop Ceramic Implants*, 1981. **1**: p. 157-160.
78. Oonishi, H., et al., Alumina versus polyethylene in total knee arthroplasty. *Clinical orthopaedics and related research*, 1992(282): p. 95.
79. Yasuda, K., N. Miyagi, and K. Kaneda, Low friction total knee arthroplasty with the alumina ceramic condylar prosthesis. *Bulletin (Hospital for Joint Diseases (New York, NY))*, 1993. **53**(2): p. 15.
80. Kurtz, S., et al., Future Young Patient Demand for Primary and Revision Joint Replacement: National Projections from 2010 to 2030. *Clinical Orthopaedics and Related Research®*, 2009. **467**(10): p. 2606-2612.
81. http://www.knee-replacement-explained.com/Partial_knee_replacement.html.
82. Colwell, C.W., Rationale for thromboprophylaxis in lower joint arthroplasty. *American Journal of Orthopedics-BELLE MEAD*, 2007. **36**(9): p. 11.
83. Ritter, M.A., E.M. Olberding, and R.A. Malinzak, Ultraviolet lighting during orthopaedic surgery and the rate of infection. *The Journal of Bone & Joint Surgery*, 2007. **89**(9): p. 1935-1940.
84. Katti, K.S., Biomaterials in total joint replacement. *Colloids and Surfaces B: Biointerfaces*, 2004. **39**(3): p. 133-142.
85. Park, J.B. and J.D. Bronzino, *Biomaterials: principles and applications*. 2002: CRC.
86. Teoh, S.H., *Engineering materials for biomedical applications*. Vol. 1. 2004: World scientific.
87. Williams, D.F., *Definitions in biomaterials : proceedings of a consensus conference of the European Society for Biomaterials*, . 1987, Amsterdam: Elsevier.
88. Pinchuk, L.S., *Tribology and biophysics of artificial joints*. Vol. 50. 2006: Elsevier Science Limited.
89. Haynes, E., *Metal alloy*, U.P. Office, Editor. 1907, Kokomo, Indiana: US. p. 2.
90. Haynes, E., *CoCr alloy*, U.P. Office, Editor. 1913: US. p. 4.
91. D.J. Medlin, R.C., Metallography of biomedical orthopaedic alloys, in *Metallography and Microstructures*, Vol 9, ASM Handbook. 2004, ASM International, . p. P961-968.
92. Scales, J. *Arthroplasty of the Hip Using Foreign Materials: A History*. in *Proceedings of the Institution of Mechanical Engineers, Conference Proceedings*. 1966: SAGE Publications.
93. McKee, G.K. and J. Watson-Farrar, Replacement of arthritic hips by the McKee-Farrar prosthesis. *Journal of Bone and Joint Surgery - Series B*, 1966. **48**(2): p. 245-259.

94. Schmalzried, T.P. and J.J. Callaghan, Current Concepts Review - Wear in Total Hip and Knee Replacements. *The Journal of Bone & Joint Surgery*, 1999. **81**(1): p. 115-136.
95. Engh, C., J. Bobyn, and A. Glassman, Porous-coated hip replacement. The factors governing bone ingrowth, stress shielding, and clinical results. *Journal of Bone & Joint Surgery, British Volume*, 1987. **69**(1): p. 45-55.
96. McKee, G., Total hip replacement—past, present and future. *Biomaterials*, 1982. **3**(3): p. 130-135.
97. Ritter, M.A. and E.D. Campbell, Long-term comparison of the Charnley, Muller, and trapezoidal-28 total hip prostheses: A survival analysis. *The Journal of Arthroplasty*, 1987. **2**(4): p. 299-308.
98. Bezzon, O.L., et al., Effect of casting technique on surface roughness and consequent mass loss after polishing of NiCr and CoCr base metal alloys: a comparative study with titanium. *The Journal of Prosthetic Dentistry*, 2004. **92**(3): p. 274-277.
99. Devine, T. and J. Wulff, Cast vs. wrought cobalt chromium surgical implant alloys. *Journal of Biomedical Materials Research*, 1975. **9**(2): p. 151-167.
100. Ratner, B.D., et al., *Biomaterials science: an introduction to materials in medicine*. 2004: Academic press.
101. Walker, P.S. and F.C. Ewald, Method of designing and manufacturing a human joint prosthesis. 1990, Google Patents.
102. Gotman, I., Characteristics of metals used in implants. *Journal of endourology*, 1997. **11**(6): p. 383-389.
103. Del Corso, G.J., Co-Cr-Mo powder metallurgy articles and process for their manufacture. 1995, Google Patents.
104. Davis, J.R., *Handbook of materials for medical devices*. 2003: ASM International (OH).
105. Marti, A., Cobalt-base alloys used in bone surgery. *Injury*, 2000. **31**: p. D18-D21.
106. Wang, K., The use of titanium for medical applications in the USA. *Materials Science and Engineering: A*, 1996. **213**(1): p. 134-137.
107. Chanlalit, C., et al., Stress Shielding Around Radial Head Prostheses. *The Journal of Hand Surgery*, 2012. **37**(10): p. 2118-2125.
108. Brunette, D.M., *Titanium in medicine: material science, surface science, engineering, biological responses, and medical applications*. 2001: Springer Verlag.
109. Bordjih, K., et al., Evaluation of the effect of three surface treatments on the biocompatibility of 316L stainless steel using human differentiated cells. *Biomaterials*, 1996. **17**(5): p. 491-500.
110. Follacci, F.M. and J. Charnley, A comparison of the results of femoral head prosthesis with and without cement. *Clinical Orthopaedics and Related Research*, 1969. **62**: p. 156-161.
111. Kurtz, S.M., *The UHMWPE handbook: ultra-high molecular weight polyethylene in total joint replacement*. 2004: Academic Press.
112. Atkinson, J. and R. Cicek, Silane cross-linked polyethylene for prosthetic applications Part I. Certain physical and mechanical properties related to the nature of the material. *Biomaterials*, 1983. **4**(4): p. 267-275.
113. Wroblewski, B., P. Siney, and P. Fleming, Low-friction arthroplasty of the hip using alumina ceramic and cross-linked polyethylene. *Journal of Bone and Joint Surgery-British Volume*, 1999. **81**: p. 54-55.
114. McKellop, H., et al., Effect of Sterilization Method and Other Modifications on the Wear Resistance of Acetabular Cups Made of Ultra-High Molecular Weight Polyethylene A Hip-Simulator Study. *The Journal of Bone and Joint Surgery (American)*, 2000. **82**(12): p. 1708-1708.

115. Dorr, L.D., et al., Clinical Performance of a Durasul Highly Cross-Linked Polyethylene Acetabular Liner for Total Hip Arthroplasty at Five Years. *The Journal of Bone & Joint Surgery*, 2005. **87**(8): p. 1816-1821.
116. Willmann, G., Ceramics for total hip replacement--what a surgeon should know. *Orthopedics*, 1998. **21**(2): p. 173-177.
117. Masonis, J.L., et al., Zirconia femoral head fractures: A clinical and retrieval analysis. *The Journal of arthroplasty*, 2004. **19**(7): p. 898-905.
118. Hummer Iii, C.D., R.H. Rothman, and W.J. Hozack, Catastrophic failure of modular Zirconia—Ceramic femoral head components after total hip arthroplasty. *The Journal of arthroplasty*, 1995. **10**(6): p. 848-850.
119. Sclippa, E. and K. Piekarski, Carbon fiber reinforced polyethylene for possible orthopedic uses. *Journal of Biomedical Materials Research*, 1973. **7**(1): p. 59-70.
120. Wang, A., et al., Suitability and limitations of carbon fiber reinforced PEEK composites as bearing surfaces for total joint replacements. *Wear*, 1999. **225**: p. 724-727.
121. Hilerio, I., T. Mathia, and C. Alepee, 3D measurements of the knee prosthesis surfaces applied in optimizing of manufacturing process. *Wear*, 2004. **257**(12): p. 1230-1234.
122. Pillai, R., S.G. Pilhii, and A. Damodaran, The lost-wax casting of icons, utensils, bells, and other items in South India. *JOM Journal of the Minerals, Metals and Materials Society*, 2002. **54**(10): p. 12-16.
123. Marinescu, I., H. Tonshoff, and I. Inasaki, *Handbook of ceramic grinding and polishing*. 2000: William Andrew Publishing.
124. Marinescu, I., E. Uhlmann, and T. Doi, *Handbook of lapping and polishing*. 2006: CRC.
125. Marinescu, I., *Tribology of abrasive machining processes*. 2004: William Andrew.
126. Kalpakjian, S. and S. Schmid, *Manufacturing processes for engineering materials*. 1991.
127. <http://www.grinding.com/>.
128. Blunt, L., *The metallurgy of centreless ground surfaces*, in *Department of Manufacturing Systems*. 1989, Coventry Polytechnic: Coventry.
129. <http://www.siemens.com>.
130. Wang, A., et al., Effect of femoral head surface roughness on the wear of ultrahigh molecular weight polyethylene acetabular cups. *The Journal of arthroplasty*, 1998. **13**(6): p. 615-620.
131. ISO7207-2, *Implants for surgery —Components for partial and total knee joint prostheses*, in *Part 2: Articulating surfaces made of metal, ceramic and plastics materials*. 2011, BS: Switzerland
132. Stout, K., Blunt, Liam, *Three-dimensional surface topography*. 2000: Butterworth-Heinemann.
133. Fan, K.-C., C.-D. Su, and J.-I. Mou, Error analysis for a diffraction grating interferometric stylus probing system. *Measurement science and technology*, 2001. **12**(4): p. 482.
134. Zhang, H., *The Influence of Stem Design and Fixation Methods on the Lifetime of Total Hip Replacement in School of Computing and Engineering*. 2009, University of Huddersfield: Huddersfield. p. 186.
135. Wojciech Kaplonek, C.L., *Coherence Correlation Interferometry in Surface Topography Measurements. Recent Interferometry Applications in Topography and Astronomy*, ed. D.I. Padron. 2012.
136. James Millerd, N.B., John Hayes, Brad Kimbrough, Michael North-Morris, James Wyant, *Vibration insensitive interferometry*, in *6th International Conference on Space Optics*. 2006: Noordwijk, The Netherlands.
137. Kimbrough, B., et al. *Low coherence vibration insensitive Fizeau interferometer*.

138. Komanduri, R., D.A. Lucca, and Y. Tani, Technological Advances in Fine Abrasive Processes. *CIRP Annals - Manufacturing Technology*, 1997. **46**(2): p. 545-596.
139. Walker, D.D., et al. The precessions process for efficient production of aspheric optics for large telescopes and their instrumentation. 2002.
140. Evans, C., et al., Material removal mechanisms in lapping and polishing. *CIRP Annals Manufacturing Technology*, 2003. **52**(2): p. 611-633.
141. <http://www.kemet.co.uk/>.
142. Charlton, P., The Application of Zeeko Polishing Technology to Freeform Femoral Knee Replacement Component Manufacture. 2011, University of Huddersfield.
143. <http://www.buehler.com/>.
144. <http://www.universalphotonics.com/>.
145. Zeng, S., Overview of polishing technology and initial experiments (PhD Annual report). 2010, Centre for Precision Technology: Huddersfield.
146. Marinescu, I.D., Tribology of abrasive machining processes. 2004: William Andrew.
147. Schiepers, R.C.J., F.J.J. van Loo, and G. de With, Reactions between α -Silicon Carbide Ceramic and Nickel or Iron. *Journal of the American Ceramic Society*, 1988. **71**(6): p. C-284-C-287.
148. Suphantharida, P. and K. Osseo-Asare, Cerium oxide slurries in CMP. Electrophoretic mobility and adsorption investigations of ceria/silicate interaction. *Journal of the Electrochemical Society*, 2004. **151**(10): p. G658-G662.
149. Sabia, R. and H.J. Stevens, Performance characterization of cerium oxide abrasives for chemical-mechanical polishing of glass. *Machining science and technology*, 2000. **4**(2): p. 235-251.
150. Brinksmeier, E., O. Riemer, and A. Gessenharter, Finishing of structured surfaces by abrasive polishing. *Precision Engineering*, 2006. **30**(3): p. 325-336.
151. Samuels, L.E., Metallographic polishing by mechanical methods. 2003: ASM International (OH).
152. Beilby, G.T., Aggregation and flow of solids: being the records of an experimental study of the micro-structure and physical properties of solids in various states of aggregation, 1900-1921. 1921: Macmillan and co., limited.
153. Bowden, F.P. and D. Tabor, The friction and lubrication of solids. Clarendon Press, 1986, 1986: p. 374.
154. Tian, X., et al., The development and use of thin film thermocouples for contact temperature measurement. *Tribology Trans.*, 1992. **35**(3): p. 491-499.
155. Tian, X. and F.E. Kennedy. Contact surface temperature models for finite bodies in dry and boundary lubricated sliding. 1992.
156. Komanduri, R., On Material Removal Mechanisms in Finishing of Advanced Ceramics and Glasses. *CIRP Annals - Manufacturing Technology*, 1996. **45**(1): p. 509-514.
157. Wang, C.-C., S.-C. Lin, and H. Hochen, A material removal model for polishing glass-ceramic and aluminum magnesium storage disks. *International Journal of Machine Tools and Manufacture*, 2002. **42**(8): p. 979-984.
158. Schinhaerl, M., et al., Mathematical modelling of influence functions in computer-controlled polishing: Part I. *Applied Mathematical Modelling*, 2008. **32**(12): p. 2888-2906.
159. Schinhaerl, M., et al., Mathematical modelling of influence functions in computer-controlled polishing: Part II. *Applied Mathematical Modelling*, 2008. **32**(12): p. 2907-2924.
160. Shorey, A.B., Mechanisms of material removal in magnetorheological finishing (MRF) of glass, PhD thesis. 2000.

161. DeGroot, J.E., et al., Removal rate model for magnetorheological finishing of glass. *Appl Opt*, 2007. **46**(32): p. 7927-7941.
162. Lambropoulos, J.C., S. Xu, and T. Fang, Loose abrasive lapping hardness of optical glasses and its interpretation. *Applied optics*, 1997. **36**(7): p. 1501-1516.
163. Miao, C., J.C. Lambropoulos, and S.D. Jacobs, Process parameter effects on material removal in magnetorheological finishing of borosilicate glass. *Appl Opt*, 2010. **49**(10): p. 1951-1963.
164. Jin, M., et al. Material Removal Model and Contact Control of Robotic Gasbag Polishing Technique. in *Robotics, Automation and Mechatronics*, 2008 IEEE Conference on. 2008: IEEE.
165. Cheung, C., et al., Modelling and simulation of structure surface generation using computer controlled ultra-precision polishing. *Precision Engineering*, 2011. **35**(4): p. 574-590.
166. Zhang, L., et al., An investigation of material removal in polishing with fixed abrasives. *Proceedings of the Institution of Mechanical Engineers, Part B: Journal of Engineering Manufacture*, 2002. **216**(1): p. 103-112.
167. Wang, S. and Y. Su, An investigation on machinability of different materials by hydrodynamic polishing process. *Wear*, 1997. **211**(2): p. 185-191.
168. Xie, Y. and B. Bhushan, Effects of particle size, polishing pad and contact pressure in free abrasive polishing. *Wear*, 1996. **200**(1-2): p. 281-295.
169. Huang, M.-F., T.-R. Lin, and H.-C. Chiu, Effect of machining characteristics on polishing ceramic blocks. *The International Journal of Advanced Manufacturing Technology*, 2005. **26**(9): p. 999-1005.
170. Trezona, R.I., D.N. Allsopp, and I.M. Hutchings, Transitions between two-body and three-body abrasive wear: influence of test conditions in the microscale abrasive wear test. *Wear*, 1999. **225-229**(Part 1): p. 205-214.
171. Stachowiak, G.B. and G.W. Stachowiak, The effects of particle characteristics on three-body abrasive wear. *Wear*, 2001. **249**(3-4): p. 201-207.
172. Su, Y.-T., et al., Effects of tool surface irregularities on machining rate of a hydrodynamic polishing process. *Wear*, 1996. **199**(1): p. 89-99.
173. Kasai, T., K. Horio, and A. Kobayashi, Improvement of Conventional Polishing Conditions for Obtaining Super Smooth Surfaces of Glass and Metal Works. *CIRP Annals - Manufacturing Technology*, 1990. **39**(1): p. 321-324.
174. Savio, G., R. Meneghello, and G. Concheri, A surface roughness predictive model in deterministic polishing of ground glass moulds. *International Journal of Machine Tools and Manufacture*, 2009. **49**(1): p. 1-7.
175. ISO25178-2, Geometric Product Specifications (GPS)-Surface Texture: Areal-Part 2: Terms, Definitions and Surface Texture Parameters. 2009.
176. Blunt, L. and X. Jiang, Advanced techniques for assessment surface topography: development of a basis for 3D surface texture standards" surfstand". 2003: Butterworth-Heinemann.
177. Xi, F. and D. Zhou, Modeling surface roughness in the stone polishing process. *International Journal of Machine Tools and Manufacture*, 2005. **45**(4-5): p. 365-372.
178. Jones, R.A., Optimization of Computer Controlled Polishing. *Applied optics*, 1977. **16**(1): p. 218-224.
179. Fang, H., P. Guo, and J. Yu, Dwell function algorithm in fluid jet polishing. *Appl Opt*, 2006. **45**(18): p. 4291-4296.
180. Zhou, L., Study on Theory and Technology in Ion Beam Figuring for Optical Surfaces (in Chinese), in *School of Mechatronic Engineering and Automation*. 2008, National University of Defense Technology: Changsha.

181. Deng, W.J., et al. Novel method for optimizing polishing tool-path in CCOS based on weighted-iterative algorithm. 2009.
182. Carnal, C.L., C.M. Egert, and K.W. Hylton, Advanced matrix-based algorithm for ion-beam milling of optical components. 1992: p. 54-62.
183. Mori, Y., K. Yamauchi, and K. Endo, Elastic emission machining. *Precision Engineering*, 1987. **9**(3): p. 123-128.
184. Su, Y.-T., et al., Investigation of elastic emission machining process: lubrication effects. *Precision Engineering*, 1995. **17**(3): p. 164-172.
185. Mori, Y., K. Yamauchi, and K. Endo, Mechanism of atomic removal in elastic emission machining. *Precision Engineering*, 1988. **10**(1): p. 24-28.
186. Golini, D., et al. Magnetorheological finishing (MRF) in commercial precision optics manufacturing. 1999: SPIE.
187. Jacobs, S. and S. Arrasmith, Overview of magnetorheological finishing (MRF) for precision optics manufacturing. *Ceram. Trans*, 1999. **102**: p. 185-199.
188. Wilson, S., D. Reicher, and J. McNeil, Surface figuring using neutral ion beams. *Advances in Fabrication and Metrology for Optics and Large Optics*: p. 74-81.
189. Gailly, P., et al., Ion beam figuring for precision optics.
190. Zhou, L., et al., Optimum removal in ion-beam figuring. *Precision Engineering*, 2009.
191. Ji, S., et al., Design of spinning-inflated-gasbag polishing tool and its automated system for free-form mould. *WSEAS Transactions on Systems*, 2006. **5**(6): p. 1448-1454.
192. Bingham, R., D. Walker, and D. Kim, et al. A Novel automated process for aspheric surfaces. in *Proc. SPIE 2000*. San Diego, CA, USA
193. Walker, D., R. Freeman, and G. McCavana, et al. The Zeeko/UCL process for polishing large lenses and prisms. 2001: SPIE.
194. Walker, D.D., A. Beaucamp, and D. Brooks, et al. Novel CNC polishing process for control of form and texture on aspheric surfaces. in *International Symposium on Optical Science and Technology*. 2002: SPIE.
195. Dunn, C.R. and D.D. Walker, Pseudo-random tool paths for CNC sub-aperture polishing and other applications. *Opt Express*, 2008. **16**(23): p. 18942-18949.
196. Walker, D.D., et al. Precessions process for efficient production of aspheric optics for large telescopes and their instrumentation. in *Astronomical Telescopes and Instrumentation*. 2003: International Society for Optics and Photonics.
197. Li, H., et al., Modelling and measurement of polishing tool influence functions for edge control. *Journal of the European Optical Society-Rapid publications*, 2011. **6**.
198. Walker, D., G. Yu, and H. Li, et al, Edges in CNC polishing: from mirror-segments towards semiconductors, paper 1: edges on processing the global surface. *Opt Express*, 2012. **20**(18): p. 19787-19798.
199. Walker, D., et al. Commissioning of the first Precessions 1.2-m CNC polishing machines for large optics. in *Optics & Photonics*. 2006: International Society for Optics and Photonics.
200. Walker, D.D., D. Brooks, and R. Freeman, et al. First aspheric form and texture results from a production machine embodying the precession process. in *International Symposium on Optical Science and Technology*. 2001: SPIE.
201. Walker, D., et al. Automated optical fabrications: first results from the new Precessions 1.2 m CNC polishing machine. 2006.
202. Walker, D.D., et al. New results from the Precessions polishing process scaled to larger sizes. in *Proceedings of SPIE*. 2004.
203. Walker, D., et al., Zeeko 1 metre polishing system. 2005.
204. www.zeeko.co.uk.

205. Welghtman, B. and D. Light, The effect of the surface finish of alumina and stainless steel on the wear rate of UHMW polyethylene. *Biomaterials*, 1986. **7**(1): p. 20-24.
206. Liang, H., et al., Applications of plasma coatings in artificial joints: an overview. *Vacuum*, 2004. **73**(3-4): p. 317-326.
207. Roy, R., A primer on the Taguchi method. 1990: Society of Manufacturing.
208. Liu, C.H., C.C.A. Chen, and J.-S. Huang, The polishing of molds and dies using a compliance tool holder mechanism. *Journal of Materials Processing Technology*, 2005. **166**(2): p. 230-236.
209. Jiang, M. and R. Komanduri, Application of Taguchi method for optimization of finishing conditions in magnetic float polishing (MFP). *Wear*, 1997. **213**(1-2): p. 59-71.
210. Tsai, F.C., et al., A Taguchi and experimental investigation into the optimal processing conditions for the abrasive jet polishing of SKD61 mold steel. *International Journal of Machine Tools and Manufacture*, 2008. **48**(7-8): p. 932-945.
211. Lin, T.-R., The use of reliability in the Taguchi method for the optimisation of the polishing ceramic gauge block. *The International Journal of Advanced Manufacturing Technology*, 2003. **22**(3): p. 237-242.
212. Liao, H.-T., J.-R. Shie, and Y.-K. Yang, Applications of Taguchi and design of experiments methods in optimization of chemical mechanical polishing process parameters. *The International Journal of Advanced Manufacturing Technology*, 2008. **38**(7): p. 674-682.
213. Zeng, S., et al. Investigation of the material removal characteristic for polishing CoCr alloy. in CEARC 10. University of Huddersfield.
214. Robert H. Lochner, J.E.M., *Designing for Quality – An Introduction to the Best of Taguchi and Western Methods of Statistical Experimental Design*. First ed. 1990: Chapman and Hall.
215. Stout, K.J. and L. Blunt, eds. *Three-Dimensional surface topography*. 1994, Penton press.
216. S. Timoshenko, J.N.G., *Theory of elasticity*. 1951, New York: McGraw-Hill.
217. Jianfeng, L., *Integrated modeling of chemical mechanical planarization/polishing (CMP) for intergrated circuit fabrication: from particle scale to die and wafer scales*. 2003, University of California, Berkeley: Berkeley.
218. Speich, M. and R. Börret, Mould fabrication for polymer optics. *Journal of the European Optical Society-Rapid publications*, 2011. **6**.
219. Miao, C., et al., Shear stress in magnetorheological finishing for glasses. *Applied optics*, 2009. **48**(13): p. 2585-2594.
220. Cumbo, M.J., *Chemo-Mechanical interactions in optical polishing*, in *The Institute of Optics*. 1993, University of Rochester: Rochester.
221. Rososhansky, M., X. Fengfeng, and L. Yuwen. Coverage based tool path planning for automated polishing using contact stress theory. in *Automation Science and Engineering (CASE)*, 2010 IEEE Conference on. 2010.
222. Tam, H.-y. and H. Cheng, An investigation of the effects of the tool path on the removal of material in polishing. *Journal of Materials Processing Technology*, 2010. **210**(5): p. 807-818.
223. Mizugaki, Y., M. Sakamoto, and T. Sata, Fractal Path Generation for a Metal-Mold Polishing Robot System and Its Evaluation by the Operability. *CIRP Annals - Manufacturing Technology*, 1992. **41**(1): p. 531-534.
224. Tam, H.-y., O. Chi-hang Lui, and A. C.K. Mok, Robotic polishing of free-form surfaces using scanning paths. *Journal of Materials Processing Technology*, 1999. **95**(1-3): p. 191-200.

225. Jones, R.A., Optimization of computer controlled polishing. *Appl. Opt.*, 1977. **16**(1): p. 218-224.
226. Quesada, M.J., D.R. Marker, and M.A. Mont, Metal-on-Metal Hip Resurfacing: Advantages and Disadvantages. *J Arthroplasty*, 2008. **23**(7, Supplement): p. 69-73.
227. Dowson, D., Tribological principles in metal-on-metal hip joint design. *Proceedings of the Institution of Mechanical Engineers, Part H: Journal of Engineering in Medicine*, 2006. **220**(2): p. 161-171.
228. Doorn, P.F., et al., Tissue reaction to metal on metal total hip prostheses. *Clin Orthop Relat Res*, 1996. **329**: p. S187-S205.
229. Dobbs, H. and M. Minski, Metal ion release after total hip replacement. *Biomaterials*, 1980. **1**(4): p. 193-198.
230. Anissian, H.L., et al., The wear pattern in metal-on-metal hip prostheses. *J Biomed Mater Res*, 2001. **58**(6): p. 673-678.
231. Liu, F., et al., Effect of wear of bearing surfaces on elastohydrodynamic lubrication of metal-on-metal hip implants. *Proc Inst Mech Eng H J Eng Med*, 2005. **219**(5): p. 319-328.
232. Vassiliou, K., et al., The effect of 'running-in' on the tribology and surface morphology of metal-on-metal Birmingham hip resurfacing device in simulator studies. *Proc Inst Mech Eng H J Eng Med*, 2006. **220**(2): p. 269-277.
233. Meng, Q., et al., Contact mechanics and elastohydrodynamic lubrication in a novel metal-on-metal hip implant with an aspherical bearing surface. *J Biomech*, 2010. **43**(5): p. 849-857.
234. Hu, X.Q., et al., The tribological behaviour of different clearance MOM hip joints with lubricants of physiological viscosities. *Proc Inst Mech Eng H J Eng Med*, 2011. **225**(11): p. 1061-1069.
235. ISO17450-1, Geometrical product specification (GPS)—General concepts—Part1: Model for geometric specification and verification. 2005.
236. Savio, E., L. De Chiffre, and R. Schmitt, Metrology of freeform shaped parts. *CIRP Annals - Manufacturing Technology*, 2007. **56**(2): p. 810-835.
237. Farin, G.E., *Curves and Surfaces for Computer-Aided Geometric Design: A Practical Code*. 1996: Academic Press, Inc. 429.
238. Piegl, L.A. and W. Tiller, *The NURBS book*. 1997: Springer Verlag.
239. Barker, R., et al., *Software Support for Metrology Best Practice Guide No. 4*. 2004.
240. Zhang, X., *Freeform surface fitting for precision coordinate metrology*. 2009, University of Huddersfield: Huddersfield. p. 200.
241. Chen, S., *Geometrical approach to subaperture stitching interferometry for aspheric surfaces*. 2006, National University of Defense Technology: Changsha.
242. Horn, B.K.P., Closed-form solution of absolute orientation using unit quaternions. *JOSA A*, 1987. **4**(4): p. 629-642.
243. Kwak, J.-S., Application of Taguchi and response surface methodologies for geometric error in surface grinding process. *International Journal of Machine Tools and Manufacture*, 2005. **45**(3): p. 327-334.
244. Zhang, L., et al., Investigation into electrorheological fluid-assisted polishing. *International Journal of Machine Tools and Manufacture*, 2005. **45**(12-13): p. 1461-1467.
245. Nalbant, M., H. Gökaya, and G. Sur, Application of Taguchi method in the optimization of cutting parameters for surface roughness in turning. *Materials & Design*, 2007. **28**(4): p. 1379-1385.

246. Walker, D.D., A.T. Beaucamp, and R.G. Bingham, et al. Precessions aspheric polishing: new results from the development program. in *Optical Science and Technology, SPIE's 48th Annual Meeting*. 2004: International Society for Optics and Photonics.
247. Miao, C., et al. Frictional investigation for magnetorheological finishing (MRF) of optical ceramics and hard metals. 2008: Optical Society of America.